Report
P-17-15
August 2017

Calibrated modelling of resaturation in the Bentonite Rock Interaction Experiment (BRIE)

Task 8D of SKB Task Forces EBS and GWFTS

Steven Baxter
David Holton
Andrew Hoch

SVENSK KÄRNBRÄNSLEHANTERING AB

SWEDISH NUCLEAR FUEL
AND WASTE MANAGEMENT CO

Box 3091, SE-169 03 Solna
Phone +46 8 459 84 00
skb.se

SVENSK KÄRNBRÄNSLEHANTERING

ISSN 1651-4416
SKB P-17-15
ID 1589359
August 2017

Calibrated modelling of resaturation in the Bentonite Rock Interaction Experiment (BRIE)

Task 8D of SKB Task Forces EBS and GWFTS

Steven Baxter, David Holton, Andrew Hoch
Amec Foster Wheeler

Abstract

Radioactive Waste Management Limited (RWM) has been established to manage the safe disposal of high level wastes and spent fuel within the UK Geological Disposal Facility (GDF). The UK does not currently have a final disposal concept for its GDF, instead RWM is considering a number of generic designs which include the possible use of bentonite as a buffer material, forming part of an engineered barrier system (EBS) to surround certain containers being considered for disposal.

Task 8D, the focus of this report, forms one of the tasks of the SKB EBS Task Force, and consists of modelling the Bentonite Rock Interaction Experiment (BRIE) at the Äspö Hard Rock Laboratory (HRL). This experiment represents a unique opportunity to model an *in situ* experiment of the resaturation of bentonite in a fractured rock. It shows highly heterogeneous resaturation profiles consistent with discrete fracture inflows. The high quality data provides an opportunity to apply state-of-the-art modelling to reflect this heterogeneity. This modelling was able to capture the range of resaturation times observed, which would be necessary in predicting the range of resaturation of bentonite at a real site. Moreover, the work highlighted the importance in the resaturation of bentonite of the rock matrix (the rock between the discrete fractures). Where the rock matrix permeability is modelled to be low, the resaturation of the bentonite is slow. As the rock matrix becomes more permeable, the resaturation becomes dominated by the matrix properties. In addition, modelling the BRIE has identified the importance of the geometric distribution of water bearing fractures intersecting the deposition hole on the resaturation rates and profiles of the emplaced bentonite. When the fractures are distributed uniformly, the bentonite will resaturate much faster than if the same fractures were clustered at a discrete location within the hole.

The overall implications of the modelling results from this study are that account must be taken of both the rock matrix and the fractures when predicting the resaturation of emplaced bentonite. As such, the results presented are shown to predict the range of resaturation rates observed within the BRIE; whereas if the host rock was represented by a uniform permeability, neither the resaturation times or profiles would be predicted correctly.

Sammanfattning

Radioactive Waste Management Limited (RWM) har inrättats för att hantera en säker slutförvaring av högaktivt avfall och använt kärnbränsle inom det brittiska systemet för Geological Disposal Facility (GDF). Storbritannien har för närvarande inte ett slutförvarskoncept för sin GDF, men RWM överväger i stället ett antal generiska förvarsutformningar som inkluderar en möjlig användning av bentonit som buffertmaterial. I dessa förvarsutformningar avses det att bentoniten ska omge avfallsbehållarna och därmed ingå i ingenjörsbarriärsystemet (EBS) för slutförvaret.

Task 8D, som står i fokus för denna rapport, utgör en av modelleringsuppgifterna inom SKB EBS Task Force, innefattar modellering av Bentonite Rock Interaction Experiment (BRIE) som utfördes i Äspö Hard Rock Laboratory (HRL). Detta experiment representerar en unik möjlighet att modellera ett in situ-experiment för upptag av vatten i omättad bentonit som placerats i sprickigt berg. Bentoniten uppvisar mycket heterogena vattenupptagsprofiler som korrelerar med de diskreta sprickinflödena som har observerats. Högkvalitativa data ger möjlighet att tillämpa state-of-the-art modellering för att återspegla denna heterogenitet. Modelleringen kunde återspegla de återmättningstider som observerades, vilket är en nödvändighet för att kunna förutsäga de förväntade intervallet av återmättningen för bentonit på en verklig plats. Vidare framhöll arbetet vikten av vattenupptag i bentoniten från bergmatrisen (berget mellan de diskreta sprickorna). Om bergmatrispermeabiliteten ansatt till ett lågt värde i modelleringen är bentonitens återmättning långsam. Om bergmatrisen blir mer permeabel domineras återmättningen av matrisegenskaperna. Dessutom har modellering av BRIE identifierat vikten av den geometriska fördelningen av de vattenbärande sprickor som skär deponeringshålet med avseende på mättnadsgraden och profilerna i den inplacerade bentoniten. Om sprickorna fördelas jämnt, kommer bentoniten att återmättas mycket snabbare än om samma sprickor samlas på samma plats i hålet.

Den övergripande slutsatsen av modelleringsresultaten från denna studie är att man måste ta hänsyn till både bergmatrisen och sprickorna när man predikterar återmättnad av inplacerad bentonit. Den utförda modelleringen visar på att de presenterade resultaten förutsäger det intervall av återmättningstider som har observerats inom BRIE; emedan om berget representeras med en likformig permeabilitet, skulle varken återmättnadstiderna eller profilerna kunna förutsägas korrekt.

Executive summary

RWM is considering a number of generic designs for the disposal of high heat generating wastes that include the use of bentonite as a buffer material, forming part of an engineered barrier system (EBS) to surround the disposal containers within a geological disposal facilty (GDF). The bentonite buffer has a number of safety functions, including

- protecting the disposal containers from detrimental processes, including hydraulic, mechanical, chemical and biological effects, and
- retarding the release of radionuclides from any failed waste container.

RWM is participating in the SKB EBS Task Force, which is led by SKB, to develop the UK's capabilities in modelling of processes relevant to bentonite. Task 8 of the Task Force consists of modelling the Bentonite Rock Interaction Experiment (BRIE) at the Äspö Hard Rock Laboratory (HRL). Task 8 currently consists of five subtasks (8A–8D, 8F) of increasing complexity from initial scoping analysis up to site-scale models, including predictive modelling of various aspects of the BRIE. The fourth subtask, Task 8D, is the focus of this report, providing the opportunity to consider hydraulic interactions at the interface of a fractured bedrock and emplaced bentonite on the scale of 30 cm diameter deposition holes to more realistically capture the wetting behaviour of bentonite.

Through modelling the BRIE, the feasibility of using a physically realistic approach to simulate the interface between bentonite and fractured host rock has been demonstrated. The developed approach has identified:

- The saturation of bentonite is highly heterogeneous, and accurate representation of the surrounding fractured bedrock is critical to understanding the hydration of emplaced bentonite.
  - Previously, Task 8C developed models of the BRIE using limited data. As part of Task 8D, additional data are available, typical of the additional data generated during repository construction in support of siting decisions for deposition holes. Using this new information, both the fracture network geometry and the hydraulic properties of the Task 8C models have been refined.
- The significant potential of the combination of CONNECTFLOW and TOUGH2 software to simulate the heterogeneous hydration of the bentonite.
- During the Task 8C study, the saturation rate of bentonite in a fractured host rock was found to be significantly affected by both the locations of the water producing fractures and total volume of groundwater ingress to the deposition holes. During Task 8D, the locations of these fractures are specified deterministically; and through conditioning the local fracture network, uncertainties in the location and magnitude of inflows to the deposition holes reduced. A direct consequence of this is that the resaturation rates and saturation profiles of emplaced bentonite are constrained.
- The permeability of the rock matrix very strongly determines the prediction of the resaturation times of the emplaced bentonite. Where the rock matrix permeability is modelled to be low, the resaturation of the bentonite is slow. As the rock matrix becomes more permeable, the resaturation becomes dominated by the matrix properties. This has implications for the local characterisation of the host rock.

Although models to date have been developed that are specific to the BRIE at the Äspö HRL, the tools, calibration techniques and methodologies developed are generic, and are directly applicable to any future work carried out on UK specific issues for the simulation of bentonite hydration in a higher strength rock.

List of acronyms and abbreviations

BIPS	Borehole Image Processing System
BRIE	Bentonite Rock Interaction Experiment
CCDF	Complementary Cumulative Density Function
CPM	Continuous Porous Medium
DFN	Discrete Fracture Network
EBS	Engineered Barrier System
ECPM	Equivalent Continuous Porous Medium
EDZ	Excavation Disturbed Zone
EOS	Equation-Of-State
GDF	Geological Disposal Facility
GID	Pre- and post- processing software for numerical simulations, including geometrical modelling and meshing (http://gid.cimne.upc.edu/).
GOCAD	Subsurface modelling software, used for seismic, geological and reservoir modelling. Industry standard file formats for storing grid-scale permeabilities and porosities (http://www.pdgm.com/products/gocad.aspx).
GWFT	Groundwater Flow and Transport of solutes
HRL	Hard Rock Laboratory
HSR	Higher Strength Rocks
NDA	Nuclear Decommissioning Authority
PFL	Posiva Flow Log
RWM	Radioactive Waste Management Limited
SDM	Site Descriptive Model

Contents

1 Introduction and objectives 9
1.1 Background of Task 8 9
1.2 Scope of Task 8D 10
1.2.1 Objectives 10
1.2.2 Requested modelling results 11
1.3 Report structure 11

2 Task 8D specification 13
2.1 Geometrical data 13
2.2 Design of bentonite installation 17
2.2.1 Filling of the outer slot 21
2.3 Fracture statistics used to describe the 'background' discrete fracture network model of the rock 21
2.3.1 Development of DFN model 22
2.3.2 Input data 22
2.3.3 Orientation distribution 23
2.3.4 Spatial distribution 24
2.3.5 Size distribution 24
2.3.6 Intensity 25
2.3.7 Uncertainty 26
2.3.8 Fracture statistics 26
2.4 Deterministic fracture information 26
2.4.1 Local refinement of wfracture_01 27
2.4.2 Fracture intersection with deposition holes KO0017G01 and KO0018G01 27
2.5 Rock stresses 28
2.6 Boundary conditions 28
2.7 Initial conditions 29
2.8 Material specifications 30
2.8.1 Rock matrix 30
2.8.2 Rock fractures 31
2.8.3 Deterministic fractures 31
2.8.4 Excavated disturbed zones / shallow fractures 32
2.8.5 Bentonite 32
2.9 Calibration targets 32
2.9.1 Task 8C calibration 33
2.9.2 Ambient pressure 33
2.9.3 Inflow to TASO 34
2.9.4 Inflow boreholes 35
2.9.5 Pressure responses and flow 35
2.9.6 Inflow to 30 cm boreholes 38

3 Modelling Task 8D 41
3.1 Concepts and methodology 41
3.1.1 CONNECTFLOW 42
3.1.2 TOUGH2 44
3.2 Model description 46
3.2.1 Geometrical description 46
3.2.2 Processes considered 46
3.2.3 Boundary and initial conditions 46
3.2.4 Parameters 48
3.2.5 Proposed relationships 53
3.2.6 Numerical model 56
3.3 Calibration, variants and sensitivities 56

4 A review of modelling in Task 8C 59
4.1 Differences between Task 8C and 8D 59
4.2 Key findings from Task 8C1 59
4.2.1 Pressure build-up calculations from Task 8C1 59
4.2.2 Inflow calculations from Task 8C1 60
4.3 Key findings from Task 8C2 61

5 Task 8D1: Calibrating the Fracture Network 63
5.1 Model calibration 63
5.1.1 Background fracture intensity 64
5.1.2 Transmissivity correlation 69
5.1.3 Local description of wfracture_01 71
5.1.4 Deterministic specification of fracture intersections 72
5.1.5 Calibration summary and conclusions 76
5.2 Deposition holes KO0017G01 and KO0018G01 77
5.2.1 Upscaling 80

6 Task 8D2: Resaturation of bentonite 81
6.1 Simulation of open deposition holes 82
6.2 Resaturation of emplaced bentonite 84
6.2.1 Bentonite hydration at sensor locations 88
6.2.2 Resaturation times 96
6.2.3 Pressures in the deposition hole near field 97
6.2.4 Saturations in the deposition hole near field 97
6.2.5 Pressure evolution within the bentonite 97
6.2.6 Pressure evolution within the bedrock 105
6.3 Effects of varying parameterisation of the rock matrix 108
6.3.1 Rock matrix constitutive relationships 108
6.3.2 Rock matrix permeability (1×10^{-23} m^2) 116
6.4 Effects of varying the relative gas permeability 116
6.5 Effects of varying the bentonite permeability 122

7 Comparison with experimental results 125
7.1 Relative humidity in KO0017G01 125
7.2 Relative humidity in KO0018G01 129

8 Discussion and conclusions 133
8.1 Evaluation of conceptual models and modelling approach 133
8.1.1 Quantitative results 134
8.1.2 Qualitative discussion 134
8.1.3 Comparison to experimental results 135
8.2 Main conclusions 136
8.3 Potential model development 136
8.3.1 Heterogeneity of the rock matrix 136
8.3.2 Heterogeneity of inflows to the deposition holes 136

9 Acknowledgements 137

References 139

Appendix 1 Task 8D1: Calibration of the Fracture Network 141

Appendix 2 Task 8D2: Stochastic variability of the Fracture Network 171

1 Introduction and objectives

In the UK, the management and delivery of geological disposal for higher-activity radioactive wastes is the responsibility of Radioactive Waste Management Limited (RWM). To facilitate the safe disposal of these wastes, a multiple barrier concept is utilised to isolate the wastes from the biosphere. Currently, the UK does not have a defined concept for a Geological Disposal Facility (GDF) and is considering generic designs for a UK GDF (NDA 2010). However, for all but disposal in salt, these generic designs may utilise a bentonite buffer material or 'local backfill' as part of an engineered barrier system (EBS), surrounding the emplaced disposal container. In addition, and in combination with crushed rock spoil, bentonite could also form the mass backfill used within deposition tunnels of a GDF. The GDF concepts of a number of other countries also propose the use of a bentonite buffer material (e.g. SKB and Posiva's KBS-3 concept (SKB 2006)).

The bentonite buffer can provide several safety functions, as detailed in Holton et al. (2012) including:

- Protecting the disposal containers from detrimental processes, including hydraulic, mechanical and chemical effects.
- Retarding the release of radionuclides from any failed waste container.

The understanding of bentonite behaviour in the context of a UK GDF has been reviewed (NDA 2012, Wilson et al. 2010).

The work described in this report has been undertaken as part of SKB EBS Task Force programme, which is led by SKB. The Task Force considers coupled Thermal (T), Hydraulic (H), Mechanical (M) and Chemical (C) processes relevant to a bentonite buffer material via a number of modelling tasks. These tasks range from purely hydraulic (two-phase) models through to coupled T-H, T-H-M and T-H-C problems.

Through participation, RWM intends to strengthen and extend the UK's capabilities by assisting the development of modelling of processes relevant to bentonite, applicable either to the current GDF concepts, or to future site-specific stages of the UK disposal programme.

This report describes modelling the Bentonite Rock Interaction Experiment (BRIE) at Äspö under Task 8D of the EBS Task Force, which is investigating the hydraulic interactions between the bedrock and the bentonite buffer, under Task 8 of the EBS Task Force (Vidstrand et al. 2017). Task 8 is split into a number of subtasks and this report presents the modelling results for Task 8D. Task 8D follows on from Task 8C, which has previously been modelled by AMEC (Baxter et al. 2013) Task 8C was concerned with the prediction of resaturation of the central deposition holes of the BRIE experiment, with limited deterministic data available for constraining models. Task 8D revisits the BRIE experiment, refining resaturation predictions through the additional hydraulic data provided as part of this task (Vidstrand et al. 2017); typical of the additional data generated during repository construction in support of siting deposition holes.

It is noted that although models to date have been developed that are specific to the BRIE at the Äspö Hard Rock Laboratory (HRL), the tools, techniques and methodologies developed are generic, and are directly applicable to any hard fractured rock environment. Hence, in the UK's preparatory phase this work is of relevance to higher strength rocks (HSR) in which bentonite may provide part of the EBS.

1.1 Background of Task 8

Task 8 is a collaborative research project between the Äspö Task Force on Groundwater Flow and Transport of Solutes (GWFT) and Engineered Barrier Systems (EBS). As detailed in the task description (Vidstrand et al. 2017). Task 8 is designed to improve

- the scientific understanding of the exchange of water between the sparsely fractured rock and the bentonite,
- the predictions of the wetting of the buffer,

- the characterisation methods of container deposition boreholes, and
- the methods used for establishing deposition hole criteria.

The BRIE, conducted at the Äspö Hard Rock Laboratory (HRL), provides the basis for modelling to describe the resaturation of bentonite in Task 8. The BRIE is an experiment at the Äspö HRL, being run concurrently to Task 8. The BRIE intends to address (Vidstrand et al. 2017)

- site selection,
- the drilling of central boreholes and subsequent characterisation of the site using borehole logging and hydraulic tests, and
- the characterisation of two central boreholes for the installation of a bentonite buffer.

Task 8 is not intended to be a fully-coupled modelling exercise (Vidstrand et al. 2017); i.e. fully incorporating thermal, chemical, or mechanical aspects. Instead, the task aims to improve the knowledge of the bedrock-bentonite interface with regard to how groundwater flow resaturates the bentonite.

1.2 Scope of Task 8D

Task 8 consists of five subtasks (8A–8D, 8F) of increasing complexity from initial scoping analysis up to site-scale models, designed to provide predictive modelling of various aspects of the BRIE. Previous analysis of Task 8C (Baxter et al. 2013) provided predictions of inflow to central boreholes planned for the TASO tunnel (located at a depth ~420 m at the Äspö HRL) of the BRIE experiment.

Task 8D involves the use of additional hydraulic data (not available at the time of the Task 8C) used to refine the location of inflows to two 30 cm diameter deposition holes as well as the wetting of emplaced bentonite. The additional data provided as part of Task 8D includes

- refinement of the geometrical details of the large-scale deterministic fracture zones,
- geometric details of fracture distribution for an additional 14 boreholes drilled in the floor of the TASO tunnel and four in the tunnel walls, local to the five probe boreholes, and
- an update to measurements from the deposition holes, including
  - inflow estimates and pressure responses within the five probe boreholes from additional, short duration tests,
  - inflow estimates for the two 30 cm diameter deposition holes,
  - fracture intersections to the deposition holes,
  - inflow estimates from the "nappy" experiments[1] of the TASO tunnel, and
  - details of the installation process for the bentonite within each of the deposition holes.

Participation in Task 8D allows the opportunity to develop methodologies for calibrating models of the fractured rock using additional site measurements in an iterative way as they become available. By considering this additional data set systematically, it is possible to determine the significance of such data in reducing uncertainties.

1.2.1 Objectives

Task 8D is subdivided into two parts, Task 8D1 and Task 8D2. Task 8D1 considers the inflow to open deposition holes at atmospheric conditions. This allows a direct comparison of simulations with additional field data from the BRIE provided as input to Task 8D, allowing further calibration of the models. In summary, objectives for Task 8D1 (Vidstrand et al. 2017) are

- to calculate inflows and inflow characteristics to two 76 mm diameter probe boreholes,
- to predict inflows and inflow spatial characteristics to two 30 cm diameter open deposition holes, and

[1] Nappy experiments are performed by placing absorbent sheets (nappies) along the tunnel wall. Flow measurements are obtained by dividing the increase of weight of these nappies by the corresponding time.

- to identify boundary conditions and initial conditions to the field experiment to predict the resaturation of bentonite blocks within the two 30 cm deposition holes.

Information from the last point above is used in Task 8D2, modelling the resaturation of bentonite based on the flow models established in Task 8D1. Results from Task 8D2 are intended for use as modelling predictions of the BRIE, running concurrently to this modelling task. The objectives for Task 8D2 (Vidstrand et al. 2017) are

- to simulate profiles for the wetting of bentonite emplaced in the two deposition holes, characterised in Task 8D1,
- to evaluate the effects of heterogeneous fracture flow on the wetting of emplaced bentonite,
- to evaluate the effects of matrix properties on the wetting of emplaced bentonite, and
- to provide comparison with Task 8C.

1.2.2 Requested modelling results

The outputs required by the EBS Task Force from the modelling are predictions for the resaturation profiles of the emplaced bentonite, including

- relative humidity and saturation profiles across the bentonite and surrounding host rock, and
- times for the bentonite to reach 95 % resaturation.

1.3 Report structure

This report presents the AMEC modelling results for Task 8D, including predictions for the central deposition holes of the BRIE at the Äspö HRL. The report structure is as follows:

- Section 2 provides details of the specification of Task 8D as described in the task description (Vidstrand et al. 2017).
- Section 3 provides an overview of the concepts and methodologies used for modelling Task 8D, and a description of the numerical models developed.
- Section 4 summarises the modelling and results of Task 8C, as detailed in Baxter et al. (2013).
- Results for modelling Tasks 8D1 and 8D2 are presented in Sections 5 and 6 respectively. The former considers open boreholes / deposition holes within the BRIE, with the latter simulating the subsequent saturation of emplaced bentonite.
- Upon completion of the BRIE, relative humidity measurements taken at twelve sensor locations within the bentonite installations were provided to modelling groups of the EBS Task Force. Section 6.2.5 details comparison of the predictive modelling performed in Sections 5 and 6 with the monitored relative humidity evolution in the central deposition holes of the BRIE.
- Section 8 provides a discussion of results, outlining the main conclusions drawn from the predictive modelling of the BRIE.

2 Task 8D specification

In this section, the data set available for developing and calibrating Task 8D models is reviewed. This includes:

- Geometrical details of tunnels / probe boreholes local to the BRIE at the Äspö Hard Rock Laboratory (HRL).
- The installation process for emplacing bentonite within the deposition holes.
- Statistics for the fracture network, inferred from observations in tunnels and boreholes.
- Fractures that can be specified with some confidence or deterministically after sufficient characterisation has taken place.
- *In situ* rock stress measured local to the BRIE.
- Boundary and initial conditions, suggested for simulations.
- Specification of properties for the rock matrix, bentonite and large scale structures.
- Measurements and observations taken from tunnels and probe boreholes, providing calibration targets for developed models.

Data for Task 8D were delivered as part of the task description (Vidstrand et al. 2017) providing details necessary for calculation of

- inflows to two 30 cm diameter deposition holes, KO0017G01 and KO0018G01, and
- resaturation of emplaced bentonite in these deposition holes.

Details presented in the following subsections are based on the associated Task 8D case specification (Vidstrand et al. 2017). In general, figures and data presented within Section 2 are directly reproduced from Vidstrand et al. (2017).

2.1 Geometrical data

The geometrical set-up for Task 8D is based on the Task 8C specification, and defined in the Swedish RT90 coordinate system. The chosen model domain occupies an approximate volume of $(40)^3$ m^3, constrained by the set of coordinates given in Table 2-1.

The BRIE is situated in the TASO tunnel, with the bedrock local to the TASO tunnel area at the Äspö HRL analysed to provide specification of the model domain. The model domain proposed for Task 8D, relative to the Äspö HRL, is shown in Figure 2-1.

Geometrical specification is provided as part of task description (Vidstrand et al. 2017) via a series of CAD files:

- TASO_V0.1_TG.dxf details the Äspö HRL including location data for TASO, TASD and TASK tunnels, as well as five probing borehole established in the BRIE experiment (KO0014G01, KO0015G01, KO0017G01, KO0018G01 and KO0020G01.
- TASO_V0.1_DET.dxf provides description of three hydrogeological structures that fully intersect the proposed model domain, referred to as wfracture_01, wfracture_02 and NNW4. Further details of these deterministically specified features are presented in Section 2.4.
- TASO_V1.1_ALL.dxf covering the proposed model domain and details a complete set of geometrical information, including principal stress orientations. The key features from this file are illustrated in Figure 2-2 and Figure 2-3, including the positions of main tunnels, hydrogeological structures, and the proposed model domain.

The proposed model domain is illustrated in Figure 2-4. Boundary conditions are based on the larger scale DarcyTools model (Vidstrand et al. 2017). Porosity values from this model are shown on two slices through the domain, with bands of raised porosity corresponding to the deterministic features. For example, structure NNW4 is clearly observed, running parallel to the TASD tunnel.

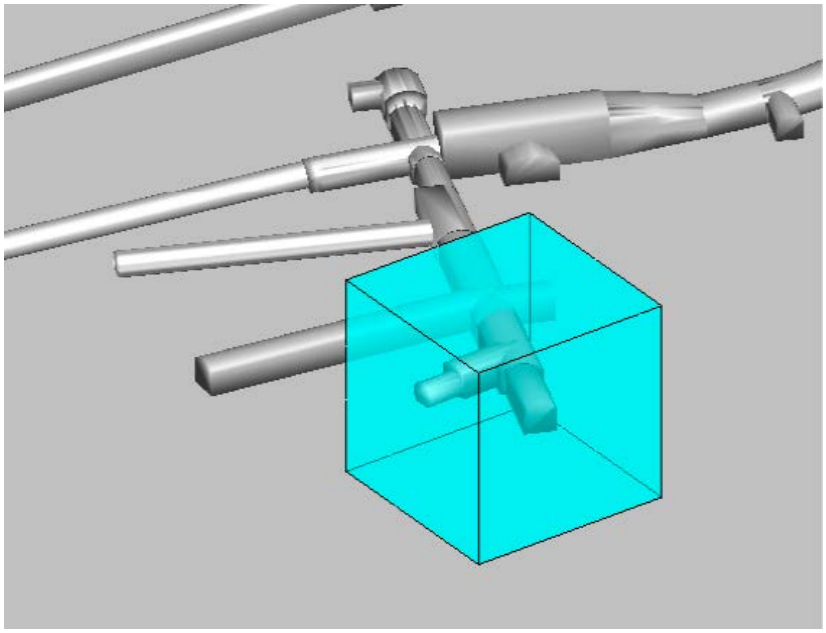

Figure 2-1. *Illustration of the suggested model domain at the Äspö HRL. The model domain includes the TASO tunnel and is approximately (40)^3 m^3. This figure is reproduced from the task description (Vidstrand et al. 2017).*

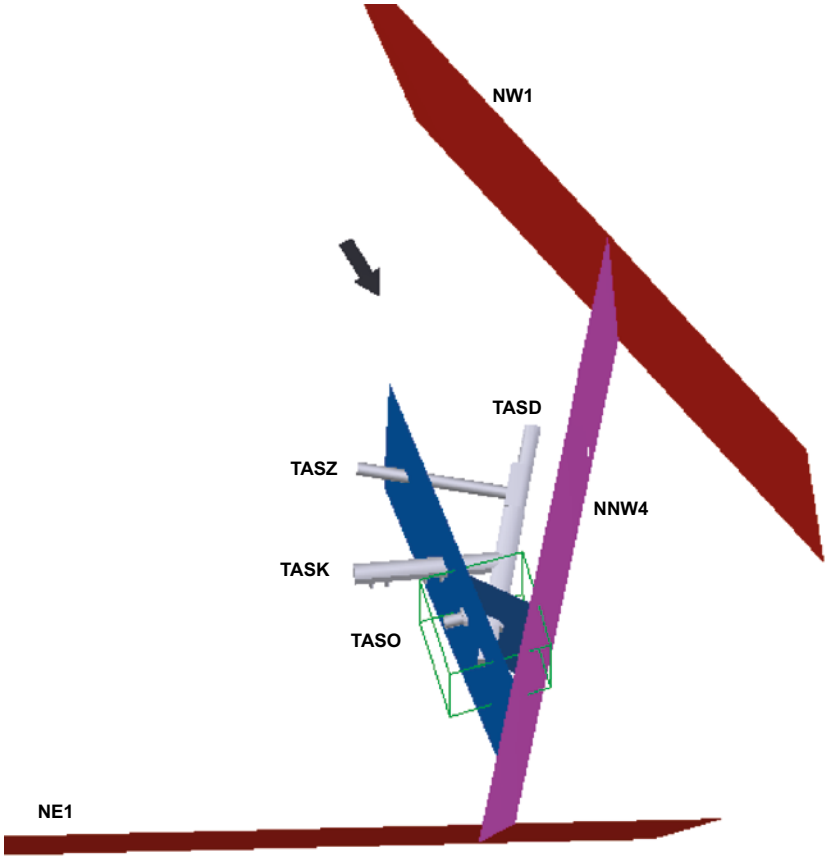

Figure 2-2. *Illustration of the CAD data along with the suggested model domain. The large structures are named according to the Äspö HRL structural model. The tunnel names are given to provide a reference orientation. The thick black arrow indicates the principal rock stress orientation. This figure is reproduced from the task description (Vidstrand et al. 2017).*

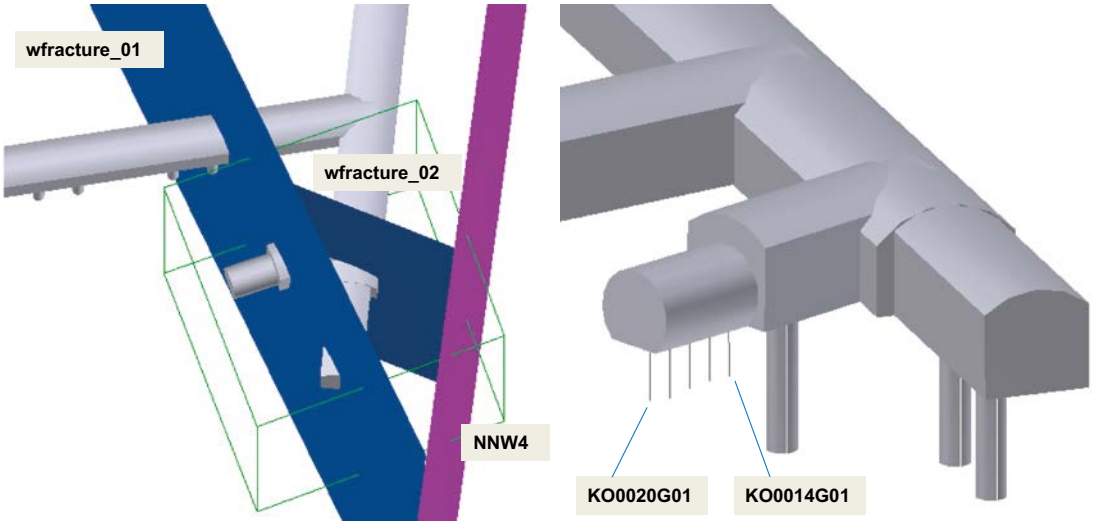

Figure 2-3. *Illustration of CAD data provided local to the TASO tunnel, naming the three deterministic hydrogeological structures that are contained within the suggested model domain. The five probing boreholes are illustrated on the right. The figure includes an indication of the location of the probe boreholes. Figure 2-5 provides an indication of the names of the probe boreholes. This figure is reproduced from the task description (Vidstrand et al. 2017).*

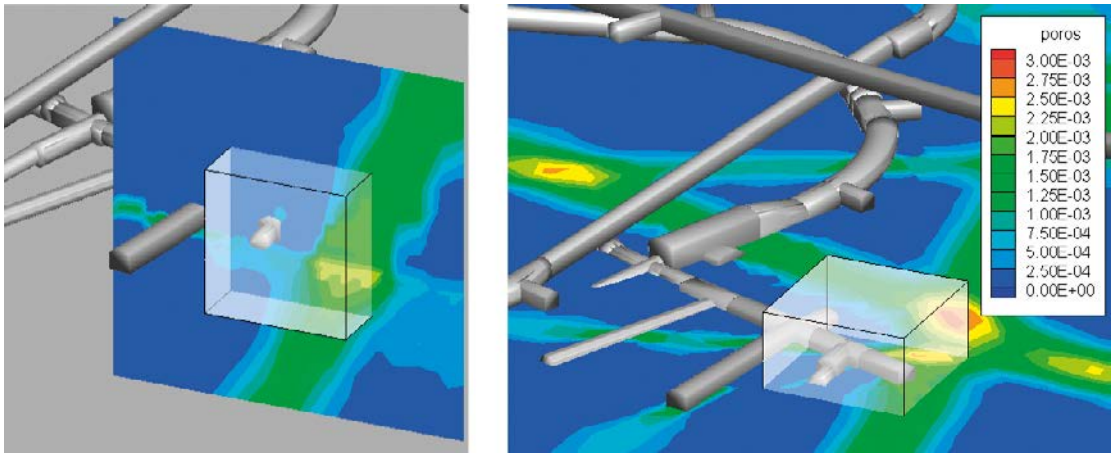

Figure 2-4. *Illustration of the proposed model domain, set within a larger scale DarcyTools model domain. One of the bounding sides broadly corresponds to a large structure, NNW4 as identified in Figure 2-2. This figure is reproduced from the task description (Vidstrand et al. 2017).*

Table 2-1. Bounding coordinates for the proposed model domain, with coordinates specified in the Swedish RT90 system. This table is reproduced from the task description (Vidstrand et al. 2017).

x	y	z
1551603	6367769	−396
1551629	6367799	−396
1551600	6367826	−396
1551573	6367796	−396
1551603	6367769	−436
1551629	6367799	−436
1551600	6367826	−436
1551603	6367769	−436

Five probing 76 mm boreholes, named KO0014G01, KO0015G01, KO0017G01, KO0018G901 and KO0020G01 have been drilled in the TASO tunnel floor as part of the BRIE, positioned as shown in Figure 2-5. In addition,

- a further fourteen boreholes have been drilled in the tunnel floor local to these probing boreholes, with locations detailed in borehole_coordinates_20121002.xls, shown in Figure 2-6,
- four boreholes have been drilled in the TASO tunnel wall, located as shown in Figure 2-7, and
- a measurement weir is located on the entrance to the TASK tunnel, 765 mm before borehole KO0013G01.

The BRIE includes the emplacement of bentonite in the central deposition holes of the TASO tunnel, KO0017G01 and KO0018G01, and as such these have been overcored to a diameter of 30 cm.

Figure 2-5. *Illustration of probe borehole spacing and naming. This figure is reproduced from the task description (Vidstrand et al. 2017).*

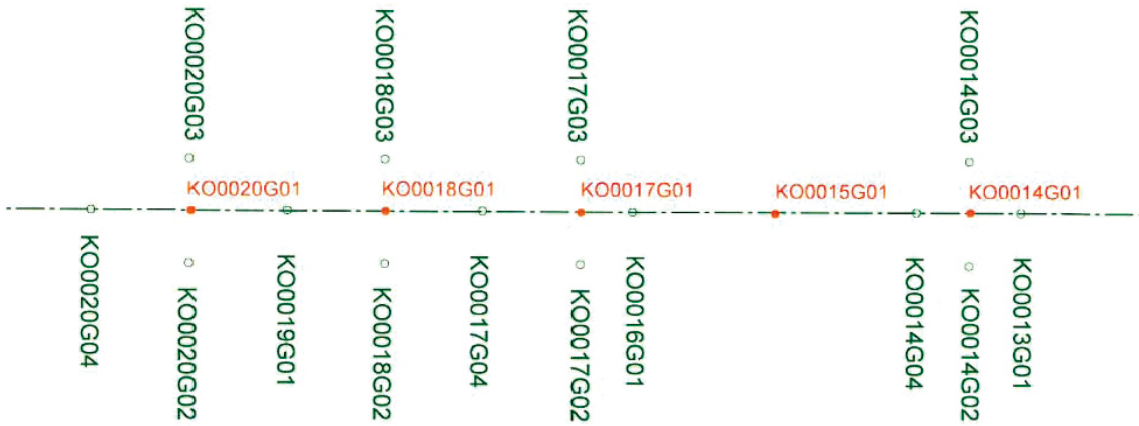

Figure 2-6. *Location of boreholes in the tunnel floor, reproduced from the task description (Vidstrand et al. 2017).*

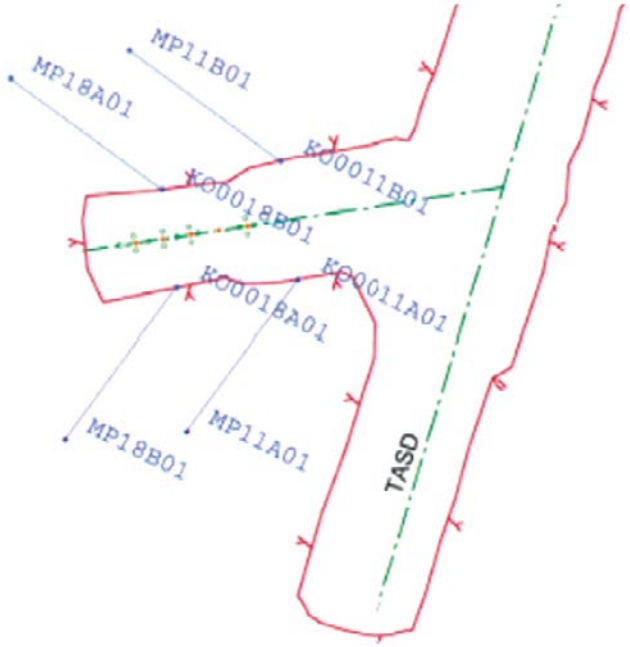

Figure 2-7. *Location of boreholes in the tunnel wall, reproduced from the task description (Vidstrand et al. 2017).*

2.2 Design of bentonite installation

This section provides a detailed description of the bentonite installation process in 30 cm deposition holes KO0017G01 and KO0018G01. Cylindrical blocks of compacted bentonite, drilled and machined to obtain well-defined properties and dimensions are threaded onto a central tube. Confining plates, welded to the top and bottom of the central tube hold the bentonite blocks in place. Details are presented in Table 2-2 and Figure 2-8.

The cylindrical blocks have a dry density slightly higher than the target dry density, as the blocks will swell to fill the outer slot between the bentonite and the deposition hole wall.

Table 2-2. Location of plates within the bentonite installation, table reproduced from the task description (Vidstrand et al. 2017).

Component	Height (mm)		Comment
	KO0018G01	KO0017G01	
Top plate	50	50	∅298 mm, welded to central tube (∅40 mm)
Bentonite	2870	3378	Initial outer diameter: 298 mm; inner diameter: 40 mm
Bottom plate	40	40	∅298 mm, welded to central tube (∅40 mm)
Sand filling	50	30	Macadam 2–4 mm

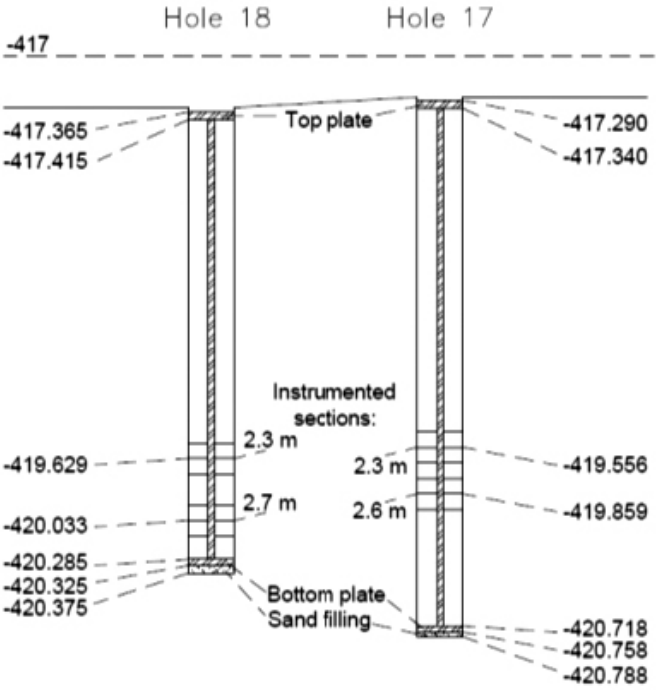

Figure 2-8. *Outline of the of the BRIE bentonite pack installations, reproduced from the task description (Vidstrand et al. 2017).*

The bottom of deposition holes KO0017G01 and KO0018G01 were both filled with tar macadam to a depth of 2–4 mm. This was to

- allow the outer slot to be filled with water, facilitated by a thin tube located within the central tube, and attached to a hole through the centre of the bottom plate,
- ensure the uneven bottom of the deposition holes was as level as possible, and
- adjust the elevation of the emplaced bentonite parcel.

The bentonite parcels are both instrumented in two sections, located in

- KO0017G01 at 2.3 m and 2.6 m, and
- KO0018G01 at 2.3 m and 2.7 m.

In each of these four sections, two instrumented blocks of bentonite are installed, with the top block containing relative humidity sensors, and the bottom block pressure sensors. A photograph of these instrumented bentonite blocks are shown in Figure 2-9. For each of the four sections, sensors within the bentonite blocks were located identically. On emplacement in the deposition holes, sections were oriented in the plane, so that pore pressure sensors were located as close as possible to the fracture of interest in each deposition hole. The position of the relative humidity and pore pressure sensors within each of the sections is illustrated in Figure 2-10.

All sensor cabling is run though the central tubes of the deposition holes, and after installation, these tubes (which lead to the sand layer at the bottom of each deposition hole) were connected to pore pressure sensors located in the TASO tunnel. A summary of coordinates of all installed sensors are shown in Table 2-3.

Figure 2-9. *Instrumentation of blocks; left: block with pressures sensors; right: block with relative humidity sensors. This figure is reproduced from the task description (Vidstrand et al. 2017).*

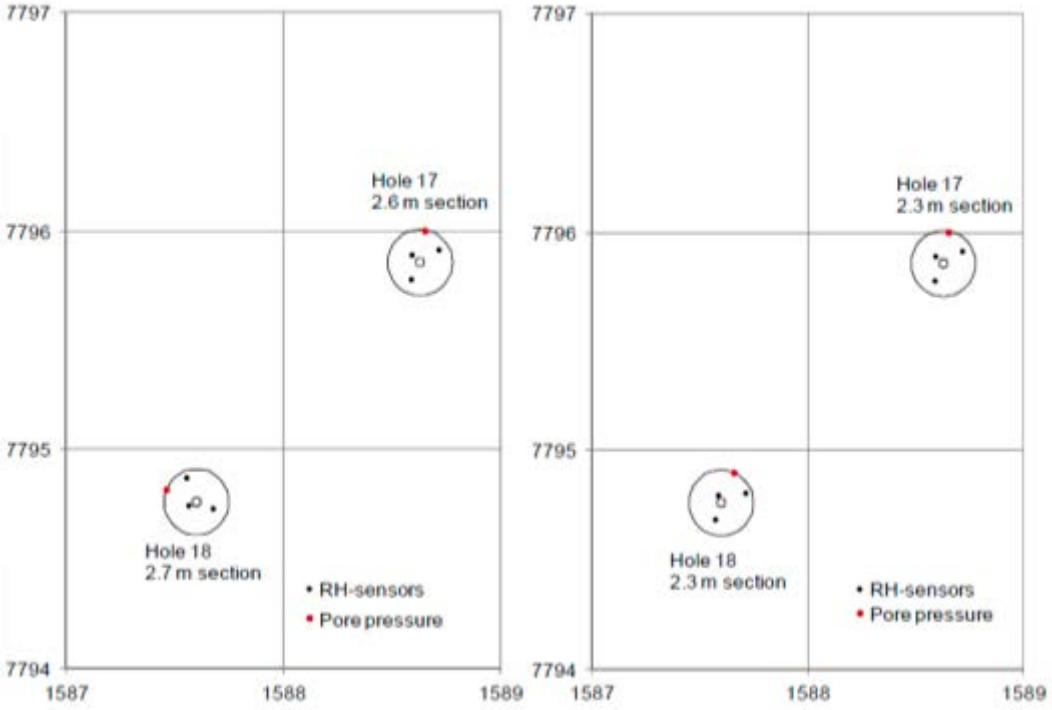

Figure 2-10. *Illustration of sensor positions in deposition holes KO0017G01 and KO0018G01, and reproduced from the task description (Vidstrand et al. 2017).*

Installations of the bentonite occurred at the following times:

- KO0018G01: 13-09-2012 17:12.
- KO0017G01: 14-09-2012 10:19.

Three photographs from the bentonite installation phase of KO007G01 are shown in Figure 2-11.

Table 2-3. Coordinate for all sensor locations in deposition holes KO0017G01 and KO0018G01, reproduced from the task description (Vidstrand et al. 2017).

Type	Sensor	x	y	z	Hole	Section	Comment
Total Pressure	PBR0001	1551588.67	6367795.81	−419.867	17	2.6	Axial
	PBR0002	1551588.51	6367795.85	−419.897	17	2.6	Radial
	PBR0003	1551588.67	6367795.81	−419.564	17	2.3	Axial
	PBR0004	1551588.51	6367795.85	−419.594	17	2.3	Radial
	PBR0005	1551587.66	6367794.7	−419.637	18	2.3	Axial
	PBR0006	1551587.5	6367794.76	−419.667	18	2.3	Radial
	PBR0007	1551587.66	6367794.82	−420.041	18	2.7	Axial
	PBR0008	1551587.6	6367794.66	−420.071	18	2.7	Radial
Pore Pressure	UBR0001	1551588.65	6367796	−419.871	17	2.6	
	UBR0002	1551588.65	6367796	−419.568	17	2.3	
	UBR0003	1551587.66	6367794.9	−419.641	18	2.3	
	UBR0004	1551587.46	6367794.82	−420.045	18	2.7	
	UBR0005	1551588.61	6367795.86	−420.758	17	3.5	In sand
	UBR0006	1551587.6	6367794.76	−420.325	18	3.1	In sand
Relative Humidity	WBR0001	1551588.59	6367795.89	−419.846	17	2.6	
	WBR0002	1551588.59	6367795.78	−419.846	17	2.6	
	WBR0003	1551588.71	6367795.92	−419.846	17	2.6	
	WBR0004	1551588.59	6367795.89	−419.543	17	2.3	
	WBR0005	1551588.59	6367795.78	−419.543	17	2.3	
	WBR0006	1551588.71	6367795.92	−419.543	17	2.3	
	WBR0007	1551587.58	6367794.8	−419.616	18	2.3	
	WBR0008	1551587.57	6367794.69	−419.616	18	2.3	
	WBR0009	1551587.71	6367794.81	−419.616	18	2.3	
	WBR0010	1551587.56	6367794.74	−420.02	18	2.7	
	WBR0011	1551587.67	6367794.73	−420.02	18	2.7	
	WBR0012	1551587.55	6367794.87	−420.020	18	2.7	

Figure 2-11. *Installation of the bentonite blocks in KO0017G01. Photographs are reproduced from the task description (Vidstrand et al. 2017).*

2.2.1 Filling of the outer slot

The process for filling the outer slot of both deposition holes is detailed below:

- KO0018G01: 3.1 litres of formation water was poured into the outer slot (between the deposition hole wall and the top-plate of the bentonite installation) at 17:45 on 13-09-2012. The outer slot appeared to be water-filled since water started to accumulate at the top-plate.
- KO0017G01: 6.85 litres of formation water was poured through the sand filling over a period of 9 minutes from 10:21 on 14-09-2012. Immediately afterwards, 1.05 litres of formation water was poured into the outer slot. Subsequent to this, observations identified water had entered the central tube of the bentonite installation, and this tube was emptied of 2.2 litres at approximately 10 am on 17-09-2012.

The total volumes of formation water that have been poured into each of the deposition hole installations can be compared with estimated pore volumes, including the outer slot, sand filling and central tube (found in KO0017G01 only). These volumes are detailed in Table 2-4. For deposition hole KO0017G01 there is a minor excess of formation water added to the installation, possibly accounted for by slots and cavities between the bentonite blocks.

Table 2-4. Simple water balance for the filling of the outer-slot of deposition holes KO0017G01 and KO0018G01. Volumes are reproduced from the task description (Vidstrand et al. 2017).

	KO0017G01	KO0018G01
Total added water volume	7.9 litres	3.1 litres[1]
Outer slot	3.5 litres	3.1 litres
Sand filling with estimated porosity of 40 %	1.6 litres[2]	2.0 litres[3]
Water in central tube	2.2 litres	–
Total	7.3 litres	5.1 litres
Excess	0.6 litres[4]	–

[1] Deposition hole KO0018G01 was wet during the installation process and therefore the theoretical volume of water will be in excess of the volume manually added. The reason for wet conditions is most likely inflow from an excavation disturbed zone (EDZ) at the top of the deposition hole.

[2] The sand volume at the bottom of deposition hole KO0017G01 is 4 litres.

[3] The sand volume at the bottom of deposition hole KO0018G01 is 5 litres.

[4] This excess volume is possibly due to slots and cavities between the bentonite blocks of the installation package.

2.3 Fracture statistics used to describe the ‘background’ discrete fracture network model of the rock

Site specific statistics are given as intensity, size and orientation data, forming the basis of the hydraulic properties of the stochastic fracture network. Fracture statistics provided as part of the Task 8D description (Vidstrand et al. 2017) are unchanged from those used in the Task 8C modelling (Baxter et al. 2013) and summarised below.

The BRIE at the Äspö Hard Rock Laboratory (HRL) is located in a granitic bedrock, with groundwater flow occurring through a series of interconnected fractures. As such, characterisation of this highly heterogeneous flow system is necessary to describe the variability of the rock. Consequently, it is expected that a Continuous Porous Medium (CPM) modelling approach, using bulk hydraulic properties, will be insufficient to accurately represent the local flow and transport pathways within the fractured bedrock. As such, a CPM model, although statistically equivalent to the underlying fracture network at a large scale, will significantly restrict the extent to which inflows and resaturation profiles can be predicted for the two central deposition holes of the BRIE. In contrast, a Discrete Fracture Network (DFN) model explicitly represents the flow conducting fractures, providing an explicit representation of the flow and transport at a local level. The DFN concept requires characterisation of several properties within its definition, including fracture orientations; fracture size and shape; fracture openings and hydraulics; and the spatial distribution of fractures. Although geological mappings can be used to define statistical distributions for properties such as orientation and intensity; others, such as fracture size and shape are more uncertain. In addition, the fracture data

used to infer the statistical distributions of the DFN model are often constrained by censoring effects due to limitations in the mapping procedures adopted in boreholes and tunnels. However, assuming sufficient characterisation data is available to adequately define the DFN, the calculation of groundwater flow through the connected fracture network will represent the inherent heterogeneity of the fractured rock; accurately predicting both inflows to deposition holes, and resaturation profiles of emplaced bentonite.

Only a handful of large structures local to the Äspö HRL can be specified deterministically, with details presented in Section 2.4. The remainder of the fracture network is unknown, although statistics for fracture intensity, orientation, size and transmissivity can be inferred from both fracture traces on tunnel walls, fracture intersections with boreholes, and hydraulic testing of the boreholes. These statistical distributions can then be used to sample parameters for fractures within a hydrogeological DFN model of the bedrock local to the TASO tunnel and the BRIE. This section discusses the development of statistical parameters used to generate the fracture models, as summarised in Table 2-5.

Table 2-5. Fracture statistics to be used for DFN modelling local to the TASO tunnel, supplied as part of the task description (Vidstrand et al. 2017).

Set	Orientation			Size		Spatial Distribution	Intensity $P_{32}(r_0,\infty)$
	Trend	Plunge	Fisher Concentration	r_0	k_r		
1	280	20	10	0.25	2.6	Poissonian	1.1
2	20	10	15	0.25	2.6	Poissonian	2
3	120	50	10	0.25	2.6	Poissonian	0.75

2.3.1 Development of DFN model

As part of the modelling in Task 8C, limitations in the data used for developing a DFN model were identified, resulting in a degree of uncertainty inherent in using the data. This reflects typical constraints initially found on a local scale, with fracture data mainly limited to tunnel mappings.

As part of Task 8D, additional hydraulic fracture data was provided; typical of the additional data available during the construction phases of the repository used in support of siting decisions for deposition holes. This additional data is detailed in Section 2.9, and will be used to further refine the statistical description used for DFN modelling.

2.3.2 Input data

Locations of fracture data available for inferring statistical distributions are shown in Figure 2-2. Subsequent to analysis, a number of limitations to the input data were identified

- orientations of fractures intersecting individual deposition holes are highly uncertain (fracture statistics, developed as part of Task 8C, do not include the orientation of fractures intersecting KO0017G01 and KO0018G01, although this information is provided for calibrating the model as part of Task 8D),
- the BRIE experiment is located in TASO tunnel, where there is a relatively small fracture data sample,
- the TASK tunnel is furthest away from the BRIE experiment, and situated in a subtly different rock type, and
- the TASD tunnel in conjunction with TASO provides a relatively large amount of data.

The identified limitations of the data allow the available primary fracture information to be ranked according to relevance, in the following order (highest to lowest)

- data from the TASO tunnel,
- data from the TASD tunnel, with
- data from the TASK tunnel and two further deposition holes interpreted in a more cautious way.

2.3.3 Orientation distribution

Orientation data from

- traces in deposition holes, DD0086G01 and DD0092G01,
- traces in tunnels, TASD, TASK and TASO, and
- a desktop study of two virtual scanlines in the floor of the tunnels TASD and TASK,

are compiled and shown in the stereonet in Figure 2-12. This interpretation does not provide obvious means for divisions of fracture orientations into sets, partly due to multiple poles being plotted on top of each other (at even 5° locations), but also because of uncertainties in the underlying orientation data, especially for deposition holes DD0086G01 and DD0092G01. By adding a small, uniformly distributed random value, ±2°, to both strike and dip, this first issue is addressed with orientations shown on a stereonet in Figure 2-13. Two sets are now visually apparent, with mean fracture poles of 280°/20° and 20°/10° trend and plunge.

Subdivision of orientation data into the three tunnels: TASD, TASK and TASO are shown on stereonets in Figure 2-14. A gently dipping set is identified with a mean pole of 120°/50° trend and plunge.

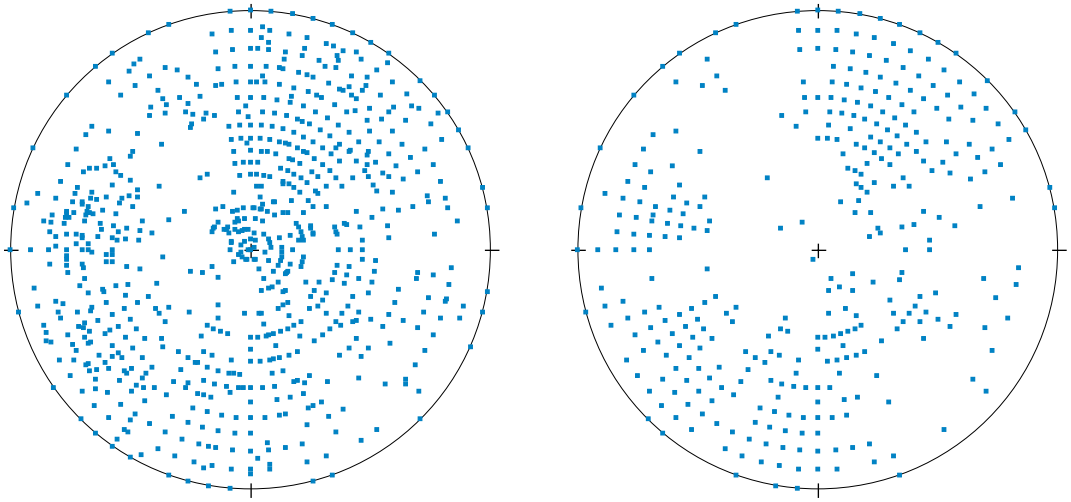

Figure 2-12. *Fracture poles. Left: Orientation of all, 1772, fractures from the two deposition holes and the three tunnels. Right: Orientation of the 762 fractures mapped on the floor of the TASD and TASK tunnels. This figure is reproduced from the task description (Vidstrand et al. 2017).*

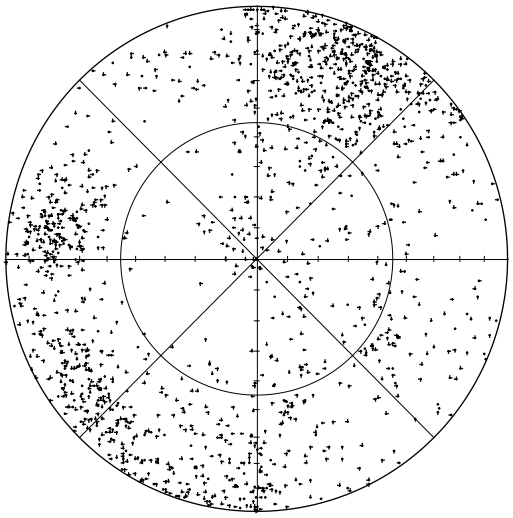

Figure 2-13. *Fracture poles, including a uniformly random value of ±2° added to both strike and dip. This figure is reproduced from the task description (Vidstrand et al. 2017).*

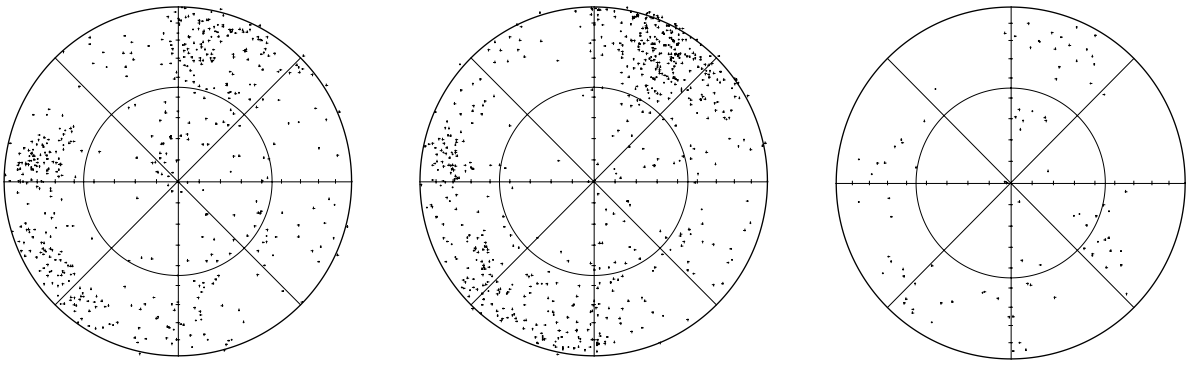

Figure 2-14. *Fracture poles from left: TASD tunnel, middle: TASK tunnel and right: TASO tunnel. This figure is reproduced from the task description (Vidstrand et al. 2017).*

Three sets defining the orientation data are interpreted from visual inspection. A Fisher distribution is proposed for each set, with Fisher concentrations, κ, estimated as 10, 15 and 10 respectively for each of the three sets. Fracture poles assigned to each of these sets is shown in Figure 2-15, and the relative intensity between each set is 0.29/0.52/0.20.

2.3.4 Spatial distribution

A Poisson point process is used to distribute fracture centres in space.

2.3.5 Size distribution

Fracture size is chosen to be distributed using a power-law relation,

$$f(r) = \frac{k_r r_0^{k_r}}{r^{k_r+1}}, \qquad (2\text{-}1)$$

for power law exponent, k_r; fracture radius, r; and location parameter, r_0.

The exponent of the power law size distribution is calculated using fracture traces mapped on the tunnel walls, roofs and floors, together with the traces in the two deposition holes. Unfortunately truncation (lower bound), as well as the censoring (upper bound), is different in each of the data sources, with lower limits of

- 0.3 m in deposition hole DD0086G01,
- 0.2 m in deposition hole DD0092G01,
- 0.4 m in TASK and TASD tunnels, and
- 1.0 m in TASO tunnel.

However, truncation and censoring will only affect the data interval, and the location of the CCDF (Complementary Cumulative Density Function) of mapped trace lengths. The slope of the curve (i.e. power law exponent) is not affected. Figure 2-16 illustrates the distribution of trace lengths for each data source, and the slope of the distribution is, by visual inspection, estimated to be −1.6. This corresponds to a power law exponent, k_r, of 2.6 for the parent fracture size distribution. Although this slope provides a reasonable fit to measurements from all five 5 sources, it is noted that the CCDF curve of the TASK tunnel does not have any straight segment where a slope can be evaluated because of the limited scale over which mapping takes place.

On analysis of scanlines in tunnels TASD and TASK, Äspö HRL geologists estimate a shortest trace length of 0.5 m, yielding a location parameter (i.e. the radius of the smallest regarded fracture) of 0.25 m. However, the location parameter, r_0, cannot readily be evaluated from trace length distributions alone, as it is closely related to the intensity of the power law function. As such, the location parameter is further discussed in the following subsection.

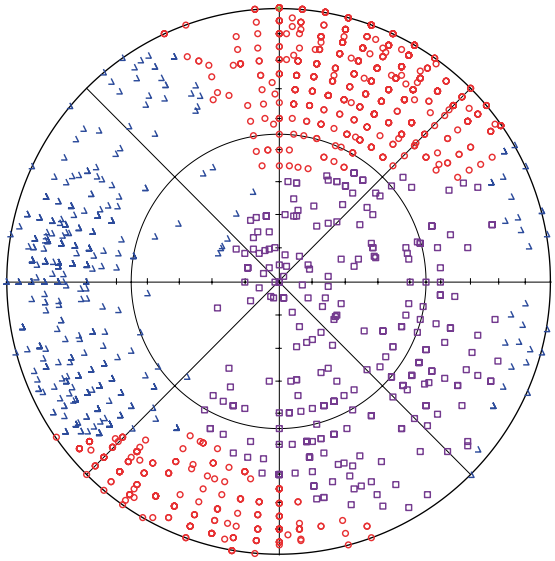

Figure 2-15. *Fracture poles assigned to the three sets. Set 1: Blue triangles, set 2: red circles and set 3: purple squares. This figure is reproduced from the task description (Vidstrand et al. 2017).*

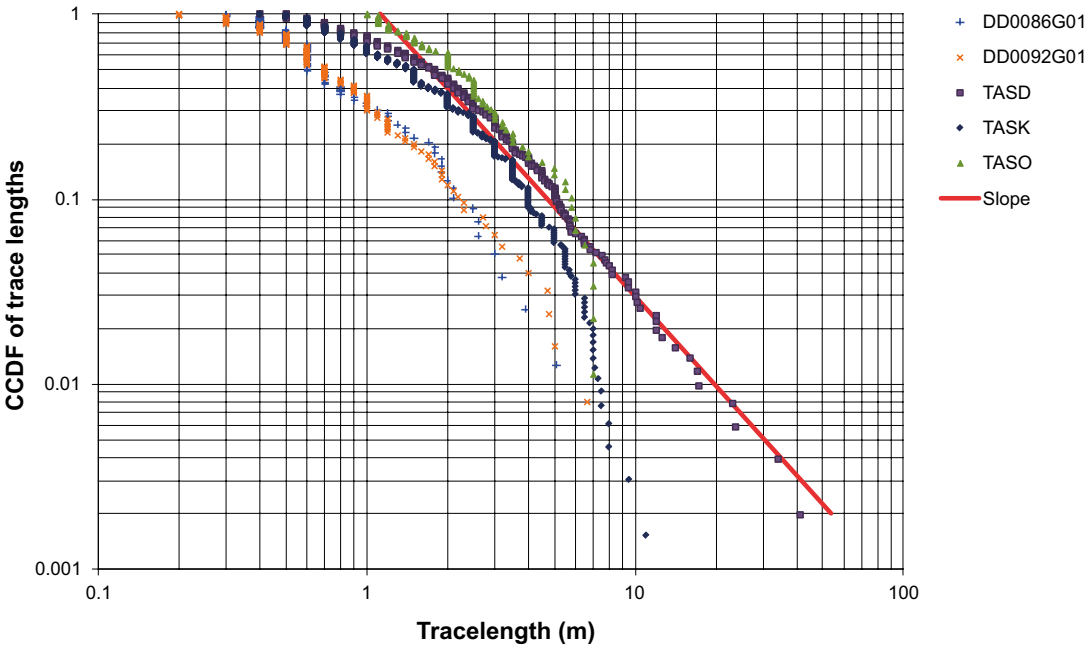

Figure 2-16. *The distribution of trace lengths from different sources. This figure is reproduced from the task description (Vidstrand et al. 2017).*

2.3.6 Intensity

Fracture intensity (surface area per unit volume), P_{32}, is estimated from Terzaghi (1965) correcting the number of fractures intersecting the scanlines. The intensity of fractures is independent of the fracture-size distribution, and consequently some modelling is required to estimate the size-intensity relationship. A scanline on the TASD tunnel floor is considered to relate to the P_{32} of underlying fracture-size distribution. Unfortunately this scanline is short, only 16.5 m with 23 intersections, making intensity The relationship between intensity (P_{32}) and location parameter (r_0) of the fracture-size distribution is considered in the task description (Vidstrand et al. 2017) by analysing 30 scanlines (consisting of three scanlines, 16.5 m long, within in ten realisations of the fracture model). Models are based on the underlying orientation model, together with the assumed relative intensities between different fracture sets as detailed in Section 2.3.3. Figure 2-17 illustrates results from these realisations; it is impossible to replicate the data measured in the TASD tunnel.

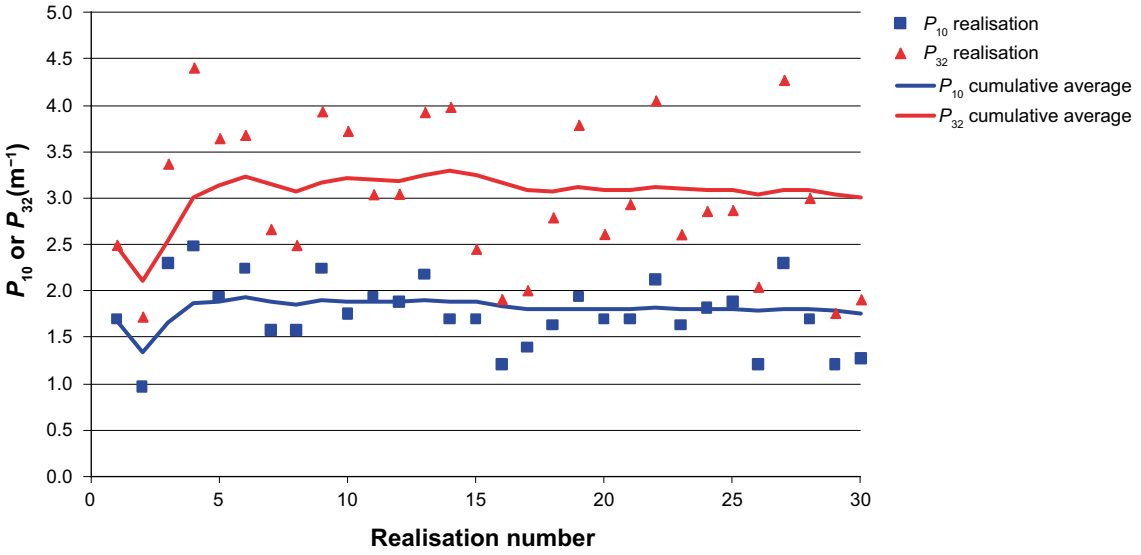

Figure 2-17. *Results from the 30 modelled scanlines. This figure is reproduced from the task description (Vidstrand et al. 2017).*

The task description (Vidstrand et al. 2017) proposes an intensity model that

- underestimates the given intensity P_{32} by approximately 10 %, and
- overestimates the linear intensity P_{10} (fracture count per unit length) by approximately 25 %.

The intensities for the three different sets, $P_{32,\, r>0.25}$ are 1.1, 2.0 and 0.75 m^2/m^3 respectively.

2.3.7 Uncertainty

Sections 2.3.3 through 2.3.6 detail statistical distributions from Vidstrand et al. (2017) required to generate stochastic DFN models local to the BRIE in the TASO tunnel. These have been derived from the analysis of limited data, and specifically, the use of lower quality data with potentially large uncertainties in the defined model. Uncertainties are estimated by Vidstrand et al. (2017) for the following parameters

- mean pole 15° (dihedral angle),
- power law exponent, $k_r \pm 0.15$, and
- fracture intensity, $P_{32} \pm 25$ %.

2.3.8 Fracture statistics

A summary of statistics for each of the three fracture sets identified local to the TASO tunnel are presented in Table 2-5. Two limitations of the data analysis are identified, possibly contradicting the proposed interpretations. These are

- fractures smaller than 1 m seem to follow slightly different statistics, and
- of the analysed data, only the inner part of TASD and the entire TASO tunnel share the same rock type.

2.4 Deterministic fracture information

Three deterministic structures were identified as part of Task 8C, named wfracture_01, wfracture_02, and NNW4. Geometrical specifications of these geological structures were provided as CAD data, as shown in Figure 2-3.

Subsequent to Task 8C, additional information regarding the geological structural model has been established, leading to an update in the deterministic fracture information. This includes

- refinement of the geometry of structure wfracture_01, local to the TASO tunnel, and
- fracture locations within the 30 cm deposition holes KO0017G01 and KO0018G01.

2.4.1 Local refinement of wfracture_01

Structure wfracture_01 has been redefined local to the TASO tunnel, and provided via the CAD file TASO_V1-c120914_only_1_fracture.dxf. The large scale wfracture_01 requires adjustment to connect with this local TASO information. Any overlap between the original and new structure is removed.

2.4.2 Fracture intersection with deposition holes KO0017G01 and KO0018G01

Groundwater producing structures identified in KO0017G001 and KO0018G01 are provided in Table 2-6. Values for the "adjusted z-elevation" correspond to the depth at which the estimated fracture plane would cross the central axis of the deposition hole. Extension of the fractures beyond the deposition hole is largely unknown, other than:

- The fracture in KO0017G01 is not identified in the tunnel floor mappings. In addition, hydraulic responses indicate the fracture has good connectivity to the structure, wfracture_01, although this is not likely to be a direct connection.
- No good connection is found between the fracture in KO0018G01 and any other observations. Also, this fracture did not supply any water to the deposition hole for the first couple of months.

Table 2-6. Fracture locations in boreholes KO0017G01 and KO0018G01. Values are reproduced from the task description (Vidstrand et al. 2017).

Borehole	Diameter [mm]	Adjusted z – elevation [m]	Strike (deg) RT90	Dip (deg) RT90
KO0017G01	300	−420.07	139.5	62.8
KO0018G01	300	−419.58	214.7	54.1

In addition to location and orientation, surface characteristics for the fractures indentified in deposition holes KO0017G01 and KO0018G01 have also been interpreted from optical measurements. These are illustrated in Figure 2-18 and Figure 2-19 for fracture intersections with each of the deposition holes.

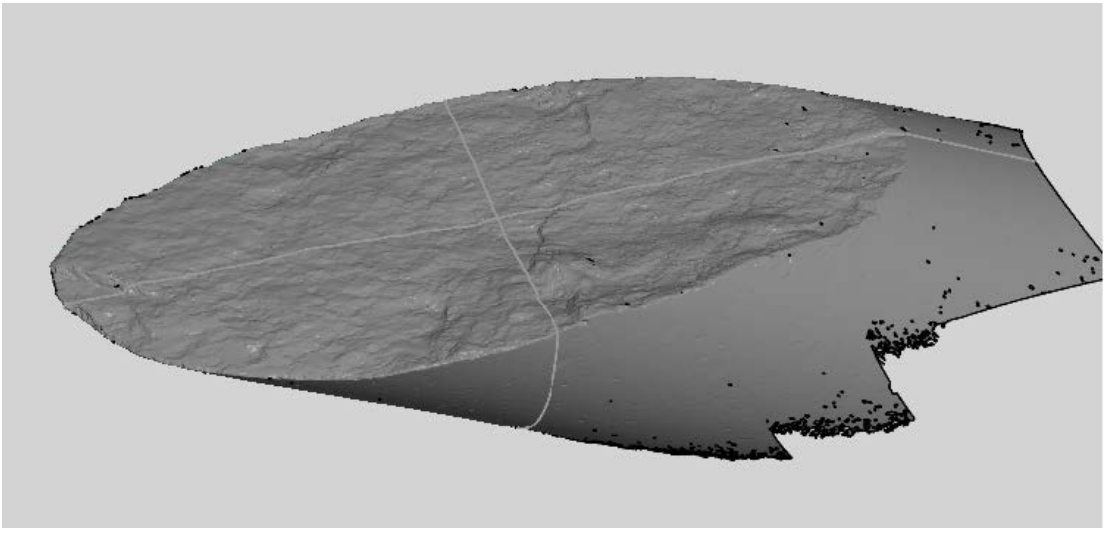

Figure 2-18. *A Scan (optical measurement) of the fracture identified at a depth of 2.9 m in the 76 mm core taken from KO0017G01. This fracture is described as planar and rough. This image is reproduced from the task description (Vidstrand et al. 2017).*

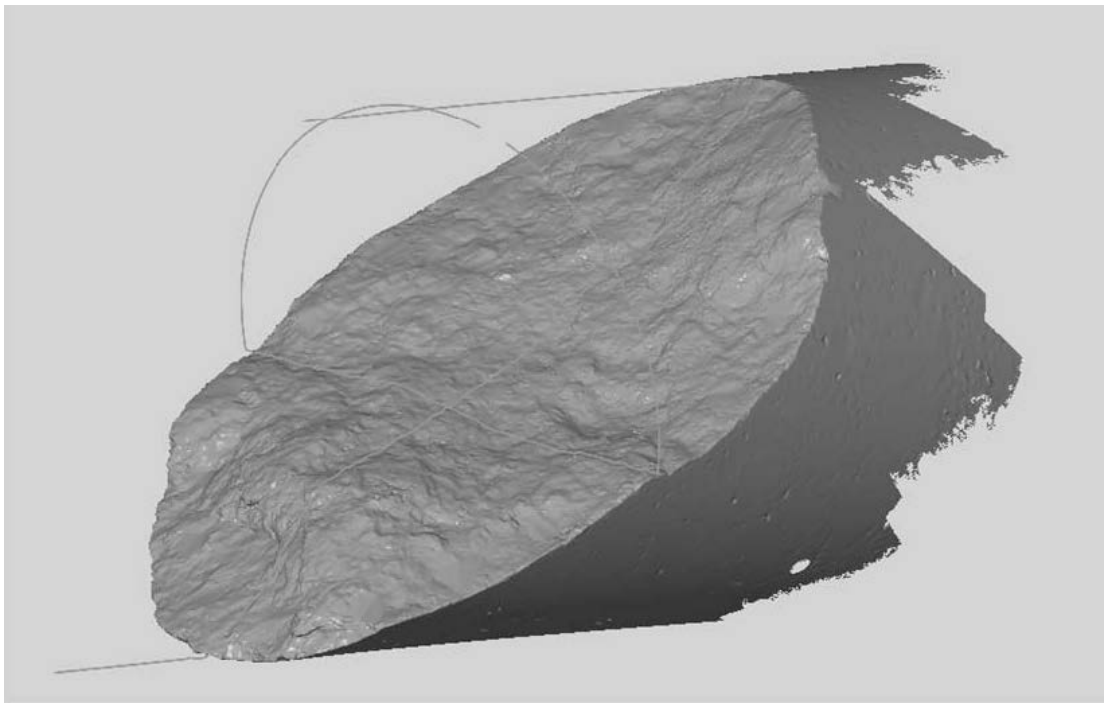

Figure 2-19. *A Scan (optical measurement) of the fracture identified at a depth of 2.3 m in the 76 mm core taken from KO0018G01. This fracture is described as undulating and rough. This image is reproduced from the task description (Vidstrand et al. 2017).*

2.5 Rock stresses

The *in situ* rock stress local to the TASQ tunnel (Andersson 2007) is provided as part of the updated Task 8D description (Vidstrand et al. 2017), and detailed in Table 2-7 below.

Table 2-7. *In situ* rock stresses local to the TASQ tunnel, reproduced from the task description (Vidstrand et al. 2017).

	σ_1	σ_2	σ_3
Magnitude (MPa)	30	15	10
Trend (RT90)	298	–	208
Plunge (from horizontal)	0	90	0

2.6 Boundary conditions

Boundary conditions for the models are supplied by the Task Force as extracted from the current, official, hydrogeological model of the Äspö HRL, based on the Laxemar Deformation Zone Model from the Site Descriptive Model (SDM). Due to its large scale, this regional scale model includes known location errors within the suggested BRIE model domain, as documented in the task description (Vidstrand et al. 2017).

Boundary conditions are unchanged from Task 8C analysis (Baxter et al. 2013), as summarised below.

A DarcyTools v3.3 sub-grid is used to extract values for pressure, salinity (from groundwater constituents), and velocities from the full regional Äspö HRL model (Äspömodel05). In the format provided (Vidstrand et al. 2017), the extracted data covers a volume approximately $(100\ \text{m})^3$, incorporating the suggested model domain. The residual pressure P^R for this model is shown in Figure 2-20 for a horizontal slice through the TASO and TASD tunnels. The total pressure P^T is related to the residual pressure by the hydrostatic pressure

$$P^T = P^R - \rho_0 g (z - z_0), \quad (2\text{-}2)$$

where the datum, $z_0 = 0$ metres above shore line is the reference altitude taken at the present day shore line, and ρ_0 is the fresh water density. The extracted data from model Äspömodel05 is supplied in spreadsheet TASO_pressure_salinity_velocities_rev20101123.xls, as part of the task description (Vidstrand et al. 2017).

The salinity mass fraction, S, is specified as part of these boundary conditions, including spatial variation across the model domain. The salinity-density dependence is defined as:

$$\rho = 1000(1 + 0.0078 \cdot S). \quad (2\text{-}3)$$

All tunnels within the model domain are assumed open, with atmospheric boundary conditions applied.

2.7 Initial conditions

Initial conditions for the inflow predictions to the five probe boreholes as part of Task 8D1 are identical to the previous Task 8C analysis (Baxter et al. 2013), and based on the "natural" conditions where

- For pressure build up measurements, all probing boreholes are packed off, assuming the packer to seal the upper 1 m of the borehole.
- For inflow measurements, each of the five probe boreholes are opened to the tunnel in turn.

An equivalent prescription of the initial conditions is made when considering inflows to the overcored boreholes KO0017G01 and KO0018G01.

For Task 8D2, initial conditions for modelling the resaturation of emplaced bentonite in the central deposition holes of the BRIE are taken from the modelling results of Task 8D1. In addition, local to deposition holes

- the emplaced bentonite is initially assumed to be at atmospheric pressure, and
- the initial water content of bentonite is 11.6 %, corresponding to an initial degree of saturation of 0.413 for the target void ratio of 0.78 (i.e. after swelling into the outer slot). This degree of saturation corresponds to an initial suction value of 70 MPa when using the retention curve detailed in Section 3.2.5.

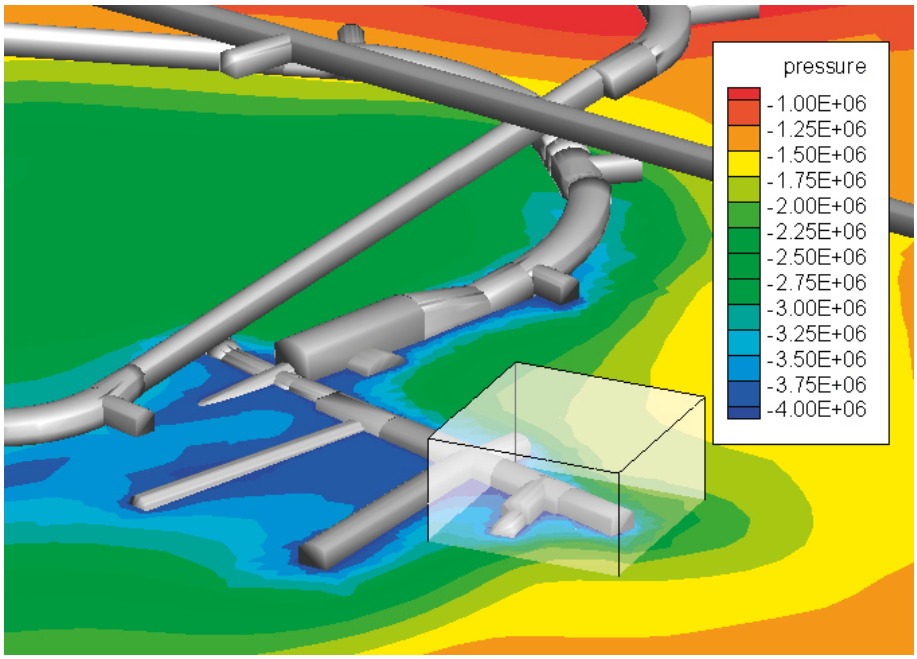

Figure 2-20. *Illustration of the pressure field (Pa), with reference elevation at the present day shore line (0 m altitude). This figure is reproduced from the task description (Vidstrand et al. 2017).*

2.8 Material specifications

Material specifications used are as detailed within the task description (Vidstrand et al. 2017), with values based on either measurement, expert judgment and/or theory. Specifications for rock matrix, fractures and bentonite are detailed in Sections 2.8.1 through 2.8.5 respectively.

2.8.1 Rock matrix

To support the modelling in Task 8D, laboratory tests have been performed on eight de-stressed matrix core samples taken from deposition holes KO0017G01 and KO0018G01. Hydraulic conductivity measurements for these samples are in the range 5.5×10^{-12} ms^{-1} to 6.0×10^{-14} ms^{-1}, as presented in Table 2-8. However, it is thought permeabilities of de-stressed core samples are typically much greater than under *in situ* stress conditions. For example, core plug investigations (Vilks 2007a, b) have found increasing the confining pressure from 2 MPa up to 15 MPa can lead to significant reduction in permeability (by a factor of between 2 to 154). *In situ* stress conditions at Äspö are detailed in Section 2.5.

Additional laboratory tests indicate porosity for the matrix rock should be in the range 0.5 %–1 %. These measurement values are consistent with previous laboratory tests conducted on Äspö type rock; indicating porosity values close to 0.5 %.

Values for specific storage of the rock matrix at BRIE have not been measured. The task description (Vidstrand et al. 2017) indicates field tests conducted at Äspö imply a range between 10^{-9} m^{-1} and 10^{-6} m^{-1} at a range of scales. In addition, Vidstrand et al. (2017) estimates specific storage of 10^{-7} m^{-1} from theoretical values for Äspö type rock.

The volumetric water content associated with a range of relative humidities have been measured in two representative rock matrix core samples, as detailed in Table 2-9. This data can be used to parameterise a van Genuchten curve[2], with further details presented in Section 3.2.5.

Table 2-8. Hydraulic conductivities of eight matrix core samples taken from KO0017G01 and KO0018G01, reproduced from the task description (Vidstrand et al. 2017).

Samples	Well	Hydraulic Conductivity [m/s]
Diorite-Pegmatite 1	KO0017G01	7.5×10^{-13}
Diorite-Pegmatite 3	KO0017G01	9.0×10^{-13}
Diorite-Pegmatite 4	KO0017G01	5.5×10^{-12}
Diorite 1	KO0018G01	6.0×10^{-14}
Diorite 3	KO0018G01	1.5×10^{-13}
Diorite 4	KO0018G01	1.5×10^{-13}
Diorite 5	KO0018G01	2.5×10^{-13}
Diorite 7	KO0018G01	3.3×10^{-13}

Table 2-9. Relative humidity and volumetric water content for two rock matrix core samples. Values are reproduced from the task description (Vidstrand et al. 2017).

Relative Humidity [%]	Volumetric Water Content [water volume / total volume]	
	Diorite A1 [%]	Granite B1 [%]
100 (saturated porosity)	0.99	0.46
85	0.30	0.15
59	0.22	0.11
33	0.16	0.08

[2] It is noted in the task description (Vidstrand et al. 2017) that relative humidities in Table 2-9 provide data at relatively low saturations, which may not be relevant to the saturation state of the granite local to emplaced bentonite. Therefore, although this data is specific to rock matrix at the BRIE, caution is required when applying the van Genuchten model at these high water saturations.

Figure 2-21. *Photographs of two core samples. The upper Diorite-pegmatite core is taken from KO0017G01, whilst the lower diorite core is taken from KO0018G01. These pictures are reproduced from the task description (Vidstrand et al. 2017).*

2.8.2 Rock fractures

In each of the two deposition holes KO0017G01 and KO0018G01, only one flowing structure has been identified with certainty. Hydraulic characterisation of these fractures yields:

- A transmissivity of 5×10^{-11} m^2/s inferred for the fracture found intersecting KO0017G01 from Posiva Flow Log (PFL) and other flow measurements.
- A specific capacity (groundwater production per unit drawdown) in the range 1×10^{-12} m^2/s to 5×10^{-12} m^2/s for the fracture found intersecting KO0018G01, with further details presented in Table 2-10.

The locations of fracture intersections, as well as fracture orientations were detailed in Section 2.1. No geometric information is available to accurately define the extension of these structures beyond the deposition hole wall.

Table 2-10. The specific capacity (groundwater production per unit drawdown) of the fracture found intersecting deposition hole KO0018G01. Values are reproduced from the task description (Vidstrand et al. 2017).

Q [ml/min]	Section [m]	Pressure [bar]	Q/dh [m^2/s]
0.01–0.03	2.1–3.1	10–17	10^{-12} to 5 10^{-12}

2.8.3 Deterministic fractures

The geological and hydraulic description of structure wfracture_01 has been updated since Task 8C, with a new, local geometry discussed in Section 2.4. From borehole, KO0011A01, hydraulic tests have been performed for zone wfracture_01, evaluating its transmissivity as 4×10^{-9} m^2/s. This compares to a value of 2×10^{-8} m^2/s, elicited from expert judgement and used in Task 8C.

The hydraulic description of structures wfracture_02 and NNW4 are identical to Task 8C and detailed in Table 2-11. Values are based solely on expert judgement, with no site-specific information available for refinement.

Table 2-11. Description of structures wfracture_01, wfracture_02 and NNW4, summarised from the task description (Vidstrand et al. 2017).

	wfracture_01	wfracture_02	NNW4
Geological width (m)	0.001	0.001	10
Transmissivity (m^2/s)	4×10^{-9}	2×10^{-9}	6.5×10^{-7}
Porosity for porous media descriptions (–)	10^{-3}	10^{-3}	10^{-3}
Transport aperture for DFN descriptions (m)	10^{-5}	10^{-5}	10^{-5}
Storativity (–)	10^{-8}	10^{-8}	10^{-7}

2.8.4 Excavated disturbed zones / shallow fractures

Hydraulic effects of an excavated disturbed zone (EDZ) local to the TASO tunnel floor for the five probe boreholes are considered. Specific capacities are presented in Table 2-12, describing the hydraulic performance of the borehole based on injection tests. In summary:

- For KO0017G01, the transmissivity evaluated for the intersecting fracture (5×10^{-11} m^2/s) is similar to the specific capacity of the borehole (8.0×10^{-11}) based on injection tests. This suggests there is little contribution from the EDZ in the upper part of the borehole.
- For KO0018G01, the specific capacity obtained between the depth 2.1 m–3.1 m, and associated with the intersecting fracture is significantly lower (several orders of magnitude) compared to the full length test. This possibly suggests substantial contribution from the EDZ in the upper part of the borehole.

Table 2-12. Borehole specific capacities from injection tests for KO0014G01 through KO0020G01, This table is reproduced from the task description (Vidstrand et al. 2017).

Borehole	Section [m]	Q/dh [m^2/s]
KO0014G01	0.50–3.00	6.0×10^{-10}
KO0015G01	0.75–3.03	1.7×10^{-7}
KO0017G01	0.50–2.97	8.0×10^{-11}
KO0018G01	0.55–3.06	4.5×10^{-7}
KO0020G01	0.82–3.10	4.2×10^{-10}

2.8.5 Bentonite

Suggested properties for the bentonite are provided by the task description (Vidstrand et al. 2017). Only values for specific storage are updated from Task 8C.

- Hydraulic conductivity = 6.4×10^{-14} m/s.
- Porosity = 0.44.
- Specific Storage = 2×10^{-6} m^{-1} (previously 1×10^{-6} m^{-1} in Task 8C).

Initially the bentonite is saturated at ~41 %. Proposed constitutive relationships for the capillary pressure and relative permeability of the bentonite are detailed in Section 3.2.5.

2.9 Calibration targets

Targets for Task 8D1 considering open borehole conditions have undergone significant update since Task 8C, providing considerably more data for model calibration, including

- inflow estimates and pressure responses within the five probe boreholes from additional, short duration tests,

- inflow estimates for the two, 30 cm diameter deposition holes, and
- inflow estimates from the “nappy” experiments of the TASO tunnel.

This section initially reviews the data available under Task 8C (Section 2.9.1) for calibration, before detailing additional measurements available in Task 8D (Sections 2.9.2 through 2.9.6).

2.9.1 Task 8C calibration

Calibration targets for Task 8C1 consist of measured inflows to the probing boreholes and pressure build-up tests. Full details are presented in the Task 8C modelling report (Baxter et al. 2013) with available data summarised in Table 2-13. Initially, all boreholes were packed off, sealing the upper 1 m of the borehole, and the built-up pressure measured. For boreholes where no pressure is provided in Table 2-13, inflows were insufficient to fill the borehole over the duration of the measurements. Thereafter, one borehole at a time was opened and the outflow measured, i.e. yielding the inflow for atmospheric pressure at the top of the boreholes.

Table 2-13. Initial pressures built-up in closed (packed off) boreholes and outflow measurements conducted in one borehole at a time thereafter. The second row indicates flow during the injection test. The no flow results in KO0018G01 and KO0015G01 for the first test may be due to measurement limitations and or “leakage” in the upper parts of the boreholes. This table is reproduced from the task description (Vidstrand et al. 2017).

	KO0020G01	KO0018G01	KO0017G01	KO0015G01	KO0014G01
Inflow	Inflows not sufficient to fill the borehole during the measurement	No inflows recorded: measurement limitations	Q ≈ 0.5 ml/min p ≈ 6 bar ≈ 2–3 m	No inflows recorded: measurement limitations	Q ≈ 1 ml/min p ≈ 3 bar ≈ 0.5–1 m
Injection	Inflows not sufficient to fill the borehole during the measurement	Above 1 m: Inflows not sufficient to fill the borehole during the measurement Below 1 m: No inflows recorded: measurement limitations	Inflows not sufficient to fill the borehole during the measurement	Inflows not sufficient to fill the borehole during the measurement	Inflows not sufficient to fill the borehole during the measurement

2.9.2 Ambient pressure

Pressure build-up measurements from floor and wall boreholes across the BRIE are available as part of Task 8D. Measurement in probe borehole KO0017G01 during December 2010 (denoted Phase 1 of BRIE) are provided in Table 2-14, indicating high pressure in the lower part of the borehole.

Subsequently, during September 2011 (denoted Phase 2 of the BRIE) pressure measurements were made as presented in Table 2-15, for a number of boreholes in the tunnel floor. Phase 2 pressure measurements for boreholes located in the tunnel wall are detailed in Table 2-16. It is observed that during drilling, pressures decrease in the boreholes (see Phase 1). This is due to increased permeability local to the boreholes, a consequence of damage caused to the rock during drilling.

It is suggested from the task description (Vidstrand et al. 2017) that pressure measurements should focus on floor borehole KO0017G01, and wall boreholes KOOO11A01, KO0011B01, KO0018A01, KO0018B01).

Table 2-14. Pressure measurements during Phase 1 of the BRIE for floor borehole KO0017G01 (12-2010). Measurement values are reproduced from the task description (Vidstrand et al. 2017).

Borehole	Section [m]	Pressure [bar]
KO0017G01	0.5–2.97	9–10
KO0017G01	2.0–2.97	17

Table 2-15. Pressure measurements during Phase 2 of the BRIE for the lower part of five floor boreholes (09-2011). Measurement values are reproduced from the task description (Vidstrand et al. 2017).

Borehole	Section [m]	Pressure [bar]
KO0015G01	2.1–3.03	5
KO0017G01	2.11–2.97	5
KO0018G01	1.42–3.06	4
KO0020G04	2.0–3.5	10.5
KO0020G03	2.0–3.5	9

Table 2-16. Pressure measurements during Phase 2 of the BRIE for four wall boreholes (09-2011). Measurement values are reproduced from the task description (Vidstrand et al. 2017).

Borehole	Section [m]	Pressure [bar]
KO0011A01[1]	1.01–10	27
KO0011B01	1.24–10	3
KO0018A01	1.11–10	26
KO0018B01	1.28–10	21

[1] The pressure measured in wall borehole KO0011A01 is slowly declining, with a current value of 25 bar.

2.9.3 Inflow to TASO

Inflows to the TASO tunnel under atmospheric conditions are also provided for calibration in Task 8D. Inflow values are based on

- scoping calculations using pressure-distance data, indicating inflow to the TASO tunnel of 0.5 l/min, and
- water collection tests (sorbing mats) which estimate inflow to TASO tunnel at 0.1 l/min. Table 2-17 and Figure 2-22 provide details on the distribution of inflows across the tunnel. Data in the first column of Table 2-17 correspond to sorbing mats located primarily by the structure wfracture_01. Through visual inspection, sorbing mats are located in the vicinity of inflows (i.e. no sorbing mat equates to no discernable inflow).

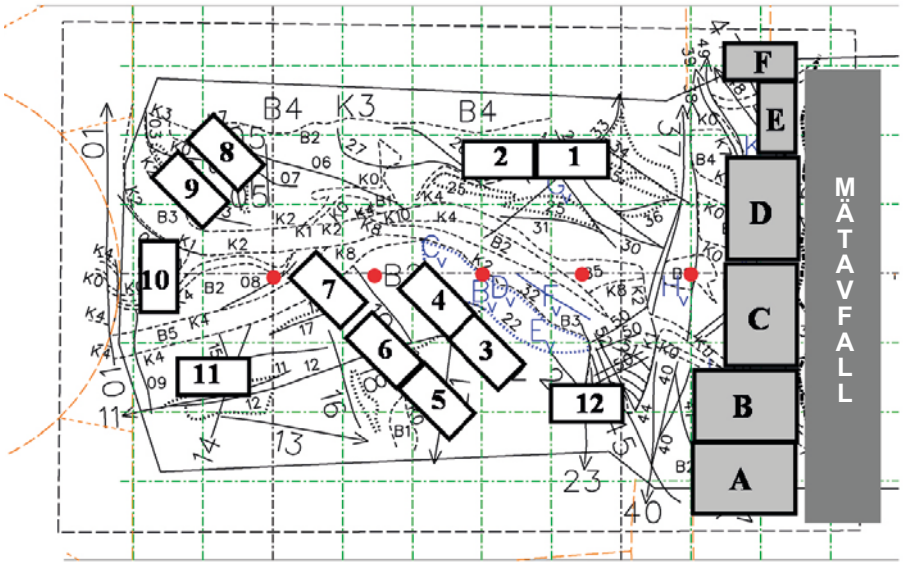

Figure 2-22. *The approximate locations of sorbing mats placed within the TASO tunnel. The measurement weir is denoted MÄTVALL within the figure. This image is reproduced from the task description (Vidstrand et al. 2017).*

Table 2-17. Distribution of inflows to the TASO tunnel, measured using sorbing mats. Values are reproduced from the task description (Vidstrand et al. 2017).

Mat no. (Def. zone)	Q [ml/min]	Mat no. (HRD)	Q [ml/min]
A	128	3	8
B	7	4	< 1
C	57	5	1
D	3	6	8
E	< 1	7	1
F	< 1	8	< 1
12	1	9	< 1
1	1	10	2
2	2	11	1

2.9.4 Inflow boreholes

Short duration inflow tests for the five probe boreholes are performed as detailed in Table 2-18. Measurement values are presented after approximately 15 minutes following the opening of each borehole. This short duration inflow profile for probing borehole KO0017G01 is shown in Figure 2-23.

Table 2-18. Short-duration (~ 15 minutes) inflow measurements taken during phase 2 of the BRIE. Inflows are reported for five probing boreholes located on the floor of TASO tunnel (09-2011). Measurements are reproduced from the task description (Vidstrand et al. 2017).

Borehole	Sec up [m]	Sec low [m]	Section length [m]	Q [ml/min]
KO0014G01	1.33	3.0	1.67	0.1
KO0015G01	2.1	3.03	0.93	0.6
KO0017G01	2.11	2.97	0.86	1
KO0018G01	1.42	3.06	1.64	0
KO0020G01	1	3.1	2.1	0.01

2.9.5 Pressure responses and flow

Long-term pressure tests for flow and recovery were performed in two boreholes,

- KO0017G01, located in TASO floor (76 mm diameter), and
- KO0011AO1, located in TASO left wall (76 mm diameter) and, intersecting structure wfracture_01.

Flow and pressure response data is provided as part of task description (Vidstrand et al. 2017) for KO0017G01 and KO0011A01 and presented in Figure 2-23 through Figure 2-26. Files detailing inflow and pressure measurements are summarised in Table 2-19.

Table 2-19. A summary of files provided for inflow and pressure data in boreholes KO0017G01 and KO0011A01. This table is reproduced from the task description (Vidstrand et al. 2017).

Excel file	Content
Phase 1 ID11 KO0017G01 flow_during_test_org_121003.xls	Flow
Phase 1 ID11 KO0017G01_105079_ID11_Inflödestest_121003.xls	Pressure
Phase 2 ID05 KO0011A01_inflow_to_tunnel_121003.xls	Flow
Phase 2 ID05 KO0011A01_Pressure_Wall_121003.xls	Pressure

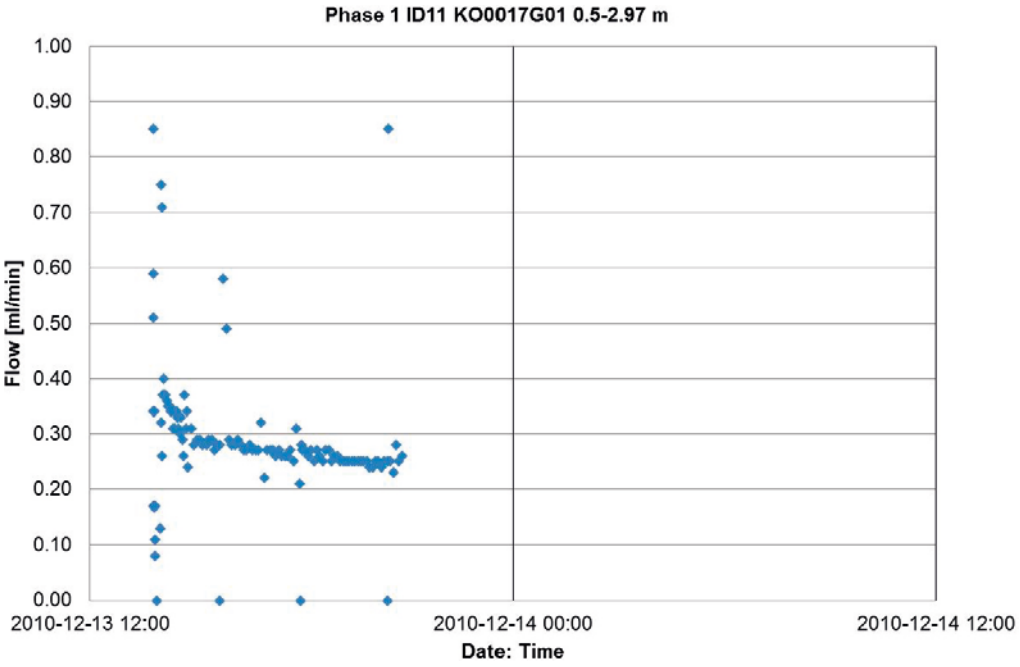

Figure 2-23. *Inflow to 76 mm probe boreholes KO0017G01, for section 0.5 m–2.97 m (12-2010). This figure is reproduced from the task description (Vidstrand et al. 2017).*

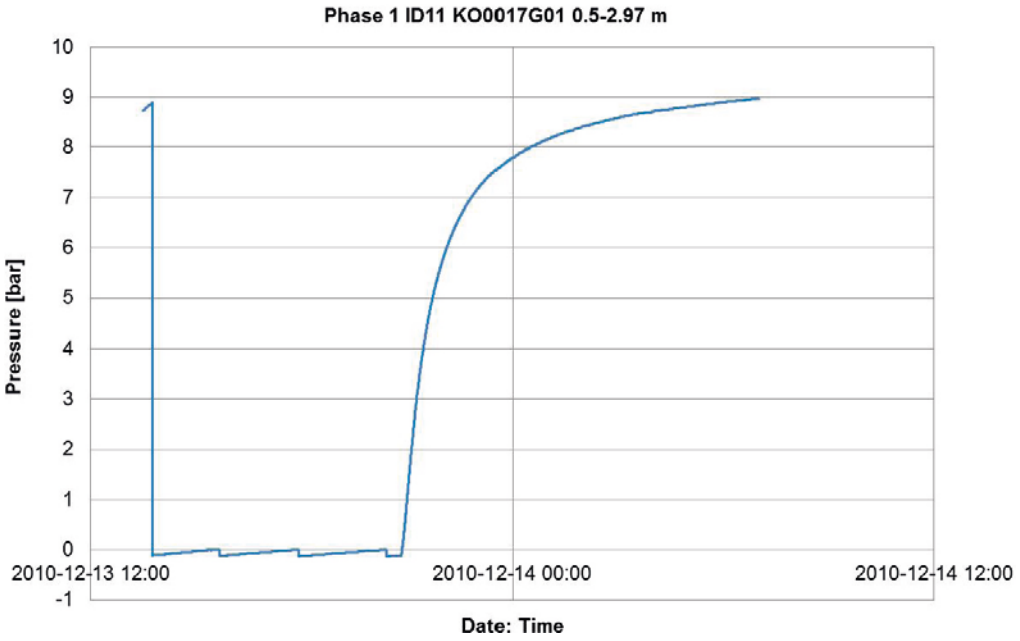

Figure 2-24. *Long-term pressure tests in 76 mm borehole KO0017G01, for section 0.5–2.97 m (12-2010). Zero pressure readings correspond to times at which inflows are still to fill the borehole section. This figure is reproduced from the task description (Vidstrand et al. 2017).*

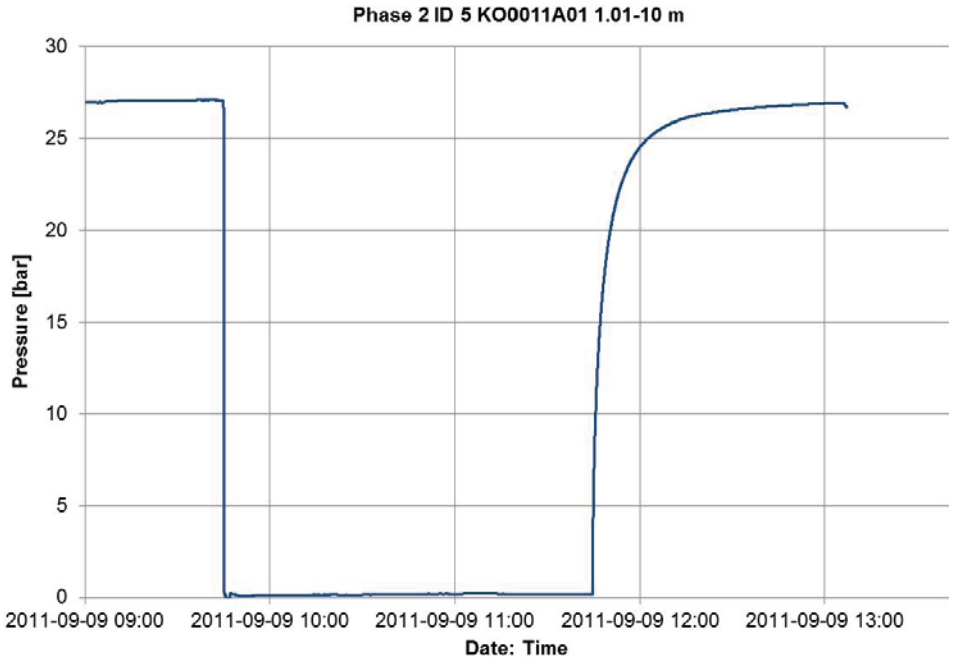

Figure 2-25. *Long-term pressure tests in 76 mm borehole KO0011A01, for section 1.01 m–10 m, and intersection with structure wfracture_01 (09-2011). This figure is reproduced from the task description (Vidstrand et al. 2017).*

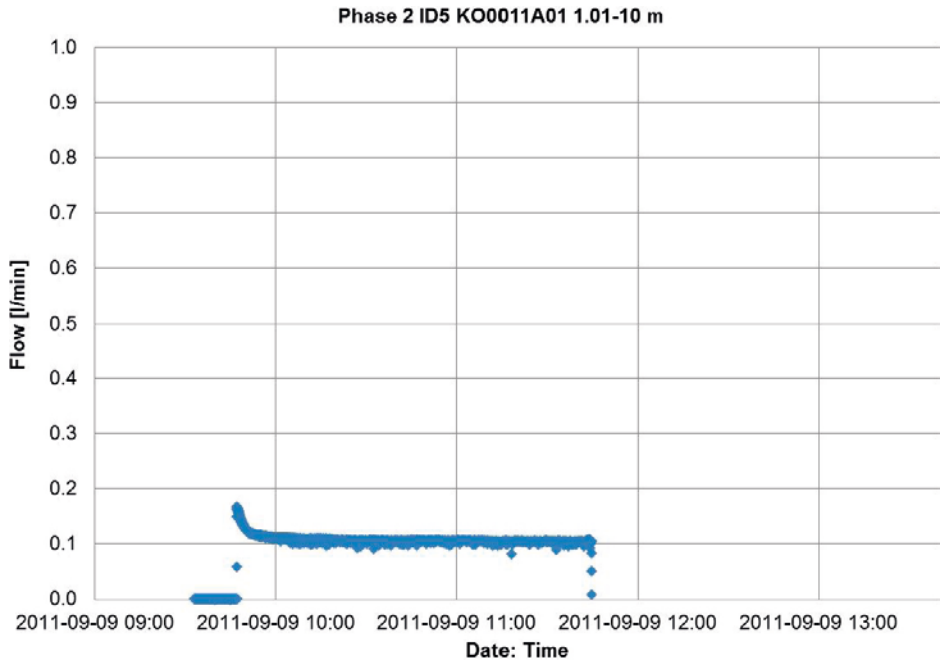

Figure 2-26. *Inflow measurements in 76 mm borehole KO0011A01, for section 1.01 m–10 m, and intersection with structure wfracture_01 (09-2011). This figure is reproduced from the task description (Vidstrand et al. 2017).*

2.9.6 Inflow to 30 cm boreholes

Inflow data to both 76 mm probe boreholes KO0017G01 and KO0018G01, as well as subsequent overcored deposition holes (diameter 30 cm) is presented in Table 2-20. For KO0017G01, measured inflows include PFL techniques in the probe borehole and nappy tests in the overcored deposition holes. For KO0018G01, inflows are only observed in the overcored hole, indicating hydro-mechanically induced changes.

Table 2-20. Flow data for borehole KO0017G01 (76 mm, PFL, 300 mm and nappy test) and KO0018G01. Measurements are reproduced from the task description (Vidstrand et al. 2017).

	KO0017G01	KO0018G01
Flow (76 mm) borehole	0.25 ml/min (0.5 m–2.97 m, ~400 min) Phase 1 (see Figure 2-23 above)	–
Flow (76 mm) borehole PFL	~0.5 ml/min (<30 ml/h or 0.5 ml/min, uncertain)	–
Flow (30 cm) borehole	0.12–0.25 ml/min (2.1 m–3.5 m, ~400 min) Phase 3	0.01–0.03 ml/min (2.1 m–3.1 m, ~400 min) Phase 3
Flow (30 cm) borehole "nappy test"	~0.1 ml/min Possibly water is entering in the lower part of the borehole (along pegmatite vein, see Table 2-21).	–

Characteristics of the inflows are provided from the nappy test, conducted on the walls of 30 cm overcored borehole KO0017G01. Nappies were distributed on the borehole wall in five rows, from 2.25 m down to 3.25 m, and 15 columns covering ~0.94 m. Inflows for individual nappies are shown in Figure 2-27. The first row of data (2.25 m–2.45 m) corresponds to a dry section of the borehole, providing a background inflow value. This can be subtracted from measurements from other nappies, allowing the contribution from specific features to be determined. The main inflows are found at approximately 2.45 m–2.65 m, oriented North to Northeast (see, for example the photograph, Figure 2-28; and the image from the Borehole Image Processing System (BIPS), Figure 2-29). The nappy test also indicates increased inflows (over background) to a depth of 3.25 m. In addition, hydraulic tests on borehole sections identified inflow in the lower section of the borehole (depths 3.25 m down to 3.5 m). All of these inflow measurements are indicated in Table 2-21, compiling data from a number of different tests. In summary, the following features of KO0017G01 require consideration

- the steeply dipping fracture (see Subsection 2.4.2) intersecting the hole at 2.9 m,
- the pegmatite vein at the bottom of borehole KO0017G01 which may be the cause of the high pressures observed in this section. No detailed information on this feature is available at present.

The task description (Vidstrand et al. 2017) provides a suggested distribution of inflows below 2.1 m, reproduced in Table 2-21. Table 2-21 details:

- ***Left:*** Inflows identified from nappy tests, where
  - the top value corresponds to the inflows with background contributions subtracted,
  - the bottom value corresponds to the total inflows recorded, and
  - The colour coding is defined as:
    - green cells correspond to major inflows identified from nappy tests, and
    - yellow cells correspond to uncertain inflows identified from nappy tests.
- ***Right:*** Measurements from hydraulic tests of borehole sections. These identify flow in the lower part of the borehole.
- ***Centre:*** An approximate distribution of inflows, inferred from compiling all available information.

Table 2-21. Distribution of inflows from both nappy and inflow tests below 2.1 m in the 30 cm over-cored hole KO0017G01. This figure is reproduced from the task description (Vidstrand et al. 2017).

Depth [m]	Nappy [ml/min]		Possible distribution	Inflow sections [ml/min]		
2,1						
2,15				0	0,12	
2,2				0,05	0,25	
2,25						
2,3						
2,35	0	0				
2,4	*0*	*0*				
2,45						
2,5						
2,55	0,018	0,017	0,05			
2,6	*0,024*	*0,023*				
2,65						
2,7						
2,75	0,009	0,01				
2,8	*0,014*	*0,016*				
2,85						
2,9						
2,95	0,009					
3	*0,015*			0,05	0,13	
3,05				0,13	0,2	
3,1						
3,15	0,006	0,014	0,05			
3,2	*0,012*	*0,024*				
3,25						
3,3						
3,35			0,05			
3,4						
3,45						
3,5			0,05	0,07		0,06-0,08

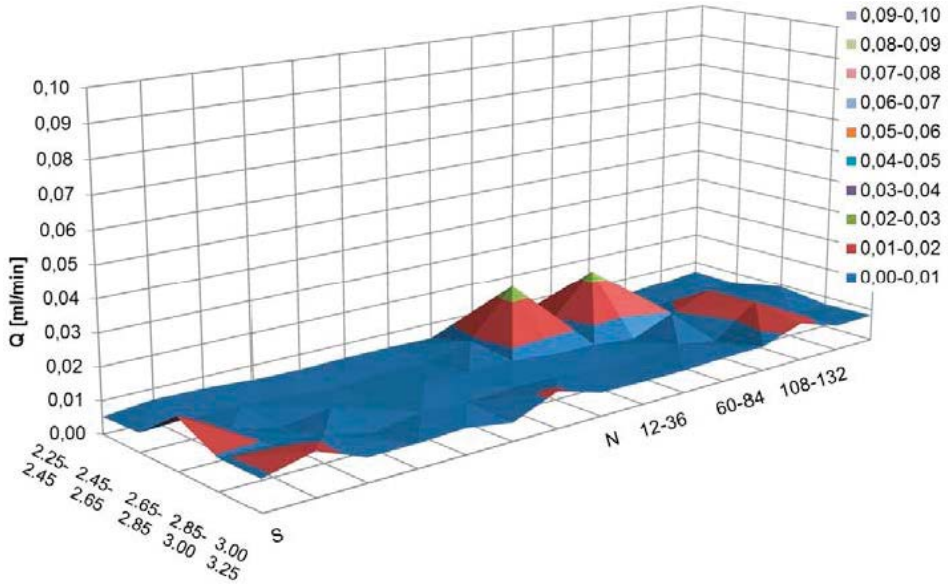

Figure 2-27. *Inflows to deposition hole KO0017G01 for individual "nappies" (nappies are distributed in five rows, 2.25 m–3.25 m, and 15 columns over ~0.94 m circumference). The main inflows are found at 2.45 m–2.65 m, oriented North to Northeast (see photo, Figure 2-28 and BIPS-image, Figure 2-29). This figure is reproduced from the task description (Vidstrand et al. 2017).*

Figure 2-28. *The location of inflows in KO0017G01, along a fracture identified at 2.9 m. See also the pegmatite vein that may conduct water. This figure is reproduced from the task description (Vidstrand et al. 2017).*

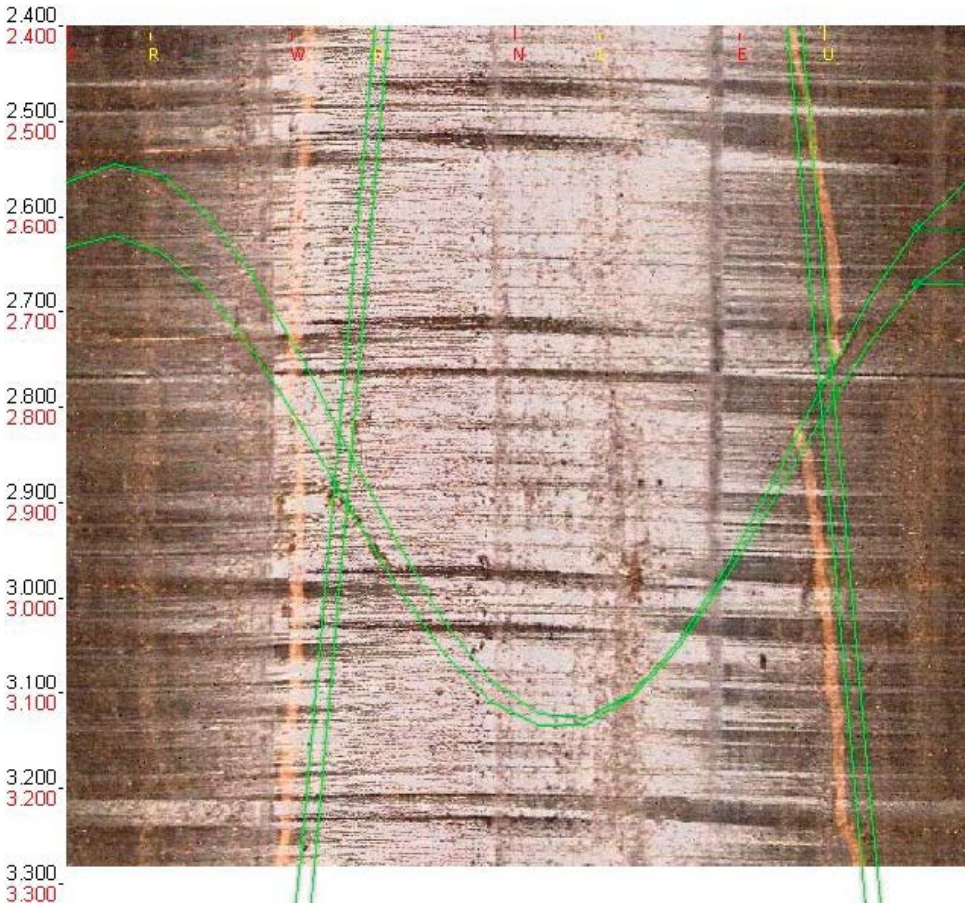

Figure 2-29. *BIPS-image from deposition hole KO0017G01. The main inflows are at approximately 2.45 m–2.65 m. The green lines identify both a fracture trace (at 2.9 m) and a pegmatite vein which is possible flowing. This figure is reproduced from the task description (Vidstrand et al. 2017).*

3 Modelling Task 8D

In this section, the modelling concepts and methodologies adopted for Task 8D are detailed. This includes

- a discussion of the chosen software packages adopted for modelling Task 8D1 and Task 8D2,
- a review of the model definition, summarising any assumptions and simplifications made for computations to remain tractable, and
- an overview of the aspects of the model that will undergo calibration using measurements and observations local to the BRIE.

Task 8D modelling comprises of three components:

1. Models developed under Task 8C containing the five, 76 mm probe boreholes are refined and calibrated using the additional information provided for Task 8D, as summarised in Section 2. This information includes:
   - refinement of the geometric description of deterministic fracture zone wfracture_01;
   - additional geometric details for fourteen boreholes drilled in the TASO tunnel floor and four in the TASO tunnel walls;
   - inflow estimates and pressure responses within the five probe boreholes from additional, short duration tests; and
   - inflow estimates from the "nappy" experiments of the TASO tunnel.
2. The conditioned models developed in Stage 1 are modified to include the overcored boreholes KO0017G01 and KO0018G01, with diameter 30 cm. The amount and location of inflow to these two 30 cm deposition holes can be compared to additional data in Task 8D, which provides:
   - inflow estimates for the two, 30 cm diameter deposition holes; and
   - fracture intersections to the deposition holes.
3. The third modelling stage considers the resaturation of bentonite emplaced in the central deposition holes. The procedure for installing the bentonite at the BRIE forms part of the Task 8D update. Initial conditions for modelling are taken from Stage 2, and subsequent hydration patterns/saturation distributions with time are calculated, along with the associated pressure development within the bentonite and the near-field bedrock.

The techniques adopted for modelling Task 8D of the BRIE are discussed in this section, and are based on a refinement of the approach implemented for Task 8C (Baxter et al. 2013). Details of the modelling concepts adopted, including a review of the chosen software packages, are presented in Section 3.1. Specific details of the adopted modelling approach for Task 8D is provided in Section 3.2, including identification of necessary assumptions and simplifications. Finally, Section 3.3 overviews the calibration approach that will be used to refine fracture models of the bedrock local to the BRIE and TASO tunnel.

3.1 Concepts and methodology

Task 8D considers the hydraulic interaction between a fractured host rock, and a bentonite buffer material on the deposition hole scale. Therefore it is imperative that modelling tools selected for this study are capable of representing the physics required for accurate prediction of bentonite resaturation profiles and times. Two software packages are identified that will be incorporated into the study of Task 8D, namely:

- CONNECTFLOW: used to provide a discrete fracture network (DFN) representation of the groundwater flow through the fractured host rock.
- TOUGH2: used to represent the multiphase flow regimes occurring during resaturation of the bentonite buffer.

This choice of software packages is identical to Task 8C (Baxter et al. 2013) with more details on both of these computer codes presented in Sections 3.1.1 and 3.1.2 below.

3.1.1 CONNECTFLOW

CONNECTFLOW is a suite of software, developed by AMEC, for modelling groundwater flow and transport on a variety of scales. It consists of

- a continuum porous media (CPM) module, referred to as NAMMU, and
- a discrete fracture network (DFN) module, referred to as NAPSAC.

The mathematical formulations adopted by CONNECTFLOW are presented in detail in AMEC (2012a,b,c,d). For a high-level description, the reader is referred to Joyce et al. (2010); summarised below for the aspects of the software directly applicable to modelling Task 8D.

The BRIE at the Äspö Hard Rock Laboratory (HRL) is located in a granitic bedrock, and the flow of groundwater is primarily through a series of interconnected, flow-conducting fractures. By applying a DFN concept, it is possible to statistically represent the groundwater path from one fracture to another at the intersections between them. As discussed in Section 2.3, there are five properties used to characterise a fracture network. These are

- the spatial distribution of fractures (e.g. Poisson, clustered),
- the fracture intensity, usually expressed as the fracture surface area per unit volume (P_{32}),
- the orientation of fractures (e.g. Fisher distributions for separate fracture sets),
- the size of fractures (e.g. log-normal, power-law distributions), and
- the hydraulic properties of fractures (e.g. transmissivity, transport aperture, etc).

The DFN concept is a powerful approach; able to model stochastically and deterministically (where sufficient characterisation has taken place) the individual flow conduits in fractured rock, and the available field data. The development of DFN models consist of fractures (represented as 2D planes) from two data sources:

- **Deterministic features:** Usually large scale features (e.g. structures such as wfracture_01, wfracture_02 and NNW4), or local scale fractures interpreted from borehole intersections (e.g. the hydraulically active fractures observed to intersect deposition holes KO0017G01 and KO0018G01).
- **Stochastic fractures:** These are used to generate fractures within the bedrock which are not readily observed through intersection with an engineered feature (tunnel / boreholes / etc). A stochastic approach is adopted, sampling fracture characteristics from probability distribution functions (PDFs) for each fracture set. These statistical distributions are usually determined through field experiments such as borehole logging and hydraulic tests. Fracture networks resulting from sampled distributions are not expected to provide the exact geometric and hydraulic properties of features within the bedrock, rather providing one possible network of fractures that can statistically describe the range of measurement. Uncertainties of a stochastic fracture network can be addressed by considering multiple realisations of the DFN model.

With regards to the emplaced bentonite, the representation of individual fractures intersecting a deposition hole is critical to understanding the potentially highly heterogeneous wetting of the buffer material. It is noted, however, that DFN models are constrained by the resolution of field data used for parameterisation (e.g. small fractures intersecting a tunnel may not be mapped), and the rock matrix (including fractures neglected in the DFN) may be relevant for bentonite wetting in deposition holes with limited fracture intersections. Therefore, to successfully model the resaturation processes, the software package TOUGH2 will be used, and described in detail in Section 3.1.2. The numerical implementation in TOUGH2 utilises a continuum concept, and it is therefore necessary to convert the heterogeneous nature of the fracture network into equivalent continuous porous medium (ECPM) block properties. This process of calculating ECPM properties is called upscaling, implemented in CONNECTFLOW by calculating both a directional permeability tensor and fracture kinematic porosity for grid cells based on the fracture network. This upscaling process uses a method that requires flow simulations to be performed through the DFN model on the scale of individual grid cells to produce an equivalent continuum model. A schematic of these flow calculations for a typical grid cell within 2D DFN model is shown in Figure 3-1. For grid cells that do not correspond to fractures in the DFN, permeabilities and porosities are assigned corresponding to a granitic rock matrix.

Although this upscaling processes reflects flow through the underlying DFN model, the methodology can yield over-prediction of hydraulic conductivity for individual grid blocks, a consequence of flows through fractures cutting the corner of the block that are unrepresentative of flows through the *in situ* fracture network (Figure 3-2). These over-predictions are especially significant in sparse heterogeneous fracture networks, where the flux through the network of interconnected fractures is affected by 'bottlenecks' through low transmissivity fractures, which is quite different to the flux through single fractures. To address this over-prediction, the upscaling methodology can be refined to simulate flow through a slightly larger domain than the grid cell required for the ECPM properties, but then calculating the flux responses through the correct cell size. The additional area around the grid cell is referred to as a "*guard zone*", and is further discussed in Rhén et al. (2009). For this study, a "*guard zone*" is defined that extends the side vectors of the grid cell by 50 % in each direction.

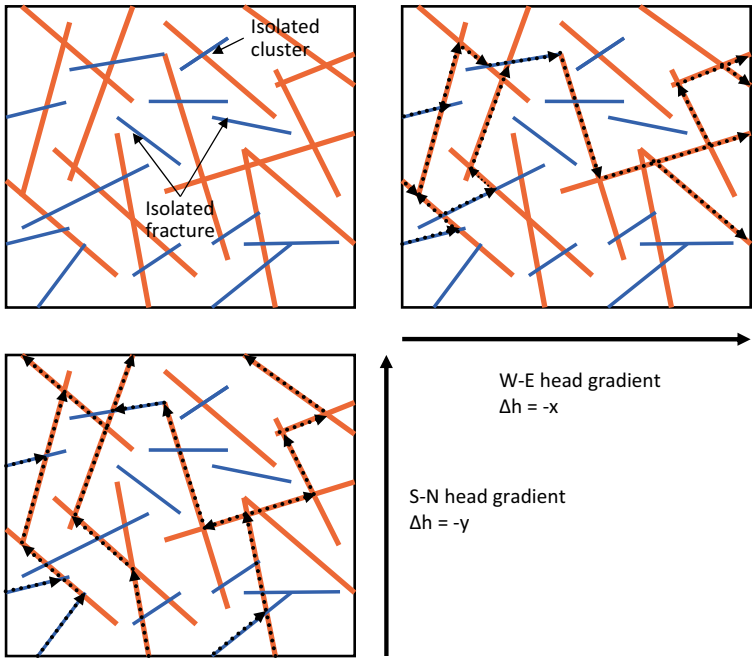

Figure 3-1. *A 2D illustration of flow through a network of fractures, reproduced from Joyce et al. (2010). Top left: illustrates a random network of fractures, with variable length and transmissivity (red fractures are highly transmissive, with blue fractures indicating low transmissivity). Top right: illustration of flow paths through the fracture network for a linear head-gradient decreasing along the x-axis. Bottom left: illustration of flow paths through the fracture network for a linear head-gradient decreasing along the y-axis.*

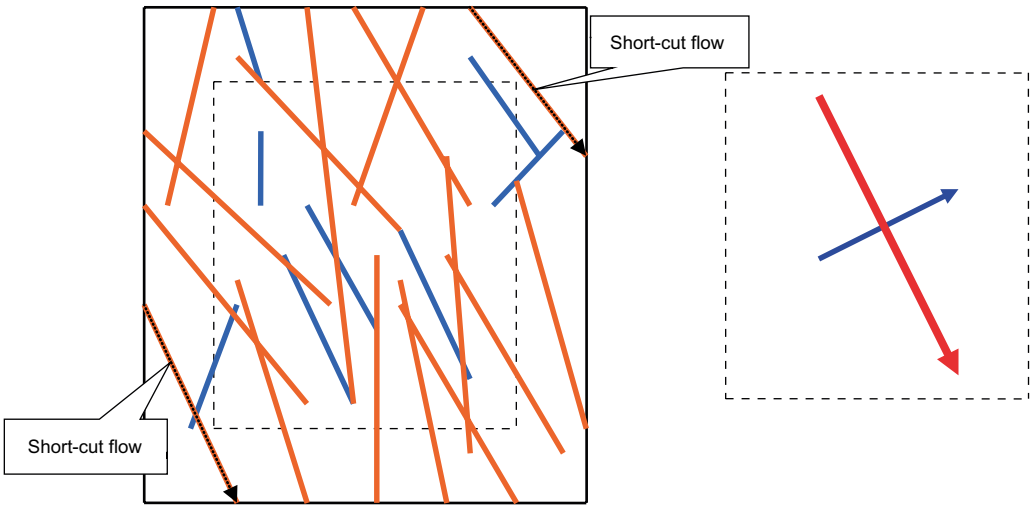

Figure 3-2. *2D illustration of how block-scale permeabilities can be overestimated. This figure is reproduced from Joyce et al. (2010).*

Calculating permeability tensors

Effective block permeabilities are calculated by simulating flux through the fracture network on the scale of individual grid cells. Within the DFN model, several groundwater flow-paths are possible due to the number and variety of connections observed across the network. Consequently, cross-flows can form, a common characteristic of DFN models, occurring non-parallel to the head gradient. An anisotropic permeability tensor is used to account for these cross-flows, and for a 3D analysis, CONNECTFLOW uses six directional components to characterise a symmetric permeability tensor. For each head gradient direction, the DFN models are used to calculate the fluxes through each face of the block. The permeability tensor is then derived by a least-squares fit to these flux responses for the fixed head gradients (Jackson et al. 2000).

Calculating kinematic porosities

The kinematic porosity, Φ, of individual grid cells is calculated by

$$\phi = \frac{\sum_f e_{tf} a_f}{V}, \tag{3-1}$$

where V is the volume of the grid cell, a_f is the area of each fracture in the block and e_{tf} is the transport aperture of the fracture. The transport aperture is related to the hydraulic aperture, e_{hf} by,

$$e_{tf} = 10 e_{hf}, \tag{3-2}$$

as used in Hartley et al. (2013) with similar relationships interpreted from tracer test programs, e.g. Hjerne et al. (2010). The hydraulic aperture for each fracture is calculated from the transmissivity, T_f, by the cubic-law:

$$e_{hf} = \left(12 \mu T_f / \rho g\right)^{1/3}. \tag{3-3}$$

3.1.2 TOUGH2

TOUGH2 is a numerical software package developed by Lawrence Berkeley National Laboratory (Pruess et al. 1999) and is licensed and distributed by the Berkeley Lab Software Center at http://esd.lbl.gov/TOUGH. TOUGH2 has been extensively used for a wide range of applications, including simulation of nonisothermal, multiphase fluid flows in both porous and fractured media.

For this study, both the bentonite packages and surrounding fractured host rock are modelled numerically using TOUGH2 on the deposition hole scale, providing predictions for the highly heterogeneous resaturation of the buffer material. This includes representation of the flow of the gas and aqueous phases by mass conservation and a modified form of Darcy's Law (including the multiphase nature of the flow via a relative permeability function).

Details of the numerical formulation used within TOUGH2, and application of the software to Task 8D modelling are discussed in the following two sections.

Numerical formulation of TOUGH2

The numerical software package, TOUGH2, is formulated based on an integrated finite-volume spatial discretisation, using upstream weighting, and a fully implicit first-order backward difference for discretisation in time. An automated algorithm based on the convergence of the model is used to optimise the time-step size applied during the transient simulation.

Newton-Raphson iterations are used to handle the non-linearities within the formulation, and for each of the Newton-Raphson iterations, a preconditioned conjugate gradient algorithm is implemented to solve the remaining system of linear equations.

TOUGH2 incorporates a number of different Equation-Of-State (EOS) modules which include fluid properties required for assembling the governing equations (Pruess et al. 1999). For this study,

the EOS7R[3] module (Oldenburg and Pruess 1995) will be used for modelling the resaturation of bentonite, and includes the mass components water, brine and air.

Salinity of the aqueous phase (i.e. groundwater) is represented within the TOUGH2 model as a mass fraction of brine, and both viscosity and density of the groundwater composition are interpolated from the water and brine end-members at reference conditions. In addition,

- the solubility of the gas phase is modelled using Henry's law (i.e. the solubility is proportional to the partial pressure of the gas), and
- the relative permeabilities and capillary pressure functions utilised in the bentonite resaturation models are as developed and discussed in Section 3.2.5.

Application of TOUGH2 to Task 8D modelling

The fractured bedrock local to the BRIE at the Äspö HRL provides a highly heterogeneous media for groundwater flow to ingress to the deposition holes and resaturate the bentonite. As discussed in Section 3.1.1, CONNECTFLOW can be used to provide ECPM block properties for individual grid cells in the model, providing a continuum approximation to the groundwater pathways existing in the fractured network. These ECPM properties consist of permeabilities and porosities on all cells of the grid, and AMEC has previously modified TOUGH2 to allow this spatially varying permeability tensor to be imported (Hawkins and Swift 2009). A summary of the methodology adopted is presented below:

- For a GID (GID) formatted mesh, permeabilities and porosities are calculated using CONNECTFLOW and exported in GOCAD (GOCAD) format. This retains the same grid cell ordering as the GID mesh file.
- A Perl script, written by AMEC, analyses the GID mesh, permeability, porosities and TOUGH2 mesh. For each cell centre of the TOUGH2 mesh, the corresponding cell within the GID mesh is located, allowing permeabilities and porosities for that grid cell to be extracted.
- Permeabilities associated with each cell in the TOUGH2 mesh are subsequently written to a file, providing a new TOUGH2 input data block denoted 'PERMA'. AMEC have modified the TOUGH2 source code to allow calculation of the permeability for each connection. This is achieved by projecting the permeability tensor for a given cell in the 'PERMA' block according to the connection direction that is being discretised.

The algorithm for locating the centre of each cell of the TOUGH2 mesh within the GID mesh (step 2 above) involves $O(n^2)$ operations, where n is the number of grid cells. Consequently, analysis times can quickly become prohibitive as mesh sizes increase. As such, the following refined algorithm has been adopted:

1. A box is defined which bounds the GID mesh.
2. This box is recursively subdivided, until containing less than 100 grid cells.
3. When searching for a TOUGH2 cell centre, the bounding box tree is traversed from the top through to the lowest level box.
4. Once the lowest level bounding box is identified, a bounding box test is conducted for each of the 100 grid cells.
5. If a point lies within the bounding box of a grid cell, that cell is further subdivided into 12 tetrahedra. A test is performed for the point being in each tetrahedron to determine whether the point is within the grid cell.

The use of this algorithm allows TOUGH2 meshes with differing cell resolution to the original upscaling to be considered.

[3] The EOS7R module has been enhanced by Amec Foster Wheeler to include additional checks to stop any variables entering unphysical regions of phase space as well as including a modification which more accurately implements mass conservation during changes in phase (e.g. upon full saturation of the bentonite).

3.2 Model description

The Task 8D model description used in this study is detailed in the following sections, with emphasis on updates incorporated since modelling performed in the Task 8C project (Baxter et al. 2013).

3.2.1 Geometrical description

The primary investigation area for the BRIE is in the vicinity of the TASO tunnel of the Äspö HRL. The size of the implemented model domain differs between subtasks, as described below.

- Task 8D1. The model domain is defined as specified in the task description (Vidstrand et al. 2017) with bounding coordinates presented in Table 2-1. The model domain forms a $(40\ m)^3$ block, as shown in Figure 3-3, and incorporates both TASO and TASD tunnels. Tunnel floors are located at an elevation of −417.0 m, with the five probe boreholes extending a further 3 m (to an elevation of −420.0 m). The dimensions for both the TASO and TASD tunnels are extracted from CAD files supplied with the task description (Vidstrand et al. 2017), as discussed in Section 2.1.
- Task 8D2. In this subtask, the resaturation of bentonite emplaced in the central deposition holes is modelled. Here, the numerical requirements are significantly greater, with extensive refinement necessary local to the resaturation front. In order for computations to remain tractable, the volume of the model domain has been reduced from that used in Task 8D1 above, providing localised refinement to the two central overcored boreholes KO0017G01 and KO0018G01. For the purposes of simulating resaturation, the other three boreholes are omitted from the model; an approximation not expected to unduly affect the calculated resaturations in KO0017G01 and KO0018G01. This is because the suction of the bentonite at an initial saturation of 41.3 % is ~70 MPa (compared to a drawdown of ~4 MPa to the open boreholes). The model domain used for Task 8D2 is shown in Figure 3-4, extending 15 m along the axis of the TASO tunnel, 12 m laterally and 6¼ m vertically.

3.2.2 Processes considered

Both Task 8D1 and 8D2 models consider hydraulic processes, with brief details provided below:

- Task 8D1: models are developed using CONNECTFLOW, calculating single-phase fresh-water flow explicitly through the fractured bedrock. Simulations are calibrated against measurements for pressure build-up and the ingress of groundwater to the probe boreholes.
- Task 8D2: models are developed using TOUGH2, performing two-phase saline groundwater flow calculations using an upscaled representation of the 8D1 bedrock. Calculations predict the resaturation profiles and times for bentonite emplaced in overcored 30 cm boreholes KO0017G01 and KO0018G01.

3.2.3 Boundary and initial conditions

Boundary and initial conditions for both pressure and salinity are provided in the task description (Vidstrand et al. 2017) as extracted from the current, official, hydrogeological model of the Äspö HRL. Pressure and groundwater salinities, interpolated onto the $(40\ m)^3$ model domain used for Task 8D1 are shown in Figure 3-5.

Using the prescribed salinity density dependence given in Equation (2-3), salinities exported from the Äspö HRL model can be used to infer variations in groundwater density over the model domain. Across the model, variation in groundwater density is very limited, with maximum and minimum values of 1005.7 kg/m^3 and 1005.1 kg/m^3 respectively. As a consequence, there is little potential for buoyancy effects to significantly affect the groundwater pathways through the fractured bedrock. Specifically, buoyancy effects are expected to be small compared to uncertainties in DFN parameters and hydraulic properties of the fracture network. Therefore:

- For inflow and pressure build up calculations in Task 8D1, the effects of salinity will be ignored, with freshwater simulations performed instead.

- For calculations of the resaturation of bentonite in Task 8D2, groundwater salinity will be included. This is because the presence of saline groundwater is an important aspect for the performance of the bentonite as a buffer material, and its ability to fulfil required safety functions such as attain suitable swelling pressures. Buoyancy effects from considering groundwater salinity in Task 8D2 are expected to be negligible. Although modelling results for the simulated evolution of salinity within emplaced bentonite are not presented in this study, they could be used to assess the peak saline concentrations in the bentonite during resaturation, ensuring concentrations do not exceed safety requirements.

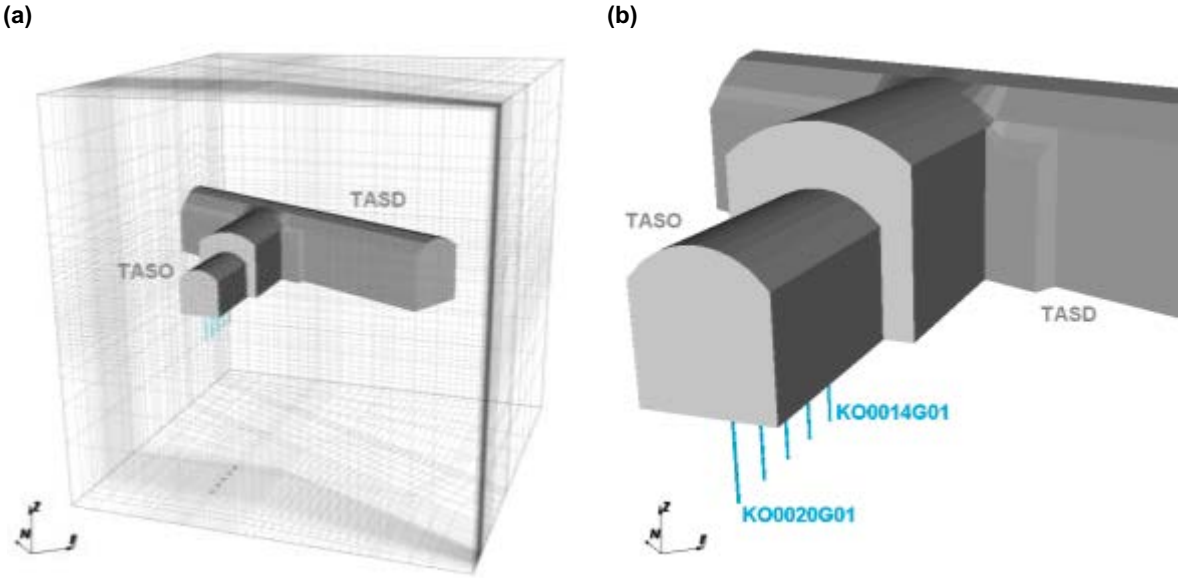

Figure 3-3. *(a) Location of BRIE experiment with the TASO and TASD tunnel at the Äspö Hard Rock Laboratory in Sweden. (b) The five boreholes for investigation as part of Task 8C are shown in blue.*

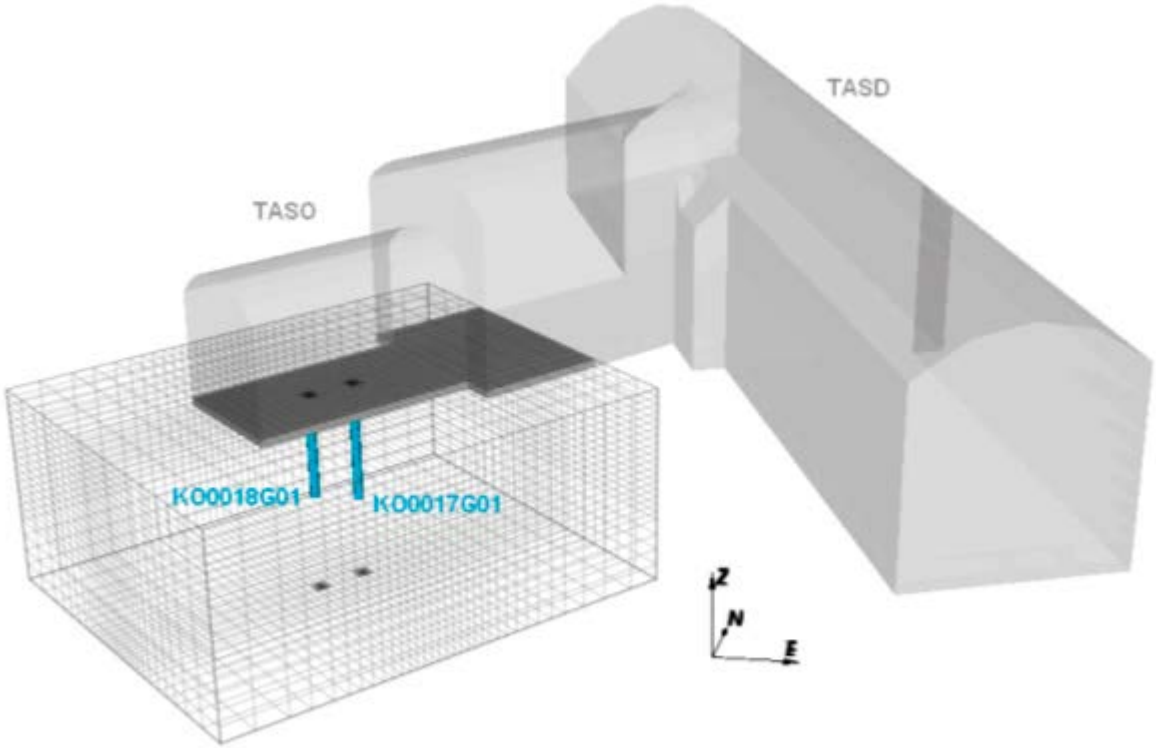

Figure 3-4. *A local region to the two overcored central boreholes, selected for mesh refinement necessary for hydration calculations.*

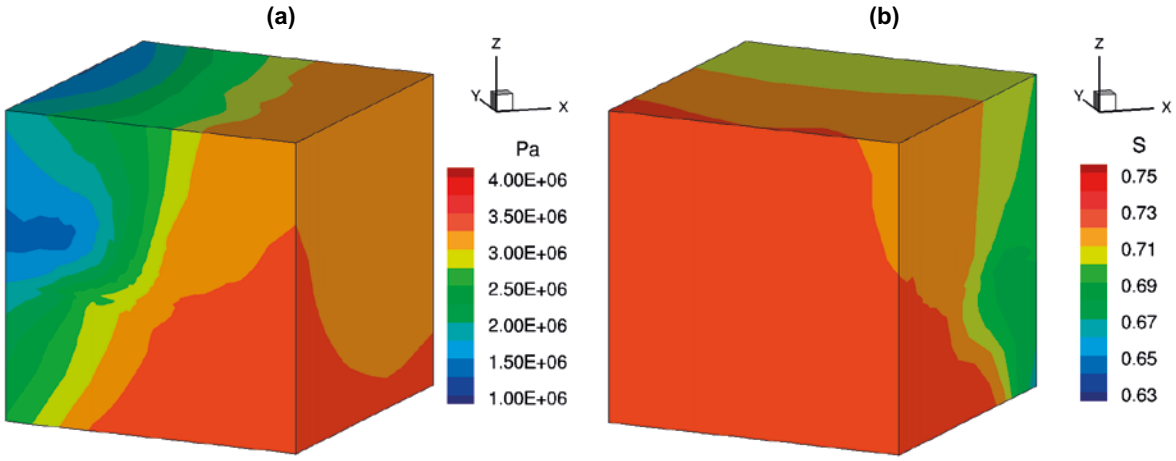

Figure 3-5. *(a) Pressure (Pa) and (b) groundwater salinity (–) prescribed for the model domain from the specified initial conditions. Values are interpolated from the task description (Vidstrand et al. 2017).*

Task 8D2 is modelled using TOUGH2, where groundwater density is interpolated between end-members of water, ρ_{water} = 997.16 kg/m^3; and brine, ρ_{brine} = 1 185.1 kg/m^3 at reference conditions of 1 bar and 25 °C. The interpolation takes the form

$$\frac{1}{\rho} = \frac{1-x}{\rho_{water}} + \frac{x}{\rho_{brine}}, \tag{3-4}$$

where the mass fraction of brine, x, is defined to provide densities consistent with the regional Äspö HRL simulation. Density variation due to salinity across the model domain is small, with the mass fraction of brine, x, ranging from 0.05321 up to 0.05327.

For each of the subtasks, the probe boreholes / deposition holes are considered differently, as detailed below.

- For Task 8D1, pressure build-up calculations are performed for the five 76 mm probe boreholes, packed off to isolate the upper 1 m from the host rock. In addition, inflows are calculated to each of the probe boreholes, calculated for open hole conditions (i.e. held at atmospheric pressure at the top of the boreholes).
- For Task 8D2, the central deposition holes KO0017G01 and KO0018G01 are overcored to 30 cm diameter, and bentonite is emplaced. In addition, the length of KO0017G01 is extended to 3.5 m, reaching an elevation of −420.5 m. Initially, the emplaced bentonite is at atmospheric pressure, and allowed to evolve with time. The bentonite is initially saturated to 41.3 %, corresponding to suction value of ~ 70 MPa when using the retention curves detailed in Section 3.2.5.

Finally, atmospheric pressure boundary conditions are applied to model the TASO and TASD tunnels.

3.2.4 Parameters

The parameters necessary for modelling both Task 8D1 and 8D2 are detailed below.

Deterministic features

As part of Task 8C, three significant geological features were identified, named wfracture_01, wfracture_02 and NNW4. These are local to the BRIE experiment, intersecting the (40 m)^3 proposed model domain from the task description (Vidstrand et al. 2017). The Task 8C prescription of these three deterministic fractures is shown in Figure 2-2 and Figure 2-3.

Subsequent to Task 8C, additional information regarding the geological structural model has been established refining the geometry of structure wfracture_01 local to the TASO tunnel. This refinement requires the adjustment of large scale wfracture_01 to connect with this local TASO information. The updated description of wfracture_01 is shown in Figure 3-6, where

- inflow data to the TASO tunnel suggests both the original and updated geometric description of wfracture_01 are necessary (see Section 2.9.3).
  - Hydraulic properties for wfracture_01 are updated for Task 8D, obtained from hydraulic tests in a single borehole (KO0011A01), and yielding a transmissivity of 4×10^{-9} m^2/s. This is in comparison to the Task 8C parameterisation, which elicited a transmissivity of 2×10^{-8} m^2/s.
  - In this study, both the localised and large scale feature wfracture_01 are parameterised using the elicited Task 8C description as the single borehole measurement from KO0011A01 is not deemed sufficient to parameterise the whole structure.
- The new local description of wfracture_01 intersects probe borehole KO0014G01. This is not observed in the borehole logs, and as such the new wfracture_01 description is truncated at −417.5 m.
- Hydraulic tests indicate possible isolation of borehole KO0014G01. Therefore, the new local description of wfracture_01 is extended vertically from −417.5 m to −420 m.

For Task 8D1, the DFN representation of the fractured bedrock includes these three deterministic features, represented as flowing fractures as shown in Figure 3-7. For Task 8D2, they form part of the upscaling process, generating equivalent rock permeabilities. The parameterisations of these three features are provided in Table 2-11.

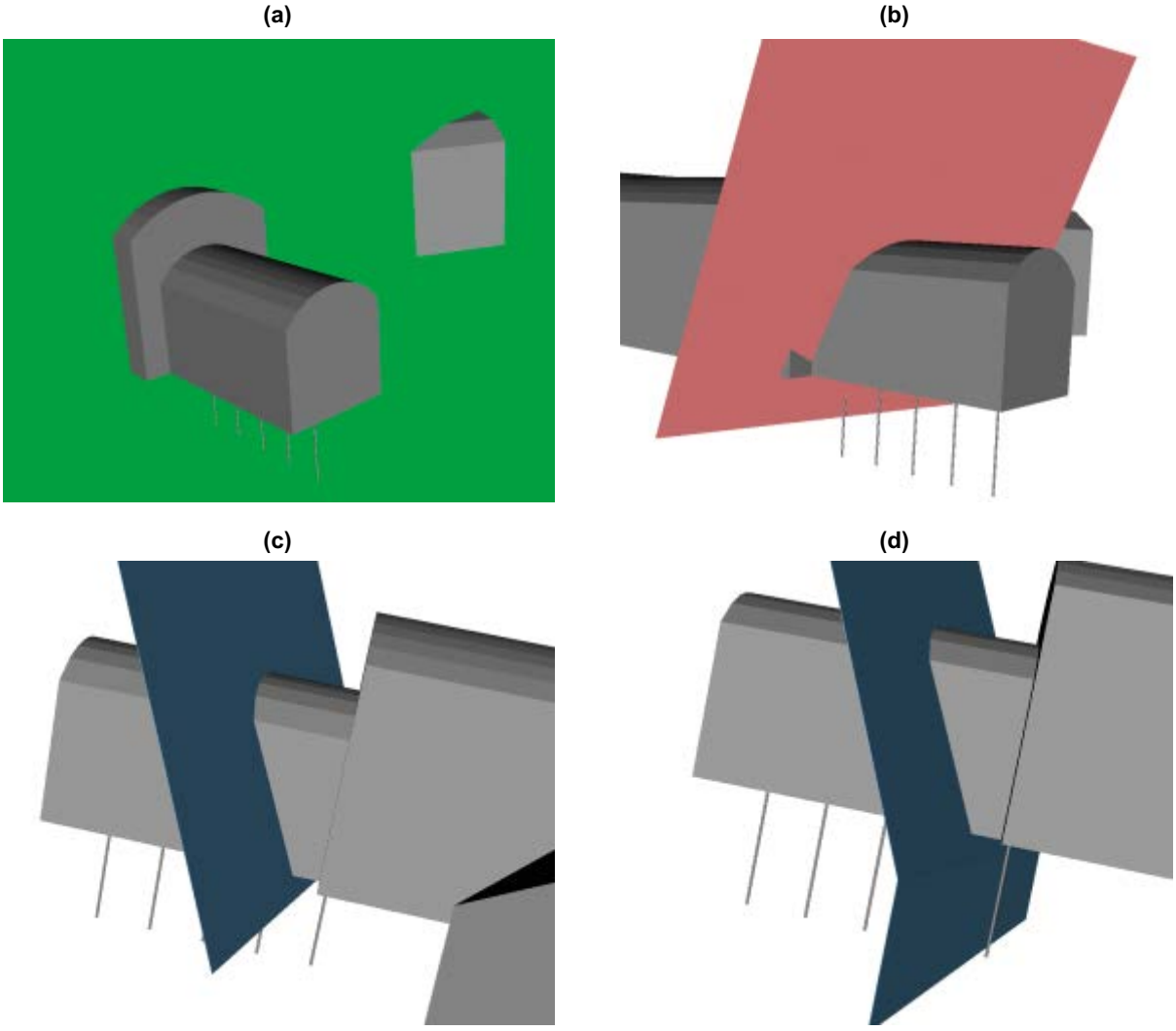

Figure 3-6. *(a) the original prescription of structure wfracture_01, taken from the task description for 8C; (b) the updated local description of wfracture_01, supplied as part of Task 8D; (c) truncation at −417.5 m of the updated local description of wfracture_01, avoiding intersection with probe hole KO0014G01; and (d) an extension of the updated local description of wfracture_01 to hydraulically isolate probe hole KO0014G01.*

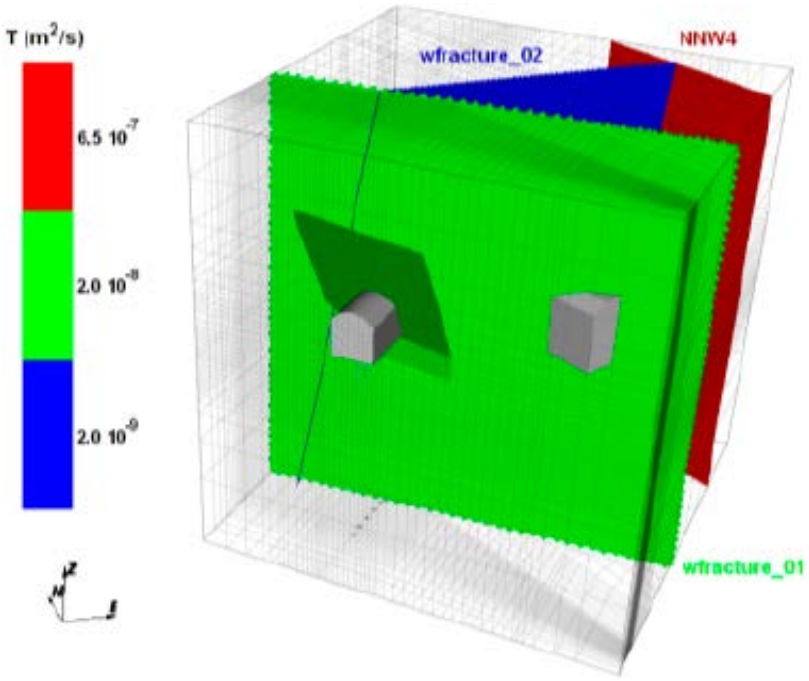

Figure 3-7. *Three large scale deterministic features, coloured by transmissivity, local to the TASO tunnel and within the model region defined. The local wfracture_01 prescription is also shown.*

Stochastic fracture statistics

Background fracture statistics for the bedrock local to the BRIE at the Äspö HRL were presented in Section 2.3. These include statistical distributions for

- fracture orientation,
- fracture intensity,
- fracture distribution, and
- fracture size relationships.

Using this parameterisation for the fractured bedrock, multiple realisations of the DFN model are generated using the CONNECTFLOW software package.

From the task description (Vidstrand et al. 2017), it has been noted that no fractures were observed to intersect the entire tunnel periphery (except for the three deterministic geological features). Therefore, in order to avoid the DFN contradicting the physical understanding of the fractured bedrock local to the BRIE, the maximum side length of stochastic fractures is limited to 10 m, as recommended by the task description (Vidstrand et al. 2017). Detailed conditioning of the maximum side length of stochastic fractures has not been performed. In addition, for calculations to remain computationally tractable, a minimum fracture side length of 0.5 m is specified. Small fractures, shorter than this lower length limit, are unlikely to form hydraulically connected pathways through the bedrock, and as such their removal is not expected to significantly affect results. Instead, flows primarily occur through larger, more transmissive features. The omission of these small fractures may potentially affect the choice of rock matrix permeabilities implemented in the model, and is discussed as a series of model variants (see Section Chapter 6).

Using the power-law size distribution for fractures, it is possible to rescale the fracture intensity according to truncation bounds on the fracture sizes according to the following equation:

$$P_{32,r_a-r_b} = P_{32,r_1-r_2} \cdot \frac{r_a^{2-k_r} - r_b^{2-k_r}}{r_1^{2-k_r} - r_2^{2-k_r}}. \qquad (3\text{-}5)$$

The fracture intensity supplied by the task description (Vidstrand et al. 2017) corresponds to a smallest fracture size, r_0, of 0.25 m, and an unbounded maximum size of fractures. Applying Equation (3-5), with

- r_a = 0.28 m, the equivalent radius to a side length of 0.5 m, and
- r_b = 5.64 m corresponding to a side length of 10 m,

the reduced fracture intensities (P_{32}) are calculated and detailed in Table 3-1 by set. These intensities form the Basecase DFN model to be implemented, before calibration of the fracture network is performed.

Table 3-1. Fracture intensities by set, used as the Basecase for Task 8D fracture generation.

Set	Intensity $P_{32}(r_0,\infty)$	Intensity $P_{32}(0.28,5.64)$
1	1.1	0.85
2	2	1.55
3	0.75	0.58

Characterisation of the site local to the BRIE identified three distinct orientations of fractures (fracture sets), as recorded in Table 2-5. Of these sets, one corresponds to sub-horizontal fractures, dipping gently to the south-east, with the other two sets sub-vertical, corresponding to steeply dipping fractures aligned approximately N–S and E–W. For all sets, the orientations of fractures are modelled using a Fisher distribution.

The prescription of fracture orientations within the stochastic model is unchanged from Task 8C, with Figure 3-8 illustrating fracture orientations observed in the five probe boreholes for 100 realisations of the stochastic fracture network (and reproduced from Baxter et al. 2013). As expected these simulated fracture poles compare favourably to those obtained during data collection (see Figure 2-15).

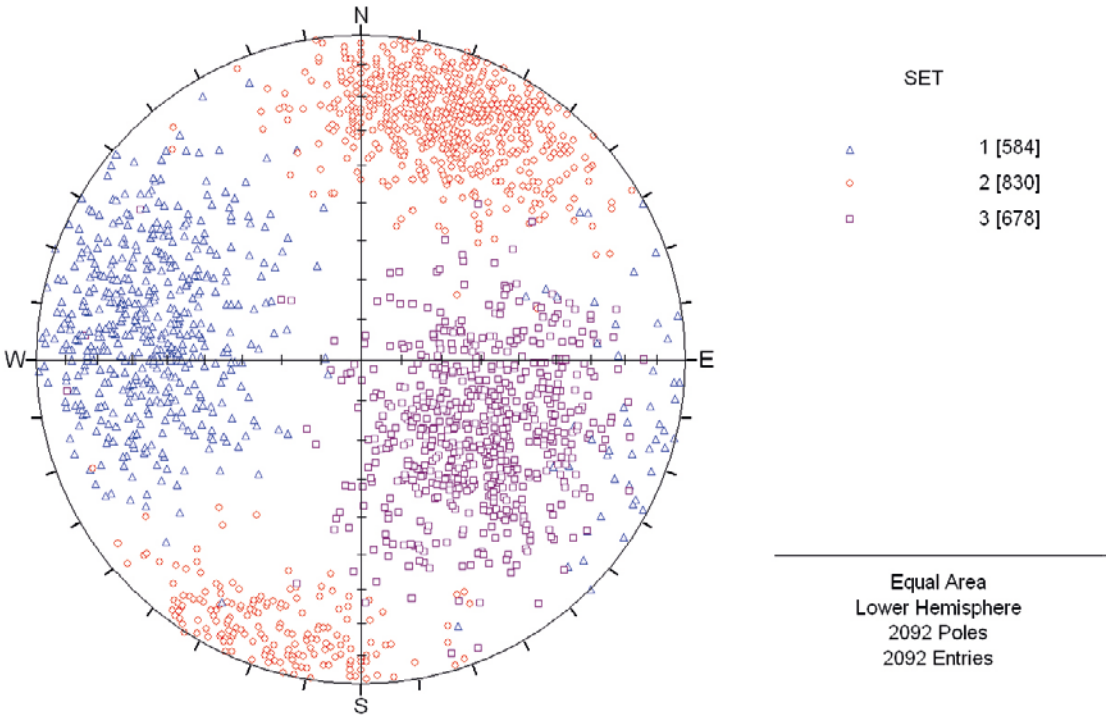

Figure 3-8. *Stereonet illustrating the orientation of fractures intersecting the probe holes for 100 realisations of the stochastic fracture network. This figure is reproduced from the Task 8C modelling report (Baxter et al. 2013).*

Hydraulic attributes of the stochastically generated fractures also require specification. This is achieved through assigning transmissivities to individual fractures in the DFN model. For a given fracture, its transmissivity (T) can be determined from its size, with measured data shown in Figure 3-9. The central (dashed) line in this figure corresponds to the following power-law relation:

$$T = 7 \cdot 10^{-11} L^{1.7} \qquad (3\text{-}6)$$

where L is the fracture length. This empirical relationship is consistent with estimates derived from a variety of fracture scales at the Äspö site. The bounding lines in Figure 3-9 correspond to transmissivities defined using Equation (3-6) considering one order of magnitude each side.

Diffusion coefficients

Groundwater flow in the fractured bedrock at Äspö is dominated by flow through a series of interconnected fractures. For Task 8D1, simulating groundwater flow explicitly through the fracture network is sufficient to accurately represent inflows and pressure build up for each of the probe boreholes. However, when modelling the resaturation of low permeability buffer material such as bentonite, the diffusive fluxes of the groundwater components can become significant. For Task 8D2, the simulation code TOUGH2 is used to perform the two-phase hydration calculations of emplaced bentonite to the central deposition holes, and diffusion coefficients within both the aqueous and gas phases are required. Diffusion coefficients in the gas phase are provided by Marrero and Mason (1972). For the liquid phase, the diffusion of brine is taken from Hoch and James (2011), with the diffusion for air calculated from Cussler (1984) and Han and Bartels (1996). All diffusion coefficients used in Task 8D2 modelling are detailed in Table 3-2.

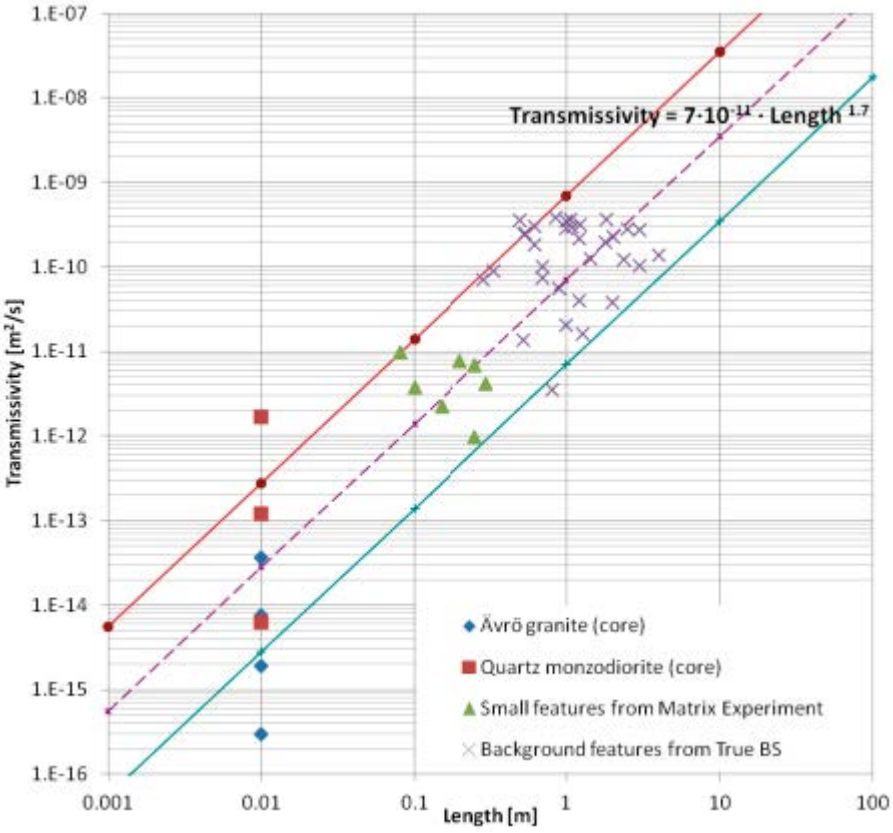

Figure 3-9. *Transmissivity correlation applied to stochastic fractures within the BRIE. The central dashed line corresponds to Equation (3-6), with the red and blue lines indicating plus and minus one order of magnitude from this power-law relation.*

Table 3-2. Diffusion coefficients for water, brine and air within both gas and liquid phases. Values are obtained from sources Marrero and Mason (1972) through Han and Bartels (1996).

Component	Gas Phase	Liquid Phase
Water	2.09×10^{-5} m^{2}s^{-1}	–
Brine	–	1.0×10^{-9} m^{2}s^{-1}
Air [1]	1.79×10^{-5} m^{2}s^{-1}	1.9×10^{-9} m^{2}s^{-1}

[1] Air is assumed to be composed of 80 % nitrogen, 20 % oxygen, with diffusion coefficients interpolated from nitrogen and oxygen endmembers.

Porosities

Upon upscaling the fracture network, the porosity of each grid block within the model will be calculated. In addition, the porosity of the rock matrix is taken as 0.5 %, consistent with measurements from laboratory samples reported in Section 2.8.1. These porosity measurements have been updated from the Task 8C study, where expert elicitation estimated the porosity of intact rock (fracture free matrix) as 10^{-5}. The increased porosity of the laboratory samples is assumed to take into account unmapped microfractures which do not form part of the DFN description.

3.2.5 Proposed relationships

Constitutive relationships detailing the capillary pressure and relative permeability functions are required for

- the bentonite,
- the rock matrix, and
- the fractured rock.

The Task 8D description (Vidstrand et al. 2017) provides a reference case, used to form the basis of the constitutive relationships implemented within TOUGH2. These relationships are detailed below for each of the model components listed above. It is noted that TOUGH2 calculations constrain the maximum capillary pressure of the bentonite to 95 MPa. Also, gas trapping mechanisms are not considered in any of the simulations performed.

Constitutive relations for bentonite

The capillary pressure (P_{cap}) of the bentonite uses a model suggested by van Genuchten (1980),

$$P_{cap} = -P_o\left(\widetilde{S}^{-1/\lambda} - 1\right)^{1-\lambda}, \tag{3-7}$$

where

$$\widetilde{S} = \frac{S_a - S_{ar}}{1 - S_{ar}}, \tag{3-8}$$

and S_a is the saturation of the aqueous phase; S_{ar} is the residual saturation of the aqueous phase; and parameters λ and P_0 are empirical constants.

Within the bentonite, the Fatt and Klikoff (1959) cubic-law representation of the relative permeabilities for the aqueous (k_{ra}) and gas (k_{rg}) phase is considered,

$$\begin{aligned} k_{ra} &= \widetilde{S}^3, \\ k_{rg} &= \left(1 - \widetilde{S}\right)^3. \end{aligned} \tag{3-9}$$

Required parameters for the capillary pressure and relative permeability functions of the bentonite are detailed in Table 3-3.

Table 3-3. Parameterisation of the capillary pressure and relative permeability functions for the bentonite.

Parameter	Capillary Pressure	Relative Permeability
Functional description	Equation (3-7)	Equation (3-9)
λ (–)[1]	0.3	–
P_0 (MPa)[1]	9.23	–
S_{ar} (–)	0	0.01

[1] Value obtained from the task description (Vidstrand et al. 2017).

Constitutive relations for the rock matrix

The capillary pressure of the rock matrix is modelled identically to the bentonite, Equation (3-7). Relative permeabilities for the aqueous (k_{ra}) and gas (k_{rg}) phases also use a van Genuchten function (Luckner et al. 1989):

$$k_{ra} = \sqrt{\widetilde{S}}\left(1-\left[1-\widetilde{S}^{1/\lambda}\right]^{\lambda}\right)^2,$$
$$k_{rg} = \sqrt{1-\widetilde{S}}\left(1-\widetilde{S}^{1/\lambda}\right)^{2\lambda}. \quad (3\text{-}10)$$

Required parameters for the capillary pressure and relative permeability functions of the rock matrix are detailed in Table 3-4.

Table 3-4. Parameterisation of the capillary pressure and relative permeability functions for the rock matrix.

Parameter	Capillary Pressure	Relative Permeability
Functional description	Equation (3-7)	Equation
λ (–)[1]	0.24	0.24
P_0 (MPa)[1]	0.6	–
S_{ar} (–)	0	0.01

[1] Value obtained from the task description (Vidstrand et al. 2017), and updated for Task 8D based on the relative humidities for core samples presented in Table 2-9. These measurements are taken at relatively low saturations, and not necessarily applicable to the saturation state of the granite local to emplaced bentonite. As such, despite parameterisation of capillary pressure and relative permeability functions now based on data specific to the rock matrix local to the BRIE, caution is required when applying the van Genuchten model at high water saturations.

Constitutive relations for fractured rock

The capillary pressure of the fractured rock is modelled using the van Genuchten model, Equation (3-7). The parameters λ and P_0 for fractured rock are inferred from Figure 3-10, provided as part of the task description (Vidstrand et al. 2017). Here

$$\lambda = 1 - 1/n,$$
$$P_o = \rho g/\delta, \quad (3\text{-}11)$$

and the mean hydraulic aperture for the fractures is approximately 3.8×10^{-3} mm, calculated from the transmissivity correlation, Equation (3-6); and cubic law, Equation (3-3) for fully saturated conditions. For fractured bedrock, relative permeabilities for the aqueous and gas phases are modelled using the same functional form (van Genuchten) as the rock matrix, Equation (3-10).

Required parameters for the capillary pressure and relative permeability functions of the fractured rock are detailed in Table 3-5, as estimated from Figure 3-10 where $\ln(3.8 \times 10^{-3}) = -5.6$ yielding values for n and δ of 2.25 and 2.0 respectively.

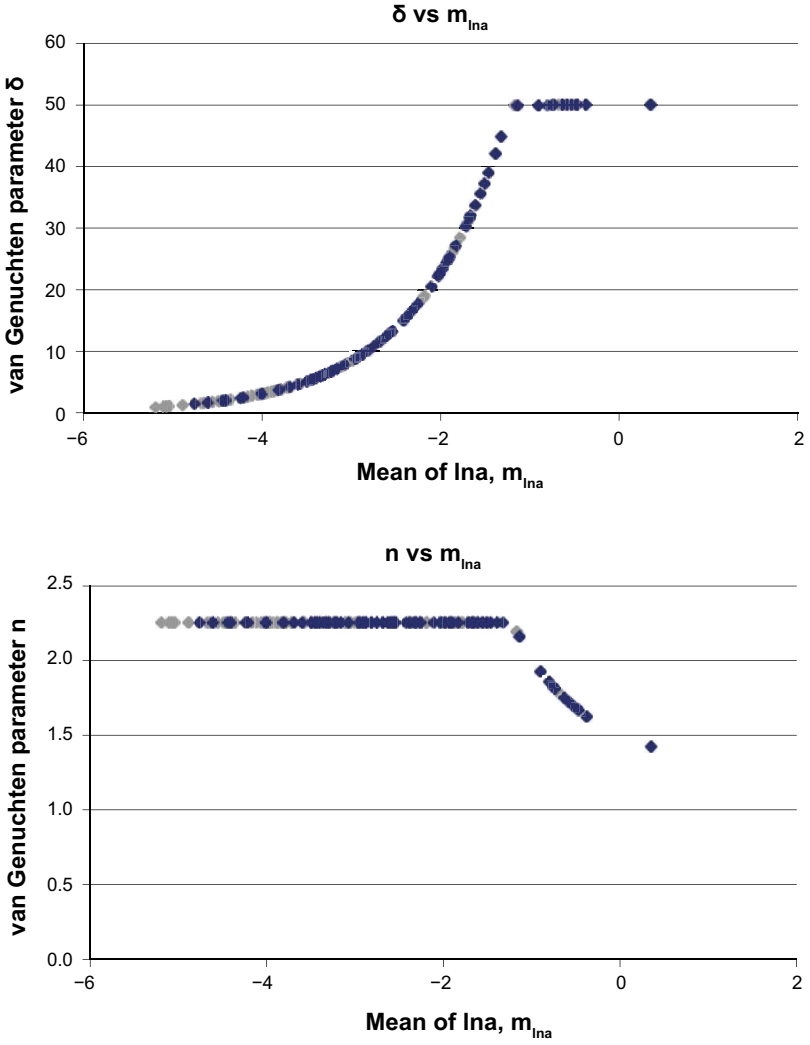

Figure 3-10. *Retention curves for van Genuchten capillary pressure, Equation (3-7) and relative permeability, Equation (3-10) functions for the fractured rock. The van Genuchten parameters δ and n are plotted for a range of mean hydraulic apertures of the fracture network. Equation (3-11) relates the plotted parameters δ and n to the constitutive relations presented in Section 3.2.5. Graphs are reproduced from the task description (Vidstrand et al. 2017).*

Table 3-5. Parameterisation of the capillary pressure and relative permeability functions for the fractured rock.

Parameter	Capillary Pressure	Relative Permeability
Functional description	Equation (3-7)	Equation (3-10)
λ (–)[1]	0.56	0.56
P_0 (MPa)[1]	4.905×10^{-3}	–
S_{ar} (–)	0	0.01

[1] Value are inferred from Figure 3-10, reproduced from the task description (Vidstrand et al. 2017) and using the relationships provided in (3-11) along with mean hydraulic aperture of 3.8 μm.

3.2.6 Numerical model

The models developed for numerical simulation of Task 8D1 and Task 8D2 are quite different, as summarised below:

- **Task 8D1.** For this subtask, the fractured bedrock is represented explicitly; created from a combination of the large scale deterministic features identified local to the BRIE and the stochastically generated background fractures sampled from parameters outlined in Section 2. Steady-state flow solutions are considered, consistent with stabilised measurements of pressure build-up and inflows. To consider uncertainties in the sampled background fracture network, ten realisations of the stochastic DFN component are considered for each of the calibration model cases (see Section 3.3). The software package CONNECTFLOW is used for Task 8D1 modelling, and for Basecase parameters (pre-calibration) models containing approximately 223 000 individual fractures of which around 164 000 form a connected network.
- **Task 8D2.** For this subtask, TOUGH2 is used to model the transient resaturation of bentonite emplaced within the central deposition holes of the BRIE. The numerical formulation of TOUGH2 utilises a continuum approach, and the mesh must be refined sufficiently to capture the saturation front within the bentonite. The central overcored boreholes have a diameter of 0.3 m, with KO0018G01 3 m deep, and KO0017G01, 3.5 m deep. The bentonite emplaced within the TOUGH2 mesh is discretised 8 times azimuthally, 8 times radially, with elements 0.25 m long (vertically). In addition, although the DFN conceptual model from Task 8D1 and the continuum model used in Task 8D2 are equivalent by the use of upscaling (see Subsection 3.1.1) at the scale of individual grid blocks within the mesh, the upscaling approach will result in some "homogenisation" of the fracture properties. Therefore it is necessary to also include sufficient refinement of the host rock within the grid to suitably discretise the fractures intersecting the deposition holes. These refined grids provide challenging whilst maintaining computationally tractable simulations. Finally it is noted that if the mesh considered in the TOUGH2 continuum model was sufficiently refined, predicted inflows to open deposition holes using TOUGH2 should equate to the predictions made by CONNECTFLOW in Task 8D1, within the limits of the different underlying assumptions between the two conceptual models.

3.3 Calibration, variants and sensitivities

The modelling conducted as part of Task 8C (Baxter et al. 2013) provided predictions of resaturation profiles and times to bentonite emplaced in the central deposition holes of the BRIE. These models were generated solely from fracture statistics for the site. For Task 8D, the models developed under Task 8C can be refined, and calibrated to the additional hydraulic fracture data available. In particular, calibration of the following aspects of the model is considered:

- The fracture network statistics detailed in Section 2.3 are unchanged from Task 8C modelling. In particular, uncertainties related to fracture intensity are significant (±25 %). It is also noted that the fracture statistics derived are for all fractures, rather than those hydraulically active. Therefore all fractures within the DFN are capable of flow depending on their connectivity to the wider network. However, this forms an upper limit on connectivity and flow, and one calibration approach will consider only a proportion of the total fracture area open to flow (with the remaining fracture area sealed). This calibration approach is pertinent as inflow simulations based on Task 8C statistics typically overpredicted inflows to the boreholes and overcored deposition holes.
- The intensity of background fractures generated within the DFN will be analysed and compared to measurements from engineered features, e.g. trace lines observed within the tunnels, and intersection counts in boreholes.
- The Task 8D description identifies individual water producing features intersecting deposition holes KO0017G01 and KO0018G01. This additional data will be used to modify the stochastic fracture networks generated, with models including deterministic fractures parameterised to reproduce each of the intersections identified.

A number of model variants will be considered, aimed at calibrating the DFN model to better reproduce the additional measurements and observations available in Task 8D1. A summary of seven model cases are detailed below, and for further details, the reader is referred to Section 5:

- Basecase: Original statistics for stochastically generated fractures, including the new local scale hydrozone wfracture_01 (truncated from KO0014G01).
- Variant 1: Identical to the Basecase, but with the intensity (P_{32}) of stochastically generated fractures reduced to 75 % of the Basecase.
- Variant 2: Identical to the Basecase, but with the intensity (P_{32}) of stochastically generated fractures reduced to 50 % of the Basecase.
- Variant 3: Based on Variant 2, but using an alternative transmissivity-size correlation for the hydraulic aspects of the stochastically generated fractures.
- Variant 4: Based on Variant 3, but using an alternative geometric description of the locally defined feature wfracture_01, updated to fully isolate borehole KO0014G01.
- Variant 5: Based on Variant 3, but including deterministic features to represent observed fracture intersections within deposition holes KO0017G01 and KO0018G01.

4 A review of modelling in Task 8C

In this section the modelling approach from Task 8C is reviewed, with key differences to Task 8D emphasised. In addition,

- Results from Task 8C1 are summarised, detailing key findings from pressure build-up and inflow calculations performed, and
- Results from Task 8C2 are reviewed, providing details of resaturation rates and profiles for bentonite emplaced within five probe boreholes, overcored to 30 cm diameter.

Task 8D modelling presented in this report follows on from the previous Task 8C study (Baxter et al. 2013) refining predictions of the resaturation front for emplaced bentonite in the central deposition holes of the BRIE. This section provides an overview of the previous Task 8C modelling, including

- a summary of the key differences between the two tasks,
- a review of results obtained in Task 8C1, including predictions of inflows and pressure build-up in the five probe boreholes, and
- a review of results obtained in Task 8C2, including typical resaturation profiles and times for emplaced bentonite.

4.1 Differences between Task 8C and 8D

Task 8D modelling is designed to supersede the previous subtask Task 8C. Both produce local site models of the BRIE at the Äspö Hard Rock Laboratory (HRL), predicting inflow and pressure-build up in boreholes as well as resaturation profiles of emplaced bentonite. However, Task 8D provides additional site measurements, allowing calibration of the models developed as part of Task 8C for the fractured rock. Through conditioning the DFN, it is anticipated that predictions of resaturation of emplaced bentonite in the central deposition holes will be revised. Table 4-1 summarises key similarities and differences between the Task 8C and 8D description.

4.2 Key findings from Task 8C1

Task 8C1 modelling predicted both pressure build-up and inflows to each of the five probe boreholes of the BRIE. The main modelling results reported in Baxter et al. (2013) are summarised below.

4.2.1 Pressure build-up calculations from Task 8C1

Models of pressure tests were performed as part of Task 8C1 for each of the 5 probe boreholes, packing off the top 1 m, and recording the build-up of pressure. Ten realisations of the stochastic fracture model were considered, and pressures observed for each of these realisations were relatively consistent. From the entire ensemble of realisations, pressure build-up within 50 probe boreholes (10 realisations, 5 boreholes) was calculated, and of these, three did not exhibit any response to being closed, i.e. they were disconnected from the wider fracture network. This was found to be inconsistent with measurements, where only two of the five probe boreholes observed pressure. Two possibilities for this difference were identified:

Table 4-1. A summary of the key differences between the Task 8C and 8D model descriptions.

Model component	Similarities between Task 8C and 8D	Differences between Task 8C and 8D
Background fracture statistics	Background fracture statistics provided through the task description (Vidstrand et al. 2017) are unchanged. These will be used as the Basecase for Task 8D modelling, prior to any calibration efforts.	–
Deterministic features	The geometry of the large scale deterministic features are unchanged. In addition hydraulic properties for wfracture_02 and NNW4 are identical.	A new local geometry for wfracture_01 is provided in Task 8D. Hydraulic properties have also been updated for this feature. Additional fractures intersecting the central deposition holes have been interpreted.
Material specifications – Bentonite	Permeability and porosity are unchanged.	Both specific storage and initial degree of saturation have been updated.
Material specifications – Fractured rock	Capillary pressure and relative permeability functions unchanged	–
Material specifications – Rock matrix	–	Additional measurements for rock matrix permeability and porosity are available in Task 8D. New relative humidity measurements update the parameterisation of capillary pressure and relative permeability functions.
Calibration data	–	Many additional hydraulic tests have been performed for open borehole conditions, including 1. short duration inflow tests, 2. TASO tunnel inflows, 3. Pressure build-up measurements, and 4. Inflows to the overcored central boreholes.

1. Measurement limitations: The build-up of pressure will only register on measurement devices once the packed off region of the borehole has filled with groundwater. For small inflows, this may take longer than the duration of the measurement.
2. Fracture network connectivity: As discussed in Section 2.9, fracture statistics do not differentiate between fractures hydraulically active, and those closed to flow. As such the hydrogeological fracture models have the tendency to over predict the intensity of potentially flowing fractures.

4.2.2 Inflow calculations from Task 8C1

Inflow calculations to the five probe boreholes of the BRIE form part of Task 8C1 modelling. Ten realisations of the stochastic DFN model were considered, and across these realisations results for groundwater ingress to the probe boreholes was found to be relatively consistent, and within the range expected from stochastic variations. Calculated inflows ranged from below the detection limit 0.1 ml/min to over 10 ml/min between boreholes and realisations. Results from Task 8C1 modelling found average inflows to each of the five probe boreholes to be over estimated by c. factor 8.

Due to the limited measurement data available as part of Task 8C, no model calibration was performed. Specifically, Baxter et al. (2013) noted that

“although the aggregated inflows from simulations are larger than those measured, there is no statistical basis for calibrating the DFN models such that the average inflow corresponds directly to observations. Rather, it is sufficient that the inflow magnitudes measured are within an appropriate confidence interval when considering an ensemble of realisations.”

One specific realisation of the stochastic DFN (realisation 2) provided the most consistent inflow magnitudes with observations. When considering pressure build-up results for this realisation

- boreholes KO0017G01 and KO0014G01 were consistent with observations, differing from measurements by −0.4 bar, and +1.0 bar respectively, and
- simulations predict pressure build-up in boreholes KO0015G01 and KO0018G01 due to their connection to the wider fracture network. From measurements, no pressure build-up was observed in these boreholes.

4.3 Key findings from Task 8C2

Task 8C2 used the findings from Task 8C1 to consider the resaturation of bentonite buffer at the BRIE. For Task 8C, all five of the probe boreholes are assumed to be overcored to a diameter of 30 cm, and with bentonite emplaced. For the realisations considered, the fracture statistics for the site were sufficient to hydraulically connect the overcored holes to the wider fracture network in all cases. Through modelling Task 8C it became clear that to fully understand the resaturation of emplaced bentonite; it was critical to have an accurate representation of the fractured host rock. Results for the hydration profiles of bentonite for five realisations of the fracture network, as well as a number of sensitivity cases, were presented. In summary it was found that:

- Bentonite saturation from the surrounding fractured bedrock was highly heterogeneous, with significant differences observed between stochastic realisations of the fracture network:
  - The minimum resaturation time calculated was for deposition hole KO0015G01 for realisation 1 of the fracture network, taking 7.4 years to reach 99 % saturation.
  - The maximum resaturation time calculated was for deposition hole KO0018G01 for realisation 2 of the fracture network, taking 75.4 years to reach 99 % saturation.
- For bentonite hydration, locations of groundwater ingress (i.e. the locations of deposition hole intersections with groundwater producing fractures) were significant to the prediction of saturation times.
- Representing the fractured bedrock with homogeneous permeability values did not capture the heterogeneous processes that occur during resaturation.
- The hydraulic performance of the rock matrix was found to significantly affect the resaturation times of emplaced bentonite.
- An increase in the permeability of the rock matrix by one order of magnitude decreased resaturation times significantly. Task 8D1: Calibrating the Fracture Network.

5 Task 8D1: Calibrating the Fracture Network

Details of the fracture network calibration process are presented in this section, reviewing additional data provided as part of Task 8D, and amending model definitions as required to better conform to this data. The calibration process initially considers a Basecase model parameterised by the task description (Vidstrand et al. 2017) as detailed in Section 2. A number of model variants are then considered, revising

- the fracture intensity statistics,
- the transmissivity-size model required for determining hydraulic properties of fractures,
- the geometric description of structure wfracture_01, and
- conditioning deposition holes to directly represent the groundwater producing fracture traces observed.

The validity of the model calibrations performed are assessed by comparing calculated inflows and pressure build-up in the five probe boreholes with BRIE measurements. Using the calibrated fracture models, predictions are made to the inflows of overcored boreholes, drilled as part of the BRIE as necessary for the installation of bentonite packages.

Task 8D1 constitutes modelling of both inflow and pressure-build up for the five, 76 mm probe boreholes of the BRIE. Initially a Basecase model is identified, parameterised according to the task description (Vidstrand et al. 2017) including the refined interpretation of wfracture_01. From modelling results of this Basecase, a series of calibrations are performed to the fracture network in order to better reflect the additional geometric and hydraulic data local to the BRIE. A detailed overview of this additional data, available as part of Task 8D is discussed Section 2.9.

The calibration cases considered as part of this study are identified in Section 5.1. For each of these, the ConnectFlow software package is used to

- generate ten realisations of the DFN, and
- provide steady-state solutions of the pressure and flow fields.

On obtaining a calibrated DFN model for the host rock local to the BRIE, inflows are calculated to over-cored 30 cm diameter boreholes KO0017G01 and KO0018G01. Results are presented in Section 5.2, and provide both

- further confirmation of the validity of the DFN calibrated to pilot hole data, i.e. on overcoring to 30 cm diameter holes, are measured inflows adequately reproduced, and
- initial conditions for simulations of the resaturation of emplaced bentonite, detailed in Section 6.

5.1 Model calibration

The DFN models generated as part of Task 8D combine both deterministic representation of interpreted features (i.e. large structures) and a stochastic fracture network (parameterised by statistical distribution of fracture intensity, orientation, size and transmissivity). Model calibration considers both of these aspects of the DFN, as summarised below:

- Stochastic DFN component:
  - The intensity (fracture surface area per unit volume of bedrock, P_{32}) of generated fractures.
  - The transmissivity-size distribution adopted for calculating hydraulic properties of individual fractures in the network.
- Deterministic DFN component:
  - The local description of feature wfracture_01, and isolation of probe hole KO0014G01.
  - The inclusion of fractures specified to recreate interpreted intersection with overcored boreholes KO0017G01 and KO0018G01.

Each of these aspects of the DFN is discussed in detail in the following subsections, including modelling results from a number of variant model cases. The Basecase model parameterisation is based on the task description (Vidstrand et al. 2017) as reviewed in Sections 2 and 3 of this report.

5.1.1 Background fracture intensity

From data local to the BRIE, the task description (Vidstrand et al. 2017) infers statistical distributions required to generate the stochastic DFN, with parameterisation reviewed in Section 2.3. Specifically, a scanline on the TASD tunnel floor was considered to relate to the P_{32} of the underlying fracture-size distribution, and used to calibrate intensity to the fracture-size model. These fracture statistics are unchanged from the Task 8C analysis (Baxter et al. 2013). Due to limited data, the statistical models for the fracture network have appreciable uncertainty, with uncertainties in fracture intensity of ±25 % (Vidstrand et al. 2017). In addition, fracture intensities correspond to all fractures within the bedrock, with hydraulically connected fractures forming a subset of all fractures. In this section the fracture intensity model is analysed as summarised below:

- The intensity of fractures within the stochastic DFN are calibrated, comparing simulated trace lengths and borehole intersections with those observed in engineered features (Geometric).
- The effects of changing fracture intensity on simulations of pressure build-up and inflow tests (Hydraulic).

In general, for very sparse networks, geometric parameterisation (intensity, size, etc) of the fracture network will dominate the percolation of groundwater through the DFN, with the connectivity of fractures critical to the path of groundwater flow. When fracture intensity increases such that fracture connectivity provides multiple pathways for groundwater flow, the relative hydraulic properties (transmissivity, viscosity, etc) between fractures becomes significant.

Geometric calibration

Across the modelling domain, additional data are now available for assessing the suitability of Task 8C statistics for the background fracture intensity. Using both fracture trace data on the TASO tunnel, as well as fracture logs within the probe boreholes, conformance tests can be performed for the underlying fracture intensities, estimated from TASD scanlines, for the stochastic DFN. Fracture traces on the TASO tunnel corresponding to a single realisation of the DFN are shown in Figure 5-1.

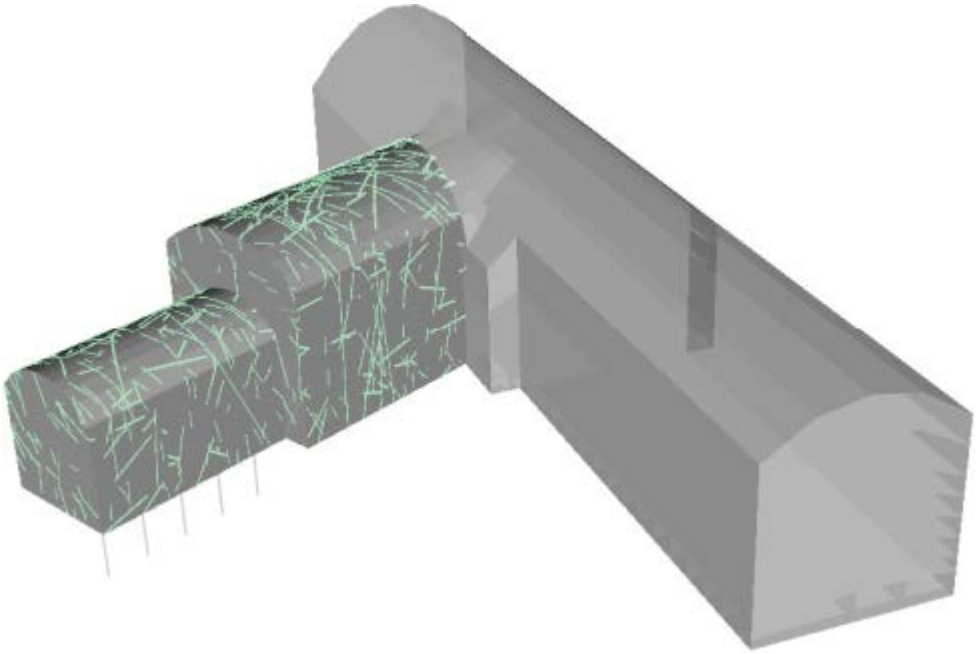

Figure 5-1. *Simulated fracture trace lengths within the TASO tunnel for a single realisation of the DFN, generated using the Task 8C fracture statistics.*

For the Task 8C fracture statistics, a comparison of the measured trace lengths with those simulated and aggregated over ten realisations of the stochastic DFN model is shown in Figure 5-2. The distribution of fracture trace lengths simulated within the TASO tunnel generally appears consistent with observations, providing confidence in the power-law fracture-size model adopted.

It is clear that mappings will concentrate on fracture intersections that are readily observed; with the shortest intersection length recorded at 1.0 m. Matters are further complicated by the rough surfaces of the TASO tunnel wall and floor, obscuring fracture traces. Therefore, based on the available data, a confidence function for the fracture mappings (to reflect the reliability of the trace measurements) has been assumed, with

- 100 % of trace lengths greater than 1.25 m mapped,
- 50 % of trace lengths between 1 m and 1.25 m mapped, and
- no trace lengths mapped less than 1 m.

Using the intensity of fractures provided as part of the Task 8C description, simulations significantly over predict the number of fracture traces on the TASO tunnel. Aggregated over ten realisations of the DFN model, simulations predict approximately 210 fracture traces on the TASO tunnel when using the above confidence function, compared to just 89 mapped. As such, two model variants are proposed for the confidence functions used, reducing the fracture intensity[4]:

- **Variant 1:** Fracture intensity is reduced by 25 % from the Task 8C Basecase.
- **Variant 2:** Fracture intensity is reduced by 50 % from the Task 8C Basecase.

For each of these variant cases, ten realisations of the stochastic DFN are generated. Subsequently, the intensity of hydraulically connected fractures (P^{c}_{32}) is calculated by removing features that are isolated, and values are presented in Table 5-1 for each of the model cases. As the intensity of all fractures decreases, the fracture network becomes sparser, and more of the fractures become isolated/hydraulically inactive. Table 5-2 details the number of simulated traces on the TASO tunnel wall and floor, aggregated over ten realisations of each of three model cases identified (Basecase, Variant 1 and Variant 2). On comparison of trace count alone, Variant 2 provides the closest match to those mapped, generating on average 105 traces compared to the 89 observed.

Table 5-1. Intensity (P^{c}_{32}) of hydraulically connected fractures aggregated over ten realisations of the stochastic fracture network. Results are presented for a range of intensities (P_{32}) for all fractures.

Intensity of all fractures including large structures (P_{32})	Intensity of hydraulically connected fractures (P^{c}_{32})
3.12	2.79 (89.3 % hydraulically connected)
2.36 (25 % reduction in stochastic DFN)	1.91 (80.9 % hydraulically connected)
1.59 (50 % reduction in stochastic DFN)	1.04 (65.1 % hydraulically connected)

Table 5-2. The number of simulated traces on the TASO tunnel walls and floor; aggregated over ten realisations of the DFN. Results are presented for the Basecase, Variant 1 and Variant 2 models, as well as the trace count for mapped observations.

Statistic	P_{32}	Trace Count
TASO Mapped Traces	–	89
Av. TASO simulated traces	original	211
	75 %	159
	50 %	105

[4] Note that when reducing the intensity of all fractures, the fracture network becomes sparser, and more of the fractures become isolated/hydraulically inactive. Consistency should be sought between the intensity of all fractures (e.g. estimated from geological fracture mappings in the TASO tunnel) and the intensity of hydraulically active fractures (i.e. flowing features).

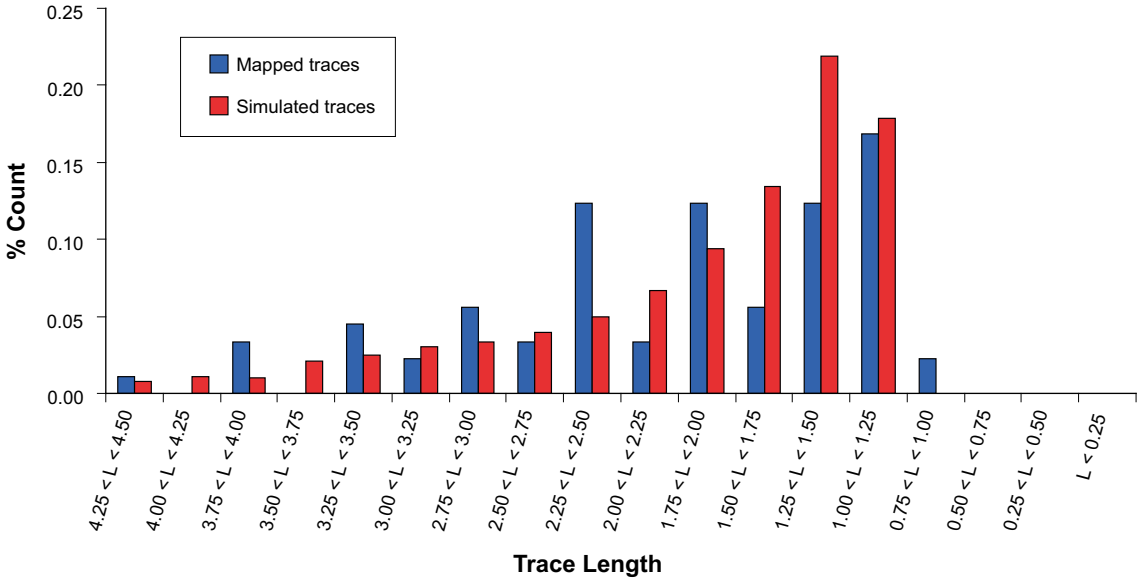

Figure 5-2. *Distribution of trace lengths aggregated over ten realisations of the DFN, generated using the Task 8C fracture statistics. Comparison is made to mapped traces.*

So far, the intensity of the stochastic fracture network has been calibrated using the fractures traces mapped from the TASO tunnel. In addition, data are available for observed fracture intersections logged within each of the five probe boreholes KO0014G01, KO0015G01, KO0017G01, KO0018G01, and KO0020G01, as detailed in Table 5-3.

Analysis of the borehole logs indicate clustering of the fracture network (not readily observed in the TASO tunnel mappings), with multiple fractures occurring at similar depth. These fracture clusters form minor hydraulic zones, and should be considered as a single combined structure when calculating fracture intensities. The analysis of fractures interpreted from borehole logs is based on the grouping of observations within the borehole using their proximity to neighbouring fracture intersections. Details of the methodology used for identifying fracture groupings are summarised below:

- On selecting the critical fracture spacing, each probe borehole is analysed such that the separation between consecutive fracture intersections is calculated and if less than the critical fracture spacing, grouped.
- On grouping fractures, no consideration is given to the orientation of the separate intersections observed. This would provide a possible refinement to the grouping method, as fracture clustering within a single hydraulic pathway is expected to consist of features with similar orientation.

Figure 5-3 illustrates the number of fracture groups identified within the five probe boreholes for different values of critical fracture spacing. Up to a critical fracture spacing of 5 cm, there is a rapid decrease in the average number of grouped fracture intersections per borehole, from 15.6 to 8.4. Subsequent to this, grouped fracture intersections per borehole continue to decrease, with an average value of 2.6 corresponding to a spacing of 40 cm. Table 5-4 provides comparison of the grouped intersections interpreted from borehole logs with those simulated. The Basecase, Variant 1 and Variant 2 are all considered, corresponding to changes in the fracture intensity (Variant 1 is 75 % of Basecase intensity, Variant 2 is 50 % of Basecase intensity). For each of these model cases, the simulation results in Table 5-4 are calculated by aggregating over ten realisations of the DFN. From this analysis, Variant 2 provides the most consistent simulation results when compared with the grouped intersections observed from borehole logs of KO0014G01, KO0015G01, KO0017G01, KO0018G01, and KO0020G01.

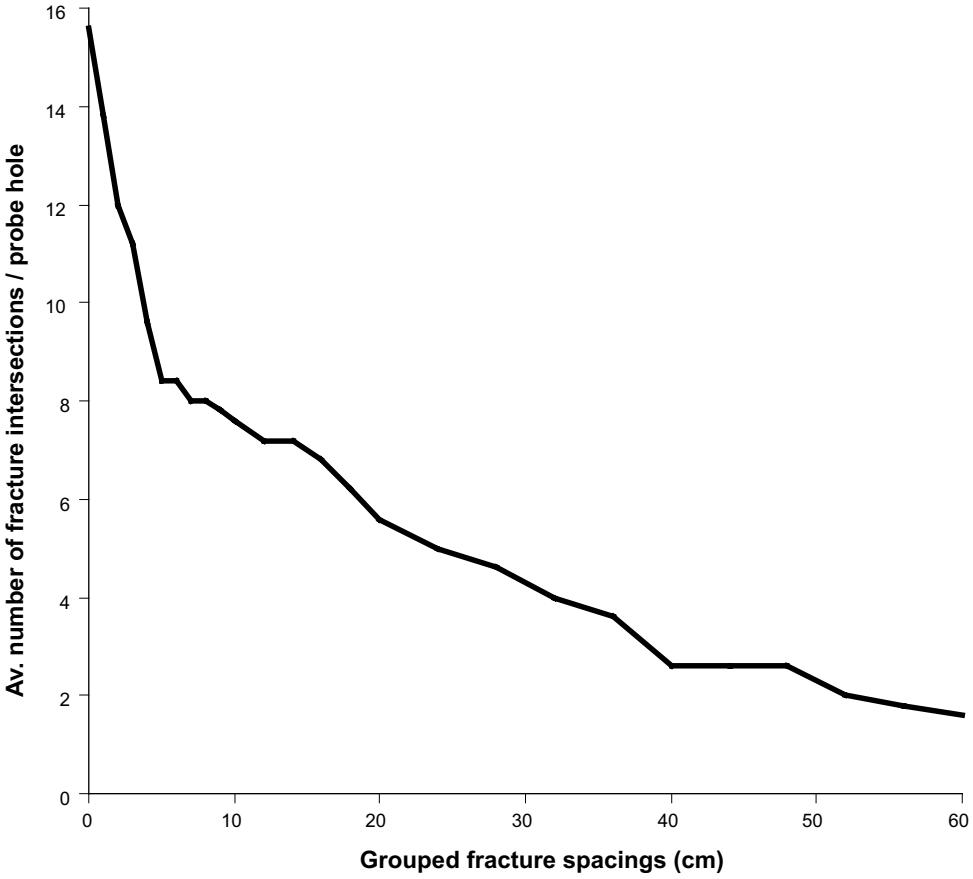

Figure 5-3. *The number of fracture intersections logged, and averaged across the five probe holes. Logged intersections occurring in each probe hole within the critical fracture spacing of another fracture intersection are combined as a single feature.*

Table 5-3. The total number of fracture intersections with each of the five probe holes KO0014G01, KO0015G01, KO0017G01, KO0018G01, and KO0020G01.

Borehole	Logged fracture intersections
KO0014G01	22
KO0015G01	17
KO0017G01	8
KO0018G01	12
KO0020G01	19

Table 5-4. Comparison of logged fracture intersections with those simulated. Model results are aggregated for ten realisation of the fracture network.

			Av. Simulated fracture intersections		
Borehole	**Logged fractures**	**Logged fractures 40 cm spacing**	**Original P_{32}**	**75 % P_{32}**	**50 % P_{32}**
KO0014G01	22	2	4.1	3.5	2.1
KO0015G01	17	3	4.1	3.2	1.8
KO0017G01	8	3	3.9	3.0	1.9
KO0018G01	12	2	5.5	4.1	2.2
KO0020G01	19	3	3.9	2.6	1.2
Total	**78**	**13**	**21.5**	**16.4**	**9.2**

Hydraulic calibration

Pressure-build up and inflows are calculated for the Basecase, Variant 1 and Variant 2 models. In each case

- pressure build-up calculations correspond to packing off the top 1 m of the borehole, and
- for inflow calculations, each of the five probe boreholes are opened in turn to atmospheric conditions at the tunnel.

Simulated pressure build-ups, aggregated over realisations of the DFN where boreholes intersect the wide fracture network, are shown in Table 5-5 for model cases: Basecase, Variant 1 and Variant 2. For each of the model cases, average pressures are relatively consistent, and within the range expected from stochastic variations. Observations record a build-up of pressure in two of the five probe boreholes. This is in contrast to the Basecase model, where 46 of the 50 probe borehole realisations (five boreholes, ten realisations for each) simulate a build-up of pressure. These discrepancies could be cause by:

- **Measurement limitations:** Pressures are only recorded once the packed-off borehole sections have filled with groundwater, requiring sufficient time to elapse between isolating the borehole and performing the measurement.
- **Fracture network connectivity:** From the above analysis it is proposed that the Basecase model overestimates the fracture intensity of the bedrock. As the intensity is reduced (Variant 1 and 2), the likelihood of packed-off boreholes connecting to the wider network also reduces.

When considering model cases Variant 1 and Variant 2, the number of realisations predicting pressure build-up reduces:

- **Variant 1:** Simulations calculate pressure build-up in 43 of the 50 probe boreholes.
- **Variant 2:** Simulations calculate pressure build-up in 31 of the 50 probe boreholes.

Results for pressure build-up for individual realisations of the Basecase, Variant 1 and Variant 2 models are shown in Appendix 1 (Figure A1-1).

Table 5-6 presents a comparison of measured inflow rates to each of the probe boreholes, aggregated over ten realisations of the stochastic fracture network model. The detection limit for measurements is 0.1 ml/min, and inflows below this value are not recorded. A reduction in the fracture intensity of all fractures by 50 % (Variant 2) provides significantly better correlation to the observed inflows than the other model cases considered. In addition, for the Variant 2 model case, probe borehole KO0014G01 has, on average, greater inflows. This is because KO0014G01 is in close proximity to the new local structure wfracture_01, which provides good hydraulic connection to the model boundary, providing a more direct pathway for flow. Results for inflows for individual realisations of the Basecase, Variant 1 and Variant 2 models are shown in Appendix 1 (Figure A1-5).

Summary of findings

Uncertainties related to the intensity of background fractures have been examined in this section, comparing the Basecase model (parameterised by the task description (Vidstrand et al. 2017) with two model variants (1 and 2) defined with 75 % and 50 % of Basecase intensity respectively. Simulation results for each of these model cases are aggregated over ten realisations of the DFN, and compared

- mapped traces within the TASO tunnel,
- grouped fracture intersections observed in each probe borehole; and
- measured inflows.

Results indicate model Variant 2 provides the most representative description of the background fracture intensity.

Table 5-5. The average pressure build-up calculated in the five probe boreholes for the Basecase, Variant 1 and Variant 2 models. In each, the average pressure is calculated over the DFN realisations where the borehole connects to the wider network. Results are compared to pressure observations within each borehole.

		Min/Average/Max Pressure (bar)		
Borehole	Measured pressure build-up (bar)	Basecase: Original P_{32}	Variant 1: 25 % P_{32} reduction	Variant 2: 50 % P_{32} reduction
KO0020	–	2.5/**8.5**/18.7	1.2/**7.8**/14.3	1.9/**3.9**/6.6
KO0018	–	2.0/**7.2**/13.3	1.5/**5.4**/10.1	1.1/**4.2**/10.0
KO0017	6	3.3/**5.2**/9.8	1.2/**5.2**/10.8	1.5/**5.1**/10.1
KO0015	–	1.9/**6.2**/10.4	3.6/**6.1**/10.1	1.1/**3.6**/6.2
KO0014	3	2.7/**5.0**/7.6	3.4/**5.0**/8.5	2.4/**8.1**/16.8

Table 5-6. The average simulated inflow to the five probe boreholes for the Basecase, Variant 1 and Variant 2 models. In each case ten realisations of the stochastic DFN are considered. Results are compared to measured inflows with a lower detection limit of 0.1 ml/min.

		Min/Average/Max simulated inflow (ml/min)		
Borehole	Measured inflow (ml/min)	Basecase: Original P_{32}	Variant 1: 25 % P_{32} reduction	Variant 2: 50 % P_{32} reduction
KO0020	–	0.0/**7.8**/36.1	0.0/**2.3**/17.9	0.0/**0.5**/4.3
KO0018	–	0.7/**23.1**/185.3	0.0/**9.1**/81.8	0.0/**1.1**/6.6
KO0017	0.5	0.0/**2.0**/7.8	0.0/**1.4**/3.8	0.0/**0.8**/4.0
KO0015	–	0.0/**4.9**/22.1	0.0/**3.0**/17.5	0.0/**0.7**/6.6
KO0014	1	0.4/**10.4**/32.3	0.1/**6.0**/14.5	0.0/**2.6**/9.5

5.1.2 Transmissivity correlation

Hydraulic properties of the stochastically generated background fractures are also required to perform simulations of inflow and pressure build-up. This is achieved by specifying a transmissivity for each fracture, and for the Basecase model transmissivities are correlated to fracture size using Equation (3-6). This power-law relation is shown by the central (dashed) line in Figure 3-9, which also includes measurements local to the BRIE. These measurements suggest fracture transmissivities are spread around the power-law relationship by as much as ±1 order of magnitude, as shown by the red and blue lines in Figure 3-9. Therefore an alternative transmissivity correlation is proposed, better representing this variation,

$$\log[T] = \log\left[7 \cdot 10^{-11} L^{1.7}\right] + \sigma_{\log(T)}\,\mathrm{N}(0,1) \qquad (5\text{-}1)$$

where the spread in fracture transmissivities $\sigma_{\log(T)} = 0.5$, such that 95 % of observations lie within two standard deviations (1 order of magnitude) of the mean.

An additional model case, denoted Variant 3, is developed utilising this semi-correlated, transmissivity-size distribution for stochastically generated background fractures. All other model parameters are as defined in Variant 2, the optimal model case identified in Section 5.1.1.

Calculations for pressure build-up for the Variant 2 and Variant 3 model cases are shown in Table 5-7. The average pressure is calculated from DFN realisations where boreholes are found to intersect with the wider fracture network. Using the semi-correlated transmissivity distribution, the average pressure values generated in KO0017G01 and KO0014G01 are consistent with observations. Results for pressure build-up for individual realisations of the Basecase, Variant 2 and Variant 3 models are shown in Appendix 1, Figure A1-2.

Inflow calculations to each of the probe boreholes are simulated for Variant 3, aggregated over ten realisations of the stochastic DFN, with results shown in Table 5-8. It is observed that on changing from a correlated to semi-correlated transmissivity model, inflows to probe boreholes have typically increased. Two potential causes are identified:

- The maximum possible transmissivity for large fractures is greater for the semi-correlated transmissivity-size model than the correlated model.
- For probe boreholes intersected by more than one fracture, there is an increased likelihood that at least one will be highly transmissive for any given realisation of the DFN.

Results for inflows for individual realisations of the Basecase, Variant 2 and Variant 3 models are shown in Appendix 1, Figure A1-6.

Summary of findings

On aggregation of the ten realisations, pressure-build up and inflow calculations for both Variant 2 (correlated transmissivity distribution) and Variant 3 (semi-correlated transmissivity distribution) are consistent with measurements at the BRIE. However, Variant 3 improves the representation of the variability in transmissivity with fracture size, observed from experimental data, as shown in Figure 3-9. Model Variant 3 reflects this and is thus postulated to provide the most representative description of the hydraulic properties of the background fracture network.

Further calibration of the inflows could be achieved by representing the individual features intersecting each of the probe boreholes deterministically. This calibration is discussed in Section 5.1.4.

Table 5-7. The average pressure build-up calculated in the five probe boreholes for Variant 2 and Variant 3 model cases. Both implement a 50 % reduction in the Basecase fracture intensity. In each, the average pressure is calculated over the DFN realisations where the borehole connects to the wider network. Results are compared to pressure observations within each borehole.

		Min / Average / Max Pressure (bar)	
Borehole	Measured pressure build-up (bar)	Variant 2: Using Correlated Transmissivity model	Variant 3: Using semi-correlated Transmissivity model
KO0020	–	1.9 / **3.9** / 6.6	1.3 / **4.7** / 9.1
KO0018	–	1.1 / **4.2** / 10.0	1.3 / **3.1** / 8.3
KO0017	6	1.5 / **5.1** / 10.1	1.3 / **5.2** / 10.8
KO0015	–	1.1 / **3.6** / 6.2	1.1 / **3.3** / 7.9
KO0014	3	2.4 / **8.1** / 16.8	1.4 / **3.4** / 7.9

Table 5-8. Simulated inflow to the five probe boreholes averaged over ten realisations of the stochastic discrete fracture network. Results compare the Variant 2 and Variant 3 model cases, both implementing a 50 % reduction in the Basecase fracture intensity. Results are compared to measured inflows with a lower detection limit of 0.1 ml/min.

		Min / Average / Max simulated inflow (ml/min)	
Borehole	Measured inflow (ml/min)	Variant 2: Using Correlated Transmissivity model	Variant 3: Using semi-correlated Transmissivity model
KO0020	–	0.0 / **0.5** / 4.3	0.0 / **0.2** / 1.2
KO0018	–	0.0 / **1.1** / 6.6	0.0 / **2.5** / 12.3
KO0017	0.5	0.0 / **0.8** / 4.0	0.0 / **3.1** / 12.2
KO0015	–	0.0 / **0.7** / 6.6	0.0 / **3.8** / 24.2
KO0014	1	0.0 / **2.6** / 9.5	0.0 / **2.8** / 26.8

5.1.3 Local description of wfracture_01

As part of Task 8D (Vidstrand et al. 2017) an updated description of structure wfracture_01 local to the TASO tunnel has been provided. A detailed interpretation of this geometry update is provided in Section 0. All model cases considered to date (Basecase through Variant 3) utilise the new local description of wfracture_01, truncated to avoid intersection with probe borehole KO0014G01, as shown in Figure 3-6c.

There is some evidence from hydraulic tests performed at the BRIE that KO0014G01 is hydraulically isolated from the other probe boreholes. An alternative prescription of the local description of wfracture_01 is also considered, extending vertically from −417.5 m to −420.0 m as shown in Figure 3-6d.

The effects of hydraulically isolating probe boreholes KO0014G01 is considered in the model case Variant 4. This is an extension of Variant 3, defined in the previous section, and in summary is the Basecase with:

- Fracture intensity of the stochastic fracture network reduced by half (Section 5.1.1).
- Fracture transmissivities sampled from a semi-correlated distribution (Section 5.1.2).
- An alternative description of the structure wfracture_01, updated to hydraulically isolate KO0014G01 from the other four boreholes considered.

Results are shown in Table 5-9 for pressure build-up calculations using the Variant 3 and Variant 4 model cases, aggregated over realisations of the fracture network where the boreholes connect to the wider fracture network. The change to the local description of structure wfracture_01 causes only minor effects to the average pressure values calculated in all five probe boreholes. Results for pressure build-up for individual realisations of the Basecase, Variant 3 and Variant 4 models are shown in Appendix 1, Figure A1-3.

Simulated inflows to each of the probe boreholes for the Variant 4 model case are recorded in Table 5-10. Inflow values are aggregated over ten realisations of the stochastic DFN in each case. As observed for the pressure build-up simulations, changing the local description of wfracture_01 causes only limited effects on the average simulated inflows to each of the probe boreholes. Results for inflows for individual realisations of the Basecase, Variant 3 and Variant 4 models are shown in Appendix 1, Figure A1-7.

Table 5-9. The average pressure build-up calculated in the five probe boreholes for Variant 3 and Variant 4 model cases. Both implement a 50 % reduction in the Basecase fracture intensity. In each, the average pressure is calculated over the ten DFN realisations where the borehole connects to the wider network. Results are compared to pressure observations within each borehole.

		Min / Average / Max Pressure (bar)	
Borehole	Measured pressure build-up (bar)	Variant 3: wfracture_01 truncated at −417.5 m	Variant 4: wfracture_01 isolating KO0014G01
KO0020	–	1.3 / **4.7** / 9.1	1.3 / **4.4** / 9.0
KO0018	–	1.3 / **3.1** / 8.3	1.3 / **3.0** / 7.2
KO0017	6	1.3 / **5.2** / 10.8	1.7 / **4.9** / 10.0
KO0015	–	1.1 / **3.3** / 7.9	1.1 / **2.9** / 5.4
KO0014	3	1.4 / **3.4** / 7.9	3.0 / **3.4** / 4.3

Table 5-10. Simulated inflow to the five probe boreholes averaged over ten realisations of the stochastic discrete fracture network. Results compare the Variant 3 and Variant 4 model cases, both implementing a 50 % reduction in the Basecase fracture intensity. Results are compared to measured inflows with a lower detection limit of 0.1 ml/min.

		Min / Average / Max simulated inflow (ml/min)	
Borehole	Measured inflow (ml/min)	Variant 3: Wfracture_01 truncated at −417.5 m	Variant 4: wfracture_01 isolating KO0014G01
KO0020	–	0.0 / **0.2** / 1.2	0.0 / **0.2** / 0.8
KO0018	–	0.0 / **2.5** / 12.3	0.0 / **2.2** / 10.5
KO0017	0.5	0.0 / **3.1** / 12.2	0.0 / **2.8** / 9.9
KO0015	–	0.0 / **3.8** / 24.2	0.0 / **3.5** / 23.0
KO0014	1	0.0 / **2.8** / 26.8	0.0 / **3.8** / 33.8

Summary of findings

The effects of changing the geometry of wfracture_01 local to the TASO have limited effects on the simulated build-up of pressure in, and inflows to, the five probe boreholes. Although limited data are available these suggest KO0014G01 is hydraulically isolated from the remaining probe boreholes, it is therefore not sufficient to warrant the implementation of the modification to structure wfracture_01. Consequently, for the calibrations of the fracture network currently performed, the Variant 3 model case is deemed optimal for providing accurate representation of the fractured bedrock local to the BRIE.

5.1.4 Deterministic specification of fracture intersections

On the scale of deposition holes (30 cm diameter), individual fracture intersections have been logged. Both of the overcored probe boreholes KO0017G01 and KO0018G01 have been investigated, with the hydraulic properties of observed features assessed. The stochastic component of the DFN is modified, removing sampled fractures which intersect either of these deposition holes, and incorporating the hydraulic connections to the wider fracture network deterministically. Although this modification to the DFN network will alter the fracture statistics of the model from the prescription in the Task Description (Vidstrand et al. 2017) such changes are assumed minimal and typically require removing c. 10 fractures from a model comprising of c. 110 000. The remaining stochastic fractures generated in the "far-field" of the model are significant to the ingress of groundwater to open deposition holes only to the extent of providing suitable hydraulic connectivity to the deterministically specified local fractures. As such, variations in inflow to KO0017G01 and KO0018G01 between realisations are expected to be reduced for this modelling variant.[5]

One water-producing feature has been observed in each of the deposition holes, as detailed in Section 2.4. From the task description (Vidstrand et al. 2017) the orientation of the fracture has been interpreted, as well as the location of the intersection, provided as an elevation along the central axis of the deposition hole. Flow tests have also been performed within each of the deposition holes, providing information on the hydraulic properties for each of these key water producing intersections. In summary:

[5] The use of deterministic fractures should not belie the significance of developing a representative statistical model of the fracture network local to the BRIE. Although deterministically specifying the fractures intersecting the deposition holes of interest removes one of the major uncertainties between realisations of the DFN, the stochastic fracture network still provides (i) a mechanism for sampling fracture properties of the deterministic features that cannot be measured from mapping (e.g. size and shape); and (ii) provides the supply of water to these deterministic features for ingress into the deposition holes. Finally, it is worth noting that when considering a full repository comprising of thousands of deposition holes, detailed characterisation of fractures in each hole is likely unfeasible, and instead the stochastic DFN model can be used to understand the range of resaturation behaviours to be expected.

- KO0017G01: A single water producing feature is observed with a transmissivity of 5×10^{-11} m^2/s (Vidstrand et al. 2017).
- KO0018G01: A single water producing feature is observed with specific capacity, Q/dh, ranging from 1×10^{-12} m^2/s to 5×10^{-12} m^2/s (Vidstrand et al. 2017). Using these values, the steady-state Theim solution (Kasenow 2001) can be used to estimate transmissivities for this feature, using a 20 m radius of influence. Taking the maximum specific capacity, a transmissivity of 3.9×10^{-12} m^2/s is calculated.

For both of these features, their extent into the bedrock is somewhat unknown, other than

- they are not observed in the tunnel mappings,
- significant hydraulic connections between KO0018G01 and other monitored features are not observed, and
- KO0017G01 is in good hydraulic connection with local structure wfracture_01 (although this connection is not expected to be direct).

In order to infer the extent of each of these hydraulic features into the surrounding rock, the following three assumptions are made. Firstly, each feature is assumed to be centred on the central axis of each deposition hole; secondly, the fracture is assumed to comply with the transmissivity-size model used for the stochastic DFN component; and thirdly the fractures are assumed to be square[6].

For the correlated transmissivity model, used as part of the Basecase, fracture lengths for features interpreted in each of the probe boreholes are calculated as:

- **KO0017GO1:** Side length, L = 0.82 m.
- **KO0018GO1:** Side length, L = 0.18 m.

Using this transmissivity model fracture lengths inferred are typically too short to connect to the wider fracture network. This is especially the case for KO0018G01, where a fracture side length of 0.18 m will barely extend beyond the 30 cm diameter deposition holes.

As part of this calibration phase, an alternative, semi-correlated transmissivity-size model has been considered as specified in Section 5.1.2. In summary, this model is based around a mean transmissivity-size distribution identical to the correlated model, but with transmissivities normally distributed around this mean value using a standard deviation of 0.5. Using Equation (5-1), and assuming fracture transmissivities lie at the lower 95 % confidence level, the transmissivity-size correlation becomes

$$\log[T] = \log\left[7 \cdot 10^{-11} L^{1.7}\right] + 0.5 \times -2, \qquad (5\text{-}2)$$

and the fracture size for features interpreted in each of the probe boreholes are calculated as:

- **KO0017GO1:** Side length, L = 3.18 m.
- **KO0018GO1:** Side length, L = 0.71 m.

Both of these fractures are shown in Figure 5-4, along with the updated local description of wfracture_01 for context. Both of these fractures are now sufficiently long to include possible intersections with the wider fracture network (although not guaranteed). Fractures of this length are consistent with the general observations of the extent of these features, as detailed earlier in this section.

[6] The shape and size of fractures is somewhat unknown, as data is typically limited to fracture mappings from surface data such as tunnel walls or outcrops. However, there is no evidence not to make aspect ratios of the fractures lows. In addition, the fracture intensity is maintained whatever the aspect ratio (measured as fracture surface area per unit volume).

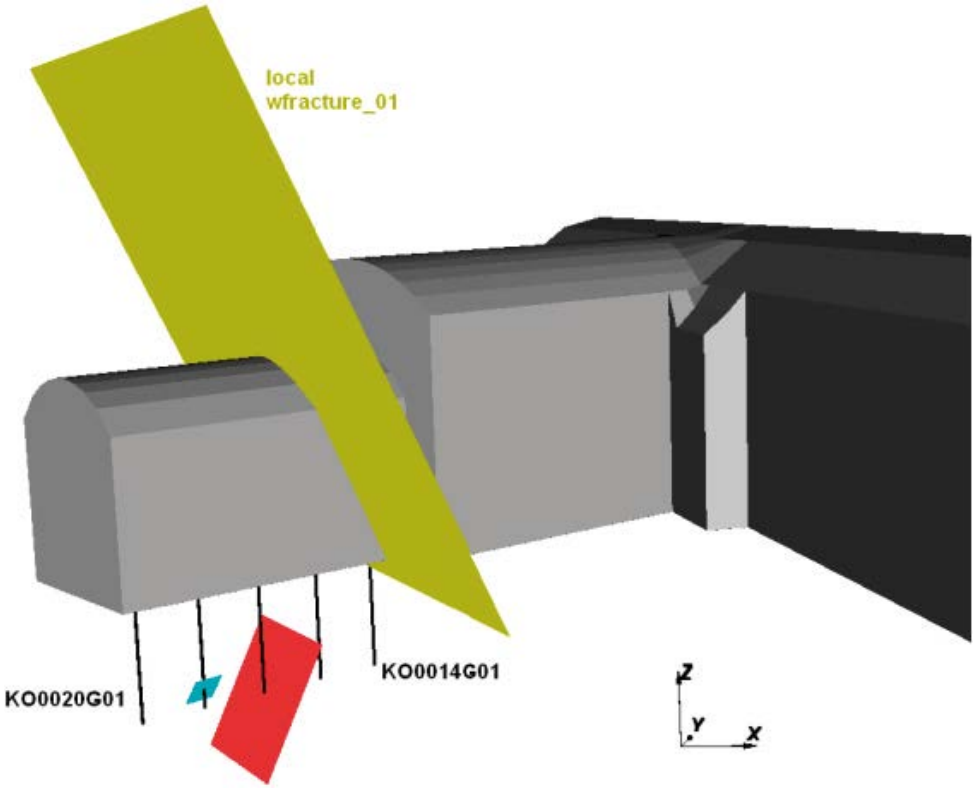

Figure 5-4. *Deterministically specified fractures used to represent the indentified inflow locations in both overcored boreholes KO0017G01 and KO0018G01. The local description of wfractrure_01 is also shown for context.*

Variant 5 is defined to constrain the fracture network local to deposition holes KO0017G01 and KO0018G01 by removing stochastically generated fractures intersecting these holes, and instead incorporating the deterministic prescriptions defined above. All other aspects of this model variant are identical to Variant 3, i.e. the Basecase with:

- Fracture intensity of the stochastic fracture network reduced by half (Section 5.1.1).
- Fracture transmissivities sampled from a semi-correlated distribution (Section 5.1.2).

The local description of wfracture_01 is truncated at −417.5 m, and not extended to fully isolate KO0014G01 as considered in Variant 4.

Results from pressure build-up calculations for model Variant 3 and Variant 5 are detailed in Table 5-11. The average pressure is calculated from DFN realisations where boreholes are found to intersect with the wider fracture network. Using the deterministic representation of fracture intersections with KO0017G01 and KO0018G01, pressures are broadly consistent with observations and within the range statistically expected from stochastic variations. Results for pressure build-up for individual realisations of the Basecase, Variant 3 and Variant 5 models are shown in Appendix 1, Figure A1-4.

Inflows to each of the probe boreholes are summarised in Table 5-12, calculated as the average over ten realisations of the stochastic DFN. As found experimentally, the average simulated inflows to KO0018G01 is below the lower detection limit of observations. The range of modelled inflows to KO0017G01 are also consistent with measurements (when possible uncertainties in the measurements is taken into account). It is noted that although probe boreholes KO0014G01, KO0015G01 and KO0020G01 are not conditioned by direct observation, the average inflow is still significantly reduced compared to those obtained in Variant 3. This is because any stochastic fracture intersecting one of these boreholes, and either KO0017G01 or KO0018G01, will be removed from the DFN model; reducing the possible fracture pathways for groundwater ingress to these probe boreholes. Results for inflows for individual realisations of the Basecase, Variant 3 and Variant 5 models are shown in Appendix 1, Figure A1-8.

Table 5-11. The average pressure build-up calculated in the five probe boreholes for Variant 3 and Variant 5 model cases. Both implement a 50 % reduction in the Basecase fracture intensity. In each, the average pressure is calculated over the DFN realisations where the borehole connects to the wider network. Results are compared to pressure observations within each borehole.

		Min / Average / Max Pressure (bar)	
Borehole	Measured pressure build-up (bar)	Variant 3: Stochastic intersection with KO0017 and KO0018	Variant 5: Deterministic intersection with KO0017 and KO0018
KO0020	–	1.3 / **4.7** / 9.1	1.3 / **3.8** / 9.2
KO0018	–	1.3 / **3.1** / 8.3	3.3 / **11.3** / 23.1
KO0017	6	1.3 / **5.2** / 10.8	3.3 / **9.4** / 19.5
KO0015	–	1.1 / **3.3** / 7.9	1.1 / **2.9** / 6.1
KO0014	3	1.4 / **3.4** / 7.9	1.7 / **2.8** / 5.5

Table 5-12. Simulated inflow to the five probe boreholes averaged over ten realisations of the stochastic discrete fracture network. Results compare the Variant 3 and Variant 5 model cases, both implementing a 50 % reduction in the Basecase fracture intensity. Results are compared to measured inflows with a lower detection limit of 0.1 ml/min.

		Min / Average / Max simulated inflow (ml/min)	
Borehole	Measured inflow (ml/min)	Variant 3: Stochastic intersection with KO0017 and KO0018	Variant 5: Deterministic intersection with KO0017 and KO0018
KO0020	–	0.0 / **0.2** / 1.2	0.0 / **0.1** / 0.5
KO0018	–	0.0 / **2.5** / 12.3	0.00 / **0.01** / 0.05
KO0017	0.5	0.0 / **3.1** / 12.2	0.1 / **0.2** / 0.4
KO0015	–	0.0 / **3.8** / 24.2	0.0 / **0.1** / 0.5
KO0014	1	0.0 / **2.8** / 26.8	0.0 / **0.2** / 0.6

Figure 5-5 illustrates two slices taken through realisation 1 of the DFN, one vertical cross-section incorporating all five probing boreholes, and one horizontal cross-section cutting through at the depth of −418.5 m. Fracture slices are coloured by transmissivity, and the correlation of fracture size to transmissivity is clearly seen, and as expected for a semi-correlated transmissivity-size model. Deterministically specified fractures are denoted by the thicker lines in Figure 5-5, where

- the large orange fracture trace, crossing vertically in both Figure 5-5a and Figure 5-5b is deterministic fracture wfracture_01 ($2.0\ 10^{-8}$ m^2/s, note the Task 8C parameterisation is used here), and
- the highly transmissive (red) fracture trace found at the bottom right-hand corner of Figure 5-5b is deterministic fracture NNW4 ($6.5\ 10^{-7}$ m^2/s).

Equivalent illustrations for stochastic fracture realisations 2 through 10 are shown in Appendix 1, Figure A1-9 through Figure A1-17 respectively.

Figure 5-6 illustrates equivalent fracture slices to those shown in Figure 5-5, depicting the solution pressures for realisation 1 of the DFN. Model results correspond to the scenario of shut-in pressures to the five boreholes packed off at 1 m. The drawdown caused by the TASO / TASD tunnels as well as deposition boreholes held at atmospheric conditions is clearly evident. Equivalent illustrations for stochastic fracture realisations 2 through 10 are shown in Appendix 1, Figure A1-18 through Figure A1-26 respectively.

Summary of findings

The Variant 5 model case includes deterministically specifying water producing features indentified in probe boreholes KO0017G01 and KO0018G01. On conditioning these boreholes, inflow and pressure build-up simulations provide very consistent results when compared to observations. Therefore of all the model cases considered, Variant 5 is identified as providing the most representative description of the fracture network local to the BRIE relevant to the two boreholes considered.

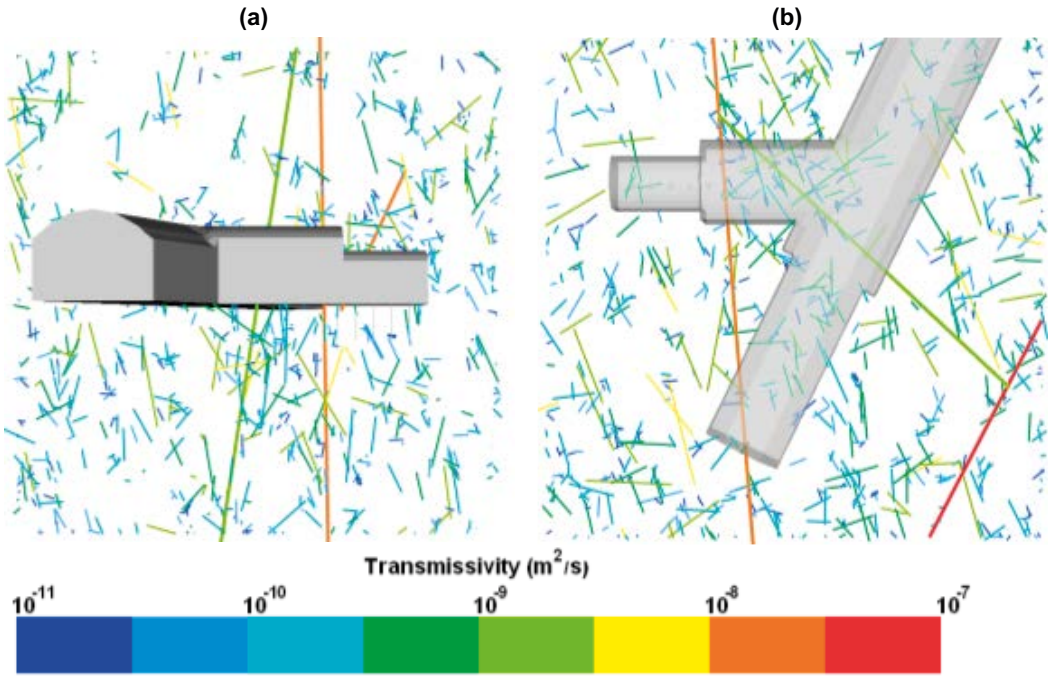

Figure 5-5. *Transmissivity (m^2/s) in the borehole near-field for (a) a vertical slice through all five probe boreholes; and (b) a horizontal slice at an elevation of −418.5 m. Results are shown for realisation 1 of the stochastic fracture network for model Variant 5.*

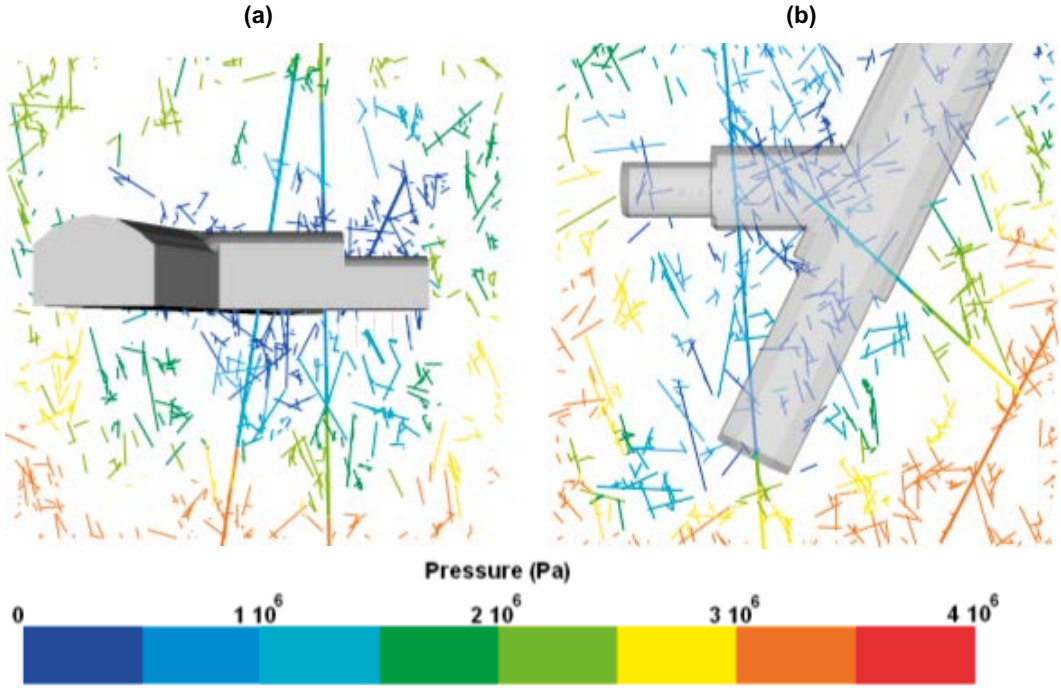

Figure 5-6. *Pressure (Pa) in the deposition hole near-field for (a) a vertical slice through all five probe boreholes; and (b) a horizontal slice at an elevation of −418.5 m. Results are shown for realisation 1 of the stochastic fracture network for model Variant 5.*

5.1.5 Calibration summary and conclusions

During the preceding sections, a number of model variants have been considered, intended to refine and calibrate the DFN to better represent the fractured rock local to the BRIE. A brief summary of each of the model cases considered are detailed below:

- **Basecase:** Based on the original statistics for stochastically generated fractures, interpreted from the task description (Vidstrand et al. 2017), and identical to Task 8C except for large-scale deterministic fractures which are updated from Task 8C to include a new local scale hydrozone wfracture_01 (truncated from KO0014G01). This model case is considered in Section 5.1.1.
- **Variant 1:** The deterministic component of the fracture network is specified identically to the Basecase. Stochastic models for fracture orientations, sizes, locations and transmissivity are also unchanged. The intensity of sampled fractures (P_{32}) is reduced to 75 % of the Basecase. This model case is considered in Section 5.1.1.
- **Variant 2:** The deterministic component of the fracture network is specified identically to the Basecase. Stochastic models for fracture orientations, sizes, locations and transmissivity are also unchanged. The intensity of sampled fractures (P_{32}) is reduced to 50 % of the Basecase. This model case is considered in Section 5.1.1.
- **Variant 3:** This model case is unchanged from Variant 2, with the exception of the transmissivity-size model used for stochastically generated fractures. For this variant, the correlated model is replaced with a semi-correlated representation of the transmissivities. This model case is considered in Section 5.1.2.
- **Variant 4:** The stochastic fracture network for this variant is identical to Variant 3 above. The deterministic component of the DFN is modified from Variant 3 to consider an alternative geometric description of the locally defined feature wfracture_01, updated to fully isolate borehole KO0014G01. This model case is considered in Section 5.1.3.
- **Variant 5:** This model case is unchanged from Variant 3, with the exception of conditioning the intersections with overcored boreholes KO0017G01 and KO0018G01. Stochastic fractures intersecting each of these holes are removed from the model and replaced with deterministic fractures. Note, wfracture_01 is defined according to Variant 3, and truncated at −417.5 m, the alternative description in Variant 4 is not used. This model case is considered in Section 5.1.4.

The calibration phase of Task 8D1 identifies the updated description of the stochastic fracture network defined through model Variant 5 as the most consistent representation of the bedrock local to the BRIE when compared to

- fracture intersections with probe boreholes and traces mapped on the TASO tunnel,
- the distribution of transmissivities observed experimentally,
- pressure build-up in the five 76 mm probe boreholes KO0014G01, KO0015G01, KO0017G01, KO0018G01 and KO0020G01,
- inflows to each of the five 76 mm probe boreholes KO0014G01, KO0015G01, KO0017G01, KO0018G01 and KO0020G01, and
- the interpreted water producing features observed in boreholes KO0017G01 and KO0018G01.

The remainder of this study uses this updated DFN prescription for calculation of both deposition hole scale inflows, and resaturation of emplaced bentonite. No further consideration is given to the Basecase, and Variant 1–4 model definitions.

5.2 Deposition holes KO0017G01 and KO0018G01

As part of the BRIE experiment, probe boreholes KO0017G01 and KO0018G01 have been overcored up to a diameter 0.3 m. During this excavation process, the length of KO0017G01 was also extended by 0.5 m, reaching an elevation of −420.5 m. The length of deposition hole KO0018G01 was unchanged. Before considering the resaturation of bentonite emplaced in these two deposition holes, inflow calculations are performed using the optimal model case identified in Section 5.1 (Variant 5). This modelling exercise provides an opportunity to

- assess the quality of the calibration processes by comparing simulated inflows to KO0017G01 and KO0018G01 with the latest measurements available for Task 8D (Vidstrand et al. 2017), and
- build confidence in the methodologies developed to date.

Figure 5-7 compares the total inflows to each of the 76 mm probe boreholes KO0017G01 and KO0018G01 with corresponding results for the deposition hole models. Inflows are shown for ten realisations each of

- the Basecase (Task 8C) model,
- Variant 3 (calibration of the stochastic DFN only), and
- Variant 5 (calibration of the stochastic and deterministic DFN).

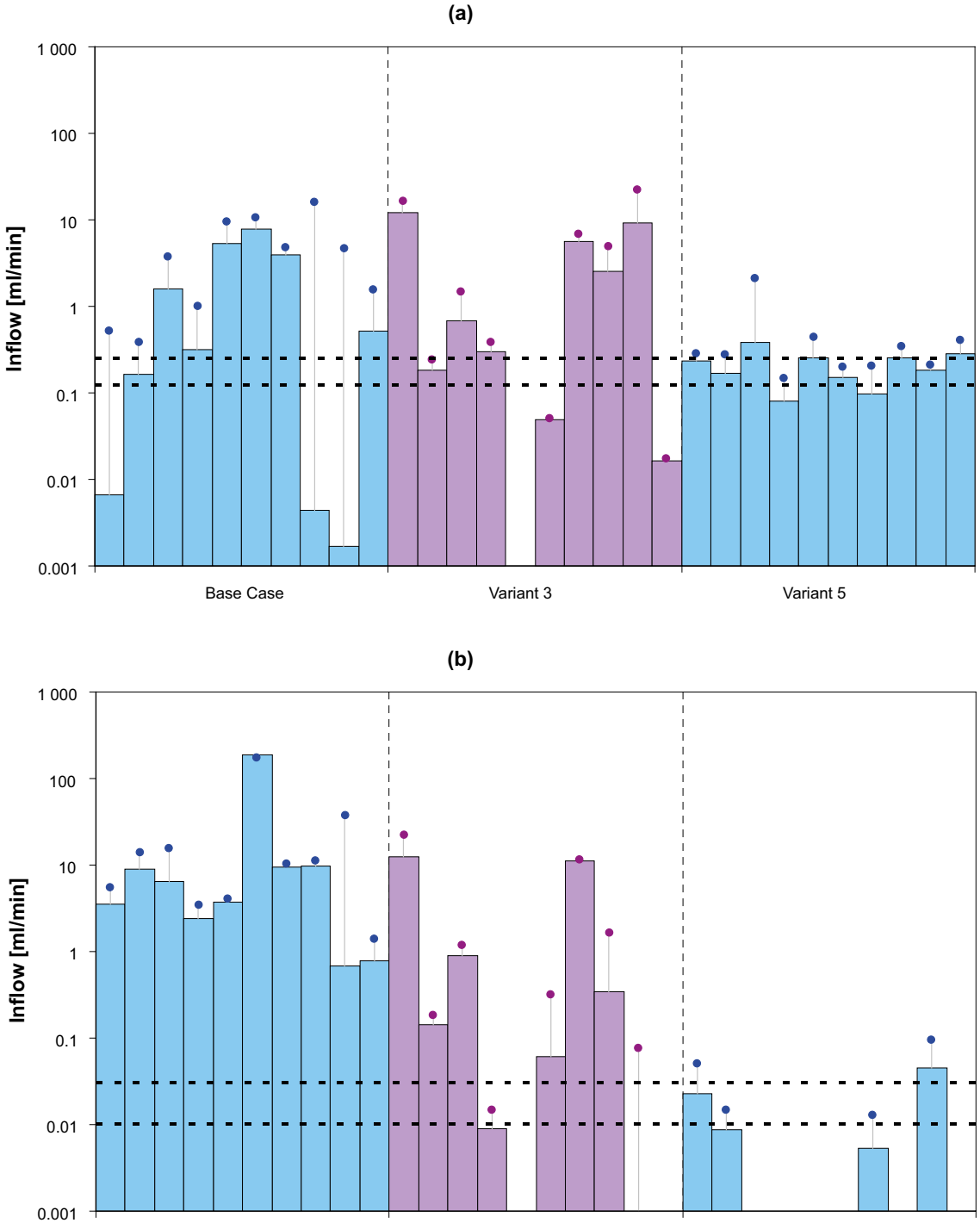

Figure 5-7. *Inflows to the boreholes (a) KO0017; and (b) KO0018, before and after overcoring compared to measured observations. Bars represent the 76 mm probe boreholes solutions, with circles corresponding to results when overcored to 30 cm diameter. Black dashed lines represent the bounds of the inflow measurements recorded in each overcored hole (Table 2-20).*

On conditioning the fracture network, simulated inflows to the overcored boreholes become increasingly consistent with measurements. For all ten realisations of the Basecase (Task 8C) model, inflows to both deposition holes are above those measured; with variations between realisations and boreholes a consequence of stochastic variation in the fracture network and the principle fractures intersections with the borehole. On calibrating the stochastic component of the DFN (Variant 3), both

- the intensity of stochastic fractures is decreased (50 % of the Basecase), and
- the transmissivities sampled for individual fractures use a semi-correlated transmissivity-size model (compared to a correlated model used in the Basecase).

These changes improve the models predictions of inflows to the two deposition holes. For KO0017G01, two realisations calculate inflows below measurements; seven realisations above; and one realisation disconnects the deposition hole from the wider network. For KO0018G01, one realisation lies in the range of inflows inferred from measurement; seven are above; and two realisations are disconnected from the wider network.

On deterministically specifying the fracture intersections with KO0017G01 and KO0018G01 (Variant 5), the spread of inflows between realisations significantly decreases. In addition, for this model variant

- 40 % of the realisations yield inflows to overcored KO0017G01 that are within the bounds estimated from measurements, and
- hydraulic connections from KO0018G01 to the wider fracture network only occur in 40 % of realisations considered. Of these realisations (1, 2, 7, and 9), the second and seventh realisations simulate inflows within the bounds estimated from measurements.

The subsequent changes to the average groundwater ingress (aggregated over the ten realisations of the fracture network) are presented in Table 5-13 for the overcored boreholes. For all model cases considered, the average inflows to both deposition holes are shown to increase on overcoring.

Likely causes of this increase are:

- For a given drawdown, increasing the borehole radius will increase rate of groundwater ingress (e.g. Thiem solution).
- As the boreholes are overcored (and in the case of KO0017G01, lengthened), they have increased potential to intersect additional fractures in the network. Through these additional intersections, the rate of groundwater ingress to the deposition hole may also increase.

Clearly, the second point outlined above is not applicable to Variant 5, as the DFN model has been calibrated such that intersections with the overcored (and consequently probe) boreholes are deterministically specified. As such, the change in groundwater ingress on overcoring KO0017G01 and KO0018G01 is dominated by the change in borehole radius. As this is the same for both deposition holes considered, the average percentage increase in calculated inflows is similar for both KO0017G01 and KO0018G01.

Table 5-13. Inflows before and after overcoring of probe holes KO0017G01 and KO0018G01 to 30 cm diameter. Values are aggregated over 10 realisations for the Basecase, Variant 3 and Variant 5 model definitions.

Borehole	Model Case	Average inflows to probe holes (ml/min)	Average inflows to overcored KO0017 and KO0018 (ml/min)	Average % increase
KO0018G01	Basecase	23.11	27.36	18.4 %
KO0018G01	Variant 3	2.50	3.70	48.2 %
KO0018G01	Variant 5	0.01	0.02	110.1 %
KO0017G01	Basecase	1.97	5.25	166.4 %
KO0017G01	Variant 3	3.08	5.23	69.8 %
KO0017G01	Variant 5	0.21	0.46	119.8 %

5.2.1 Upscaling

Cross-sections local to the overcored boreholes KO0017G01 and KO0018G01 are shown in Figure 5-8, corresponding to the first realisation of the stochastic fracture network. Cross-sections are shown in subfigures (a, b) correspond to the DFN model, and subfigures (c, d) are taken through the equivalent continuous porous medium (ECPM) model, generated by upscaling the fracture network (see Section 5.2.1). Fracture traces are coloured by transmissivity, with the vertical component of the equivalent permeability field, k_{33} shown for the ECPM properties.

Two slices are shown, one vertical, incorporating overcored boreholes KO0017G01 and KO0018G01; the other horizontal, and at a depth of −418.5 m. Regions of intense fracturing and/or high transmissivity are observed to yield correspondingly permeable blocks in the upscaled model. Equivalent results for realisation 2 through 10 of the stochastic fracture network are shown in Appendix 1, Figure A1-27 through Figure A1-35 respectively.

Using this upscaling methodology, the resultant ECPM properties allow representation of the heterogeneity of the bedrock when calculating the resaturation of emplaced bentonite using TOUGH2. Further details of these simulations are presented in Section 6 of this report.

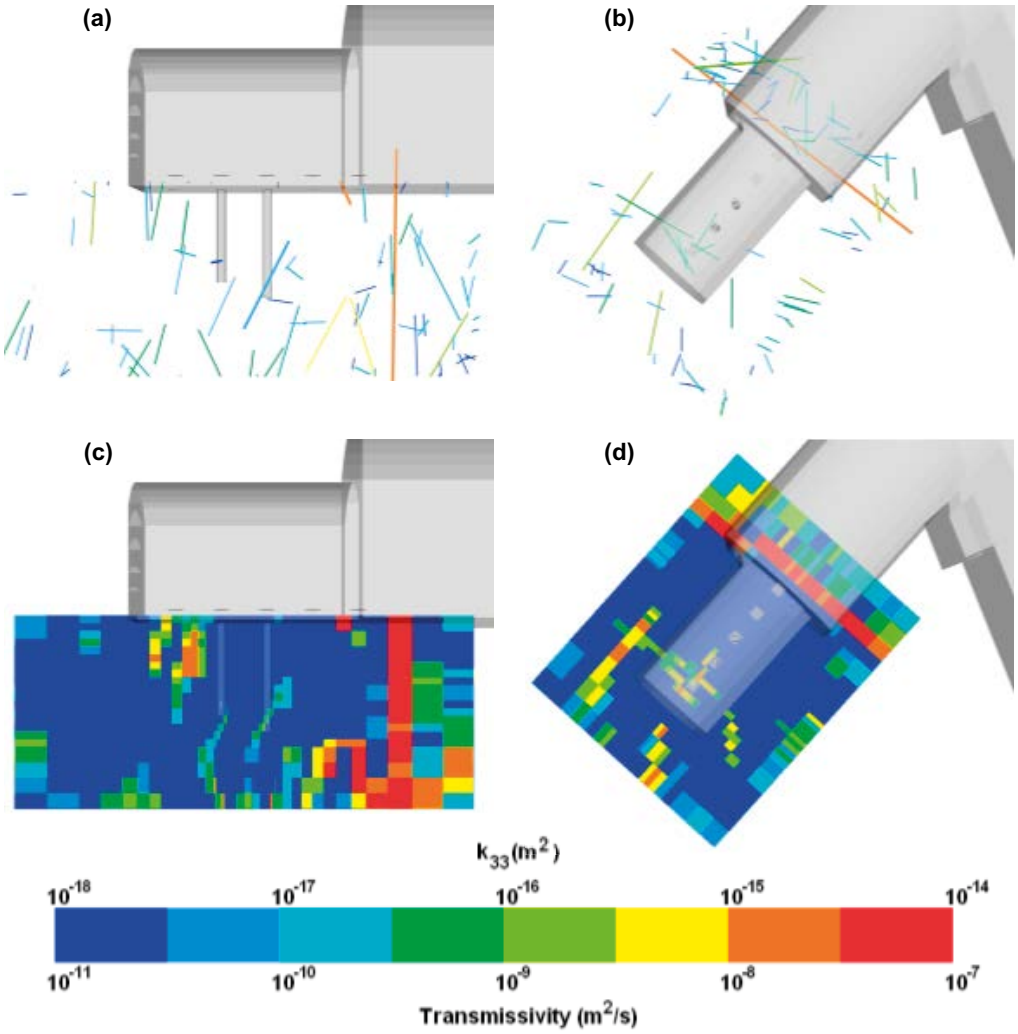

Figure 5-8. *Transmissivity (m^2/s) (a,b) and upscaled permeability (m^2) (c,d) in the deposition hole near-field for (a,c) a vertical slice through all five probe boreholes; and (b,d) a horizontal slice at an elevation of −418.5 m. Results are shown for the first realisation of the stochastic fracture network.*

6 Task 8D2: Resaturation of bentonite

The resaturation of bentonite, emplaced within two overcored boreholes, is considered in this section. Preliminary calculations consider open hole conditions, required to provide initial conditions for simulating the resaturation of the installed bentonite package. As part of Task 8D2 predictions for the resaturation front / profiles and times to 95 % liquid saturation are made from calculations for several realisations of the fracture network. In these simulations, the initial addition of water to the outer slot of the bentonite installations is not considered. The sensitivity of bentonite hydration to rock matrix permeability is also assessed through a number of model variants. Predictions are provided to the EBS Task Force for comparison with the BRIE upon completion.

Task 8D2 considers the resaturation of bentonite emplaced within the overcored boreholes KO0017G01 and KO0018G01 of the TASO tunnel. Two of the main objectives of participation in Task 8D2 are

- to develop tools and methodologies for understanding the interaction between the groundwater flow from a fractured host rock, and the resulting hydration of emplaced bentonite, and
- to refine predictions of resaturation time and profiles of the BRIE, first developed as part of Task 8C modelling (Baxter et al. 2013).

Numerical simulations use the software package TOUGH2 to represent the flow of the air and water phases during hydration of the bentonite buffer. TOUGH2 is based on a continuum concept, with full details of the numerical formulation presented in Section 3.1.2. To simulate the bentonite rock interface, and in order to retain the heterogeneity of the fracture network, the DFN model is upscaled to equivalent continuum properties. Details of upscaling methodologies are presented in Section 3.1.1, and consist of replacing the fracture network with equivalent block permeability on the model grid-scale. The mesh size is sufficiently small to not unduly spread the fractures hydraulics and consequently the bentonite resaturation. Results from the upscaling process of ten realisations of the Variant 5 (optimally calibrated) model case are shown in Figure 5-8 and Figure A1-27 through Figure A1-35. Upscaled permeability blocks for the first realisation of the fracture network are also shown in Figure 6-1, taken for a horizontal slice at −419.8 m through the TOUGH2 sub grid. Fracture traces are shown overlaying the permeability field, with regions of increased permeability corresponding to locations of enhanced fracturing.

Four realisations of the stochastic fracture network are considered, using the optimal Variant 5 model description. These realisations (1, 2, 7 and 9) correspond to those for which deposition hole KO0018G01 was found to be hydraulically connected to the wide fracture network, as detailed in Section 5.2. In addition, all deposition holes have a radius of 0.15 m, and represented within the TOUGH2 model as a uniform octagonal prism. In order to preserve the surface area of the deposition hole – host rock interface, the octagon is specified with an outer radius of 0.1539 m. Deposition hole KO0018G01 is 3 m deep, whereas KO0017G01 was lengthened during overcoring, and is now excavated to a depth of 3.5 m.

Using the upscaled properties of the fracture network for two of the four realisations (deemed optimal from the calibration and conditioning study), the transient hydration process of emplaced bentonite modelled. The methodology for the TOUGH2 simulations includes two phases:

1. Inflow calculations are performed to open hole conditions for overcored KO0017G01 and KO0018G01. These simulations utilise initial / boundary conditions provided by the task description (Vidstrand et al. 2017). Modelling results are discussed in Section 6.1.
2. Using the results from these inflow calculations as initial conditions, the resaturation of emplaced bentonite within each of the deposition holes is simulated. Details of this modelling phase are presented in Section 6.2.

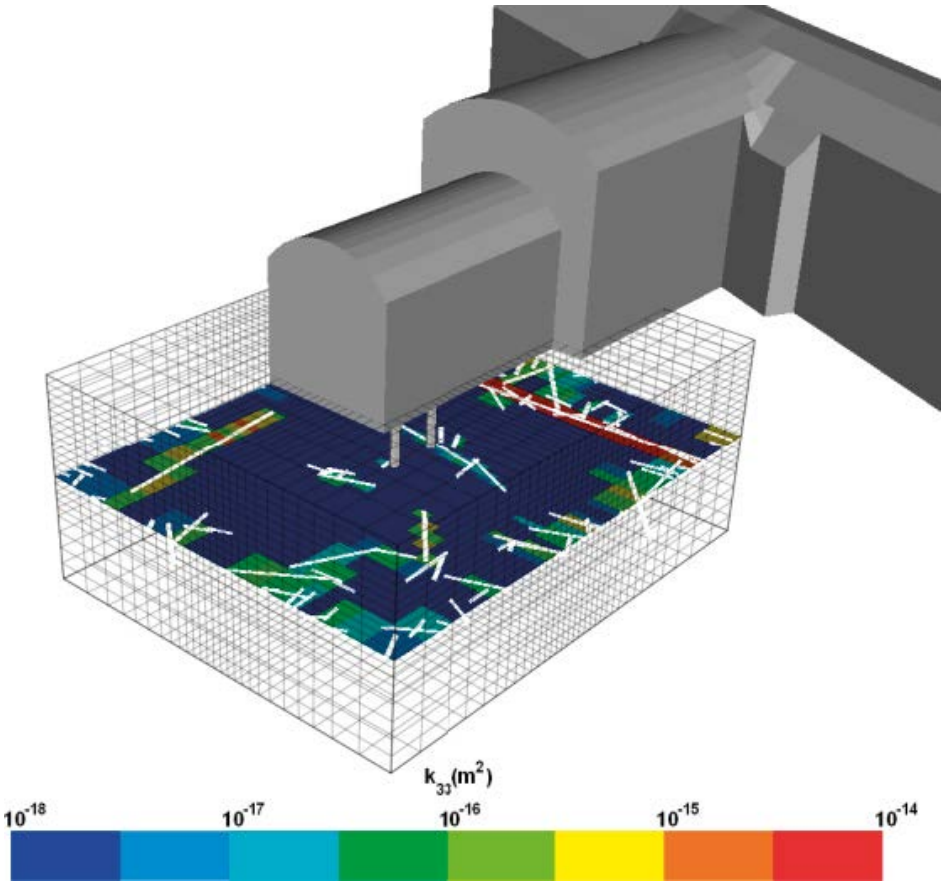

Figure 6-1. *A horizontal slice at −419.8 m of the upscaled permeability, computed on a sub-grid, in the vicinity of the overcored boreholes. Upscaled permeabilities are on a ~0.5 m scale, with the traces of the fractures overlaid.*

Three variant scenarios will also be considered:

- Resaturation of the bentonite was found to be very sensitive to rock matrix permeabilities as part of the Task 8C study (Baxter et al. 2013). A model variant, considering a rock matrix permeability of (1×10^{-23} m^2) is detailed in Section 6.3.2.
- As part of the sensitivity study (Gordon et al. 2014) an alternative constitutive relationship has been considered for the relative permeability of the gas phase. A model variant, using this alternative relative permeability model is considered in Section 6.4.
- Sensitivity of the bentonite permeability on resaturation rates and profiles is considered in Section 6.5, for a model case lowering the bentonite permeability one order of magnitude to 6.4×10^{-22} m^2.

6.1 Simulation of open deposition holes

Prior to modelling the resaturation of bentonite emplaced within overcored boreholes KO0017G01 and KO0018G01, inflows are calculated for open hole conditions using the upscaled fracture prescription. Results from these simulations provide the initial conditions for the resaturation analysis presented in Section 6.2. The following boundary conditions are applied to the inflow calculations:

- Boreholes are constrained identically to the TASO tunnel, held at atmospheric pressure, and with an assumed relative humidity of 100 %.
- Far field boundary conditions are as prescribed by the task description (Vidstrand et al. 2017).

Inflows to each of the deposition holes are illustrated in Figure 6-2 shown as a contour plot on the borehole walls. This figure corresponds to the first realisation of DFN model, using the optimal model Variant 5 defined in Section 5.1. Inflows for realisations 2, 7 and 9 of the fracture network are shown in Appendix 2, Figure A2-1 through Figure A2-3.

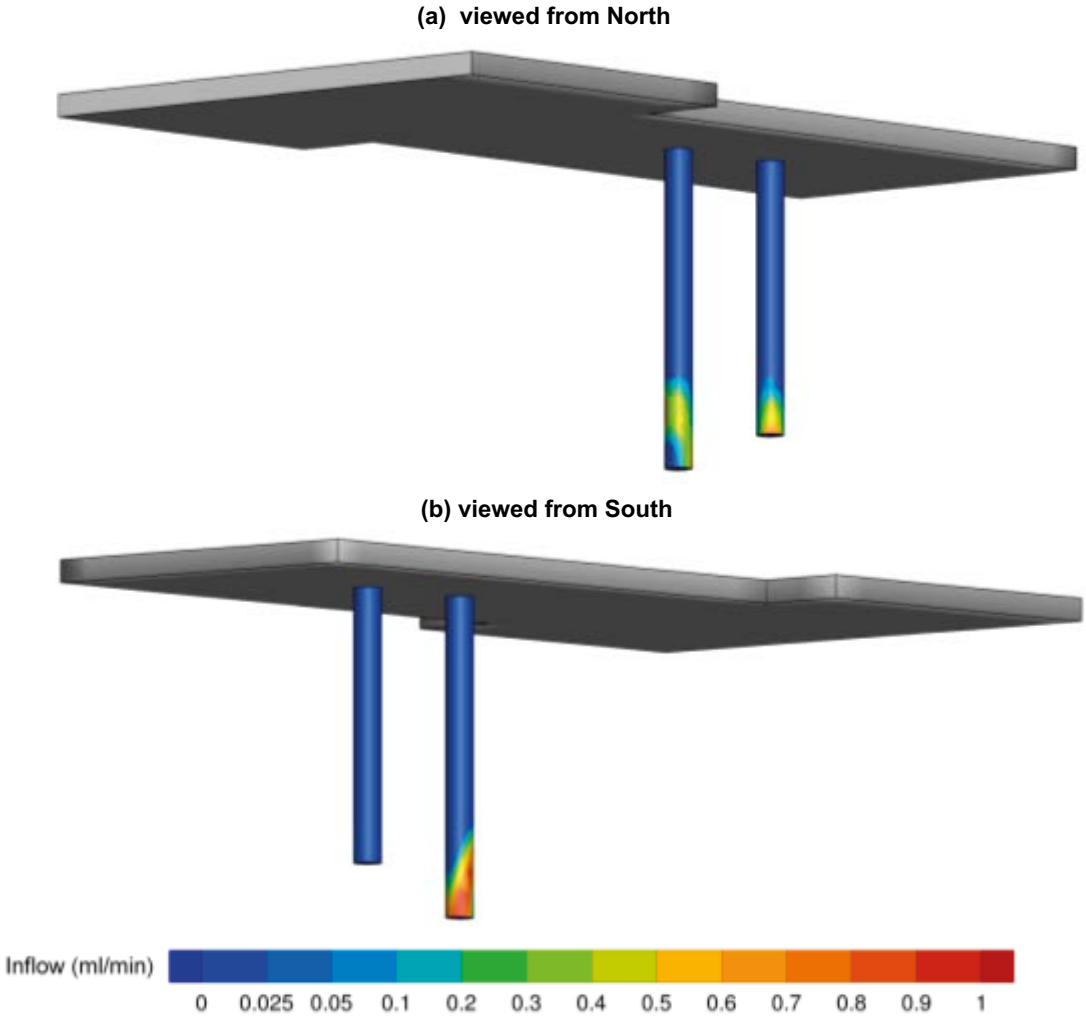

Figure 6-2. *Inflows illustrated against the walls of deposition boreholes KO0017G01 and KO0018G01, for realisation 1 of the upscaled fracture network. The view in figure (a) is taken from North, and the view in figure (b) is from the South.*

The locations of inflows to each of the deposition holes KO0017G01 and KO0018G01 are consistent with the conditioned fracture network, specifying intersecting fractures deterministically at these locations, as shown in Figure 5-4. Water-producing intersections occur towards the bottom of both of these holes, at an elevation of c. −420.1 m in KO0017G01 and c. −419.6 m in KO0018G01 (Vidstrand et al. 2017). As a consequence of the borehole conditioning, the inflows identified to each of the overcored boreholes are consistent between the realisations of the DFN considered, with the following observations noted:

- Inflows to overcored borehole KO0017G01 are typically larger than for KO0018G01, as can be seen from calculations for realisations 1, 2 and 7 of the upscaled DFN. This is as expected, with the water producing feature intersecting KO0017G01 considerably more transmissive than the equivalent feature identified in KO0018G01. However, for realisation 9, inflows to KO0018G01 are larger than for the other three realisations of the fracture model considered. This is consistent with the DFN solutions calculated using CONNECTFLOW, and presented in Figure 5-7. Consequently, the resaturation times and profiles of emplaced bentonite in the deposition holes may differ significantly between realisation 9 and realisations 1, 2 and 7 of the upscaled DFN.
- The illustration of inflows presented in Figure 6-2, Figure A2-1 through Figure A2-3 exhibit a small discrepancy. The inflow is calculated from the dot product of the inward unit normal to the deposition hole surface, and the liquid flux vector, i.e. $\mathbf{n} \cdot \mathbf{v}_l$. However, in the illustrations presented, the unit normal is calculated as the vector from the surface point of interest to the centre of the deposition hole, rather than perpendicular to the representation of the deposition hole wall. This discrepancy is not expected to be significant.

6.2 Resaturation of emplaced bentonite

Using the inflow simulations calculated as part of Section 6.1 as initial conditions, the resaturation of bentonite emplaced within each of the two overcored boreholes KO0017G01 and KO0018G01 are calculated using the optimal Variant 5 model description. Four of the ten realisations considered (1, 2, 7 and 9) hydraulically connect KO0018G01 to the wide fracture network, as detailed in Section 5.2. Of these, realisations 2 and 7 provided the best prediction of measured inflows under open hole conditions, and these two realisations are selected for subsequent resaturation calculations. In general, results presented in this section correspond to realisation 2 of the upscaled stochastic fracture network, with results from realisation 7 presented in Appendix 2 where appropriate.

As part of the Task 8D update, the rock matrix permeability is reviewed with new measurements available from core plugs taken from both deposition holes. For KO0017G01, laboratory tests estimate rock matrix permeabilities in the range 7.5×10^{-20} m^2 to 5.5×10^{-19} m^2, as measured from three samples. For KO0018G01, laboratory tests on five core plugs measure permeabilities from 6.0×10^{-21} m^2 up to 3.3×10^{-20} m^2. Full details of the measurements are presented in Section 2.8 of this report. Throughout this study, the numerical models developed for modelling the resaturation of bentonite use a homogeneous rock matrix permeability across the domain. Two cases are considered:

1. the rock matrix permeability is calculated as the geometric mean of the eight laboratory samples, with a value of 3.8×10^{-20} m^2, and
2. the rock matrix permeability is taken from the Task 8C description, elicited from expert judgement, and has a value of 1×10^{-21} m^2.

The resaturation profiles of emplaced bentonite in the two deposition holes are shown in Figure 6-3 through Figure 6-5 for the first 500 days. Three model cases are shown corresponding to:

- the optimal DFN realisation identified from Task 8C (including a rock matrix permeability of 1×10^{-21} m^2),
- realisation two of the calibrated Task 8D DFN with a rock matrix permeability of 3.8×10^{-20} m^2, and
- realisation two of the calibrated Task 8D DFN with a rock matrix permeability of 1×10^{-21} m^2.

The results obtained are broadly consistent with the Task 8C modelling (Baxter et al. 2013). On decreasing the rock matrix permeability, the calibrated fracture model is seen to hydrate the bentonite significantly slower (i.e. comparing the middle and right hand side plots in Figure 6-3 through Figure 6-5). This agrees with conclusions from Task 8C, where the permeability of the rock matrix was shown to be critical on resaturation times and profiles. Comparing the Task 8C model (left in Figure 6-3 through Figure 6-5), with the calibrated DFN model using a rock matrix permeability of 1×10^{-21} m^2 (right in Figure 6-3 through Figure 6-5), the resaturation rates and times are broadly consistent, although the location of inflows are different. This is to be expected, as one of the primary differences between Task 8C and Task 8D models is the conditioning of deposition holes to directly represent the groundwater producing fracture intersections observed.

Two opposing difficulties in using the permeabilities measured from laboratory tests performed on the eight core plugs to parameterise the rock matrix component of the model are:

1. The laboratory tests were performed in de-stressed conditions. It is expected that under the *in situ* stress field (Section 2.5) permeabilities could typically be one to two orders of magnitude lower (i.e. 3.8×10^{-21} m^2 down to 3.8×10^{-22} m^2).
2. The rock matrix component of the model consists of both the granite matrix and unmapped microfractures which are not included in the DFN component of the model. Assuming the laboratory core plugs considered are free from such microfractures, the true matrix permeability measured in the laboratory will be below those applicable for *in situ* conditions.

Therefore, due to the uncertainties in applying the laboratory measurements to the model, results presented in the remainder of this section use a rock matrix permeability as per the Task 8C description, with a value of 1×10^{-21} m^2.

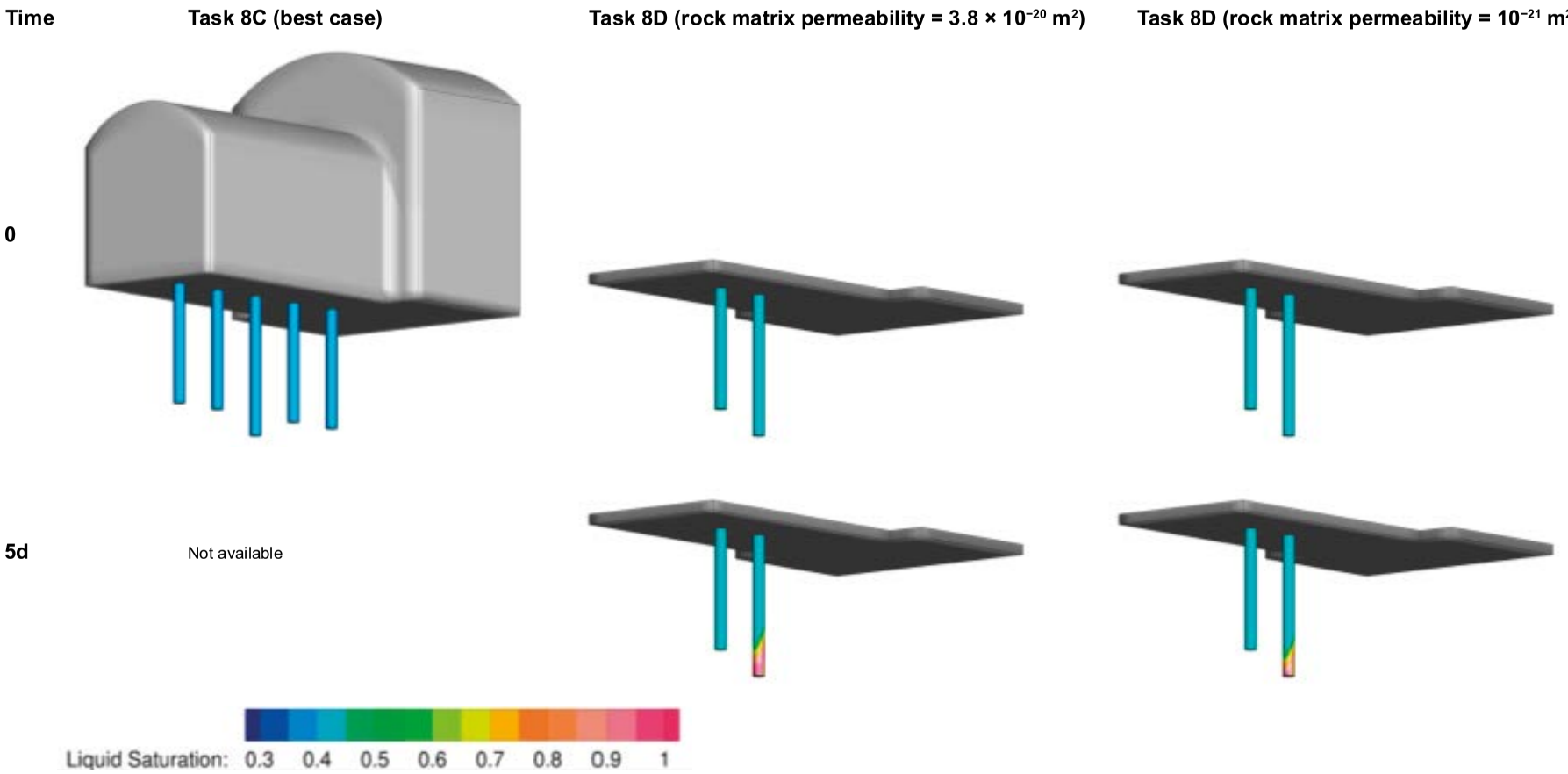

Figure 6-3. *Resaturation profiles of emplaced bentonite initially and after 5 days have elapsed. Three model cases are shown; Left: results correspond to the optimal DFN realisation from Task 8C; Middle: results correspond to realisation 2 of the calibrated Task 8D DFN with a rock matrix permeability of* 3.8×10^{-20} m^2*; and Right: results correspond to realisation 2 of the calibrated Task 8D DFN with a rock matrix permeability of* 1×10^{-21} m^2.

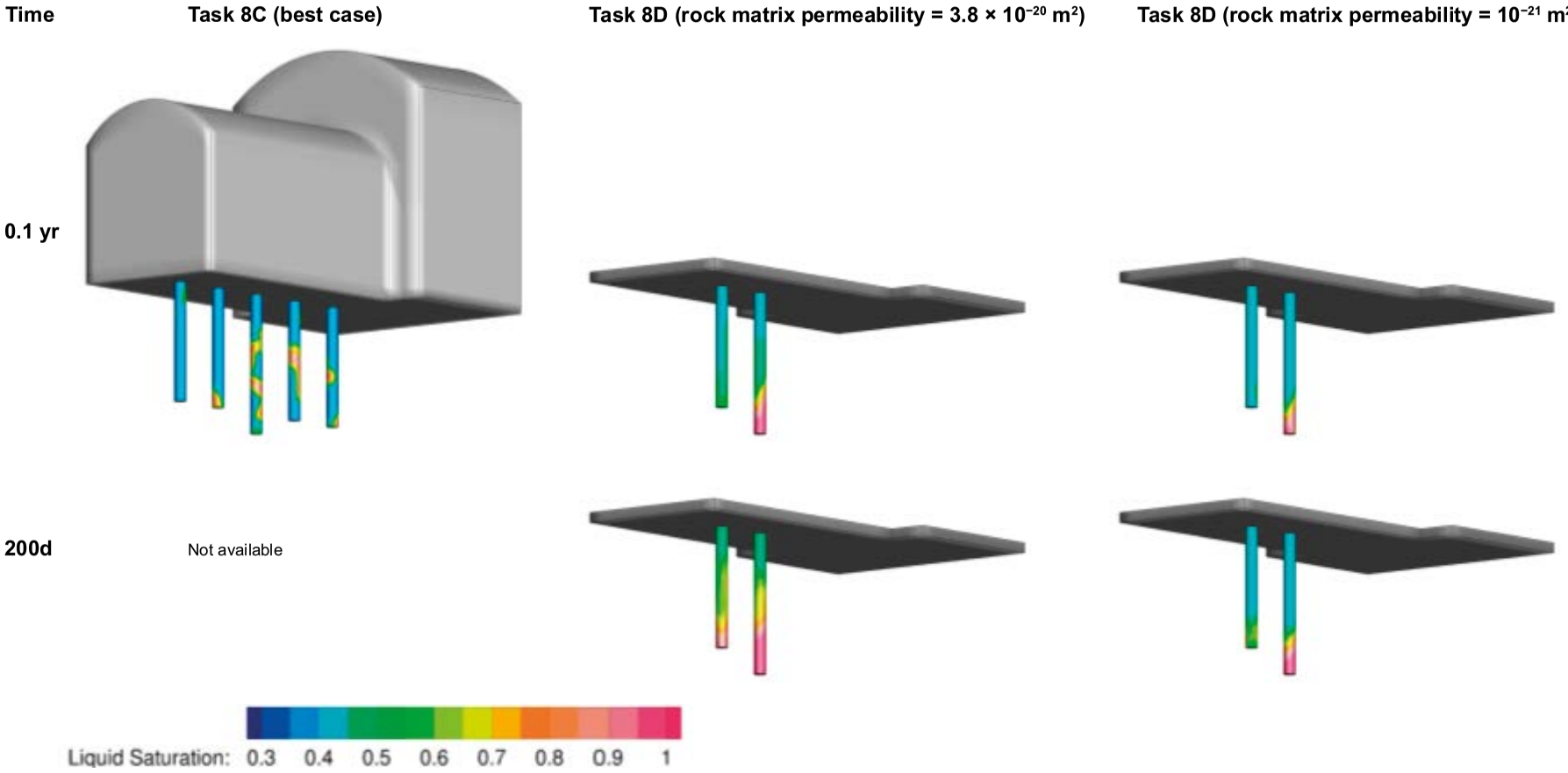

Figure 6-4. *Resaturation profiles of emplaced bentonite after 0.1 years and 200 days have elapsed. Three model cases are shown; Left: results correspond to the optimal DFN realisation from Task 8C; Middle: results correspond to realisation 2 of the calibrated Task 8D DFN with a rock matrix permeability of* 3.8×10^{-20} m^2*; and Right: results correspond to realisation 2 of the calibrated Task 8D DFN with a rock matrix permeability of* $1 \times 10^{-2}1$ m^2.

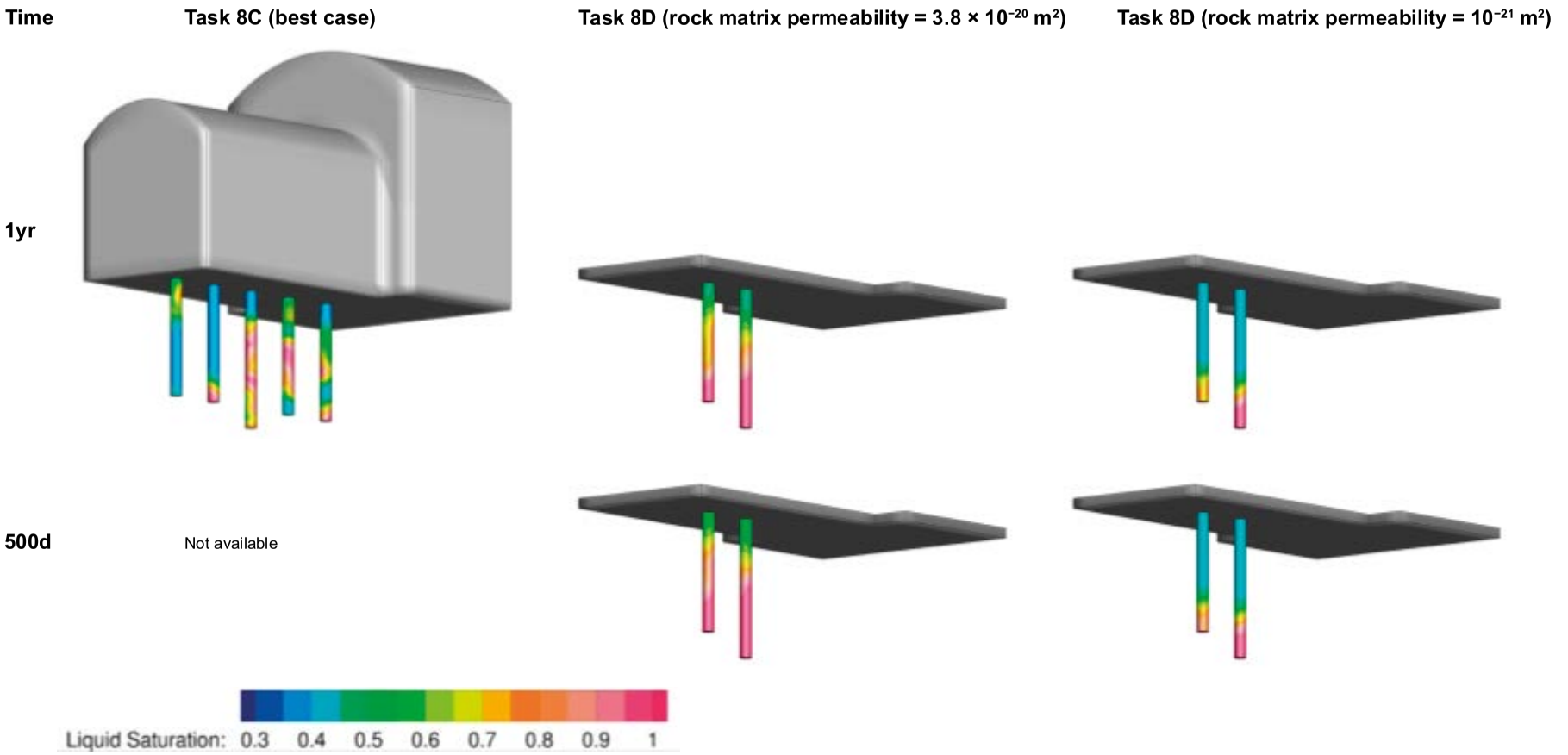

Figure 6-5. *Resaturation profiles of emplaced bentonite after 1 year and 500 days have elapsed. Three model cases are shown; Left: results correspond to the optimal DFN realisation from Task 8C; Middle: results correspond to realisation 2 of the calibrated Task 8D DFN with a rock matrix permeability of* 3.8×10^{-20} m^2*; and Right: results correspond to realisation 2 of the calibrated Task 8D DFN with a rock matrix permeability of* 1×10^{-21} m^2.

The initial liquid saturation on the outer surface of the bentonite stack is shown in Figure 6-6, along with nine subsequent times up to 100 years. Results correspond to the second realisation of the upscaled stochastic fracture network, with resaturation of the bentonite initiating towards the bottom of the deposition holes. This is consistent with both the location and orientation of intersections with water producing features as shown in Figure 5-4. Equivalent results for realisation seven of the stochastic fracture network are shown in Figure A2-04.

6.2.1 Bentonite hydration at sensor locations

Twelve sensors were placed within the bentonite during installation to monitor the relative humidity, six in KO0017G01 and six in KO0018G01. The positions of the sensors are detailed in Table 2-3, and illustrated in Figure 6-7. The modelled evolution of the relative humidity during the first 500 days since installation are presented in Figure 6-8 and Figure 6-9, corresponding to the sensors located in KO0017G01 and KO0018G01 respectively. Results correspond to the second realisation of the stochastic fracture network, with Figure A2-5 and Figure A2-6 detailing equivalent results for realisation seven. It is noted that undulations of the TASO tunnel floor are not considered in these models, with the tunnel floor approximated as a horizontal planar surface at elevation −417 m. In addition, the depth of deposition hole KO0017G01 is approximated to 3.5 m, with KO0018G01 3 m deep. As such, sensor elevations are adjusted such that they do not lie outside the bentonite package. Specifically, sensors in KO0018G01 at an elevation of −420.02 m, are sampled from the model results at −419.95 m.

The modelled evolution of relative humidity within the bentonite of both deposition holes is observed to be highly heterogeneous, with significant differences observed between sensors. For KO0017G01, sensor WBR0003 is located closest to the fracture intersection, and as such the bentonite local to this sensor undergoes the most rapid hydration, as shown by the relative humidity evolution in Figure 6-8. For deposition hole KO0018G01, the dip of the fracture is such that no relative humidity sensor is positioned in the direct vicinity of the intersecting fracture.

Contour plots of modelled saturation within the bentonite stacks emplaced in KO0017G01 and KO0018G01 are requested by the task description (Vidstrand et al. 2017). These are shown in Figure 6-10 through Figure 6-13 as a series of horizontal slices, taken at elevations detailed in Table 6-1, and corresponding to instrumented bentonite blocks. Results correspond to the second realisation of the upscaled stochastic fracture network. Calculated liquid saturations are shown after 100 days; 150 days; 200 days and 250 days; as requested by the task description.

For KO0017G01, the orientation of the water producing feature is clearly observed through the hydration profiles. The resaturation front at shallow depths progresses from the North-East, whereas towards the bottom of the deposition hole the bentonite resaturates from the South-West. This is consistent with the fracture orientation, striking 140°, as shown in Figure 5-4.

In contrast, for deposition hole KO0018G01, resaturation is primarily from the North. For this borehole, the intersected fracture is relatively small, with side length of just 0.71 m. As such, it is likely to have only limited connectivity to the wider fracture network required for the supply of groundwater. A consequence is that the resaturation profile will be dominated by the direction in which the interpreted borehole fracture connects to the remainder of the network.

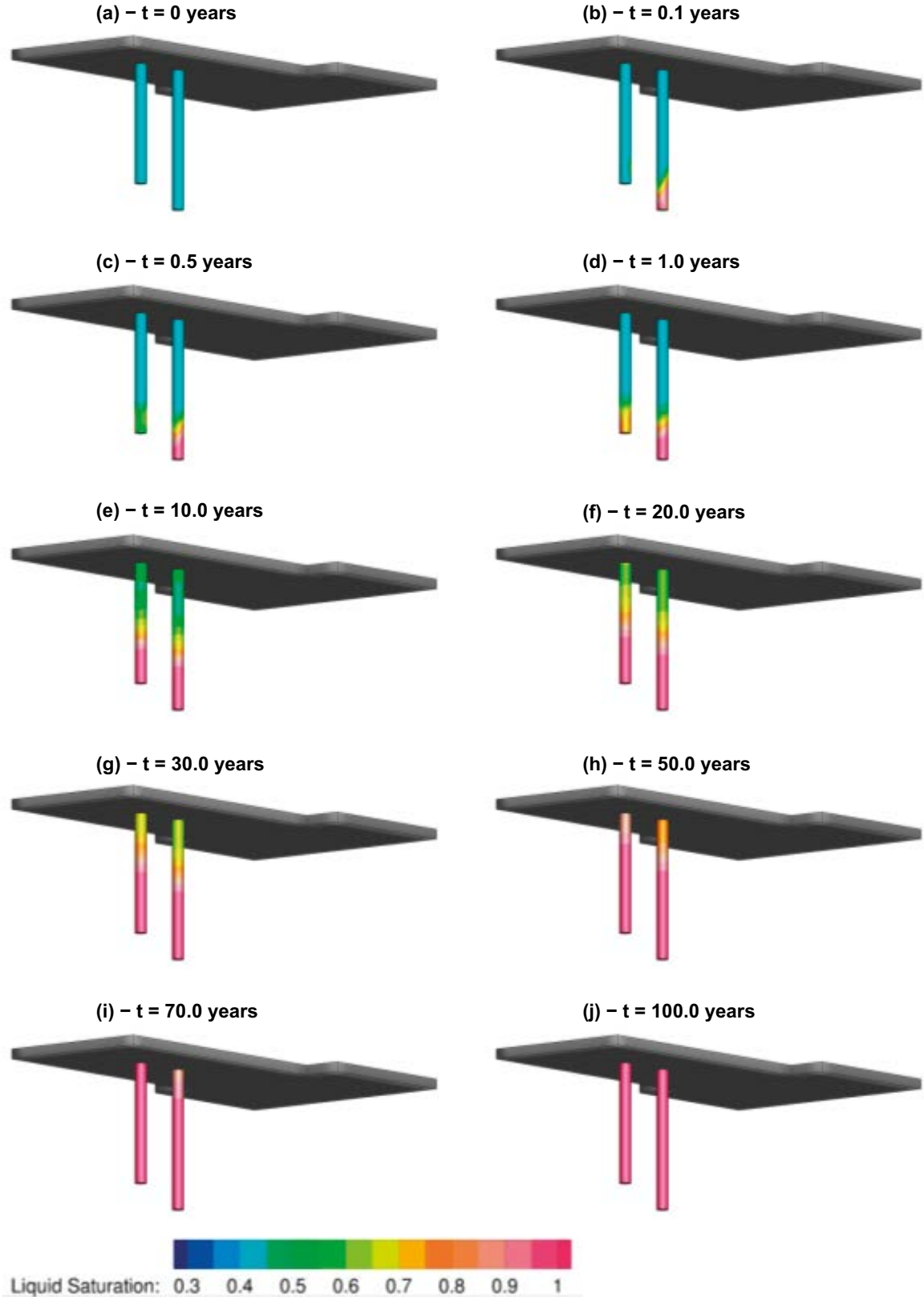

Figure 6-6. *The bentonite saturation calculated for each deposition hole at a number of different times. Results are presented for realisation two of the upscaled stochastic fracture network at times (a) 0.0 years, (b) 0.1 years, (c) 0.5 years, (d) 1.0 years, (e) 10.0 years, (f) 20.0 years, (g) 30.0 years, (h) 50.0 years, (i) 70.0 years, and (j) 100.0 years.*

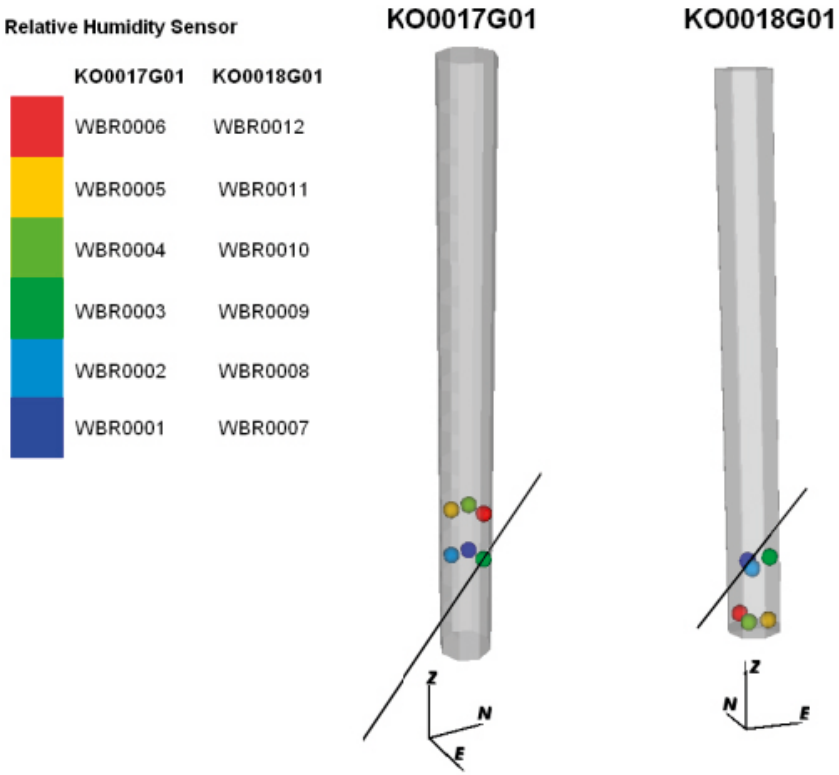

Figure 6-7. *The positions of relative humidity sensors WBR0001 through WBR0012, installed within the bentonite stacks in deposition holes KO0017G01 and KO0018G01. The location and orientation of the groundwater producing fractures intersecting each of the overcored boreholes is also shown.*

Table 6-1. Depths for requested saturation contour plots, reproduced from the task description (Vidstrand et al. 2017).

KO0017G01	KO0018G01[1]
−419.506	−419.579
−419.606	−419.679
−419.809	−419.983
−419.909	
−420.450[2]	

[1] Liquid saturation at an elevation of −420.083 m is requested in KO0018G01 by the task description (Vidstrand et al. 2017). Due to approximations made during meshing the domain, this elevation is beyond the bottom of the bentonite package modelled. No alternative elevation is considered.

[2] Liquid saturation at an elevation of −420.618 m is requested in KO0017G01 by the task description (Vidstrand et al. 2017). Due to approximations made during meshing the domain, this elevation is beyond the bottom of the bentonite package modelled. Therefore, an alternative of elevation of −420.45 m is considered, located towards the bottom of deposition hole KO0017G01.

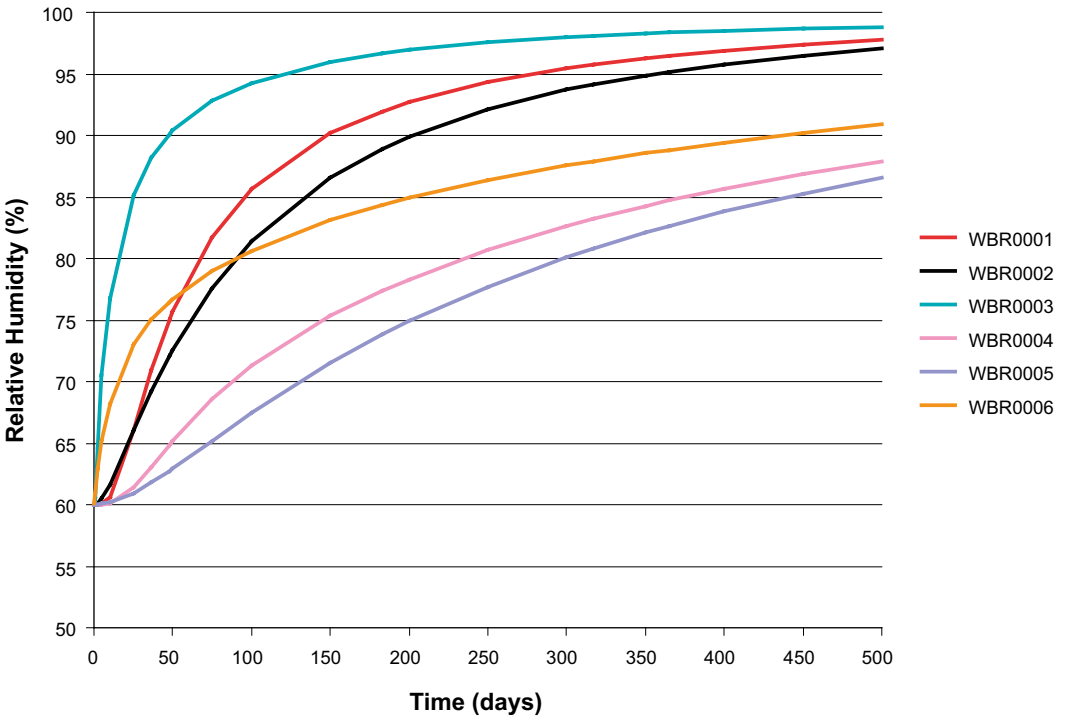

Figure 6-8. *The evolution of relative humidity calculated at sensor locations within the bentonite during the first 500 days post installation. Results are presented for sensors WBR0001 through WBR0006, corresponding to instrumented sections in deposition hole KO0017G01.*

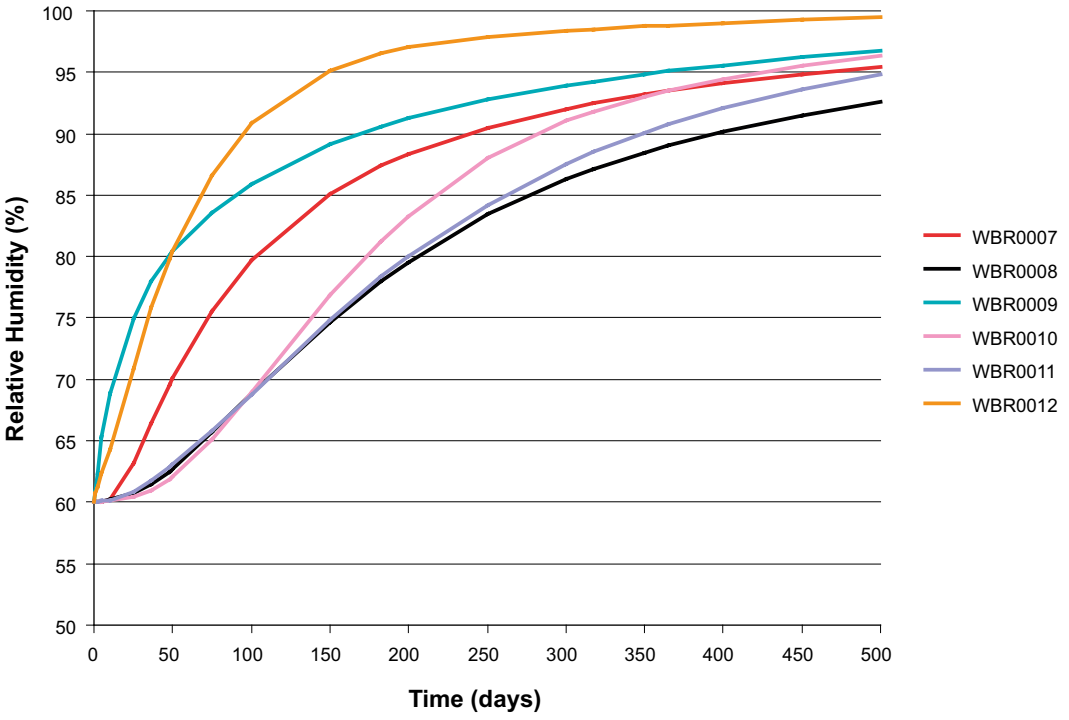

Figure 6-9. *The evolution of relative humidity calculated at sensor locations within the bentonite during the first 500 days post installation. Results are presented for sensors WBR0007 through WBR0012, corresponding to instrumented sections in deposition hole KO0018G01.*

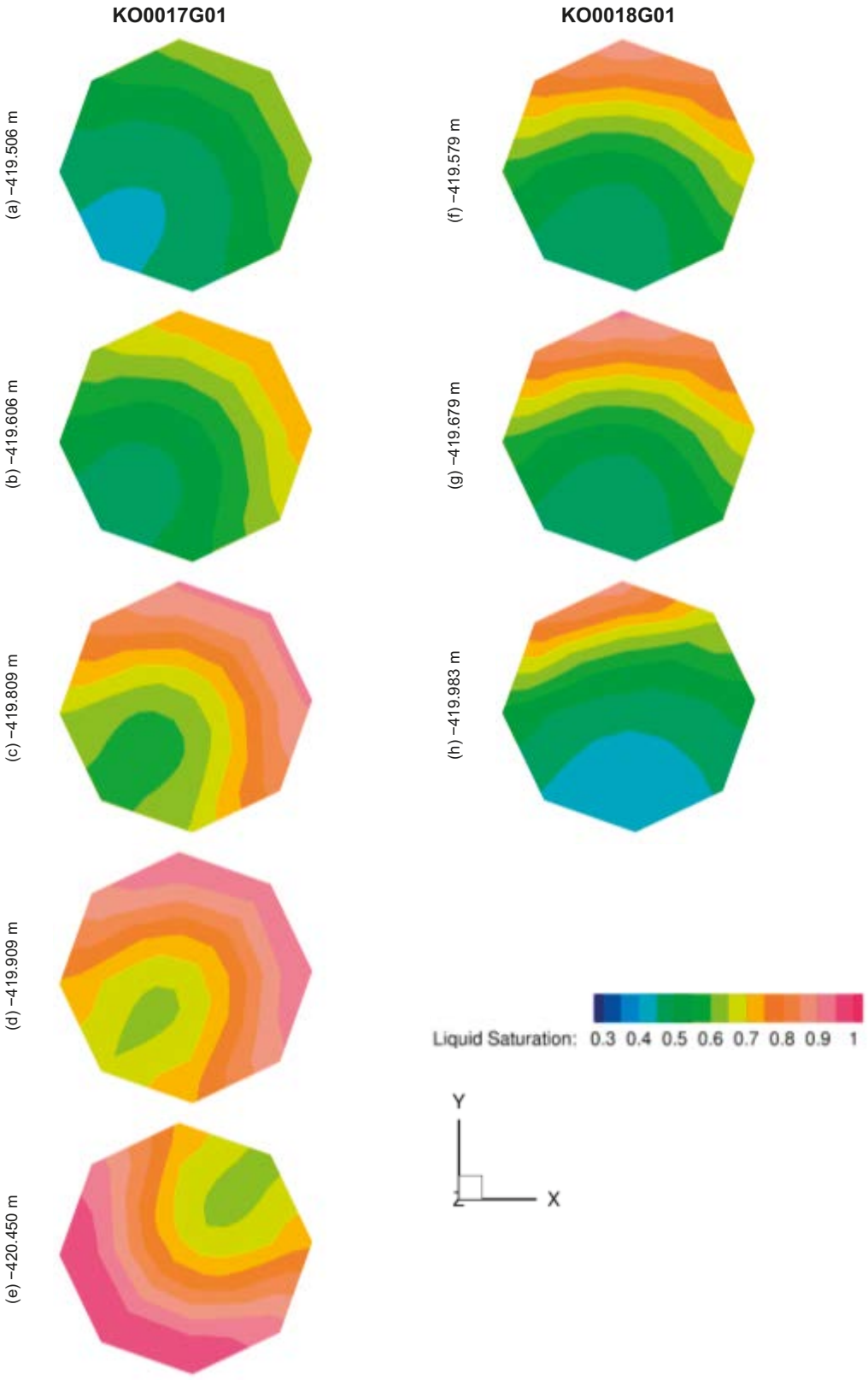

Figure 6-10. *Liquid saturation of the bentonite, contoured over several horizontal slices taken at elevations shown in Table 6-1. Results correspond to 100 days after installation of the bentonite package.*

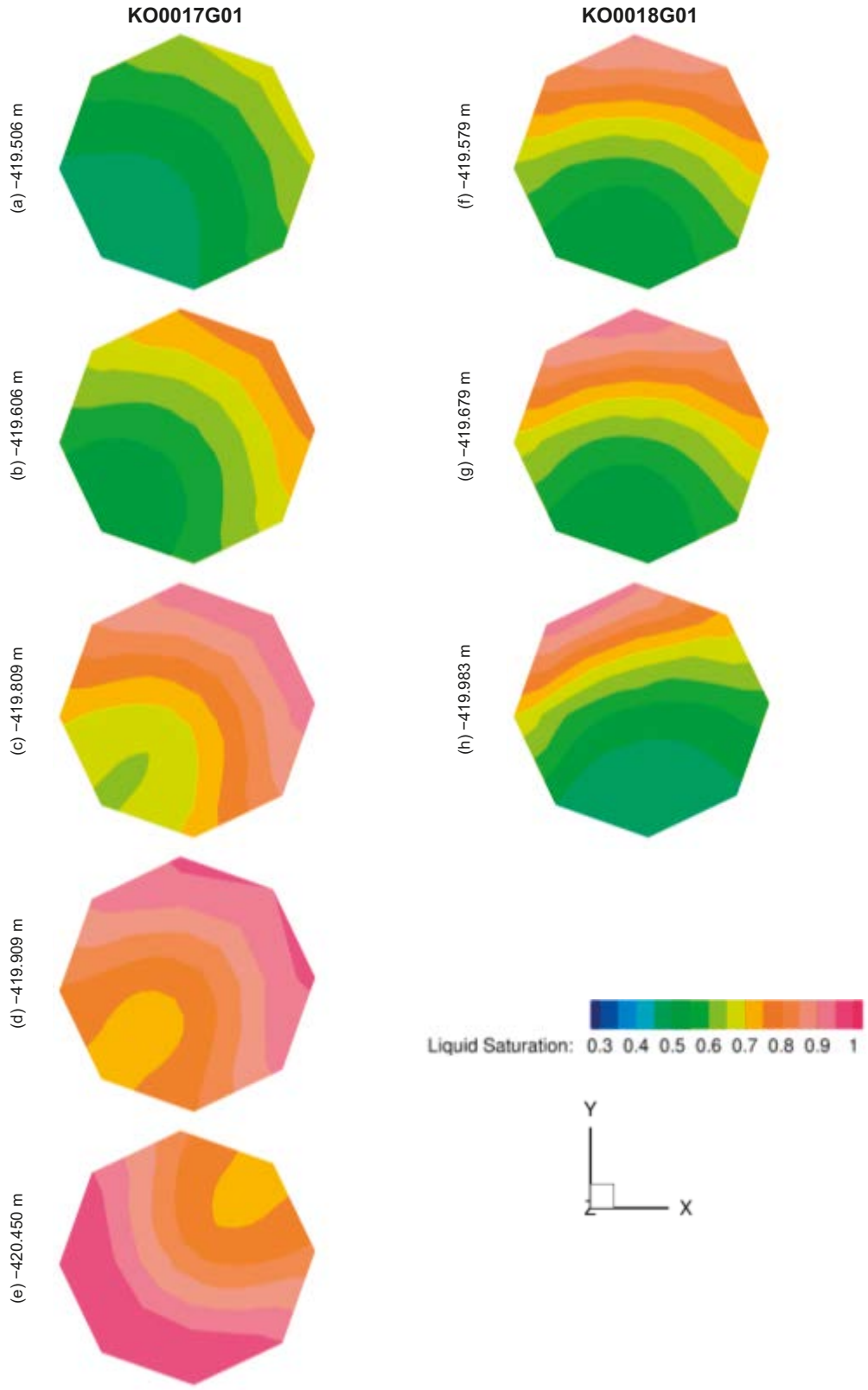

Figure 6-11. *Liquid saturation of the bentonite, contoured over several horizontal slices taken at elevations shown in Table 6-1. Results correspond to 150 days after installation of the bentonite package.*

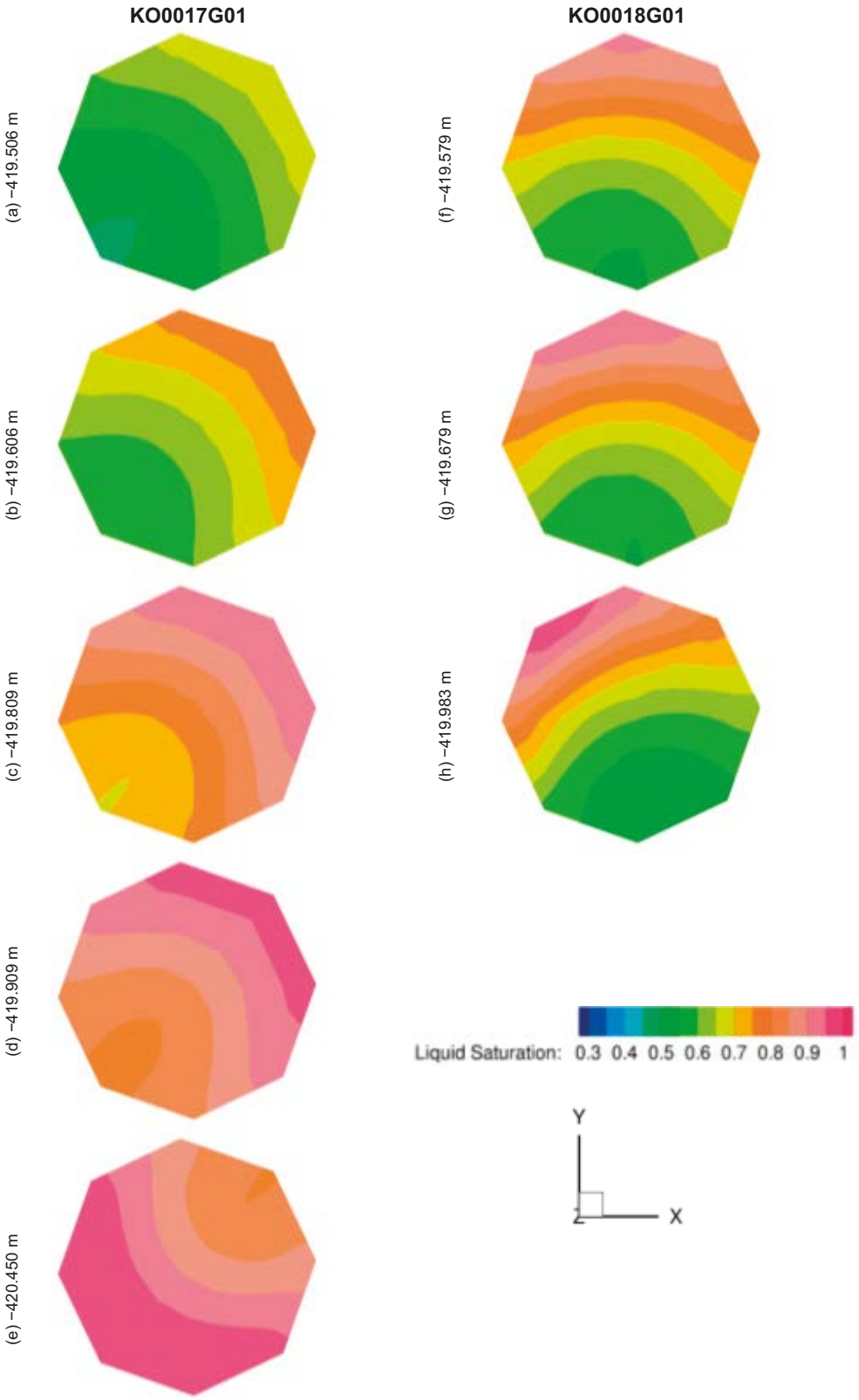

Figure 6-12. *Liquid saturation of the bentonite, contoured over several horizontal slices taken at elevations shown in Table 6-1. Results correspond to 200 days after installation of the bentonite package.*

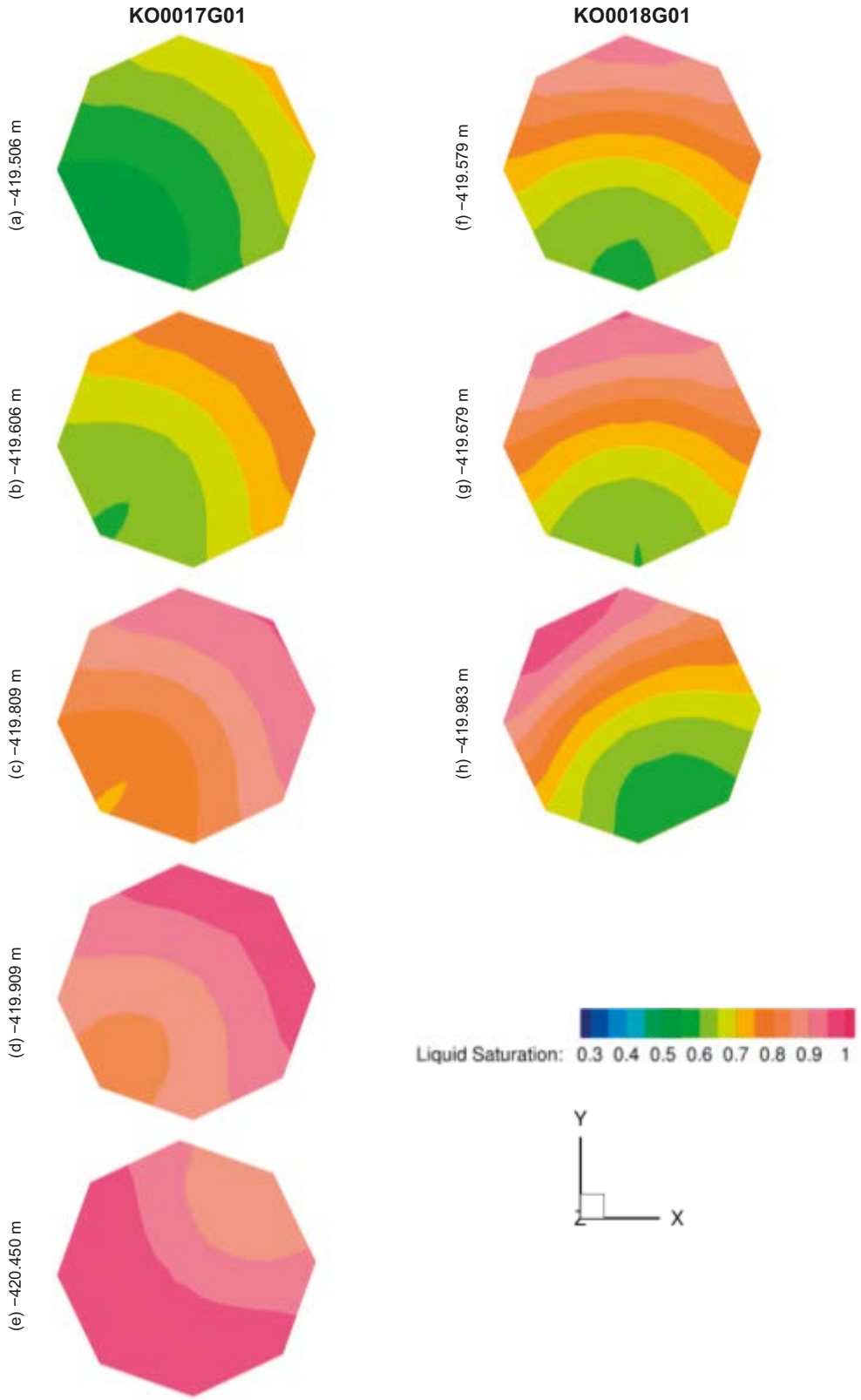

Figure 6-13. *Liquid saturation of the bentonite, contoured over several horizontal slices taken at elevations shown in Table 6-1. Results correspond to 250 days after installation of the bentonite package.*

6.2.2 Resaturation times

The time for the emplaced bentonite within each of the two overcored probe holes to reach 95 % liquid saturation are detailed in Table 6-2; and calculated as the time at which every bentonite element within each of the stacks modelled reaches 95 % liquid saturation. Results are presented for both realisations of the upscaled fracture network considered, corresponding to optimal inflow predictions for overcored boreholes KO0017G01 and KO0018G01 (see Section 5.1). For both bentonite stacks, hydration times are consistent, of the order of decades, and ranging from 60.8 years to over 100 years. For both realisations considered, the resaturation of KO0017G01 takes longer than KO0018G01, despite the larger inflows recorded under open hole conditions. Inflows in both deposition holes are located towards the bottom of the hole, and hydration times are therefore governed by the time required for the resaturation front to extend from the inflow location up to the TASO tunnel. As KO0017G01 is longer than KO0018G01 (3.5 m compared to 3 m) the time required for 95 % resaturation to be reached across the entire bentonite stack is longer.

In contrast, when considering a rock matrix permeability of 3.8×10^{-20} m^2 (taken from the task description (Vidstrand et al. 2017) and corresponding to unstressed core samples), the time taken to reach 95 % liquid saturation is significantly faster. For realisation 2 of the stochastic fracture network, KO0017G01 is found to resaturate to this level within 8.5 years, with KO0018G01 taking 6.1 years. This is approximately an order of magnitude faster than predicted from calculations using a rock matrix permeability of 1×10^{-21} m^2, and similar to results obtained for Task 8C (Baxter et al. 2013), which also considered variants of the rock matrix permeability (1×10^{-20} m^2).

Table 6-3 compares resaturation predictions to both of the deposition holes with results from the previous Task 8C analysis (Baxter et al. 2013). The rock matrix is parameterised identically in both cases, taking a value of 1×10^{-21} m^2, with differences confined to calibration and conditioning of the fracture network. The resaturation rate of emplaced bentonite is consistently slower for Task 8D compared to Task 8C model cases, a consequence of changes made to the fracture network prescription. Specifically, the conditioning of fracture intersections with overcored boreholes KO0017G01 and KO0018G01, yielding a single fracture with low transmissivity towards the bottom of both deposition holes has a major effect. Resaturation rates are constrained as much by the distribution of inflows as the total inflow to a deposition hole; especially when the groundwater supply through the rock matrix is limited. Consequently, resaturation times are significantly longer than found for Task 8C, where most realisations included multiple fracture intersections with each deposition hole, distributed randomly across the entire deposition hole.

Table 6-2. Times for bentonite emplaced within the two overcored boreholes to achieve 95 % saturation. Results are presented for both realisations of upscaled stochastic fracture network considered.

Realisation	KO0017G01	KO0018G01
2	79.3 years	60.8 years
7	100.0[1] years	72.9 years

[1] 95 % liquid saturation is not obtained over the entire bentonite installation within the 100 year simulation duration.

Table 6-3. Times for bentonite emplaced within the two overcored boreholes to achieve 95 % saturation. Results are presented for the minimum, maximum and average durations calculated for both Task 8C (5 realisations) and Task 8D (2 realisations).

Result	Task 8C		Task 8D	
	KO0017G01	KO0018G01	KO0017G01	KO0018G01
Minimum	4.6 years	5.9 years	79.3 years	60.8 years
Average	20.2 years	20.5 years	89.7[1] years	66.9 years
Maximum	36.6 years	62.3 years	100.0[1] years	72.9 years

[1] 95 % liquid saturation is not obtained over the entire bentonite installation within the 100 year simulation duration. As such, the average resaturation is also not an accurate representation of the two realisations.

6.2.3 Pressures in the deposition hole near field

Contour plots of liquid pressures in the deposition hole near field are shown in Figure 6-14 and Figure 6-15 for two separate slices through the second realisation of the upscaled fracture network model. These correspond to

- a vertical cross-section incorporating both deposition holes, and oriented parallel with the TASO tunnel central line, as shown in Figure 6-14 at 0, 0.1, 0.5, 1, 10, and 100 years,
- a horizontal cross-section positioned at an elevation of −418.5 m, and cutting through both deposition holes, as shown in Figure 6-15 at 0, 0.1, 0.5, 1, 10, and 100 years.

Within the bentonite, liquid pressures evolve from initial values of c. −70 MPa to c. 1 MPa at full saturation. The location and orientation of fracture intersections with each of the deposition holes is also clearly visible from the pressure evolution. Negative liquid pressures are also observed in the rock matrix local to the bentonite stacks.

Equivalent contour plots of liquid pressures for each of these slices are presented in Figure A2-7 and Figure A2-8 for realisation 7 of the fracture network.

6.2.4 Saturations in the deposition hole near field

Contour plots of liquid saturation in the deposition hole near field are shown in Figure 6-16 and Figure 6-17 for two separate slices through the second realisation of the upscaled fracture network model:

- Liquid saturation on a vertical cross-section, corresponding to Figure 6-14 and incorporating both deposition holes is shown inFigure 6-16 at 0, 0.1, 0.5, 1, 10, and 100 years.
- Liquid saturation on a horizontal cross-section, corresponding to Figure 6-15, and cutting through both deposition holes at −418.5 m is shown in Figure 6-17 at 0, 0.1, 0.5, 1, 10, and 100 years.

The initial saturation of the bentonite is 41.3 % as specified by the task description (Vidstrand et al. 2017). As for the evolution of liquid pressure shown in Figure 6-14 and Figure 6-15, the orientation of the intersecting fractures with the deposition holes can clearly be observed. The rock matrix also undergoes desaturation, extending a few centimetres from the bentonite stack after one year. The extent of desaturation in the rock matrix calculated for the Task 8D models is significantly reduced compared to results from the Task 8C analysis (Baxter et al. 2013), which observed desaturation effects 10's of centimetres from the deposition hole wall. It is expected that these differences are a consequence of the changes made to the constitutive relationships for the rock matrix (see Section 3.2.5). A model variant considering the Task 8C constitutive relationships is presented in Section 6.3.

Equivalent contour plots of liquid saturation for each of these slices are presented in Figure A2-9 and Figure A2-10 for realisation 7 of the fracture network.

6.2.5 Pressure evolution within the bentonite

Liquid pressures within the bentonite are extracted from the model at 24 separate locations in each of the deposition holes KO0017G01 and KO0018G01. A schematic of these locations, and the nomenclature used is shown in Figure 6-18. Corresponding figures for the evolution of liquid pressure at each of these locations is presented in Figure 6-19 and Figure 6-20, corresponding to each of the overcored probe boreholes considered. Results in this section are presented for the second realisation of the upscaled stochastic fracture network.

In both deposition holes, resaturation is dominated by the fracture intersections, providing groundwater towards the bottom of each deposition hole. Consequently, the liquid saturation within the bentonite (and therefore the liquid pressure) increase most rapidly towards the bottom of the deposition holes. Resaturation towards the top of the deposition holes is dominated by groundwater entering the bottom of the bentonite stack migrating towards the TASO tunnel, with limited contribution from the rock matrix.

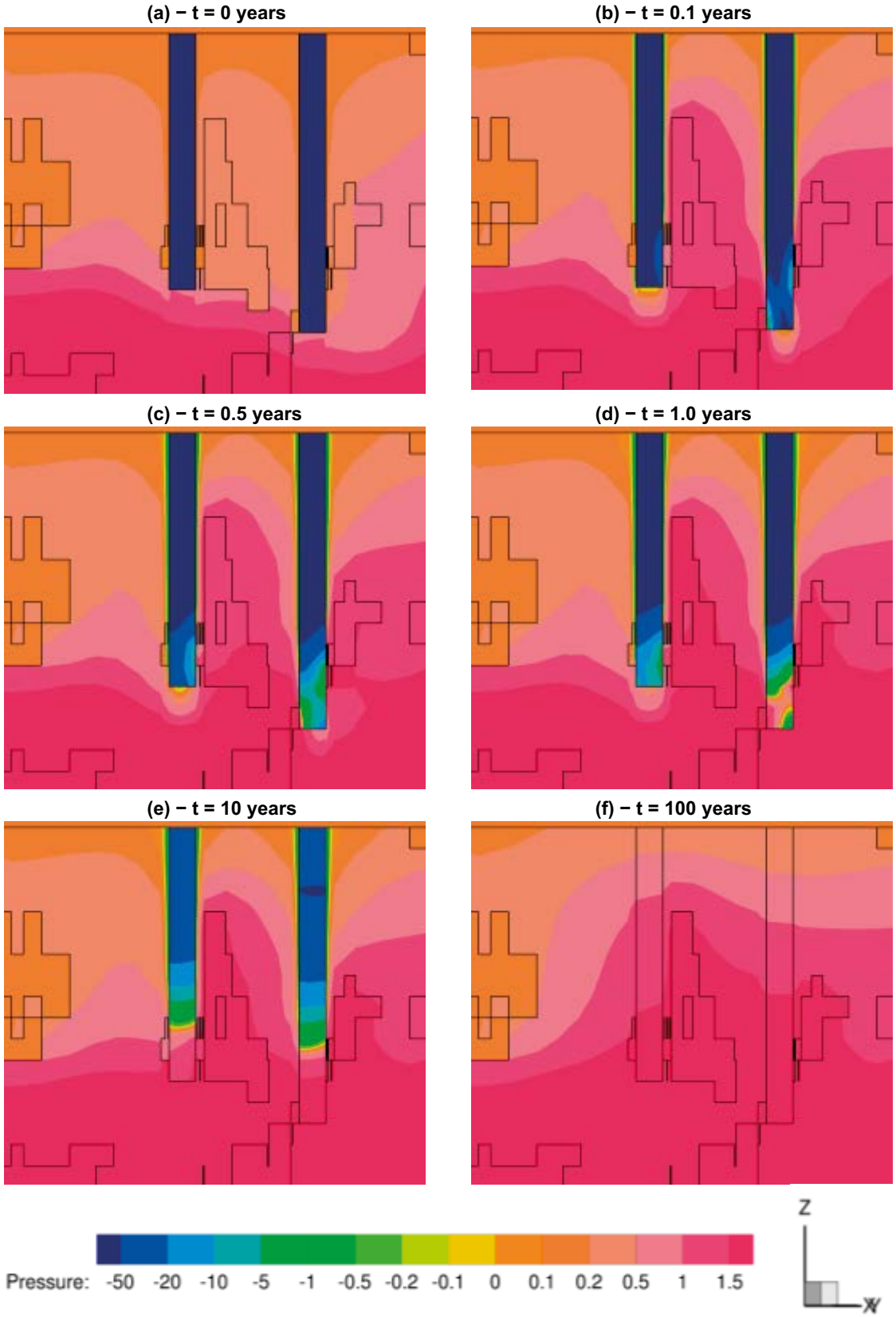

Figure 6-14. *Evolution of liquid pressure (MPa) within the bentonite for a vertical slice, oriented to include the two overcored boreholes KO0017G01 and KO0018G01. Results are shown for the second realisation of the upscaled stochastic fracture network.*

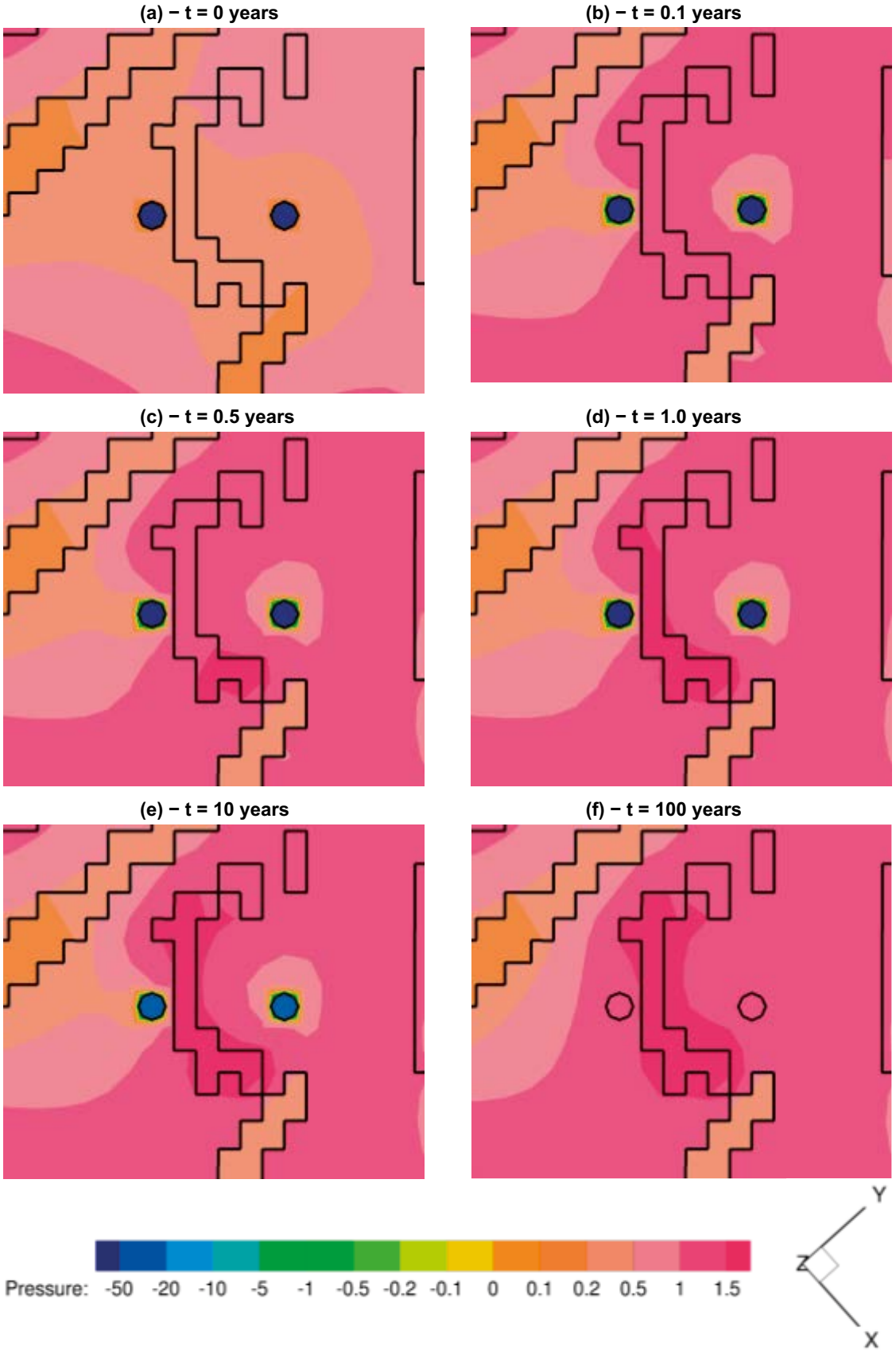

Figure 6-15. *Evolution of liquid pressure (MPa) within the bentonite across a horizontal slice, taken 1.5 m below the TASO tunnel at an elevation of −418.5 m. Results are shown for the second realisation of the upscaled stochastic fracture network.*

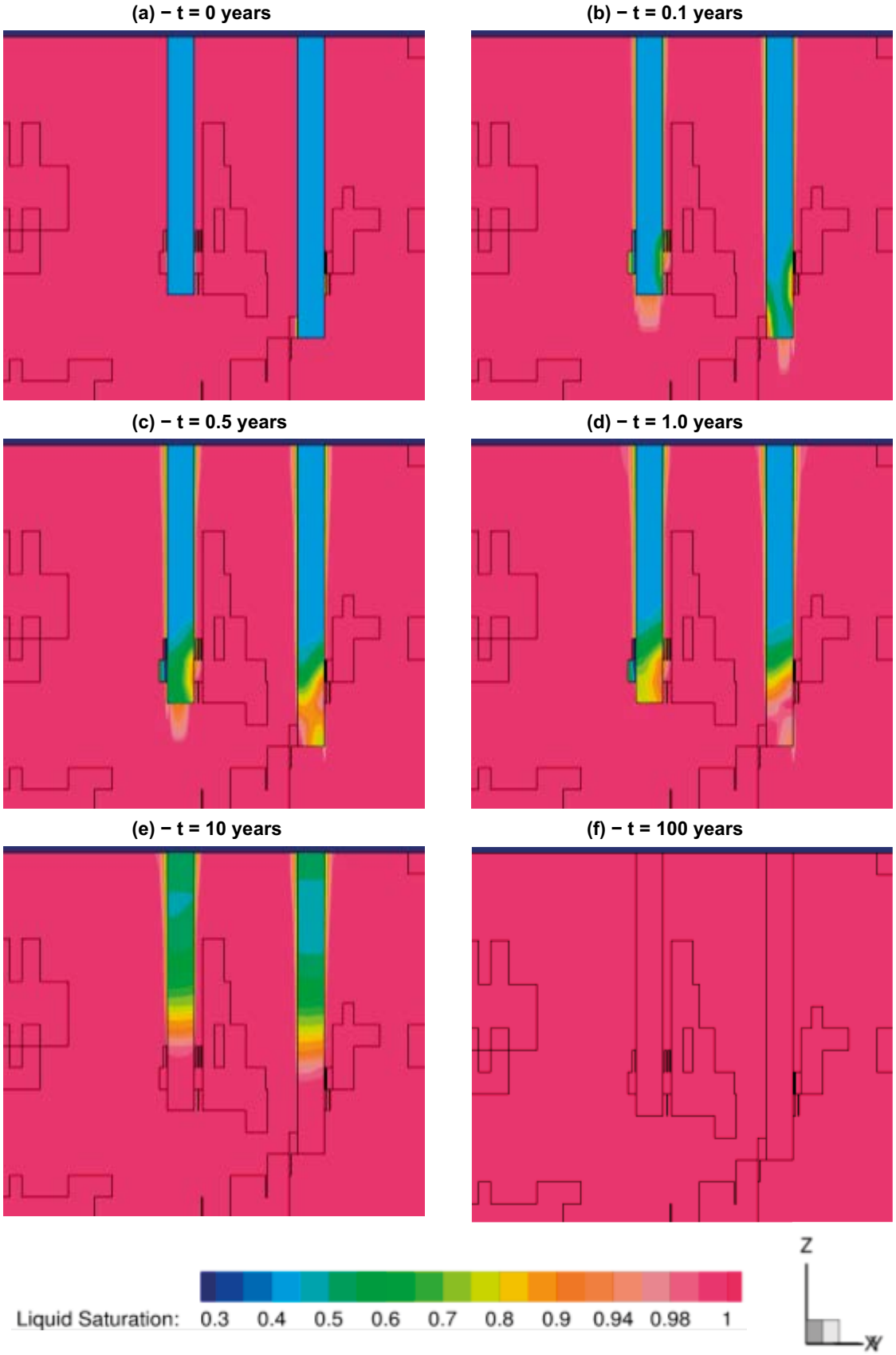

Figure 6-16. *Evolution of liquid saturation within the bentonite for a vertical slice oriented to include the two overcored boreholes KO0017G01 and KO0018G01. Results are shown for the second realisation of the stochastic fracture network.*

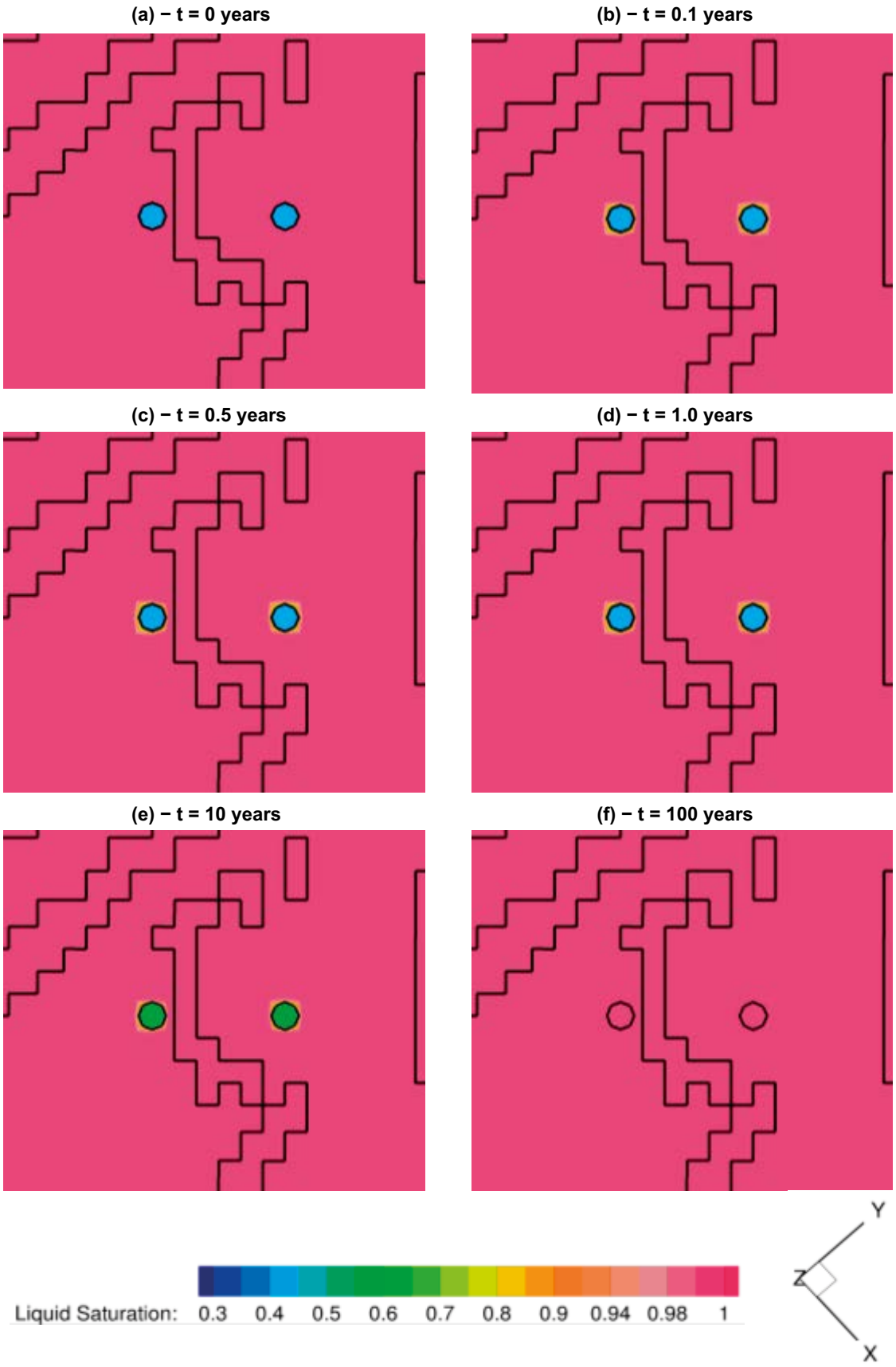

Figure 6-17. *Evolution of liquid saturation within the bentonite across a horizontal slice, taken 1.5 m below the TASO tunnel at an elevation of −418.5 m. Results are shown for the second realisation of the stochastic fracture network.*

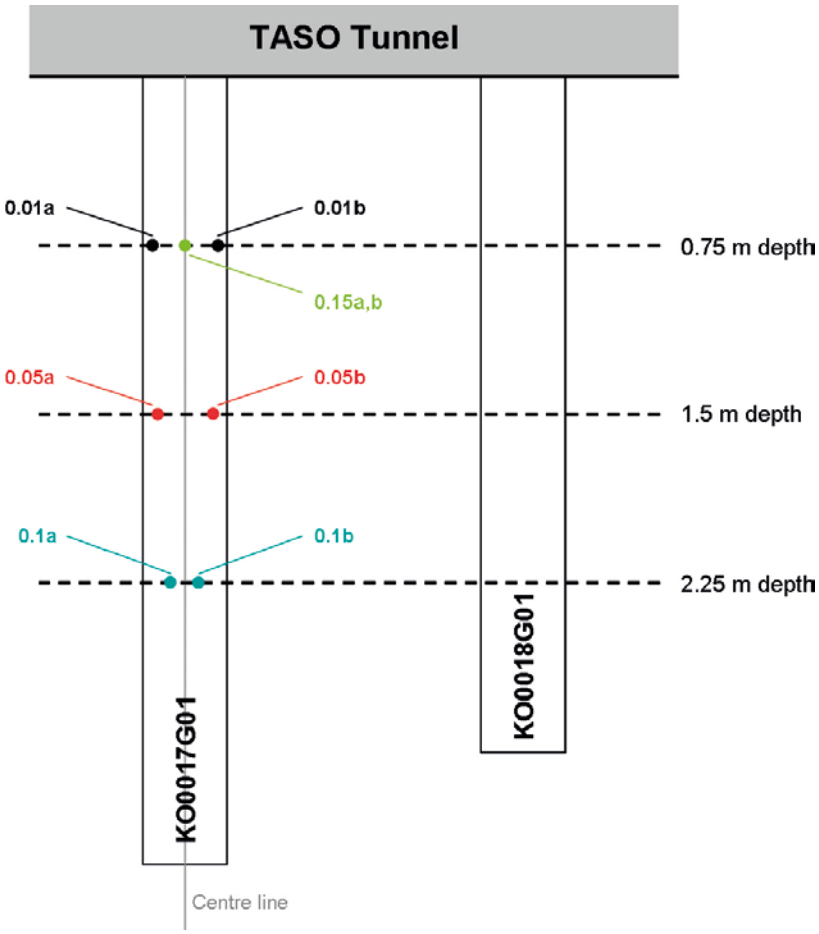

Figure 6-18. *Schematic illustrating monitored points within the bentonite, 0.01 m, 0.05 m, 0.1 m, and 0.15 m from the deposition borehole wall. All points are evaluated at all depths for the two deposition holes considered. Pressure evolutions within the bentonite at these locations are shown in Figure 6-19 through Figure 6-20.*

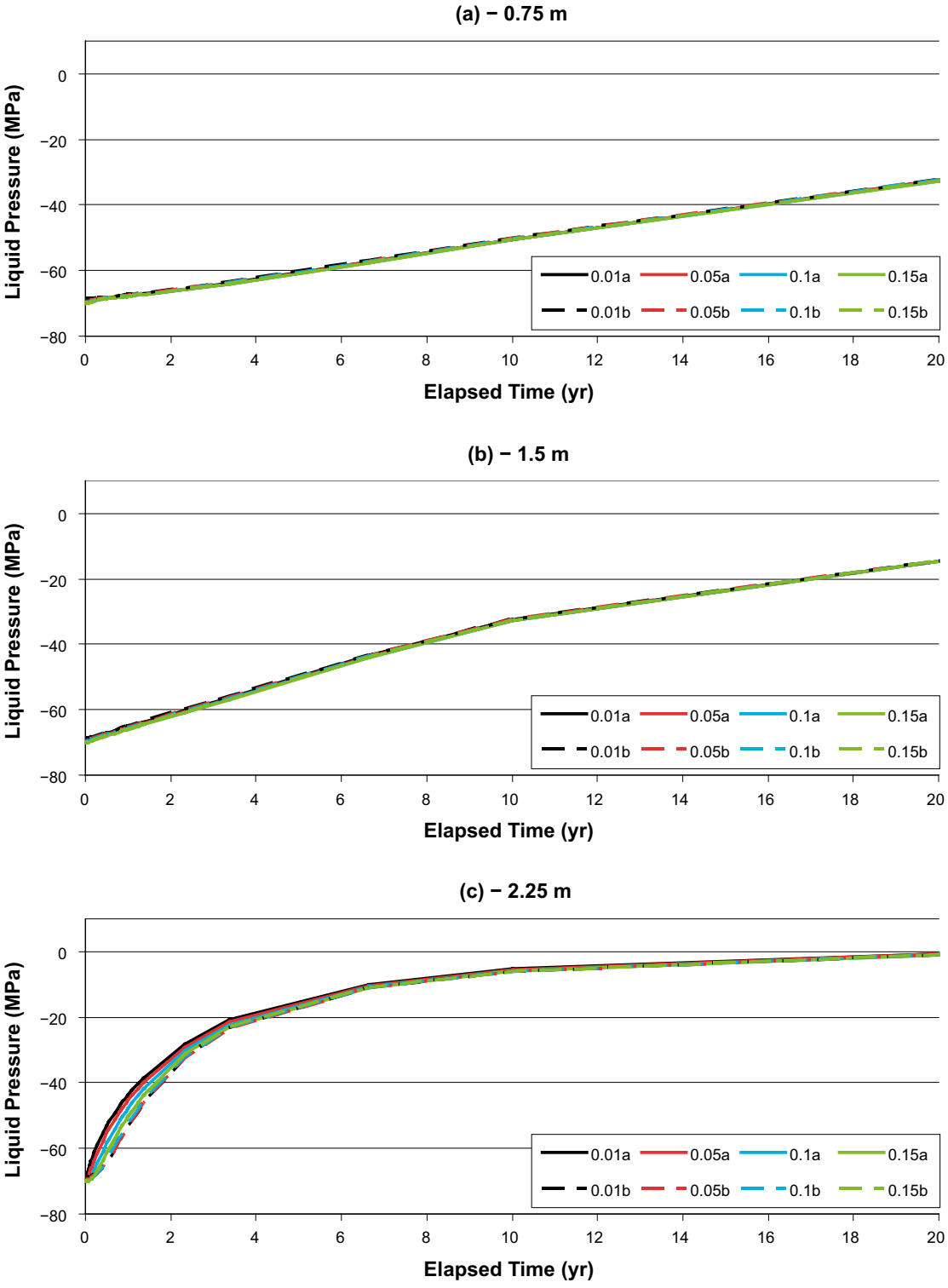

Figure 6-19. *Liquid pressure (MPa) calculated within the bentonite 0.01 m, 0.05 m, 0.1 m, and 0.15 m from the deposition borehole wall. Results are shown for a slice oriented to intersect both the boreholes, with "a" and "b" distances denoting direction from the edge of the deposition hole. The pressure curves shown correspond to the second realisation of the upscaled stochastic fracture network. Figures (a, b, c) are for borehole KO0017G01 at depths of 0.75 m, 1.5 m and 2.25 m respectively.*

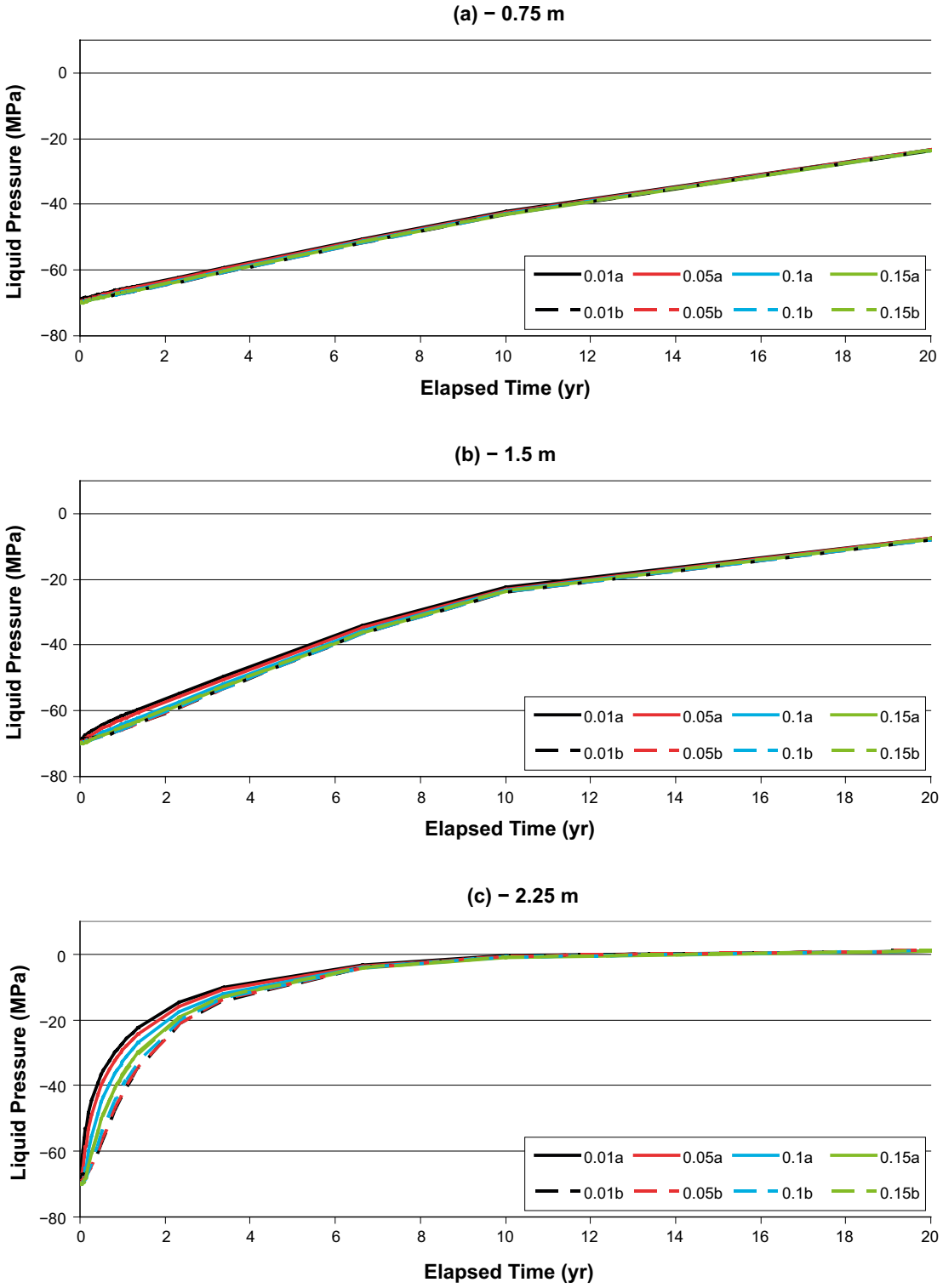

Figure 6-20. *Liquid pressure (MPa) calculated within the bentonite 0.01 m, 0.05 m, 0.1 m, and 0.15 m from the deposition borehole wall. Results are shown for a slice oriented to intersect both the boreholes, with "a" and "b" distances denoting direction from the edge of the deposition hole. The pressure curves shown correspond to the second realisation of the upscaled stochastic fracture network. Figures (a, b, c) are for borehole KO0018G01 at depths of 0.75 m, 1.5 m and 2.25 m respectively.*

6.2.6 Pressure evolution within the bedrock

Liquid pressures within the fractured bedrock are extracted from the model at 27 separate locations local to deposition holes KO0017G01 and KO0018G01. A schematic of these locations, and the nomenclature used is shown in Figure 6-21. Corresponding figures for the evolution of liquid pressure at each of these locations is presented in Figure 6-22 and Figure 6-23 corresponding to the host rock local to each of the overcored probe boreholes considered. Results in this section are presented for the second realisation of the upscaled stochastic fracture network.

Desaturation of the rock local to the emplaced bentonite results in negative liquid pressures down to −2 MPa. Desaturation is greatest closest to the bentonite as expected. Liquid pressures are slow to return to *in situ* pressures, with negative pressures still prevalent 0.01 m from the bentonite after 50 years.

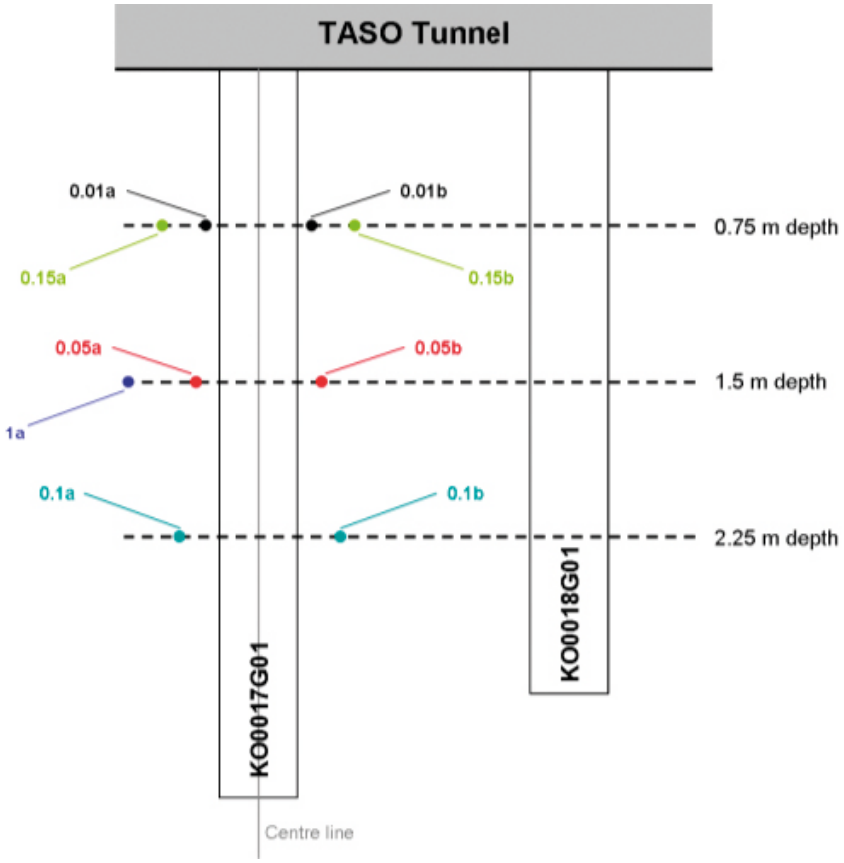

Figure 6-21. *Schematic illustrating monitored points within the bedrock, for pressure evolutions shown in Figure 6-22 through Figure 6-23*

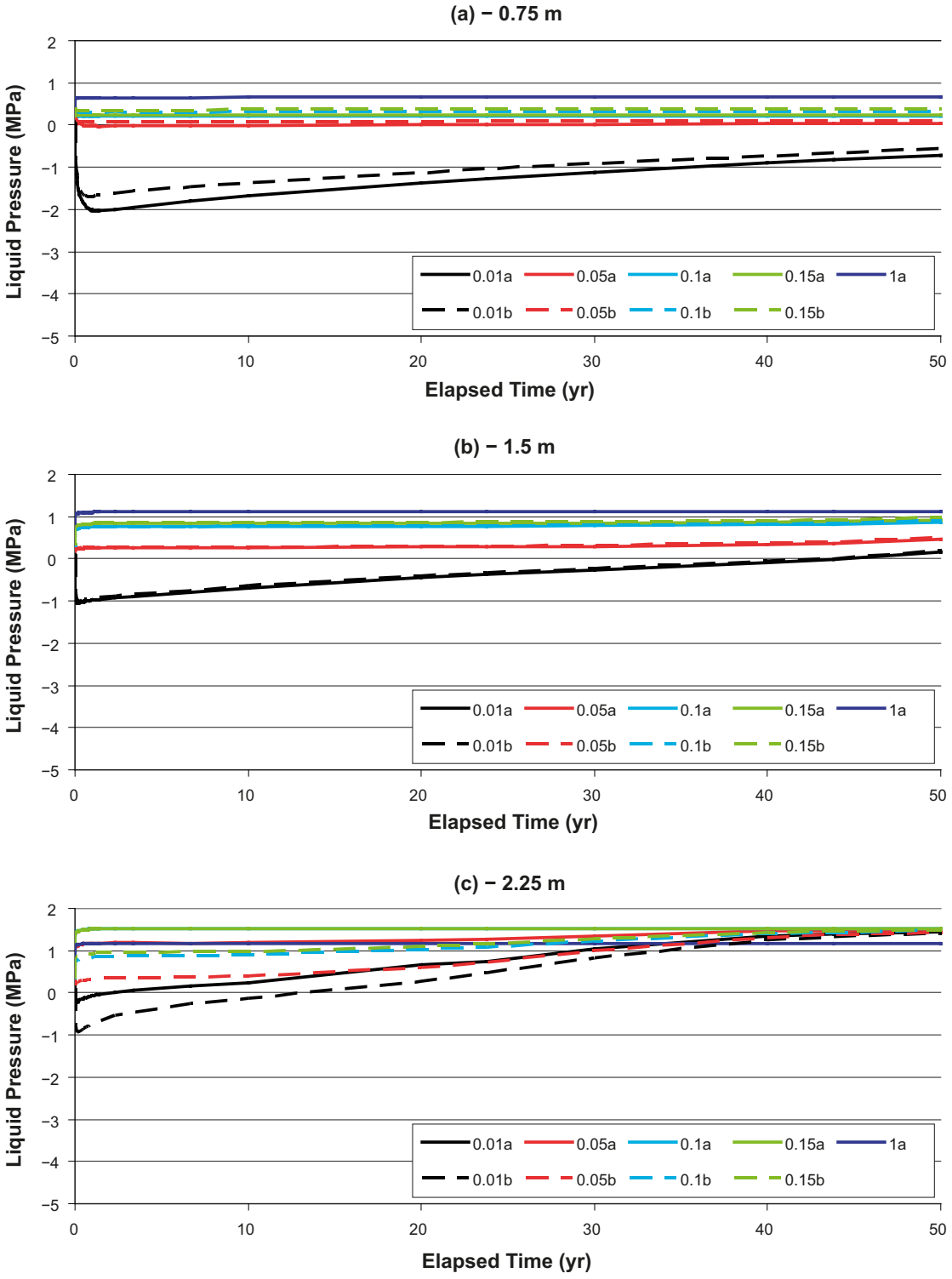

Figure 6-22. *Liquid pressure (MPa) calculated within the bedrock 0.01 m, 0.05 m, 0.1 m, 0.15 m, and 1.0 m from the deposition borehole wall. Results are shown for a slice oriented to intersect the two over-cored boreholes, with "a" and "b" distances denoting direction from the edge of the deposition hole. The pressure curves shown correspond to the second realisation of the stochastic fracture network. Figures (a, b, c) are for borehole KO0017G01 at depths of 0.75 m, 1.5 m and 2.25 m respectively.*

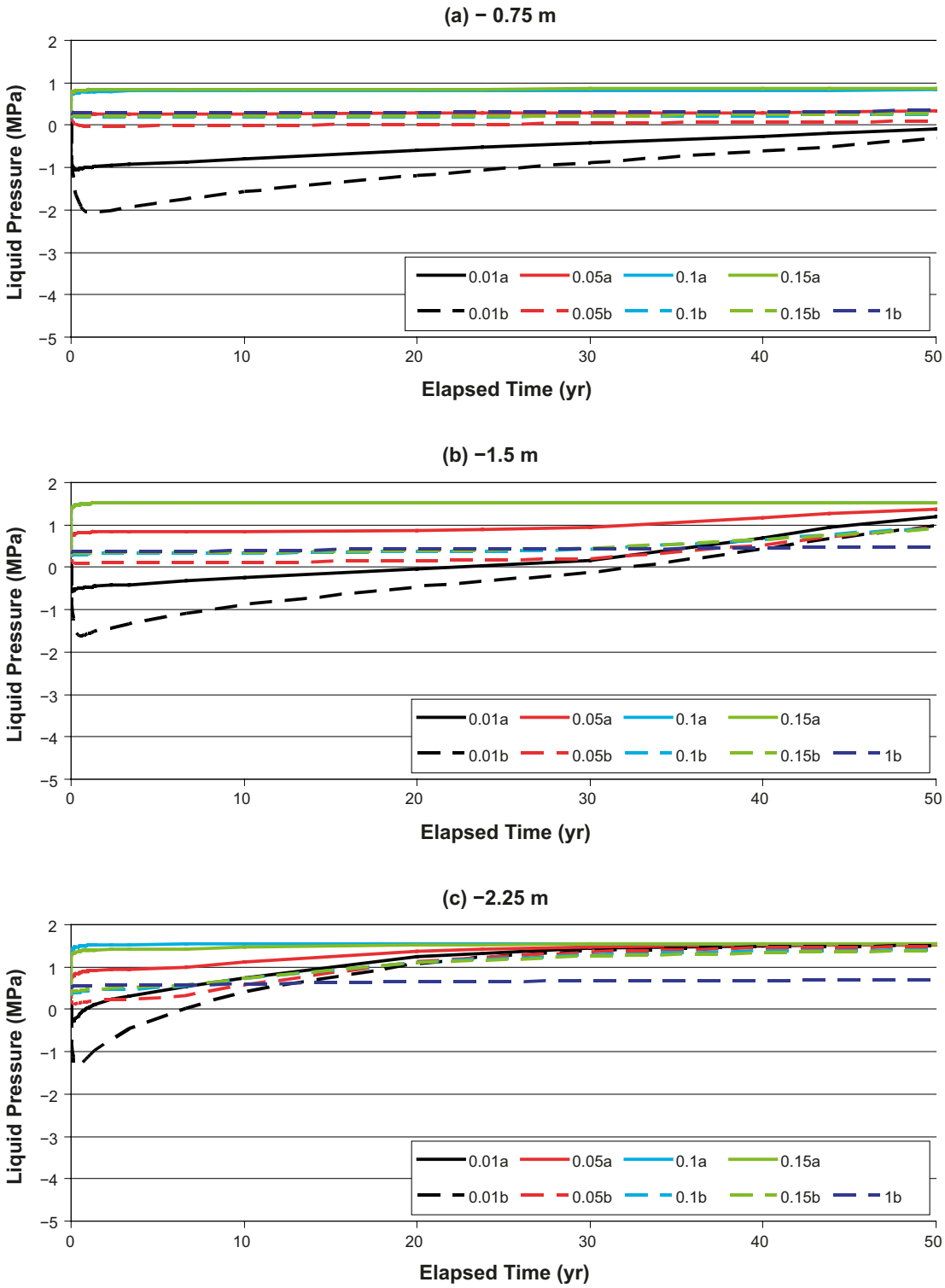

Figure 6-23. *Liquid pressure (MPa) calculated within the bedrock 0.01 m, 0.05 m, 0.1 m, 0.15 m, and 1.0 m from the deposition borehole wall. Results are shown for a slice oriented to intersect the two over-cored boreholes, with "a" and "b" distances denoting direction from the edge of the deposition hole. The pressure curves shown correspond to the second realisation of the stochastic fracture network. Figures (a, b, c) are for borehole KO0018G01 at depths of 0.75 m, 1.5 m and 2.25 m respectively.*

6.3 Effects of varying parameterisation of the rock matrix

6.3.1 Rock matrix constitutive relationships

In the previous section, results for liquid pressure and saturation within the host rock local to the deposition holes are presented (see Figure 6-14 through Figure 6-17). The extent of desaturation of the rock matrix is of the order centimetres from the deposition hole wall, significantly reduced when compared to the Task 8C results which saw dehydration 10s of centimetres into the rock. As detailed in Section 3.2 of this report, the constitutive relations for the rock matrix have been updated for Task 8D, using measurements taken from the granite local to the emplaced bentonite. However, as noted by the task description (Vidstrand et al. 2017), these measurements used to fit the constitutive relationships are taken at low saturations, which may not be applicable to the saturation state of the rock local to the deposition holes. It is expected that this change in constitutive relationships of the rock matrix is limiting the dehydration of the rock matrix local to the bentonite.

In this section a model variant is considered, using the rock matrix constitutive relations used in Task 8C for realisation 2 of the stochastic fracture network. For both Task 8C and Task 8D, van Genuchten functions are used to represent the relative permeability and capillary pressure of the rock matrix (see Equation (3-7) and Equation (3-10)). Whereas van Genuchten parameters λ and P_0 were prescribed as 0.24 and 0.6 MPa in Task 8D, for Task 8C values of 0.6 and 1.74 MPa were used.

Figure 6-24 depicts the initial liquid saturation on the outer surface of the bentonite stack along with nine subsequent times up to 100 years. For comparison, liquid saturations for the same realisation of the fracture network, but using the Task 8D rock matrix constitutive relations are shown in Figure 6-6. To reach 95 % liquid saturation, both KO0017G01 and KO0018G01 take 44.3 years, significantly faster than calculated using the Task 8D constitutive relations (79.3 years and 60.8 years respectively). This is because the Task 8C prescription of the rock matrix increases the volume of rock matrix local to the bentonite that undergoes desaturation – providing additional groundwater for hydrating the bentonite. This effect is illustrated in the following figures:

- Contour plots of liquid pressures on two slices taken through the model in the deposition hole near field are shown in Figure 6-25 and Figure 6-26. Figure 6-25 corresponds to a vertical slices, passing through the centre of both deposition holes, and Figure 6-26 is a horizontal slice taken at 1.5 m below the TASO tunnel floor (at an elevation of −418.5 m). Equivalent slices are shown in Figure 6-14 and Figure 6-15 for the same realisation of the fracture network, but using the Task 8D rock matrix constitutive relations. The orientation of the intersecting fractures with the deposition holes is clearly observable through the liquid pressure contours. In addition, the extent of negative liquid pressures within the rock matrix is much greater than calculated using the updated Task 8D constitutive relations (see Figure 6-14 and Figure 6-15)
- Contour plots of liquid saturation on two slices taken through the model in the deposition hole near field are shown in Figure 6-27 and Figure 6-28. Slices correspond to those shown above for the liquid pressures, with Figure 6-27 vertical and oriented along the centre of the TASO tunnel, and Figure 6-28 horizontal, 1.5 m below the tunnel floor. Equivalent slices are shown in Figure 6-16 and Figure 6-17 for the same realisation of the fracture network, but using the Task 8D rock matrix constitutive relations. As for the contours of liquid pressure, the orientation of hydraulically active fractures intersecting KO0017G01 and KO0018G01 are clearly observable. The rock matrix is also desaturated to a much greater extent (c. 10's of centimetres) than calculated using the updated Task 8D constitutive relations.
- Liquid pressures within the fractured bedrock are extracted from the model at 27 separate locations local to the deposition holes, as detailed in Figure 6-21. The evolution of liquid pressure at each of these locations is presented in Figure 6-29 and Figure 6-30, corresponding to the host rock local to KO0017G01 and KO0018G01 respectively. Equivalent pressure evolutions are shown in Figure 6-22 and Figure 6-23 for the same realisation of the fracture network, but using the Task 8D rock matrix constitutive relations. Desaturation of the rock surrounding the deposition holes cause negative liquid pressures to form. The use of Task 8D constitutive relations for the rock matrix reduces this effect compared to modelling results when applying the Task 8C parameterisation.

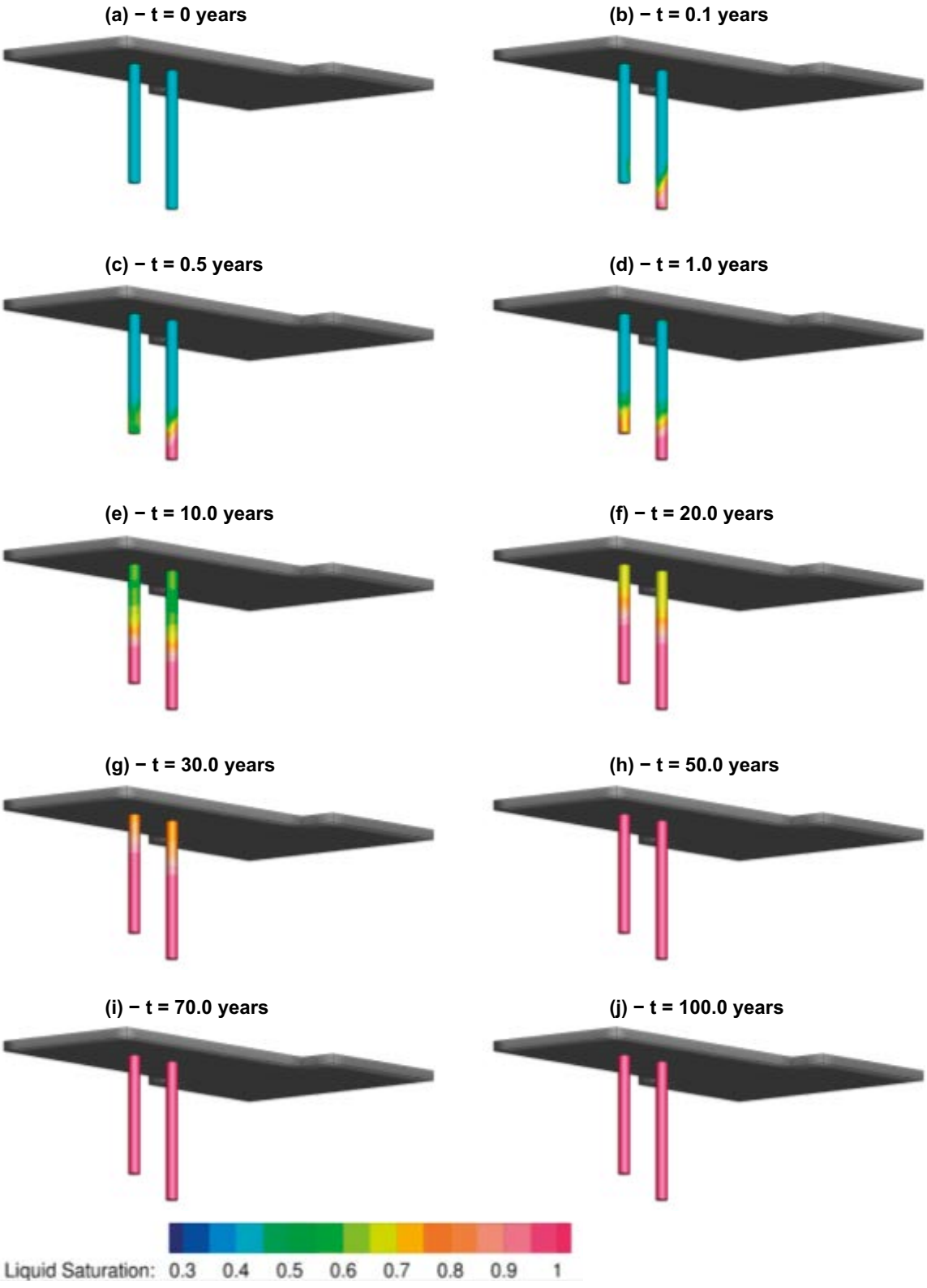

Figure 6-24. *The bentonite saturation calculated for each deposition hole at a number of different times. Results are presented for realisation two of the upscaled stochastic fracture network, using the rock matrix constitutive relations from Task 8C. Results are comparable to Figure 6-6, calculated from the same realisation of the DFN, but with the updated Task 8D constitutive relations for the rock matrix.*

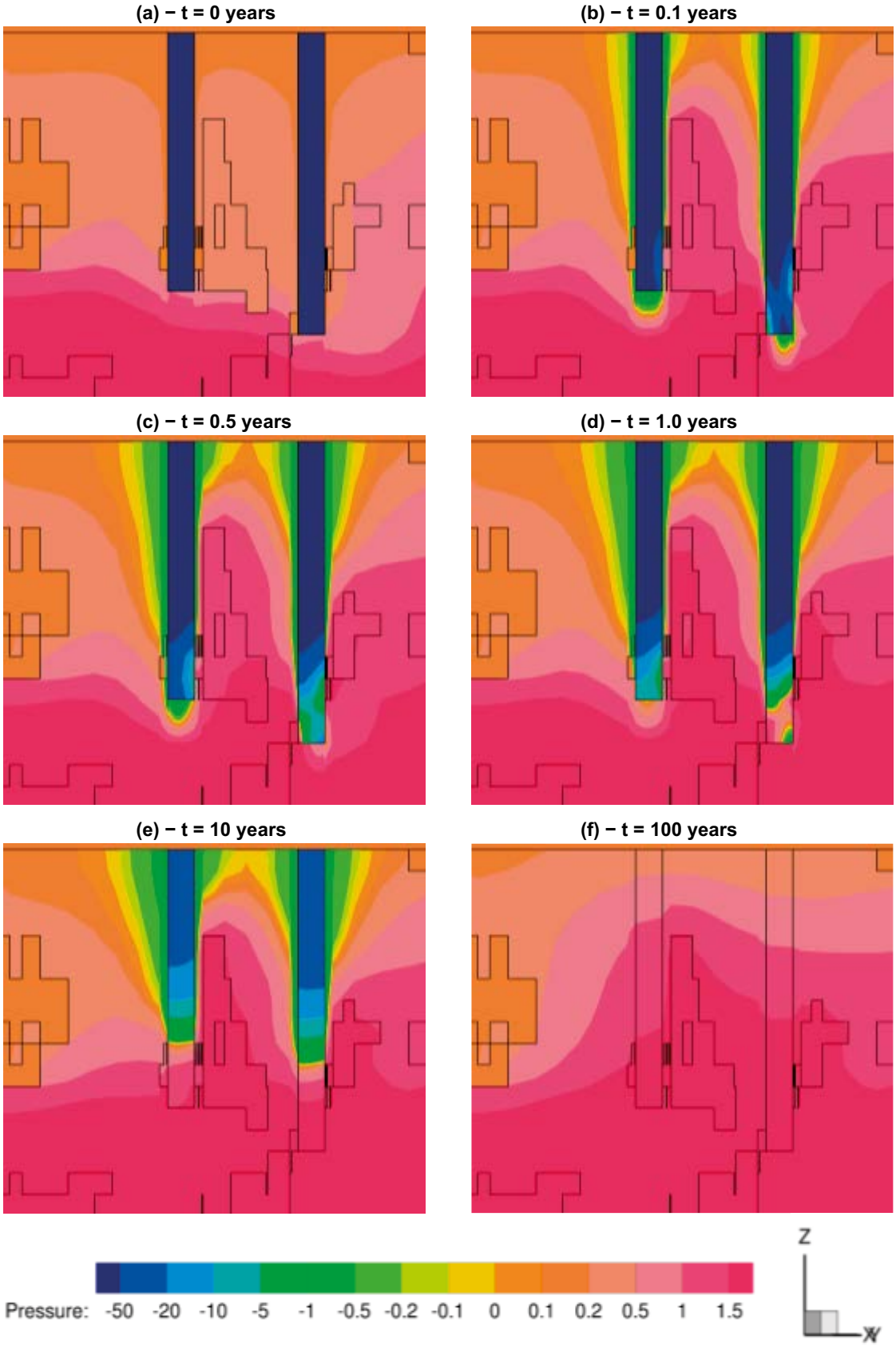

Figure 6-25. *Evolution of liquid pressure (MPa) within the bentonite for a vertical slice, oriented to include the two overcored boreholes KO0017G01 and KO0018G01. Results are shown for the second realisation of the upscaled stochastic fracture network using Task 8C constitutive relations for the rock matrix.*

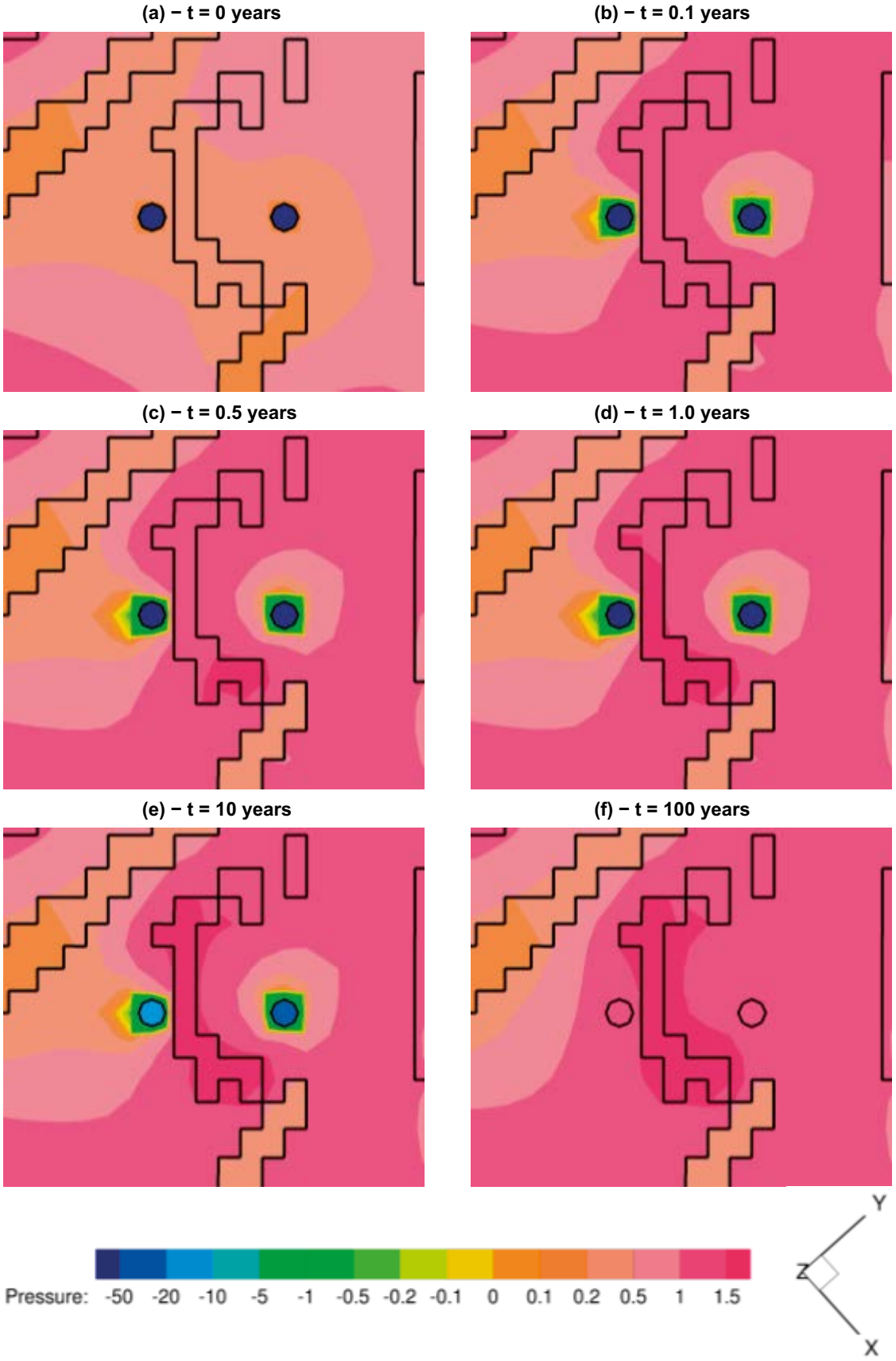

Figure 6-26. *Evolution of liquid pressure (MPa) within the bentonite across a horizontal slice, taken 1.5 m below the TASO tunnel at an elevation of −418.5 m. Results are shown for the second realisation of the upscaled stochastic fracture network using Task 8C constitutive relations for the rock matrix.*

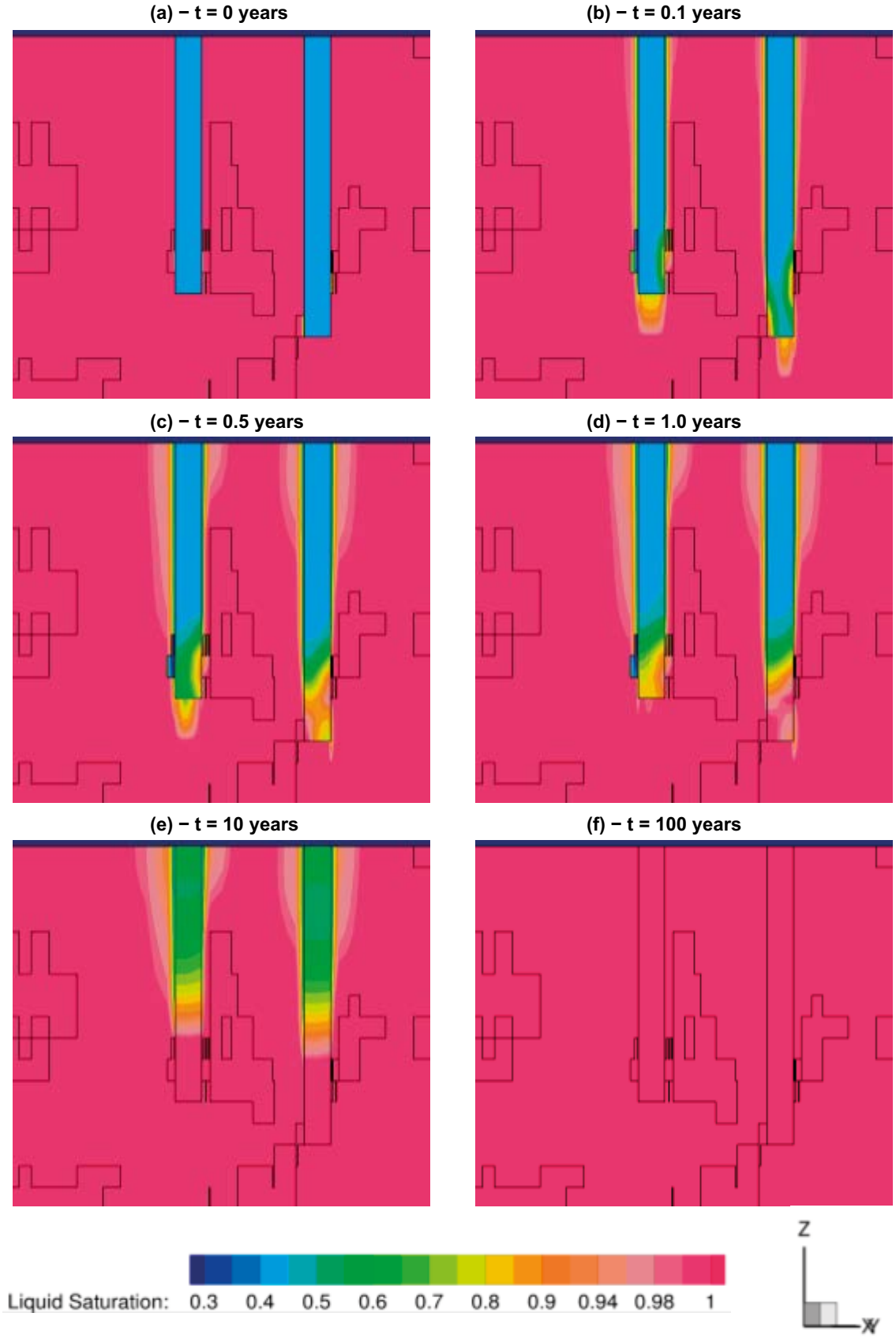

Figure 6-27. *Evolution of liquid saturation within the bentonite for a vertical slice oriented to include the two overcored boreholes KO0017G01 and KO0018G01. Results are shown for the second realisation of the stochastic fracture network using Task 8C constitutive relations for the rock matrix.*

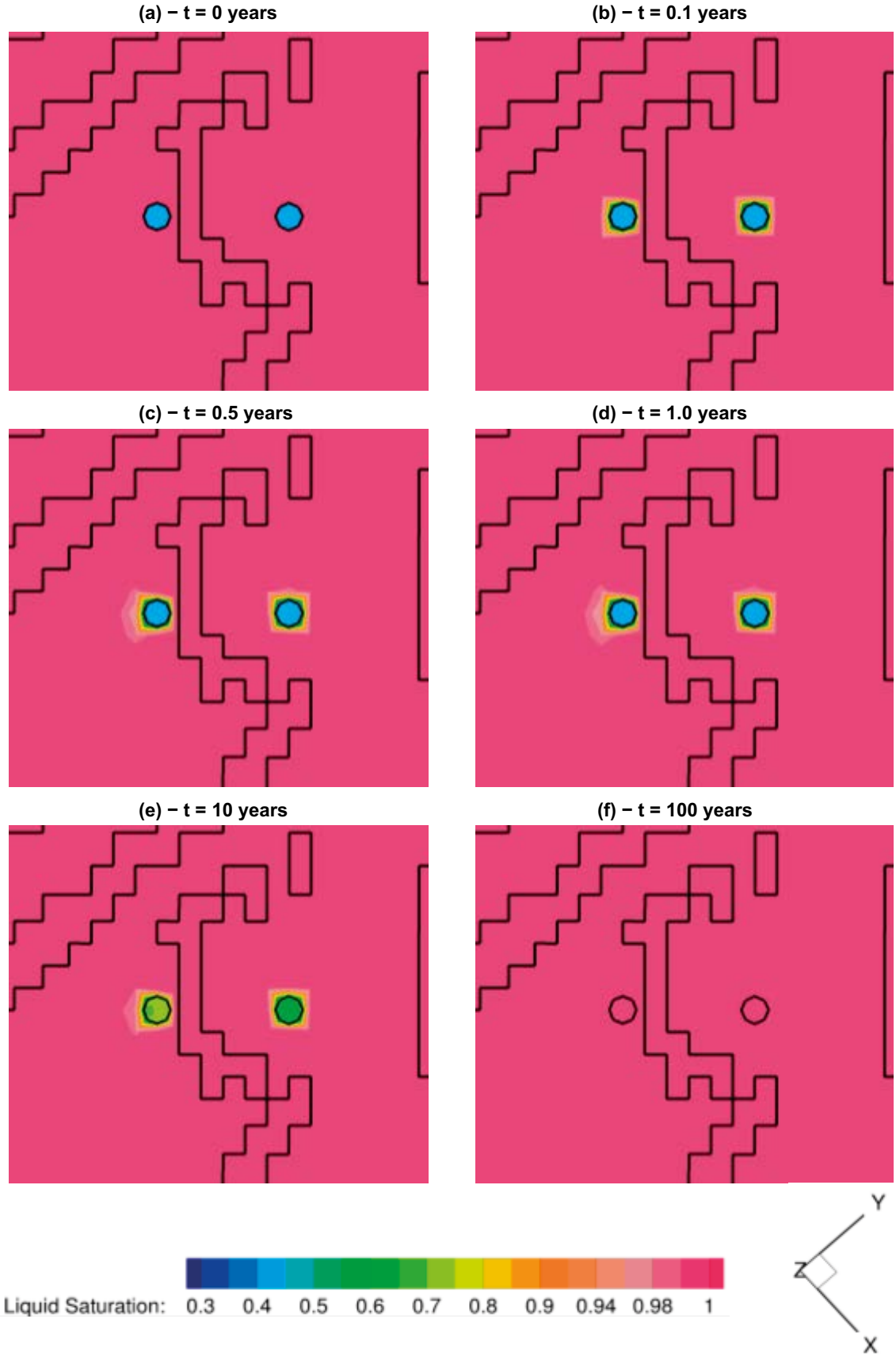

Figure 6-28. *Evolution of liquid saturation within the bentonite across a horizontal slice, taken 1.5 m below the TASO tunnel at an elevation of −418.5 m. Results are shown for the second realisation of the stochastic fracture network using Task 8C constitutive relations for the rock matrix.*

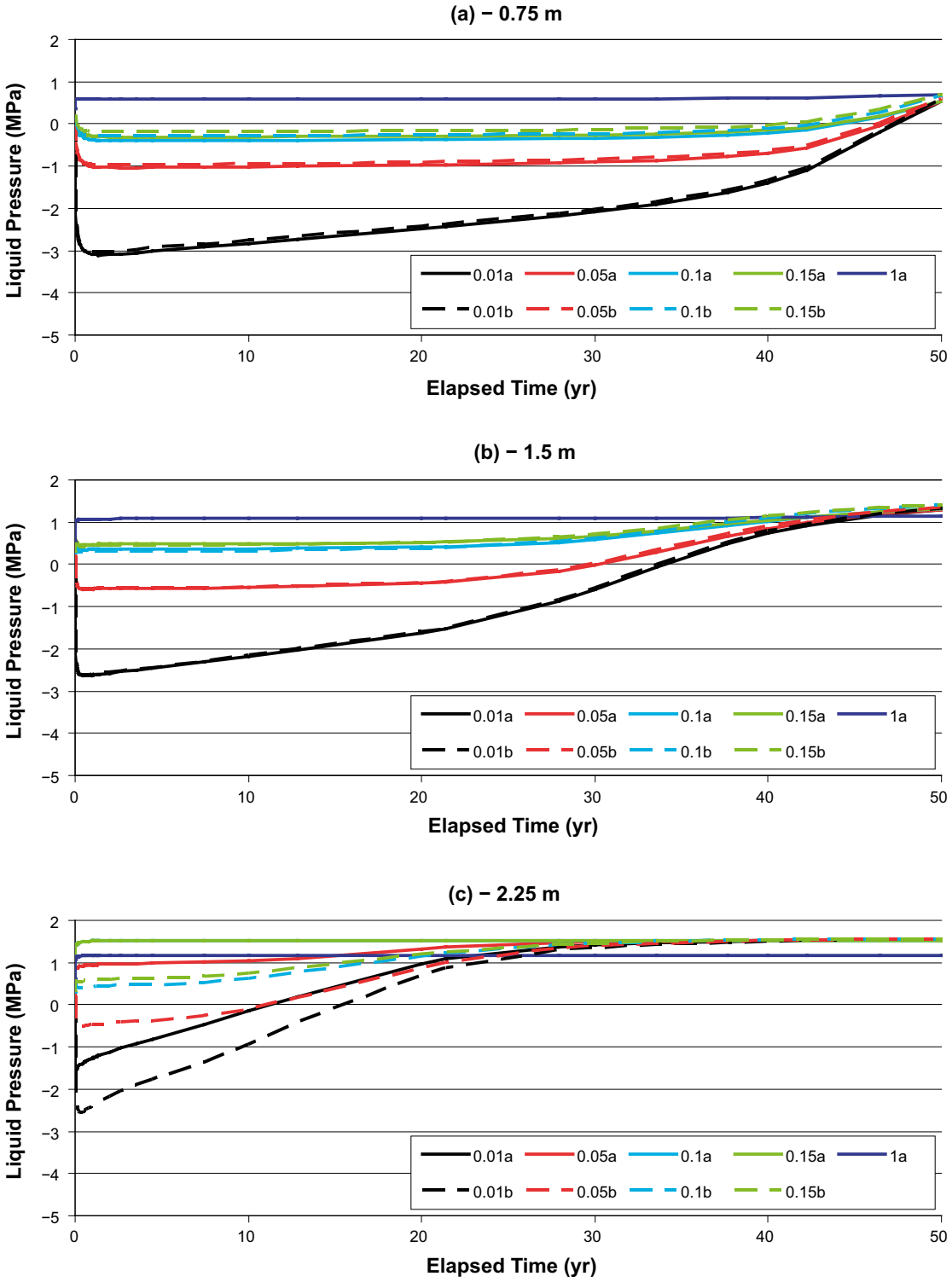

Figure 6-29. *Liquid pressure (MPa) calculated within the bedrock 0.01 m, 0.05 m, 0.1 m, 0.15 m, and 1.0 m from the wall of deposition hole KO0017G01. Results are shown for a slice oriented to intersect the two overcored boreholes, with "a" and "b" distances denoting direction from the edge of the deposition hole. The pressure curves shown correspond to the second realisation of the stochastic fracture network using Task 8C constitutive relations for the rock matrix.*

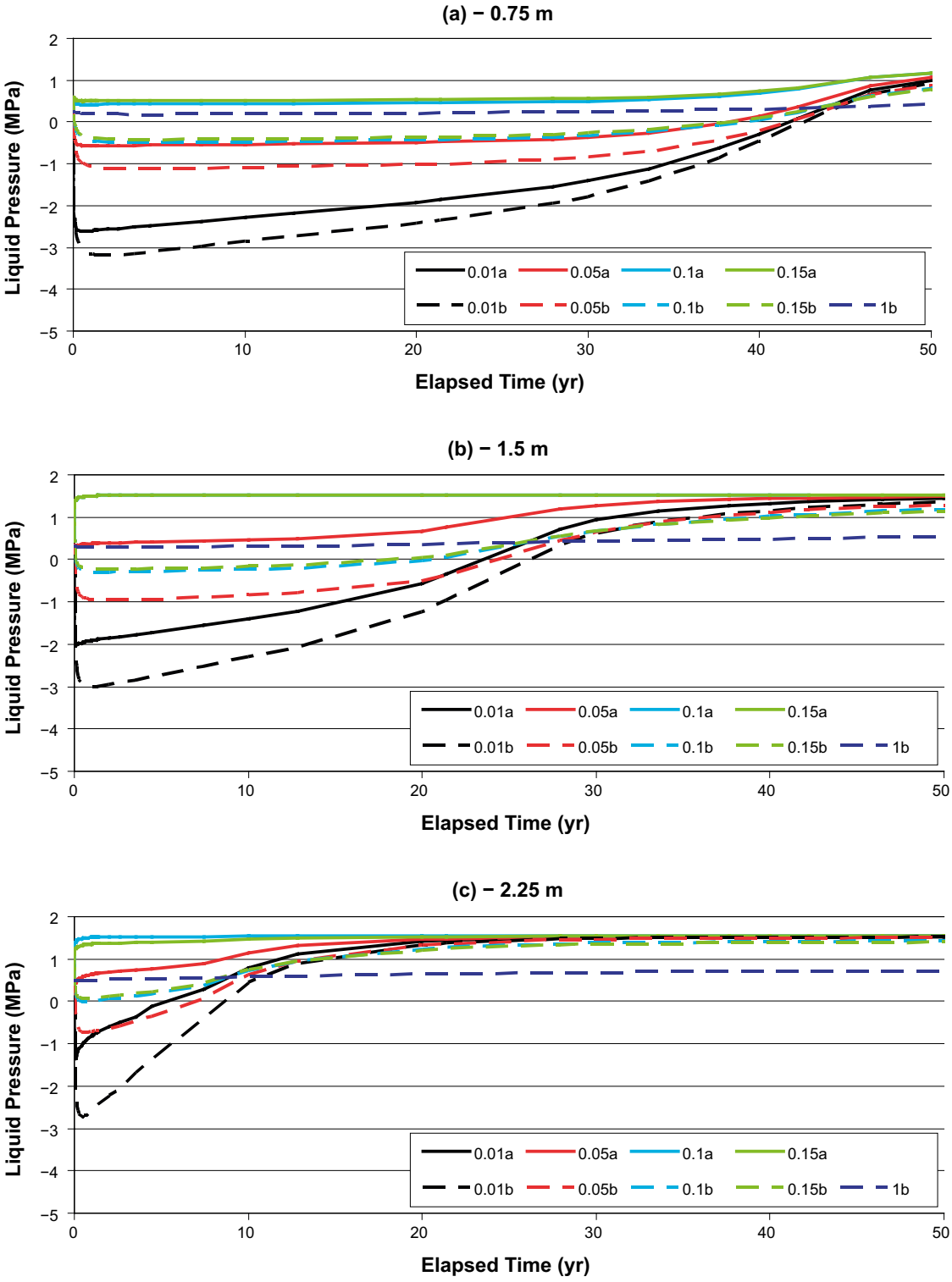

Figure 6-30. *Liquid pressure (MPa) calculated within the bedrock 0.01 m, 0.05 m, 0.1 m, 0.15 m, and 1.0 m from the wall of deposition hole KO0018G01. Results are shown for a slice oriented to intersect the two overcored boreholes, with "a" and "b" distances denoting direction from the edge of the deposition hole. The pressure curves shown correspond to the second realisation of the stochastic fracture network using Task 8C constitutive relations for the rock matrix.*

6.3.2 Rock matrix permeability (1×10^{-23} m^2)

It has been shown, both in the previous section, and the Task 8C analysis (Baxter et al. 2013), that the rock matrix permeability is critical to determining the resaturation times and profiles of bentonite emplaced on a deposition hole scale. However, only limited parameterisation of the rock matrix is available, using data concerning the rock 'matrix' permeability corresponding to unstressed core plug taken from deposition holes KO0017G01 and KO0018G01. At *in situ* stress conditions, the rock matrix permeability will reduce, although exact details of this change are uncertain. So far, two rock matrix permeabilities have been considered, corresponding to

- the geometric mean of the unstressed core plug measurements (3.8×10^{-20} m^2), and
- the elicitation from expert judgement, provided as part of Task 8C (1×10^{-21} m^2).

In this section, a model variant is considered, lowering the rock matrix to 1×10^{-23} m^2 for realisation 2 of the stochastic fracture network.

Figure 6-31 depicts the initial liquid saturation on the outer surface of the bentonite stack along with nine subsequent times up to 100 years. For comparison, liquid saturations for the same realisation of the fracture network, but with a rock matrix permeability of 1×10^{-21} m^2 are shown in Figure 6-6. By reducing the rock matrix permeability by two orders of magnitude, any contribution from the rock matrix to the bentonite resaturation is severely restricted. Therefore and as clearly observed in Figure 6-31 resaturation rates are much slower, with neither deposition hole reaching 95 % liquid saturation after 100 years.

The evolution of relative humidity within the bentonite for six sensor locations in KO0017G01 is presented in Figure 6-32. Results are directly comparable to Figure 6-8 (and reproduced by the dashed lines) for the same realisation of the DFN and a rock matrix permeability of 1×10^{-21} m^2. Equivalent results for deposition hole KO0018G01 are shown in Figure 6-33, detailing the evolution of relative humidity at the six sensor locations. Results for the same realisation of the DFN and a rock matrix permeability of 1×10^{-21} m^2 as presented in Figure 6-9 are also shown (dashed lines). For all twelve sensor locations considered, increases in relative humidity over the first 500 days post installation of the bentonite are reduced. This is a consequence of the slower resaturation rates caused by the reduction in groundwater flow from the rock matrix. However, the effects of changing the rock matrix permeability on relative humidity are more noticeable in deposition hole KO0017GO1 compared to KO0018G01, a likely consequence of geometrical differences between the two holes (i.e. the location of the intersecting fracture with respect to the sensor positions).

6.4 Effects of varying the relative gas permeability

In addition to Task 8, the EBS Task Force are considering additional modelling projects including a sensitivity and verification analysis of the numerical modelling of coupled THM processes. As part of this sensitivity task, the importance of accurately representing the gas phase has become apparent (Gordon et al. 2014), having significant effects on the resaturation profiles and times of a bentonite buffer. An alternative gas phase relative permeability function is proposed in Gordon et al. (2014), setting a high gas permeability relative to the liquid permeability in the bentonite. This has been demonstrated to be physical (Olivella and Gens 2000), with Figure 6-34 (reproduced from Olivella and Gens (2000) demonstrating that the difference between gas and liquid permeability in two different types of clay is several orders of magnitude. Therefore in this section an alternative gas permeability model for the bentonite is considered, with the gas phase relative permeability set five orders of magnitude higher than the liquid permeability in the bentonite. This is in contrast to the Fatt and Klikoff (1959) cubic-law representation of the relative permeability of the gas phase currently implemented for the bentonite, and detailed in Equation (3-9) of Section 3.2.5.

Resaturation calculations presented in this section are performed for realisation 2 of the stochastic fracture network, implementing the gas phase relative permeability function proposed (Gordon et al. 2014).

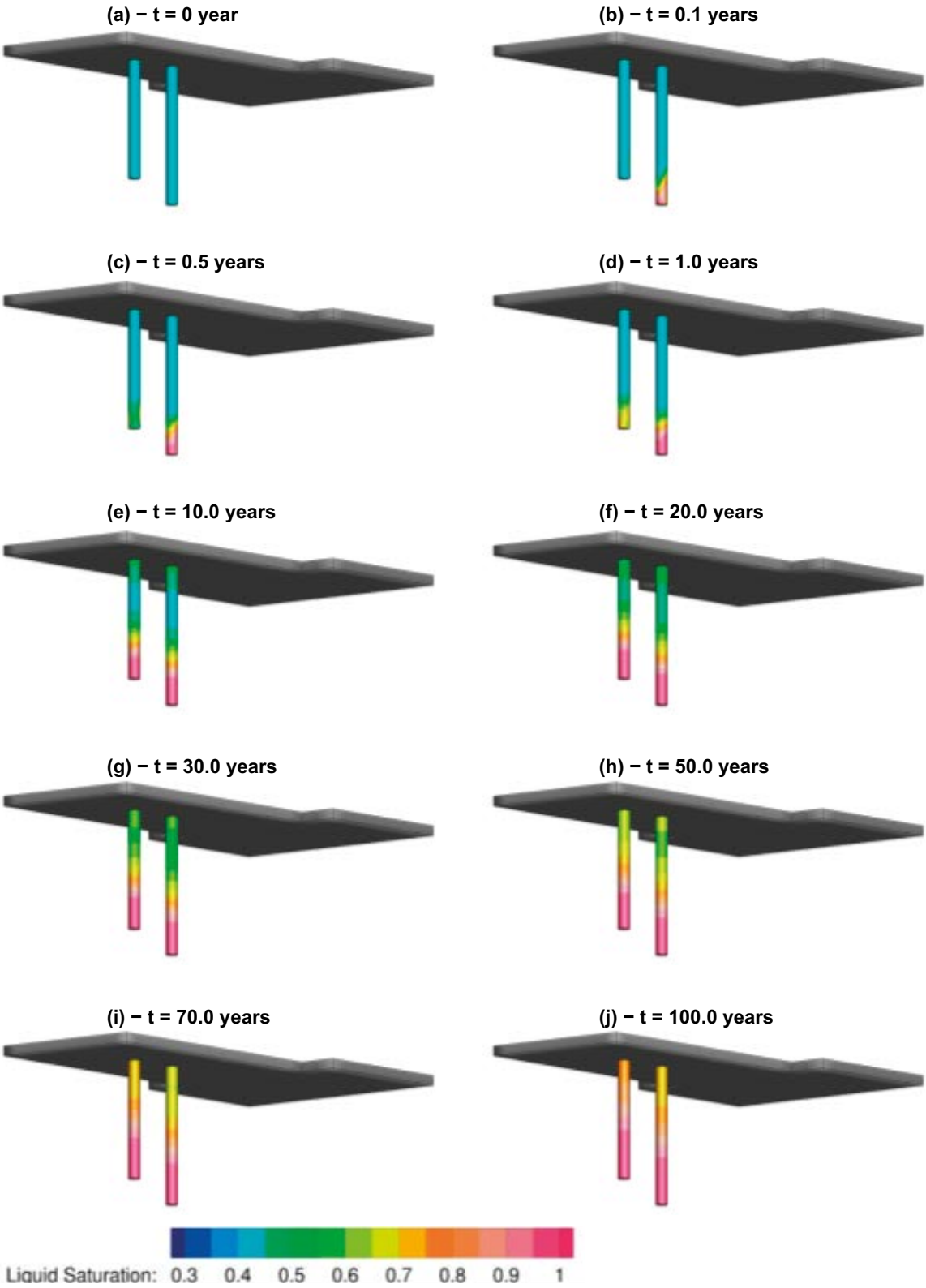

Figure 6-31. *The bentonite saturation calculated for each deposition hole at a number of different times. Results are presented for realisation two of the upscaled stochastic fracture network, with rock matrix permeability of 1×10^{-23} m^2. Results are comparable to Figure 6-6 calculated from the same realisation of the DFN, but with a rock matrix permeability of 1×10^{-21} m^2.*

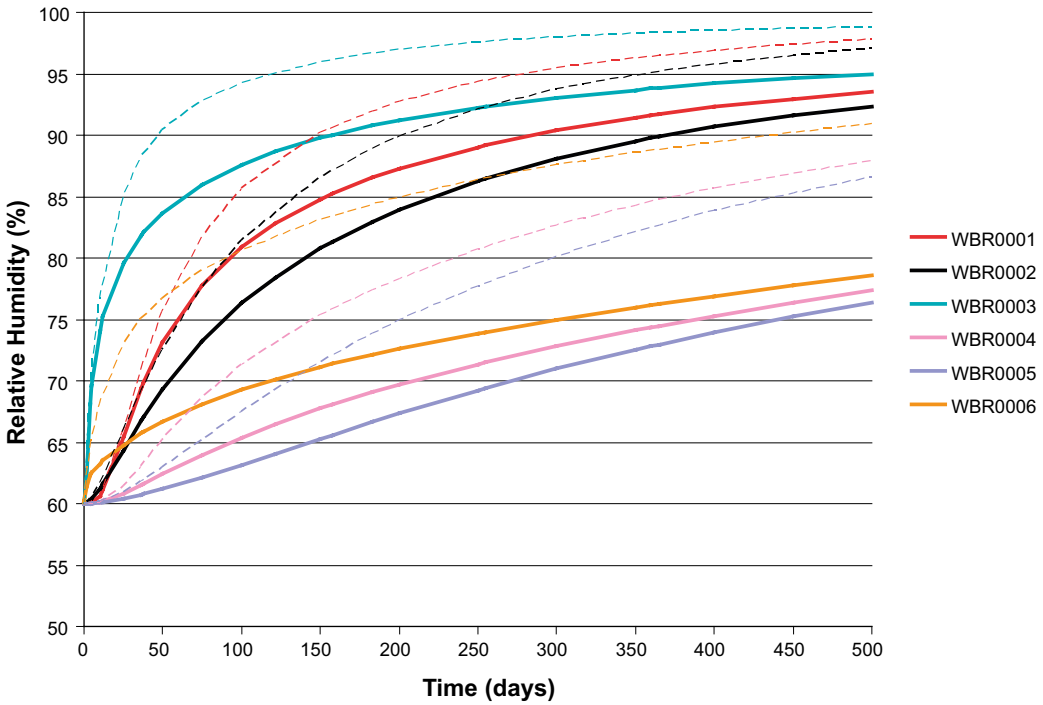

Figure 6-32. *The evolution of relative humidity calculated at sensor locations within the bentonite during the first 500 days post installation. Results are presented for sensors WBR0001 through WBR0006, corresponding to deposition hole KO0017G01. Dashed lines correspond to equivalent results for rock matrix permeability of* 1×10^{-21} m^2.

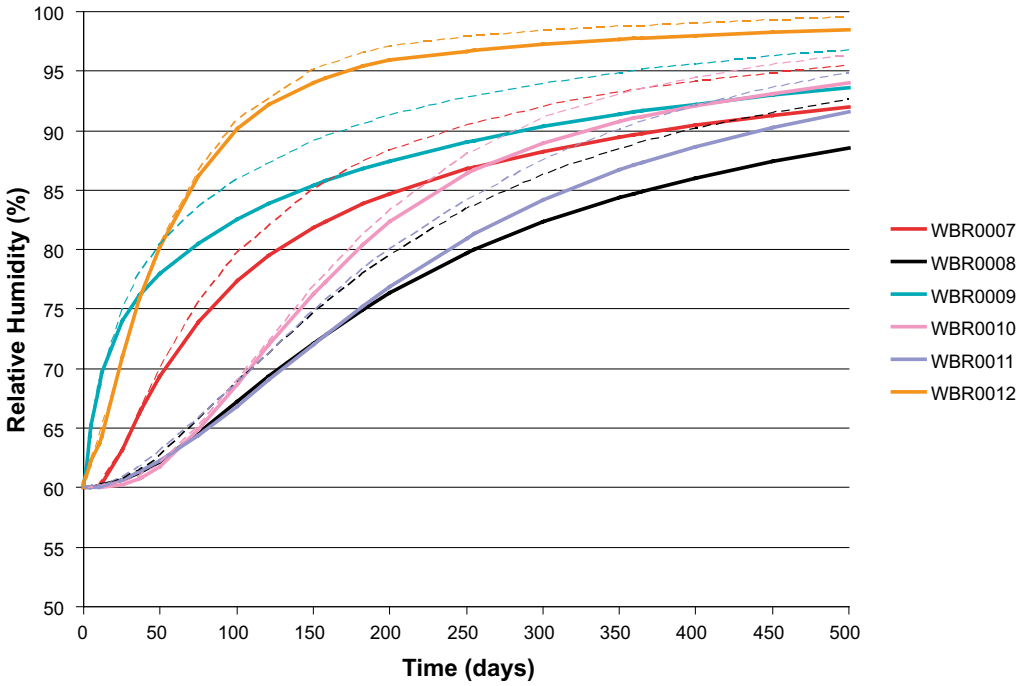

Figure 6-33. *The evolution of relative humidity calculated at sensor locations within the bentonite during the first 500 days post installation. Results are presented for sensors WBR0007 through WBR0012, corresponding to deposition hole KO0018G01. Dashed lines correspond to equivalent results for rock matrix permeability of* 1×10^{-21} m^2.

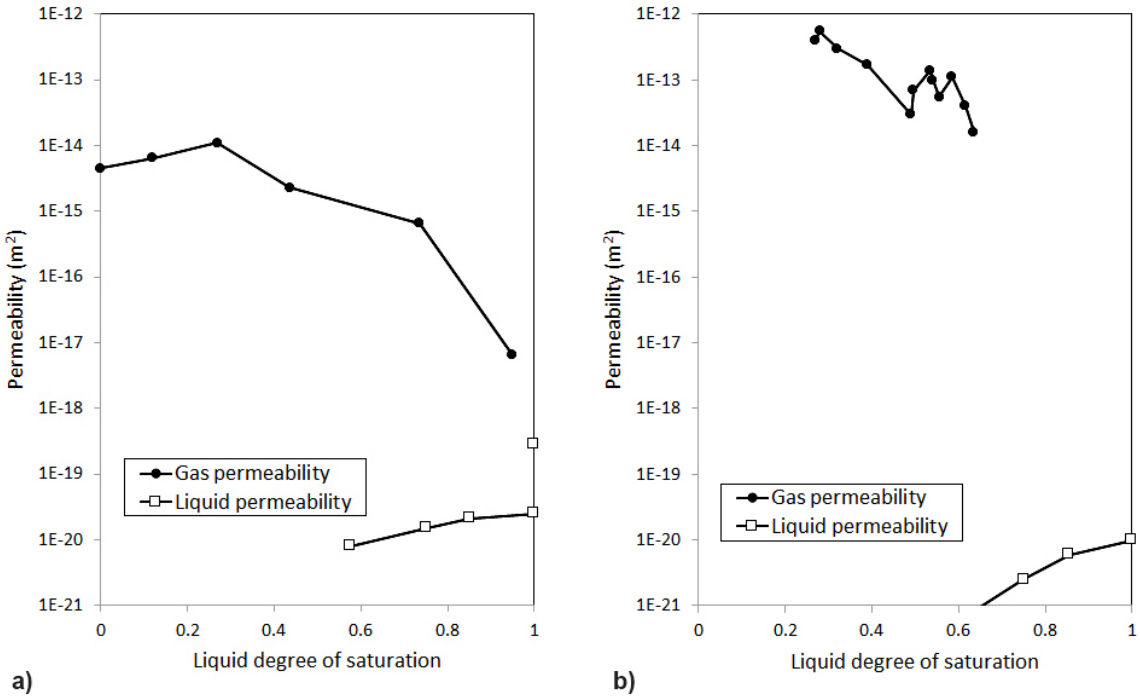

Figure 6-34. *Compiled data on permeability in (m^2) of clays in gas and water. (a) Boom Clay, (b) Febex Clay. Reproduced from Olivella and Gens (2000).*

Figure 6-35 depicts the initial liquid saturation on the outer surface of the bentonite stack, along with nine subsequent times up to 100 years. For comparison, liquid saturations for the same realisation of the fracture network, but using the Fatt and Klikoff (Pruess et al. 1999) cubic-law representation of the relative permeability of the gas phase provided as part of Task 8D are shown in Figure 6-6. The times to reach 95 % liquid saturation are 78.4 years for KO0017G01 and 60.8 years for KO0018G01. These times are broadly unchanged from simulations using the Fatt and Klikoff (Pruess et al. 1999) cubic-law representation of the gas phase relative permeability of the bentonite.

The evolution of relative humidity within the bentonite for six sensor locations in KO0017G01 is presented in Figure 6-36. Results are directly comparable to Figure 6-8 (and reproduced as dashed lines on Figure 6-36) for the same realisation of the DFN, using a Fat and Klikoff representation of the gas phase relative permeability. Equivalent results for deposition hole KO0018G01 are shown in Figure 6-37, detailing the evolution of relative humidity at the six sensor locations. Equivalent results for the same realisation of the DFN and a Fat and Klikoff representation of the gas phase relative permeability are shown (dashed lines), reproduced from Figure 6-9. For the twelve sensor locations, the relative humidity over the first 500 days post installation of the bentonite shows minimal variation upon changing the relative permeability function of the bentonite gas phase. Any changes observed tend towards slightly faster increase in relative humidity for this model variant, a consequence of the increased mobility of the gas phase.

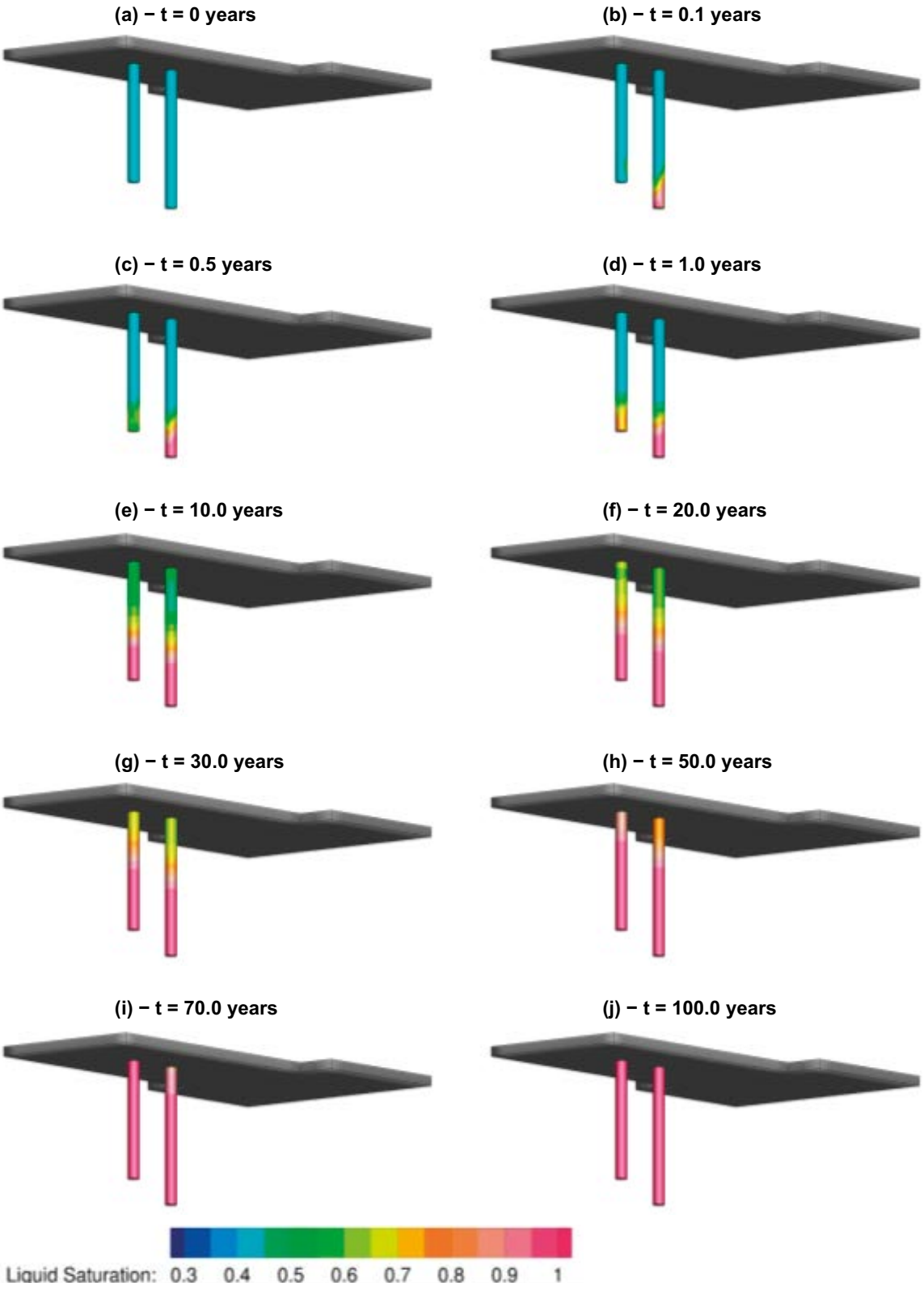

Figure 6-35. *The bentonite saturation calculated for each deposition hole at a number of different times. Results are presented for realisation two of the upscaled stochastic fracture network, using the gas phase relative permeability function proposed in Gordon et al. (2014). Results are comparable to Figure 6-6 calculated from the same realisation of the DFN, but using a Fat and Klikoff representation of the gas phase relative permeability.*

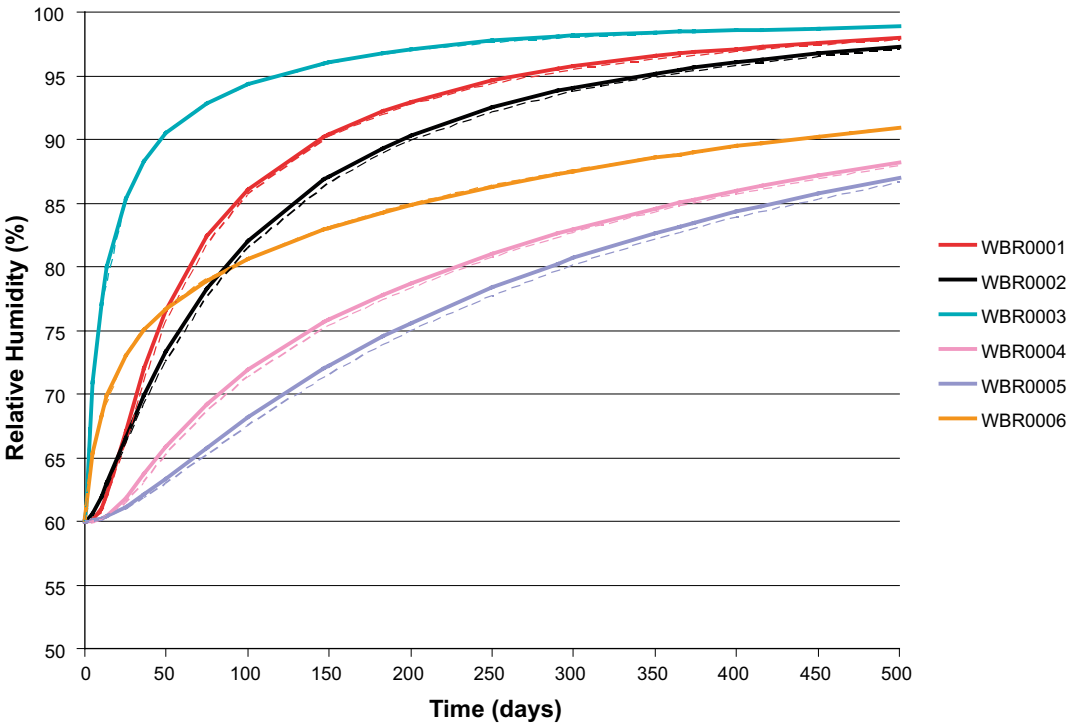

Figure 6-36. *Relative humidity evolution calculated at sensor locations WBR0001 through WBR0006, corresponding to deposition hole KO0017G01. Dashed lines correspond to equivalent results using a Fat and Klikoff representation of the gas phase relative permeability.*

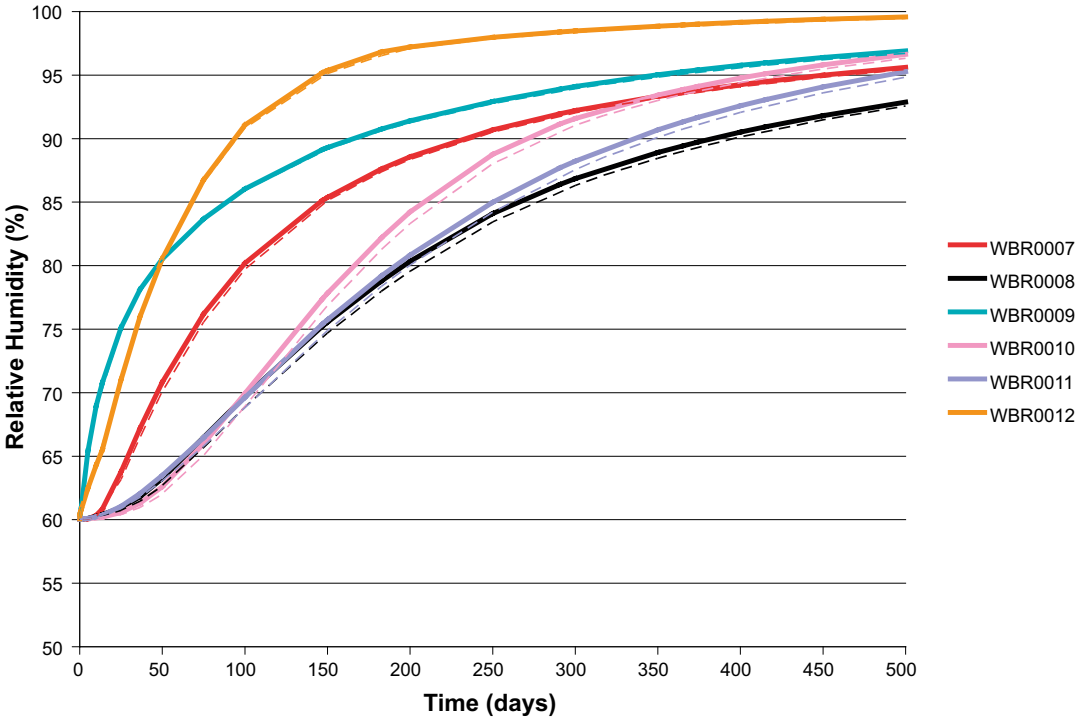

Figure 6-37. *Relative humidity evolution calculated at sensor locations WBR0007 through WBR0012, corresponding to deposition hole KO0018G01. Dashed lines correspond to equivalent results using a Fat and Klikoff representation of the gas phase relative permeability.*

6.5 Effects of varying the bentonite permeability

In Section 6.3.2 the effect of rock matrix on bentonite hydration was considered through a variant model lowering rock matrix permeability two orders of magnitude from 1×10^{-21} m^2 to 1×10^{-23} m^2. By lowering the hydraulic contribution of the rock matrix to resaturation of the emplaced bentonite, the resaturation duration was considerable increased, as shown in Figure 6-31 through Figure 6-33. In this section the effects of varying the bentonite permeability is analysed, reducing it by one order of magnitude to 6.4×10^{-22} m^2. This model variant is considered as a potential bounding case on resaturation rates, with simulations also incorporating the reduced rock matrix permeability. As such, the results in this section are directly comparable to those presented in Section 6.3.2, and correspond to realisation 2 of the stochastic fracture network.

Figure 6-38 depicts the initial liquid saturation on the outer surface of the bentonite stack along with nine subsequent times up to 100 years. For comparison, liquid saturations for the same realisation of the fracture network, but with a bentonite permeability of 6.4×10^{-21} m^2 are shown in Figure 6-31. Resaturation is initiated towards the bottom of the deposition holes, corresponding to the location of fracture intersections. Over the 100 year period, hydration of the entire bentonite stack is severely limited. In addition, resaturation is slightly enhanced towards the top of the deposition holes. This is an artefact of the modelling; allowing limited hydration of the bentonite from the humid TASO tunnel. The installation procedure (see Figure 2-8) includes a top plate that isolates the bentonite stack from the tunnel. However, for simplification, a modelling assumption to exclude this plate from the models has been made. For all previous simulations, this effect is not observable due to groundwater ingress from the surrounding bedrock dominating resaturation. This artefact does not affect resaturation profiles local to the fracture intersections towards the bottom of the deposition holes.

The evolution of relative humidity within the bentonite for six sensor locations in KO0017G01 is presented in Figure 6-39. Results are directly comparable to Figure 6-32 (and reproduced as the dashed lines) for the same realisation of the DFN and a bentonite permeability of 6.4×10^{-21} m^2. Equivalent results for deposition hole KO0018G01 are shown in Figure 6-40, detailing the evolution of relative humidity at the six sensor locations. Results for the same realisation of the DFN and a bentonite permeability of 6.4×10^{-21} m^2 are shown as dashed lines and reproduced from Figure 6-32. Through reducing the bentonite permeability, the relative humidity at the twelve sensor locations is significantly reduced during the first 500 days post installation. Specifically, sensor locations further from the hydraulically active fractures intersecting the deposition holes exhibit very limited resaturation during this time period.

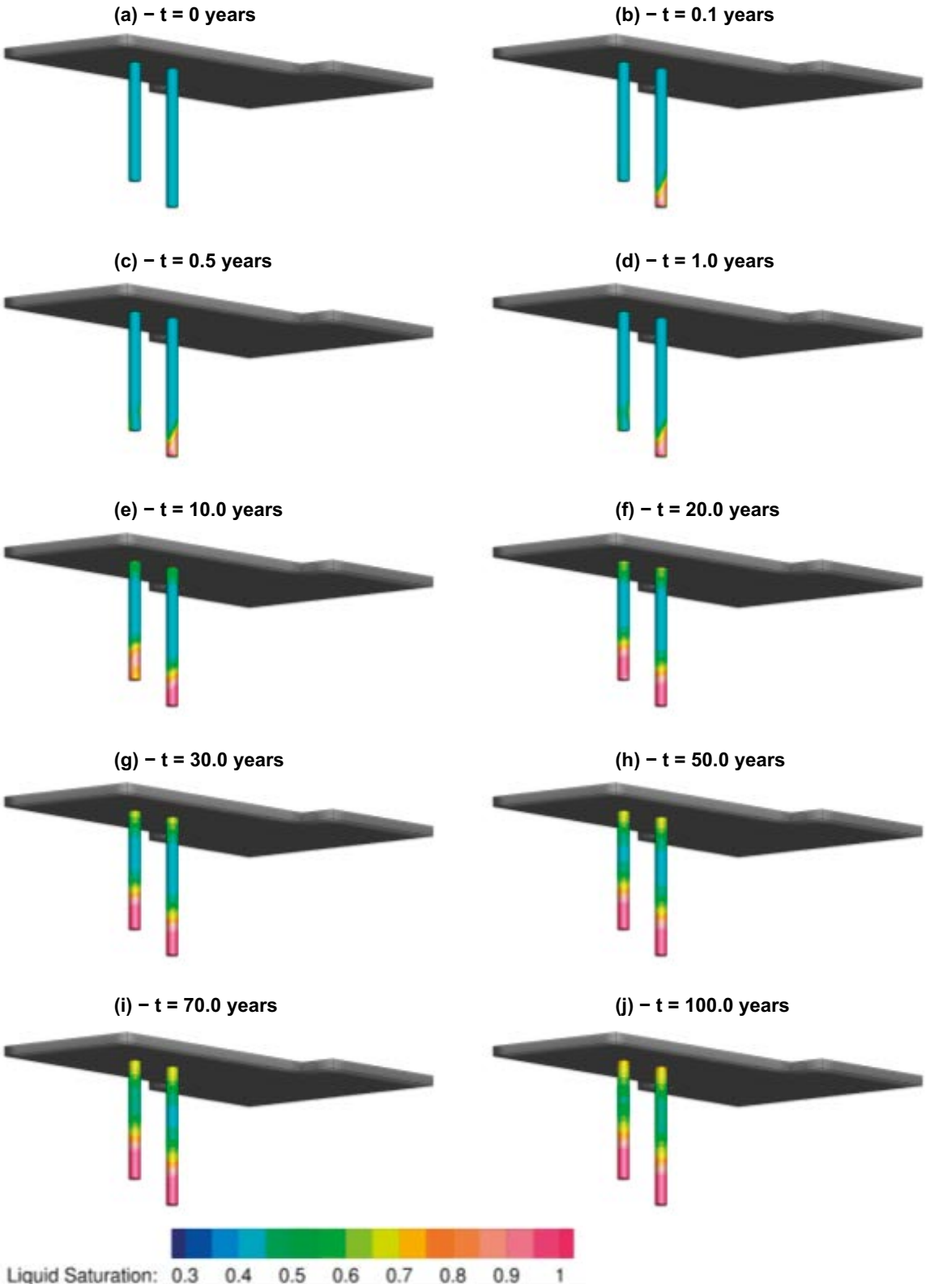

Figure 6-38. *The bentonite saturation calculated for each deposition hole at a number of different times. Results are presented for realisation two of the upscaled stochastic fracture network, with bentonite permeability of 6.4×10^{-22} m^2. Results are comparable to Figure 6-31, calculated from the same realisation of the DFN, but with a bentonite permeability of 6.4×10^{-21} m^2.*

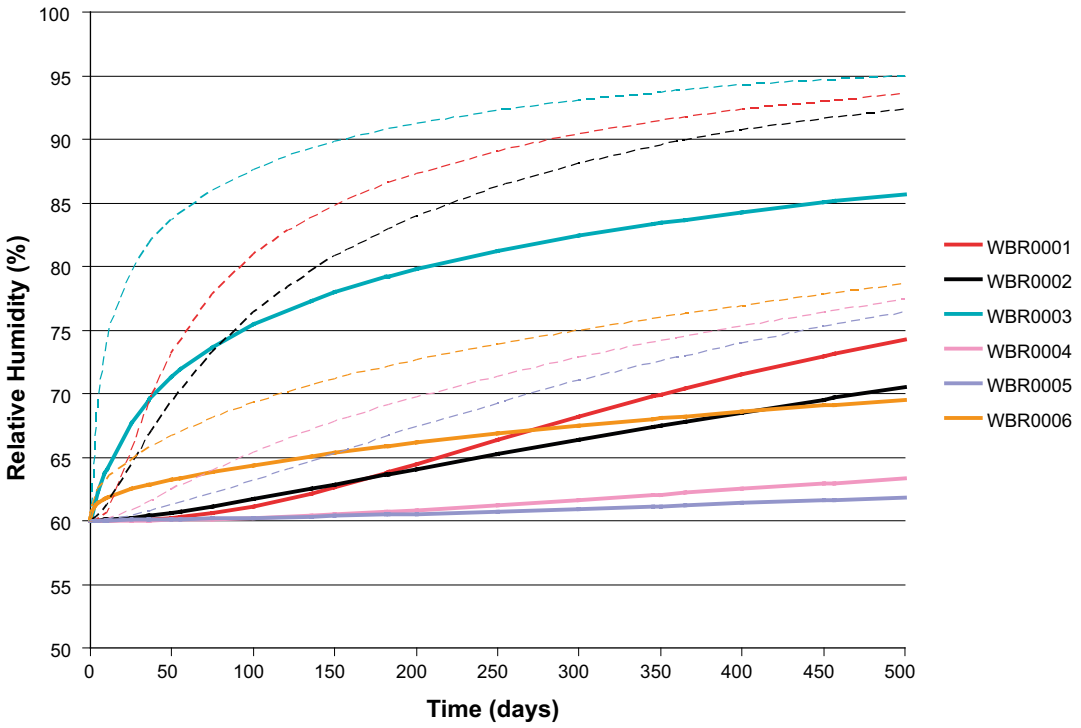

Figure 6-39. *The evolution of relative humidity calculated at sensor locations within the bentonite during the first 500 days post installation. Results are presented for sensors WBR0001 through WBR0006, corresponding to deposition hole KO0017G01. Dashed lines correspond to equivalent results for bentonite permeability of* 6.4×10^{-21} m^2.

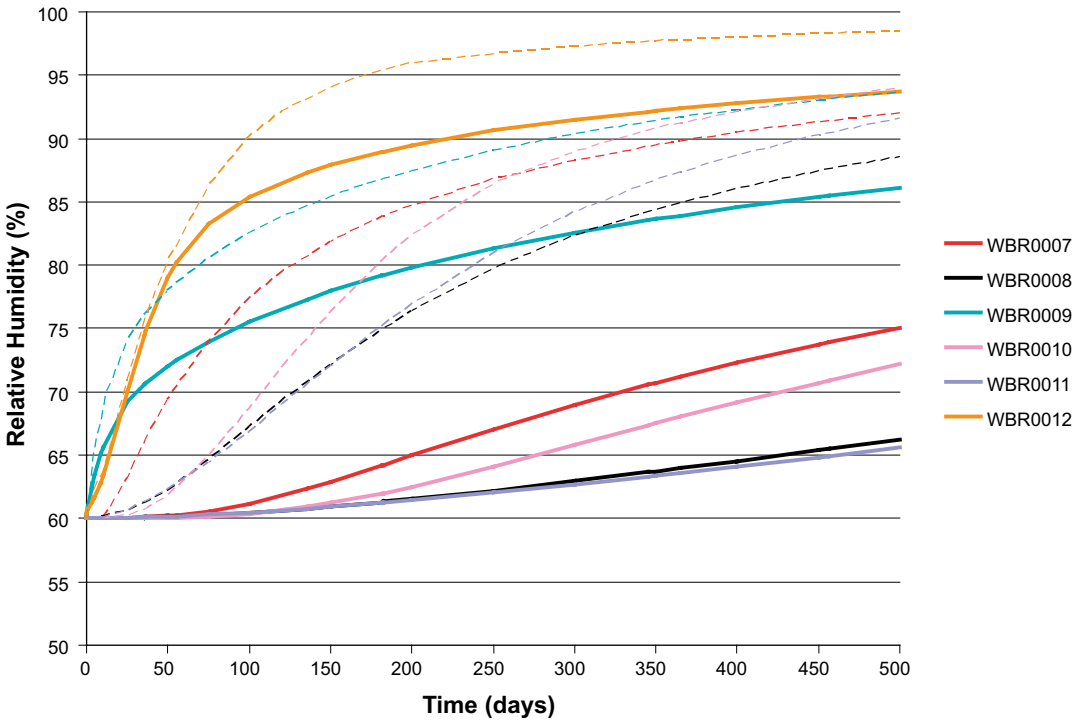

Figure 6-40. *The evolution of relative humidity calculated at sensor locations within the bentonite during the first 500 days post installation. Results are presented for sensors WBR0007 through WBR0012, corresponding to deposition hole KO0018G01. Dashed lines correspond to equivalent results for bentonite permeability of* 6.4×10^{-21} m^2.

7 Comparison with experimental results

Upon completion of the BRIE, relative humidity measurements taken at the twelve sensor locations within the bentonite installations were provided to modelling groups participating in the EBS Task Force. In this section, the predictive modelling results detailed in Section 6 are compared with the experimental data. Both the Basecase model and variants considering alternative parameterisation of the rock matrix and bentonite are presented, and in general bound the experimental data in each of the deposition holes

The bentonite installations within the central deposition holes KO0017G01 and KO0018G01 of the BRIE were excavated subsequent to the predictive modelling detailed in Section 6. From characterisation of deposition holes from the recorded inflows, it was anticipated that KO0017G01 would undergo quicker resaturation than KO0018G01 (inflows were typically a factor 10 greater in KO0017G01). As such, the bentonite package in KO0017G01 was excavated 400 days post installation, whereas the bentonite package in KO0018G01 was left *in situ* for a further 100 days.

Upon completion of the BRIE, and the reporting of predictive modelling results from the groups participating in Task 8D of the EBS Task Force, measurements taken from sensors within the bentonite installations were made available to modelling groups. This section provides comparison of the predictive models developed within this report with measurements of relative humidity taken at twelve sensor locations (six within KO0017G01, and six within KO0018G01). The location of these sensors within the bentonite packages are shown in Figure 2-8 through Figure 2-10. The following two subsections compare each of these deposition holes in turn, with results presented for a single realisation of the stochastic fracture network (realisation 2). Modelling results for both the Basecase model and variants considering alternative parameterisation of the rock matrix and bentonite are compared to the experimental results.

7.1 Relative humidity in KO0017G01

An instrumented bentonite package was emplaced in overcored borehole KO0017G01 for 400 days. Six relative humidity sensors, denoted WBR0001 through WBR0006 were installed in the bentonite and located as shown in Figure 2-8 through Figure 2-10. The experimental data for each of these sensors is shown in Figure 7-1 through Figure 7-6, as well as modelling results for

- the Basecase model corresponding to realisation 2 of the stochastic fracture network,
- the model variant considering a reduced rock matrix permeability (1×10^{-23} m^2), as detailed in Section 6.3.2, and
- the model variant considering a reduced rock matrix permeability (1×10^{-23} m^2) and a reduced bentonite permeability (6.4×10^{-22} m^2), as detailed in Section 6.5.

For all sensors other than WBR0003, the experimental data shows an initial localised peak in relative humidity. This is a consequence of the installation process of the bentonite, as described in Section 2.2, which includes the filling of both the central tube and outer slot with water. However, due to the complexity of the installation procedure and the expectation that these processes would cause only a short-duration perturbation to the resaturation profiles, installation of the bentonite has not been represented in the models. Therefore comparisons should instead focus on the consistency of the longer-term model predictions of relative humidity with measurements. Relative humidity recorded by sensor WBR0003 does not show this behaviour as it is located closest to the intersecting fracture (see Figure 6-7), and as such the surrounding bentonite resaturates on a timescale that disguises this effect. Inclusion of a detailed representation of the installation procedure within the models could form one aspect of future work.

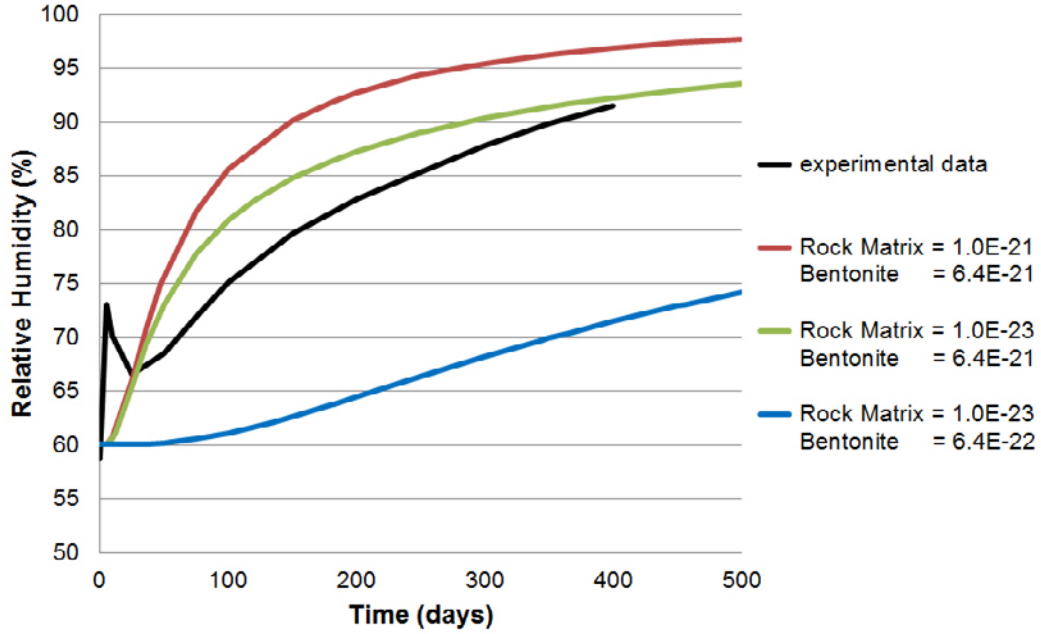

Figure 7-1. *The evolution of relative humidity calculated at sensor location WBR0001 within the bentonite during the first 500 days post installation. Results are presented for three model variants: rock matrix permeability of 1×10^{-21} m^2, bentonite permeability of 6.4×10^{-21} m^2 (red); rock matrix permeability of 1×10^{-23} m^2, bentonite permeability of 6.4×10^{-21} m^2 (green); rock matrix permeability of 1×10^{-23} m^2, bentonite permeability of 6.4×10^{-22} m^2 (blue). Measurements from the BRIE experiment are coloured black.*

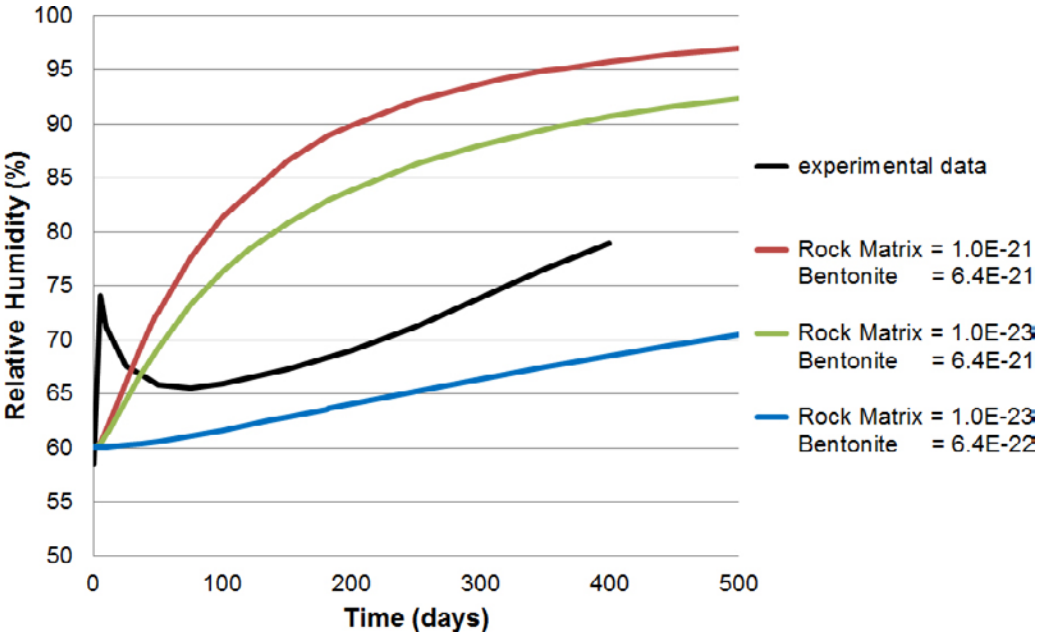

Figure 7-2. *The evolution of relative humidity calculated at sensor location WBR0002 within the bentonite during the first 500 days post installation. Results are presented for three model variants: rock matrix permeability of 1×10^{-21} m^2, bentonite permeability of 6.4×10^{-21} m^2 (red); rock matrix permeability of 1×10^{-23} m^2, bentonite permeability of 6.4×10^{-21} m^2 (green); rock matrix permeability of 1×10^{-23} m^2, bentonite permeability of 6.4×10^{-22} m^2 (blue). Measurements from the BRIE experiment are coloured black.*

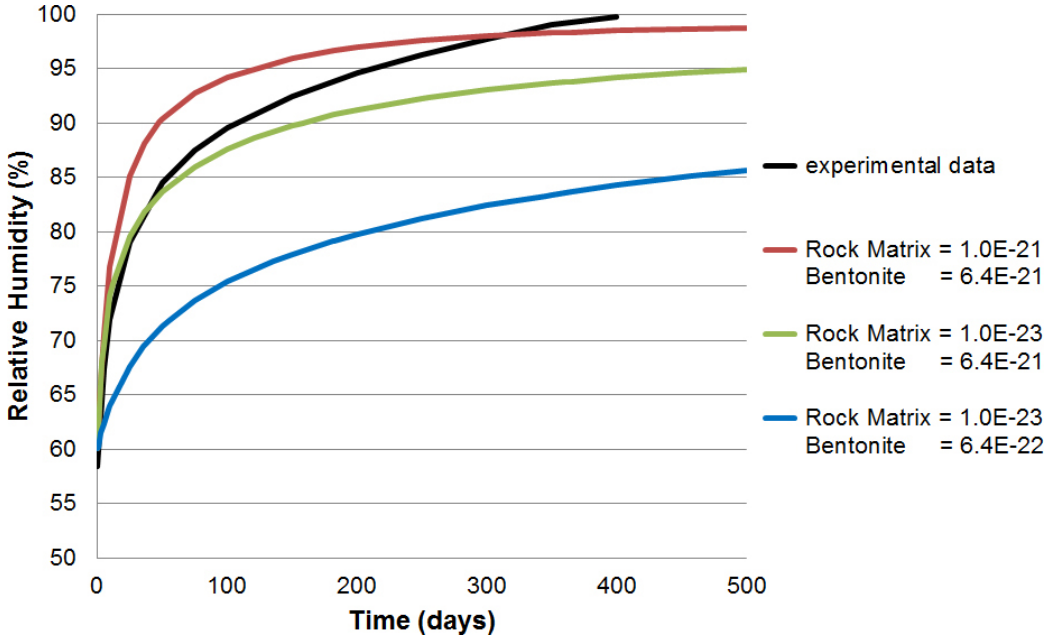

Figure 7-3. *The evolution of relative humidity calculated at sensor location WBR0003 within the bentonite during the first 500 days post installation. Results are presented for three model variants: rock matrix permeability of 1×10^{-21} m^2, bentonite permeability of 6.4×10^{-21} m^2 (red); rock matrix permeability of 1×10^{-23} m^2, bentonite permeability of 6.4×10^{-21} m^2 (green); rock matrix permeability of 1×10^{-23} m^2, bentonite permeability of 6.4×10^{-22} m^2 (blue). Measurements from the BRIE experiment are coloured black.*

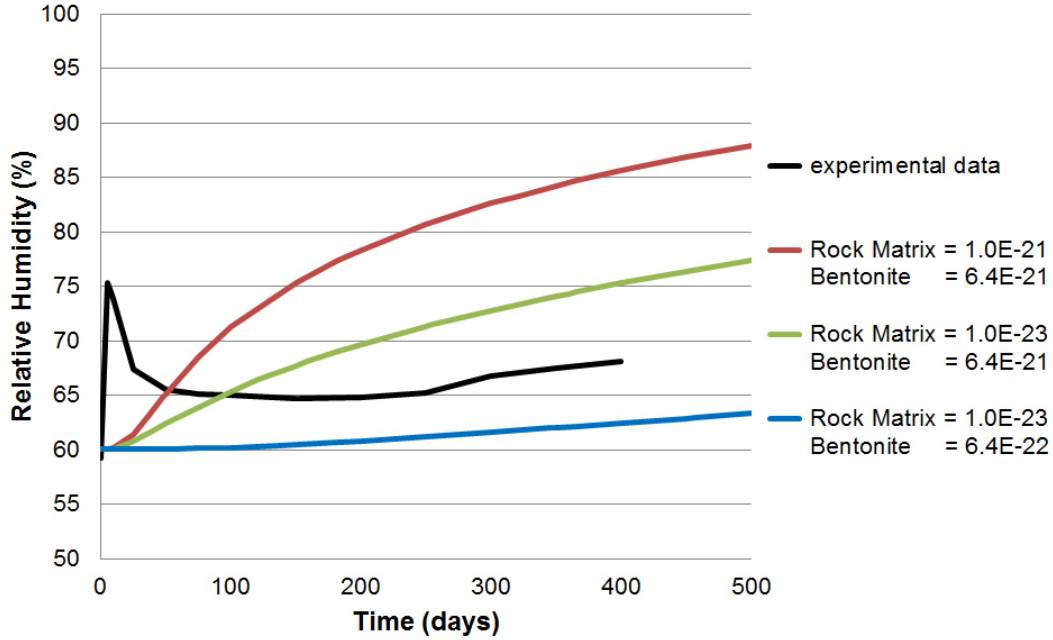

Figure 7-4. *The evolution of relative humidity calculated at sensor location WBR0004 within the bentonite during the first 500 days post installation. Results are presented for three model variants: rock matrix permeability of 1×10^{-21} m^2, bentonite permeability of 6.4×10^{-21} m^2 (red); rock matrix permeability of 1×10^{-23} m^2, bentonite permeability of 6.4×10^{-21} m^2 (green); rock matrix permeability of 1×10^{-23} m^2, bentonite permeability of 6.4×10^{-22} m^2 (blue). Measurements from the BRIE experiment are coloured black.*

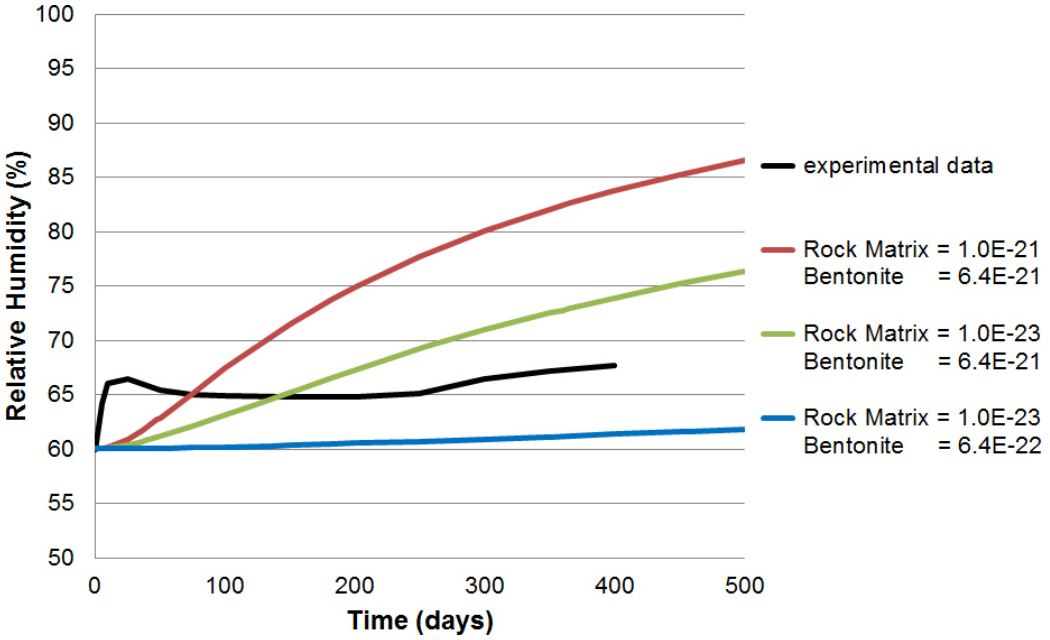

Figure 7-5. *The evolution of relative humidity calculated at sensor location WBR0005 within the bentonite during the first 500 days post installation. Results are presented for three model variants: rock matrix permeability of 1×10^{-21} m^2, bentonite permeability of 6.4×10^{-21} m^2 (red); rock matrix permeability of 1×10^{-23} m^2, bentonite permeability of 6.4×10^{-21} m^2 (green); rock matrix permeability of 1×10^{-23} m^2, bentonite permeability of 6.4×10^{-22} m^2 (blue). Measurements from the BRIE experiment are coloured black.*

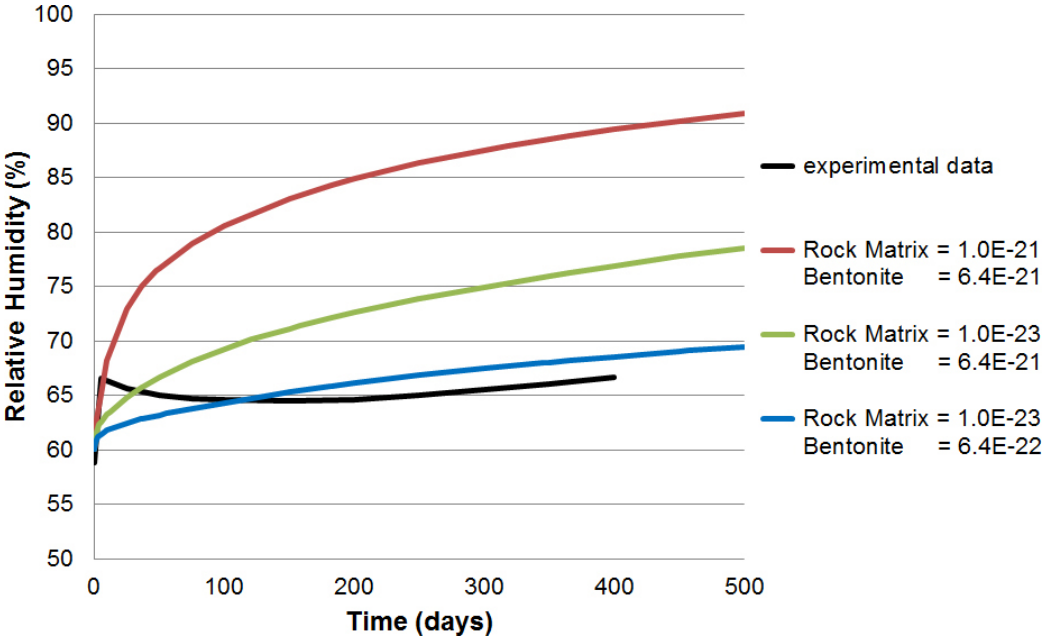

Figure 7-6. *The evolution of relative humidity calculated at sensor location WBR0006 within the bentonite during the first 500 days post installation. Results are presented for three model variants: rock matrix permeability of 1×10^{-21} m^2, bentonite permeability of 6.4×10^{-21} m^2 (red); rock matrix permeability of 1×10^{-23} m^2, bentonite permeability of 6.4×10^{-21} m^2 (green); rock matrix permeability of 1×10^{-23} m^2, bentonite permeability of 6.4×10^{-22} m^2 (blue). Measurements from the BRIE experiment are coloured black.*

7.2 Relative humidity in KO0018G01

From characterisation of inflows to the central deposition holes, the resaturation of bentonite emplaced in KO0018G01 was expected to be slower than KO0017G01 (inflows were typically a factor 10 less in KO0018G01). As such, the bentonite package in KO0018G01 was left *in situ* for a further 100 days before excavation (i.e. 500 days post installation). Six relative humidity sensors, denoted WBR0007 through WBR0012 were installed in the bentonite and located as shown in Figure 2-8 through Figure 2-10. The experimental data for each of these sensors is presented in Figure 2-8 through Figure 2-10. As for KO0017G01, modelling results are also shown for the Basecase (realisation 2 of the stochastic fracture network) and model variants considering alternative rock matrix and bentonite parameterisation. For all but WBR0012, the modelling cases presented are found to bound the experimental data recorded during this period of resaturation.

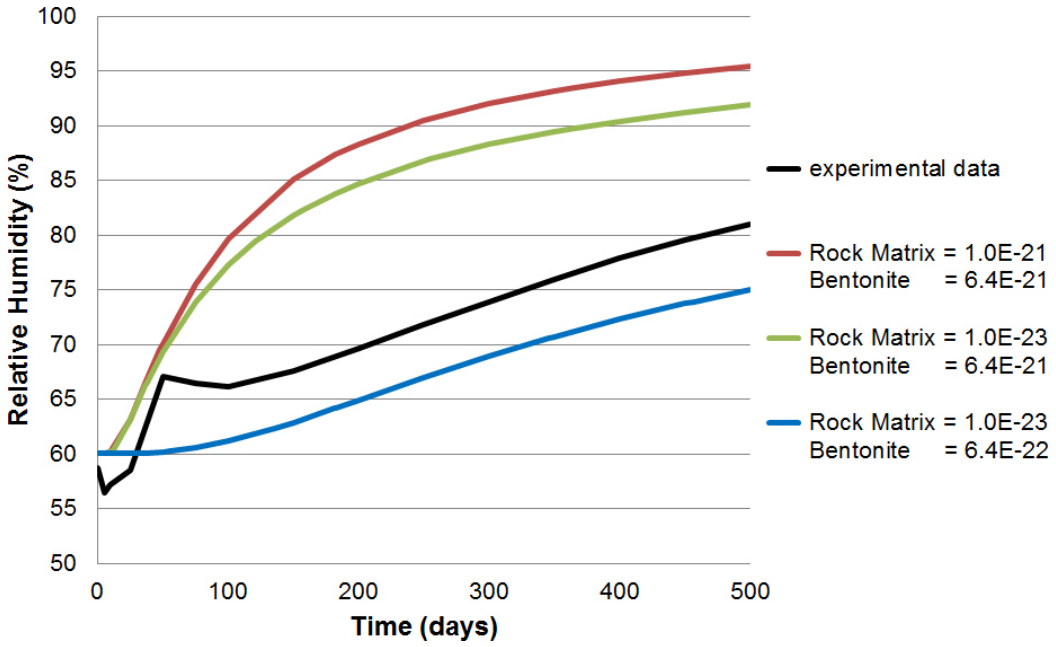

Figure 7-7. *The evolution of relative humidity calculated at sensor location WBR0007 within the bentonite during the first 500 days post installation. Results are presented for three model variants: rock matrix permeability of 1×10^{-21} m^2, bentonite permeability of 6.4×10^{-21} m^2 (red); rock matrix permeability of 1×10^{-23} m^2, bentonite permeability of 6.4×10^{-21} m^2 (green); rock matrix permeability of 1×10^{-23} m^2, bentonite permeability of 6.4×10^{-22} m^2 (blue). Measurements from the BRIE experiment are coloured black.*

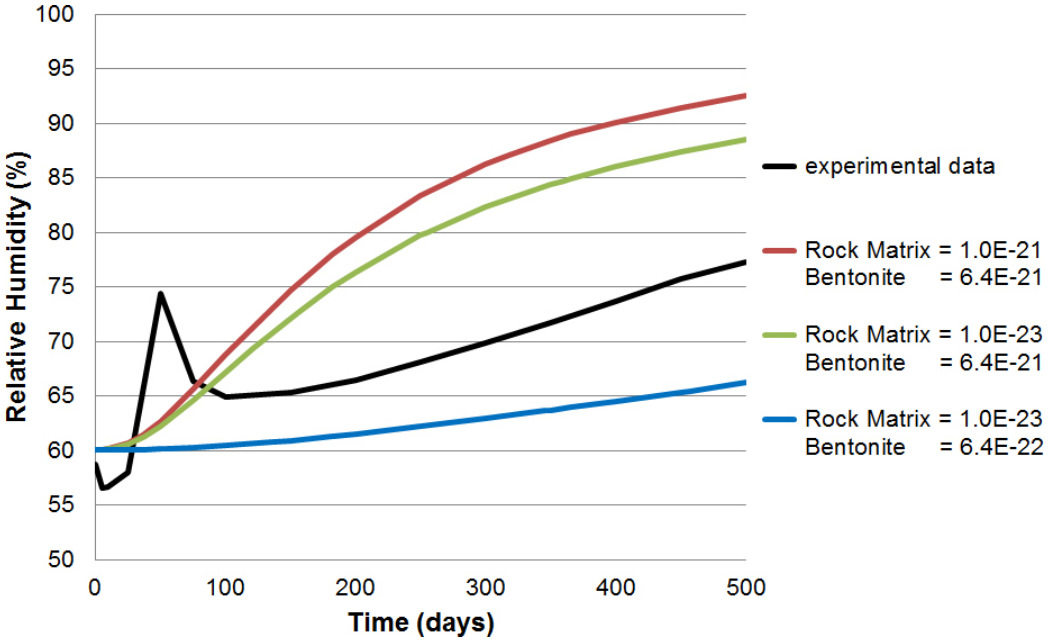

Figure 7-8. *The evolution of relative humidity calculated at sensor location WBR0008 within the bentonite during the first 500 days post installation. Results are presented for three model variants: rock matrix permeability of 1×10^{-21} m^2, bentonite permeability of 6.4×10^{-21} m^2 (red); rock matrix permeability of 1×10^{-23} m^2, bentonite permeability of 6.4×10^{-21} m^2 (green); rock matrix permeability of 1×10^{-23} m^2, bentonite permeability of 6.4×10^{-22} m^2 (blue). Measurements from the BRIE experiment are coloured black.*

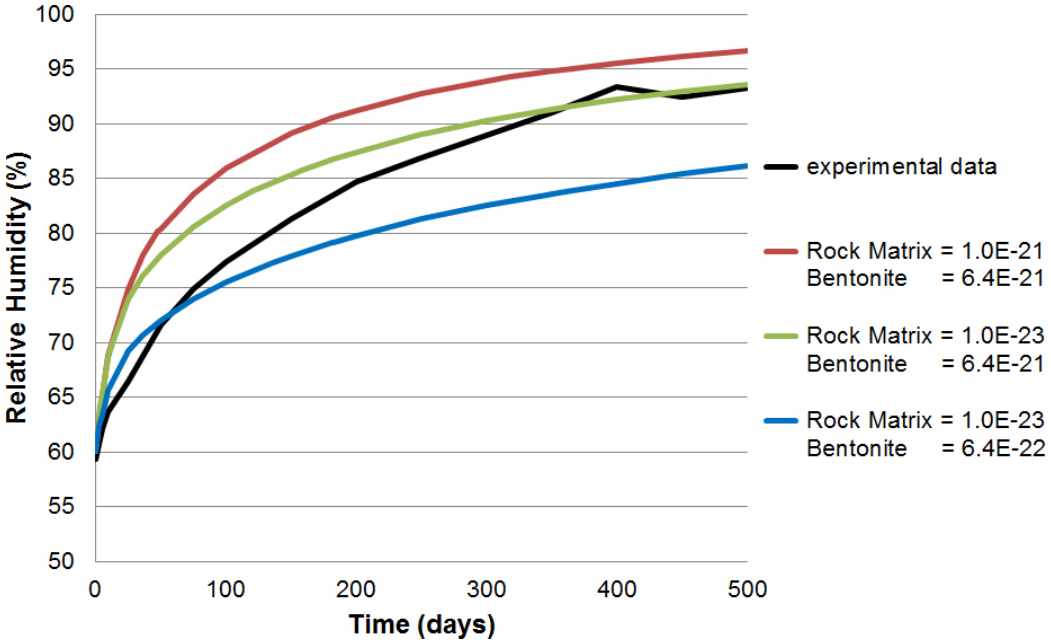

Figure 7-9. *The evolution of relative humidity calculated at sensor location WBR0009 within the bentonite during the first 500 days post installation. Results are presented for three model variants: rock matrix permeability of 1×10^{-21} m^2, bentonite permeability of 6.4×10^{-21} m^2 (red); rock matrix permeability of 1×10^{-23} m^2, bentonite permeability of 6.4×10^{-21} m^2 (green); rock matrix permeability of 1×10^{-23} m^2, bentonite permeability of 6.4×10^{-22} m^2 (blue). Measurements from the BRIE experiment are coloured black.*

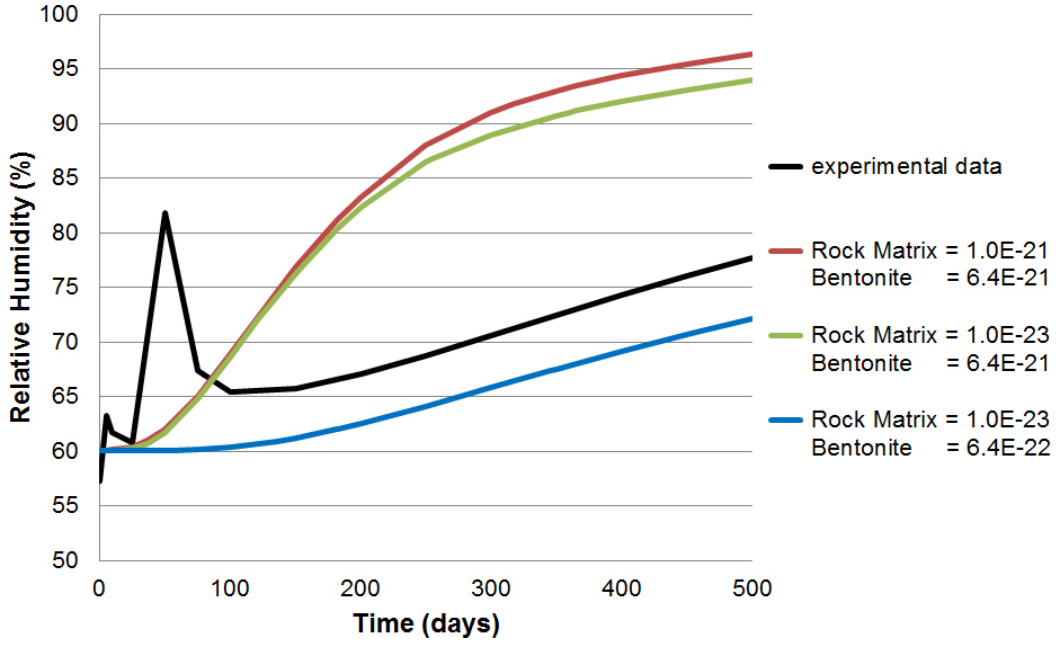

Figure 7-10. *The evolution of relative humidity calculated at sensor location WBR0010 within the bentonite during the first 500 days post installation. Results are presented for three model variants: rock matrix permeability of 1×10^{-21} m^2, bentonite permeability of 6.4×10^{-21} m^2 (red); rock matrix permeability of 1×10^{-23} m^2, bentonite permeability of 6.4×10^{-21} m^2 (green); rock matrix permeability of 1×10^{-23} m^2, bentonite permeability of 6.4×10^{-22} m^2 (blue). Measurements from the BRIE experiment are coloured black.*

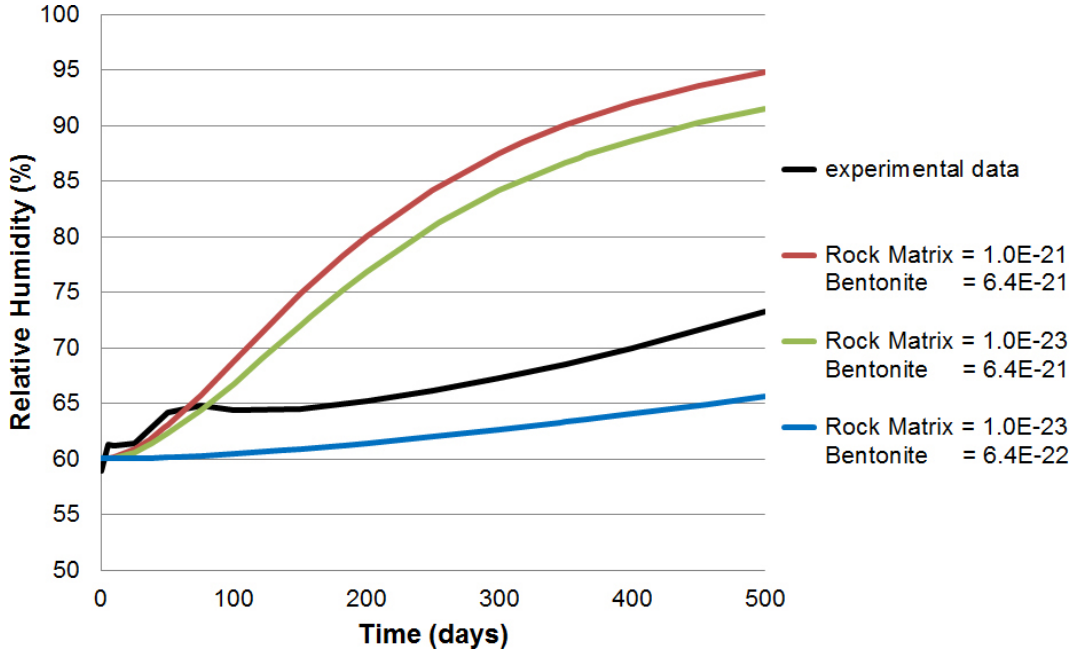

Figure 7-11. *The evolution of relative humidity calculated at sensor location WBR0011 within the bentonite during the first 500 days post installation. Results are presented for three model variants: rock matrix permeability of 1×10^{-21} m^2, bentonite permeability of 6.4×10^{-21} m^2 (red); rock matrix permeability of 1×10^{-23} m^2, bentonite permeability of 6.4×10^{-21} m^2 (green); rock matrix permeability of 1×10^{-23} m^2, bentonite permeability of 6.4×10^{-22} m^2 (blue). Measurements from the BRIE experiment are coloured black.*

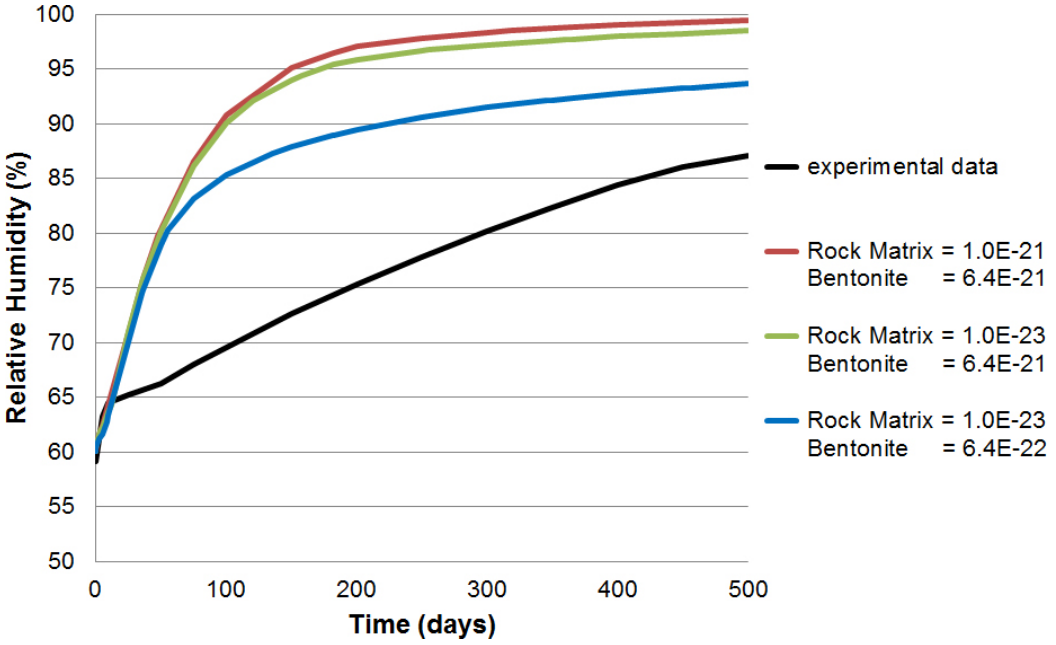

Figure 7-12. *The evolution of relative humidity calculated at sensor location WBR0012 within the bentonite during the first 500 days post installation. Results are presented for three model variants: rock matrix permeability of 1×10^{-21} m^2, bentonite permeability of 6.4×10^{-21} m^2 (red); rock matrix permeability of 1×10^{-23} m^2, bentonite permeability of 6.4×10^{-21} m^2 (green); rock matrix permeability of 1×10^{-23} m^2, bentonite permeability of 6.4×10^{-22} m^2 (blue). Measurements from the BRIE experiment are coloured black.*

8 Discussion and conclusions

This report has demonstrated the feasibility of using a physically realistic approach to simulate the rock bentonite interface through modelling Task 8D and the BRIE. This approach explicitly represents the heterogeneity of the fractured bedrock necessary to accurately predict resaturation times and profiles of emplaced bentonite (Baxter et al. 2013). In addition methodologies have been developed for calibrating and conditioning models of the fractured rock using additional site measurements as they become available. In summary:

- Experimental data from the BRIE illustrates the heterogeneity of bentonite resaturation from a fractured host rock. Therefore, the accurate representation of the fractured bedrock surrounding the emplaced bentonite is critical to understanding hydration rates and profiles:
  - Previously, Task 8C developed models of the BRIE using limited data. As part of Task 8D, additional measurements are available, typical of the additional data generated during repository construction in support of siting decision for deposition holes. Using this new information, both the fracture network geometry and the hydraulic properties of the Task 8C models have been refined. This refinement of the stochastic DFN model identified:
    - The need to correctly represent the intensity of the fractured rock across the modelling domain. If the fracture intensity is too high, the network will become overly connected, increasing inflows to the deposition holes and tunnels. For the fracture sizes considered in this study, it is necessary to accurately represent the fracture frequency a few tens of metres away from the deposition holes or tunnels of interest.
    - The need to understand the location of high transmissivity large-scale deterministic features such as deformation zones. These structures can form the primary flow conduit through the fractured rock and as such their parameterisation is important, especially if they pass close to / intersect a deposition hole or tunnel of interest.
- The developed approach has identified the significant potential of the combination of CONNECTFLOW and TOUGH2 software to simulate the heterogeneous hydration of the bentonite:
  - During the Task 8C study, the saturation rate of bentonite via a fractured host rock was found to be significantly affected by both the locations and total volume of groundwater ingress to the deposition holes. During the modelling of Task 8D, water producing intersections within the deposition holes have been specified deterministically. Through conditioning the local fracture network, the resaturation rates and profiles of emplaced bentonite can be further constrained.
- Although reducing uncertainty in resaturation profiles and times, there are still significant differences between realisations of the calibrated and conditioned DFN model, with times for 95 % liquid saturation varying on the order of tens of years.
- The permeability of the rock matrix very strongly determines the prediction of the resaturation times of the emplaced bentonite. Therefore this has implication for the local characterisation of the host rock. Unfortunately, the data concerning the rock ‘matrix’ permeability corresponds to the unstressed core plug taken from deposition holes KO0017G01 and KO0018G01. The reduction in permeability when applying *in situ* stress conditions is uncertain.

8.1 Evaluation of conceptual models and modelling approach

The following discussion covers quantitative and qualitative analysis of the Task 8D modelling performed in this report, responding to key questions identified as part of the task description (Vidstrand et al. 2017).

8.1.1 Quantitative results

What is the range of predicted inflows into an open deposition hole?

After calibration of the DFN model, four of the ten realisations of the stochastic DFN model provide hydraulic connections to both overcored boreholes KO0017G01 and KO0018G01. Inflows to open deposition holes for these four realisations are

- KO0017G01: 0.20 ml/min–0.29 ml/min, and
- KO0018G01: 0.01 ml/min–0.10 ml/min.

Of these four realisations (1, 2, 7 and 9), the second and seventh realisations simulate inflows within the bounds estimated from measurements of 0.12 ml/min–0.25 ml/min for KO0017G01, and 0.01 ml/min–0.03 ml/min for KO0018G01.

What is the range of predicted times needed to rewet the bentonite to a saturation of 95 %?

For the two realisations of the conditioned and calibrated stochastic fracture network which predict inflows to overcored deposition holes KO0017G01 and KO0018G01 within the bounds measured, resaturation calculations are performed. For these, the following range of times are calculated for 95 % liquid saturation to be reached

- KO0017G01: 79.3 years and 100 + years (note 95 % liquid saturation is not reached before the end of the simulation), and
- KO0018G01: 60.8 years and 72.9 years.

Despite larger inflows to KO0017G01, resaturation times are longer due to its increased volume (~ 0.25 m^3 compared to ~ 0.21 m^3 for KO0018G01). In addition, these resaturation times are calculated using a rock matrix permeability of 1×10^{-21} m^2 (as specified in Task 8C). The rock matrix permeability has been observed to have a significant effect on resaturation rates of the bentonite.

8.1.2 Qualitative discussion

What are the key features and properties of the natural and engineered systems that need to be known for deposition hole screening?

Although total inflow to a deposition hole is an important factor when screening holes suitable for disposal, the distribution of these inflows is also significant. This effect was first observed in the Task 8C modelling (Baxter et al. 2013). The bentonite has very low permeability, and consequently the time taken for 95 % liquid saturation to be reached over the entire bentonite stack will be significantly longer if inflows are concentrated towards the bottom of the hole compared to an even distribution over a number of fractures intersecting along the length of the hole.

The background permeability of the rock matrix is also significant for the screening of deposition holes, with resaturation times and profiles of emplaced bentonite very sensitive to changes in the rock matrix parameterisation. Consequently, characterisation of the rock matrix local to the deposition holes is also required.

What information and data from the BRIE experiment are most valuable for the overall system understanding, and model development?

When calculating resaturation rates and profiles of bentonite emplaced within a deposition hole, the following aspects are critical for accurate predictions:

- At Äspö, groundwater flow is predominately through a series of interconnected fractures. Characterisation of geometric and hydraulic properties of the fracture network is important to resaturation, providing:
  - a global scale analysis required for fractures statistics of the background fracture network, and
  - a local scale analysis required for conditioning individual deposition holes, and their hydraulic connections to the wider fracture network.
- Rock matrix permeability, measured at *in situ* stress conditions is critical to understanding resaturation rates.

- The resaturation of the emplaced bentonite is highly sensitivity to the characterisation of the bentonite (e.g. permeability).
- The relative importance of the fracture, rock mass and bentonite properties are:
  - **Local scale Vs. global scale fractures:** Resaturation of the emplaced bentonite is mostly constrained by the local scale fractures intersecting the deposition hole. The global scale stochastic fracture network is significant insofar as the hydraulic connectivity it provides to the local structures.
  - **Fractures Vs. rock matrix:** Where inflows to the deposition hole occur over a number of fractures distributed uniformly across the hole, resaturation is dominated by the fracture properties and the rock matrix is less significant to resaturation. The rock matrix will become increasingly important as the inflow is concentrated to fewer fractures intersecting the deposition hole.
  - **Rock mass Vs bentonite:** The sensitivity cases considered as part of this study are not sufficient to identify either the rock mass or bentonite parameterisation as most significant to resaturation of the emplaced bentonite. The relative importance of these factors is a balance between the host rock's capability to provide groundwater to the deposition holes; and the bentonite's ability to uptake this water. Further consideration of these two factors could be considered as part of the follow-up modelling task, Task 8F.

How does the conceptualization of the natural and engineered systems influence model predictions, and interpretation of the expected system behaviour?

The BRIE at Äspö Hard Rock Laboratory is located in granitic bedrock, with groundwater flow primarily through a series of interconnected, flow-conducting fractures. By applying a DFN concept, it is possible to represent

- the groundwater pathway statistically between interconnected fractures in the rock mass, and
- the inflow locations interpreted within individual deposition holes deterministically.

This DFN model can then be upscaled to equivalent block permeabilities and porosities, providing a highly heterogeneous description of the fractured rock for use in resaturation calculations.

An alternative approach, representing the host rock using homogeneous permeability values, was considered as part of the Task 8C modelling (Baxter et al. 2013). This representation was insufficient to fully capture the heterogeneous processes that occur during bentonite resaturation. In addition, the model systematically over predicts the resaturation rate of the bentonite.

8.1.3 Comparison to experimental results

The models developed as part of this report formed predictions supplied to the SKB EBS Task Force regarding the resaturation of bentonite emplaced in the central deposition holes. To refine predictions, models of the fractured bedrock are calibrated and conditioned based on characterisation of the fracture network local to both the TASO tunnel and central deposition holes, as well as inflow measurements. In addition, a series of sensitivity cases have also been considered, evaluating effects of alternative parameterisation of the rock matrix permeability (1×10^{-23} m^2) and bentonite permeability (6.4×10^{-22} m^2).

Upon completion of the predictive modelling exercise, the evolution of relative humidity within the bentonite installations were provided to modelling groups participating in the EBS Task Force at twelve sensor locations. Typically the sensitivity cases considered in this report are found to bound the experimental data based on the modelling assumptions made; and as expected, the bentonite resaturation was shown to be most sensitive to variations in the bentonite permeability considered. It is anticipated that further refinement of the rock matrix and bentonite permeabilities, or other model parameters (such as retention properties) could enhance model predictions of resaturation. In addition, the modelling assumptions should be reviewed and amended using additional data available to characterise the BRIE (e.g. a refined model for water-producing fractures intersecting the deposition holes). This model refinement could form part of a follow-up modelling task, Task 8F, utilising all characterisation data available upon dismantling the BRIE experiment.

8.2 Main conclusions

Using a physically realistic approach, this study has simulated the resaturation of emplaced bentonite from a fractured host rock. The main conclusions from this study are:

- Characterisation of the geometric and hydraulic properties of the fracture network is important to understanding resaturation characteristics of the bentonite. This is especially important for the near-field fractures (i.e. those intersecting) the deposition hole. The methodologies developed in this study extend the modelling work from Task 8C (Baxter et al. 2013); calibrating and conditioning models of the fractured rock based on additional information, typical of data generated during repository construction in support of siting deposition holes.
- By calibrating and conditioning the underlying fracture network, uncertainty in the resaturation rates and profiles of the bentonite can be substantially reduced:
  - For the purely stochastic Task 8C simulations, the range of resaturation rates (to 95 % liquid saturation) for KO0018 ranged from 6 years up to 62 years.
  - By conditioning and calibrating the fracture network, the range of resaturation rates for KO0018 is reduced to between 61 and 73 years. However variations in resaturation due to statistical uncertainties in the far-field fracture network are still significant.
- Sensitivity analysis highlights the importance of correctly constraining the parameterisation of both the bentonite and rock matrix on the overall resaturation times of the bentonite.
- On comparison to experimental results:
  - For KO0017, experimental measurements of relative humidity from within the bentonite are consistent with the locations and magnitudes of inflows expected from the fractures characterised in the overcored drillhole. In addition, model variants are shown to bound observations.
  - For KO0018, experimental measurements of relative humidity are generally not consistent with the water bearing fracture characterisations performed. One possible explanation for this would be if additional water bearing fractures exist in KO0018 which are below the detection limit of characterisation methods performed. The EBS Task Force intends to explore this possibility through a final modelling task, Task 8F.

8.3 Potential model development

8.3.1 Heterogeneity of the rock matrix

Parameterisation of the rock matrix has repeatedly been found critical to the resaturation times of bentonite emplaced within a sparsely fractured host rock. Present models consider the rock matrix as a homogeneous unit, with permeabilities typically around 1×10^{-21} m^2. However, spatial variations in the rock matrix, caused by changes in the lithology or *in situ* stress could be adopted in the model, and used to adjust the rock matrix parameterisation on an element-by-element basis. This additional heterogeneity will significantly affect the resaturation profiles and times, with the most significant affects in the 'dry' section of the overcored holes located far from the water bearing fractures. For example, in section 6.2.5, resaturation rates recorded at sensor locations at distance from the observed water bearing fractures (e.g. Figure 7-4 through Figure 7-6) were significantly affected when varying the homogeneous rock matrix permeability from 1×10^{-21} m^2 to $1\,10^{-23}$ m^2; providing an indication of the range of resaturation that could be expected from a heterogeneous rock matrix.

8.3.2 Heterogeneity of inflows to the deposition holes

It is clear that a detailed understanding of the inflow to the deposition hole will be necessary to predict the evolution of the saturation of the bentonite. In particular, it is likely a micro-structural model is needed to fully simulate the resaturation of bentonite as inflow for the fracture is likely to be at a series of discrete points. There is potential for this micro-structural model to significantly affect the resaturation time of emplaced bentonite. One possibility for including such an affect is to parameterise each fracture within the DFN model with heterogeneous hydraulic properties; i.e. each fracture will be sub-divided geometrically into a number of tessellates, and the hydraulic properties specified independently for each tessellate of the fracture (e.g. like a checkerboard). This heterogeneity across each fracture would provide a method for varying the hydraulic performance of the fracture at the bentonite interface; consequently varying the capability of the fracture to provide groundwater to the bentonite along the intersection.

9 Acknowledgements

AMEC would like to thank RWM for providing financial support to our participation in the SKB EBS Task Force, and Stefan Finsterle for providing a review of this study as part of the Task Force, and whose comments have been incorporated into this report.

AMEC would also like to thank SKB and Clay Technology for creating an open and engaging environment to allow modelling studies to thrive.

References

SKB's (Svensk Kärnbränslehantering AB) publications can be found at www.skb.com/publications.

AMEC, 2012a. CONNECTFLOW technical summary, Release 10.4. AMEC/ENV/CONNECTFLOW/15, AMEC, UK.

AMEC, 2012b. NAMMU technical summary, Release 10.4. AMEC/ENV/CONNECTFLOW/8, AMEC, UK.

AMEC, 2012c. NAPSAC technical summary, Release 10.4. AMEC/ENV/CONNECTFLOW/12, AMEC, UK.

AMEC, 2012d. CONNECTFLOW verification, Release 10.4. AMEC/ENV/CONNECTFLOW/16, AMEC, UK.

Andersson J C, 2007. Äspö Hard Rock Laboratory. Äspö Pillar Stability Experiment, Final report. Rock mass response to coupled mechanical thermal loading. SKB TR-07-01, Svensk Kärnbränslehantering AB.

Baxter S, Holton D, Hoch A R, 2013. Modelling Task 8. Understanding the BRIE experiment. AMEC Report D.005529/13/01, AMEC, UK.

Cussler E L, 1984. Diffusion: mass transfer in fluid systems. Cambridge: Cambridge University Press.

Fatt I, Klikoff W A, 1959. Effect of fractional wettability on multiphase flow through porous media. AIME Transactions 216, 426–432.

Gordon A, Hoch A, Holton D, Baxter S, 2014. Task Force on engineered barrier systems – Sensitivity analysis: Verification and sensitivity cases. AMEC Report 103453-AG-0001/SV012013/1, AMEC, UK.

Han P, Bartels D M, 1996. Temperature dependence of oxygen diffusion in H_20 and D_20. Journal of Physical Chemistry 100, 5597–5602.

Hartley L, Appleyard P, Baxter S, Hoek J, Roberts D, Swan D, 2013. Development of a Hydrogeological Discrete Fracture Network Model for the Olkiluoto Site Descriptive Model 2011, Volume I and II. Posiva Working Report 2012-32, Posiva Oy, Finland.

Hawkins I R, Swift B T, 2009. Simulation HS-PS2: La définition et la comparaison des différentes representations de l'EDZ vis-à-vis du transitoire hydraulique et de la migration des gaz. SERCO/TAS/002738/003, Serco, UK. (In French.)

Hjerne C, Nordqvist R, Harrström J, 2010. Compilation and analyses of results from cross-hole tracer tests with conservative tracers. SKB R-09-28, Svensk Kärnbränslehantering AB.

Hoch A R, James M, 2011. Gas migration and rock-matrix diffusion. SERCO/TAS/000450/001, Serco, UK.

Holton D, Baxter S, Hoch A R, 2012. Modelling coupled processes in bentonite: recent results from the UK's contribution to the Äspö EBS Task Force. Mineralogical Magazine 76, 2865–2871.

Jackson C P, Hoch A R, Todman S, 2000. Self-consistency of a heterogeneous continuum porous medium representation of a fractured medium. Water Resources Research 36, 189–202.

Joyce S, Simpson T, Hartley L, Applegate D, Hoek J, Jackson P, Swan D, Marsic N, Follin S, 2010. Groundwater flow modelling of periods with temperate climate conditions – Forsmark. SKB R-09-20, Svensk Kärnbränslehantering AB.

Kasenow M, 2001. Applied ground-water hydrology and well hydraulics. 2nd ed. Highlands Ranch, CO: Water Resources Publications.

Luckner L, van Genuchten M T, Nielsen D R, 1989. A consistent set of parametric models for the two-phase flow of immiscible fluids in the subsurface. Water Resources Research 25, 2187–2193.

Marrero T R, Mason E A, 1972. Gaseous diffusion coefficients. Journal of Physical and Chemical Reference Data 1. doi:http://dx.doi.org/10.1063/1.3253094

NDA, 2010. Geological disposal: generic disposal facility designs. NDA/RWMD/048, Nuclear Decommissioning Authority, UK.

NDA, 2012. Project Ankhiale: Disposability and full life cycle implications of high heat generating UK wastes, Roadmap. Issue 1. Nuclear Decommissioning Authority, UK.

Oldenburg C M, Pruess K, 1995. EOS7R: Radionuclide Transport for TOUGH2. Report LBL-34868, Lawrence Berkeley National Laboratory, Berkeley, CA.

Olivella S, Gens A, 2000. Vapour transport in low permeability unsaturated soils with capillary effects. Transport in Porous Media 40, 219–241.

Pruess K, Oldenburg C, Moridis G, 1999. TOUGH2 User's Guide – Version 2. Report LBNL-43134, Lawrence Berkeley National Laboratory, Berkeley, CA.

Rhén I, Forsmark T, Hartley L, Joyce S, Roberts D, Gylling B, Marsic N, 2009. Bedrock Hydrogeolology. Model testing and synthesis. Site descriptive modelling, SDM-Site Laxemar. SKB R-08-91, Svensk Kärnbärnslehantering AB.

SKB, 2006. Long-term safety for KBS-3 repositories at Forsmark and Laxemar – a first evaluation. Main report of the SR-Can project. SKB TR-06-09, Svensk Kärnbärnslehantering AB.

Terzaghi R, 1965. Sources of error in joint surveys. Géotechnique 15, 287–304.

van Genuchten M T, 1980. A closed-form equation for predicting the hydraulic conductivity of unsaturated soils. Soil Science Society of America Journal 44, 892–898.

Vidstrand P, Åkesson M, Fransson Å, Stigsson M, 2017. Task 8 of SKB Task Forces EBS and GWFTS: Modelling the interaction between engineered and natural barriers - An assessment of a fractured bedrock description in the wetting process of bentonite at deposition tunnel scale. A compilation of Task 8 descriptions. SKB P-16-05, Svensk Kärnbränslehantering AB.

Vilks P, 2007a. Forsmark site investigation. Rock matrix permeability measurements on core samples from borehole KFM01D. SKB P-07-162, Svensk Kärnbränslehantering AB.

Vilks P, 2007b. Oskarshamn site investigation. Rock matrix permeability measurements on core samples from borehole KLX03. SKB P-07-204, Svensk Kärnbränslehantering AB.

Wilson J, Savage D, Bond A, Watson S, Pusch R, Bennett D, 2010. Bentonite: a review of key properties, processes and issues for consideration in the UK context. QRS-1378ZG-1, Version 1.0, Quintessa Ltd., UK.

Appendix 1

Task 8D1: Calibration of the Fracture Network

Pressure build-up in the probe boreholes

Results correspond to pressure build-up in each of the five probe boreholes KO0014G01, KO0015G01, KO0017G01, KO0018G01 and KO0020G01. Each borehole is packed off to 1 m below the base of the TASO tunnel. Results are presented for ten realisations of the stochastic fracture network, with simulations performed for each of the model cases considered during the calibration phase of Task 8D.

Effects of fracture intensity

Figure A1-1 illustrates pressure build-up in each of the probe boreholes for each of the ten realisations. Results are shown for model cases

- Basecase,
- Variant 1, and
- Variant 2.

For details of the simulations, and definition of the model cases, the reader is referred to Section 5.1.1.

Effects of the fracture transmissivity model

Figure A1-2 illustrates pressure build-up in each of the probe boreholes for each of the ten realisations. Results are shown for model cases

- Basecase,
- Variant 2, and
- Variant 3.

For details of the simulations, and definition of the model cases, the reader is referred to Section 5.1.2.

Effects of an alternative geometry of wfracture_01

Figure A1-3 illustrates pressure build-up in each of the probe boreholes for each of the ten realisations. Results are shown for model cases

- Basecase,
- Variant 3, and
- Variant 4.

For details of the simulations, and definition of the model cases, the reader is referred to Section 5.1.3.

Effects of constraining intersections in KO0017G01 and KO0018G01

Figure A1-4 illustrates pressure build-up in each of the probe boreholes for each of the ten realisations. Results are shown for model cases

- Basecase,
- Variant 3, and
- Variant 5.

For details of the simulations, and definition of the model cases, the reader is referred to Section 5.1.4.

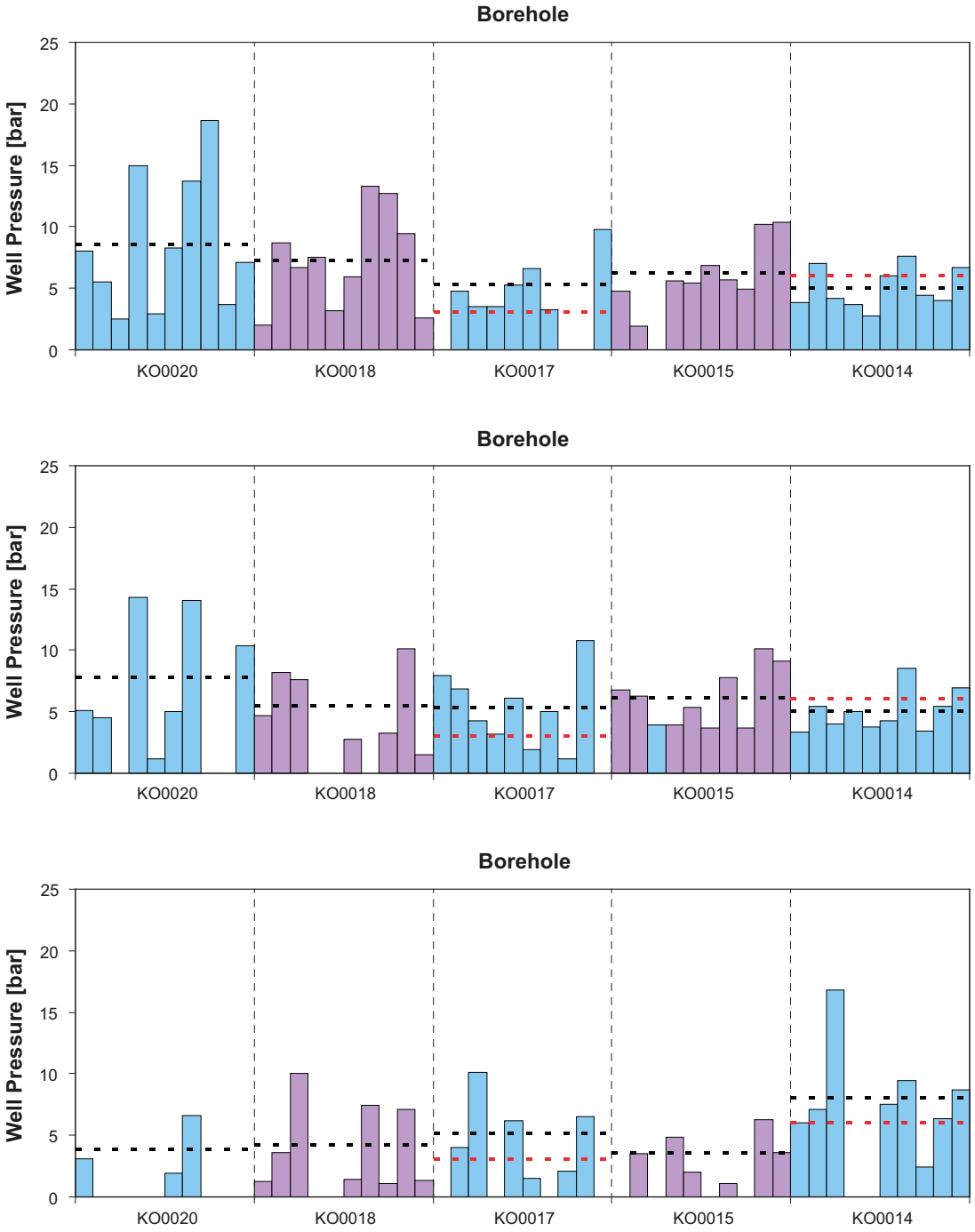

Figure A1-1. *Pressure build-up to 76 mm probe boreholes, packed off to a depth of 1 m below the TASO tunnel. Results are shown for ten realisations of each model case, top: Basecase; middle: Variant 1; and bottom: Variant 2. The black dashed lines represent average pressures to each probe borehole, calculated over the DFN realisations where the borehole connects to the wider fracture network. The red dashed line corresponds to measurements.*

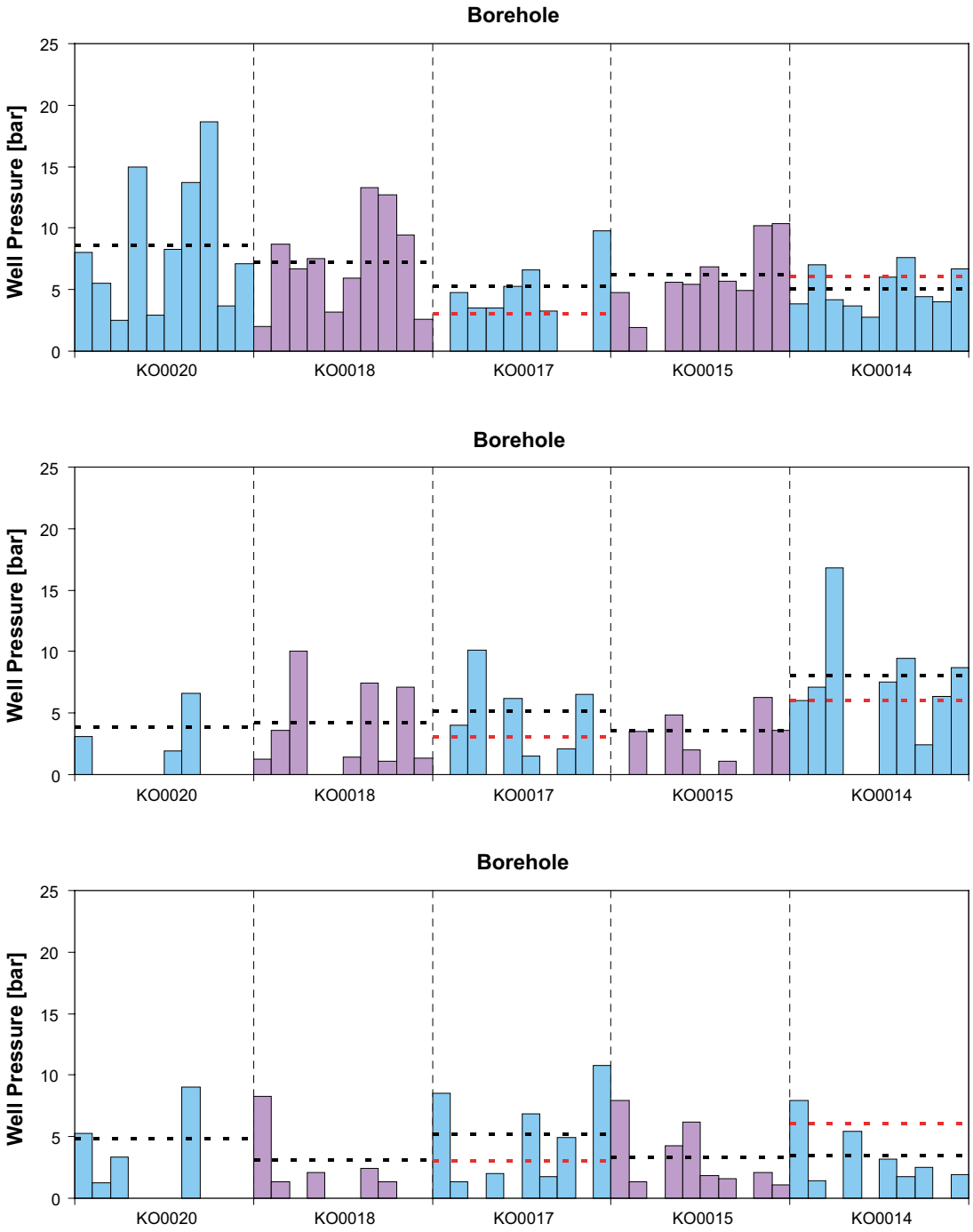

Figure A1-2. *Pressure build-up to 76 mm probe boreholes, packed off to a depth of 1 m below the TASO tunnel. Results are shown for ten realisations of each model case, top: Basecase; middle: Variant 2; and bottom: Variant 3. The black dashed lines represent average pressures to each probe borehole, calculated over the DFN realisations where the borehole connects to the wider fracture network. The red dashed line corresponds to measurements.*

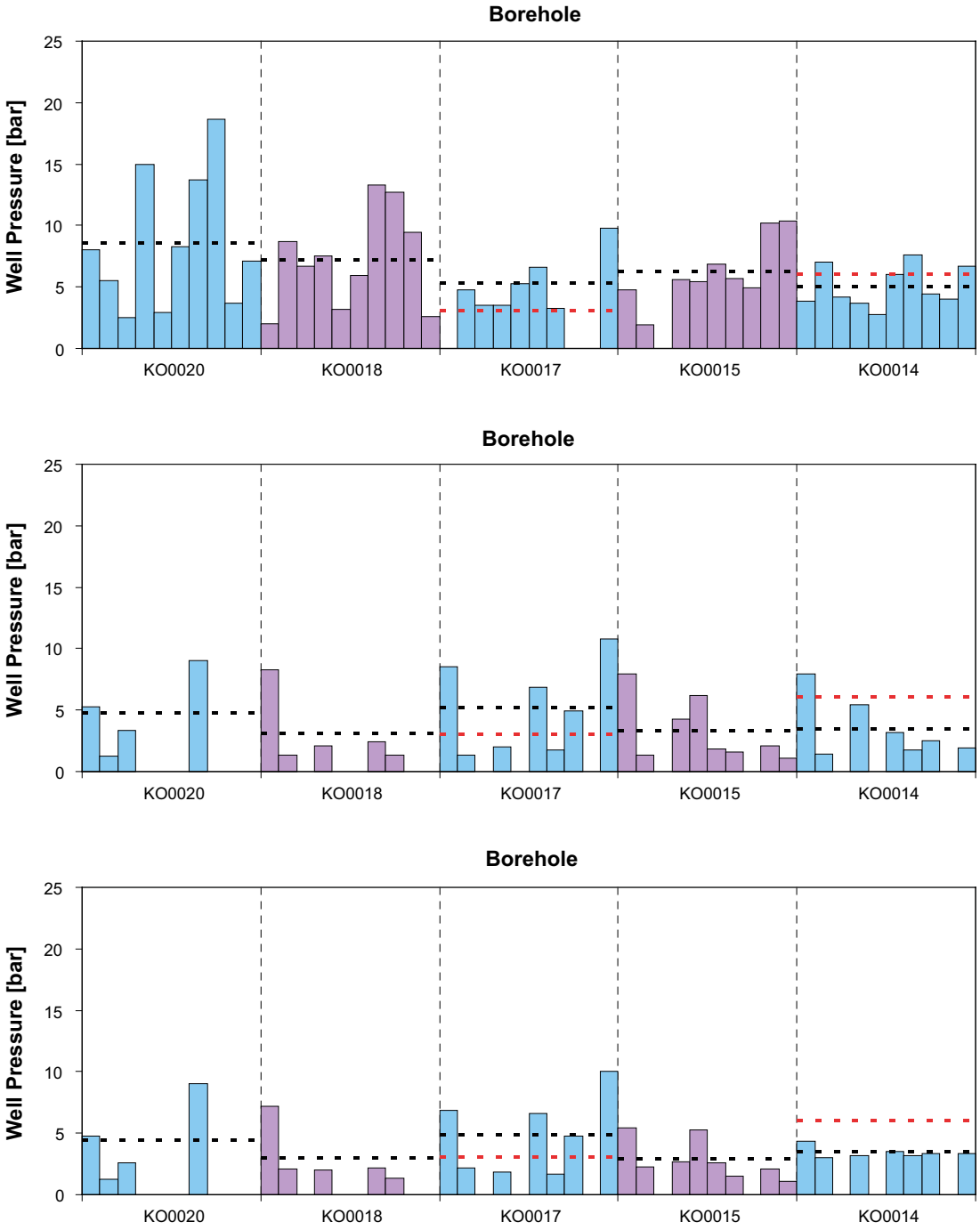

Figure A1-3. *Pressure build-up to 76 mm probe boreholes, packed off to a depth of 1 m below the TASO tunnel. Results are shown for ten realisations of each model case, top: Basecase; middle: Variant 3; and bottom: Variant 4. The black dashed lines represent average pressures to each probe borehole, calculated over the DFN realisations where the borehole connects to the wider fracture network. The red dashed line corresponds to measurements.*

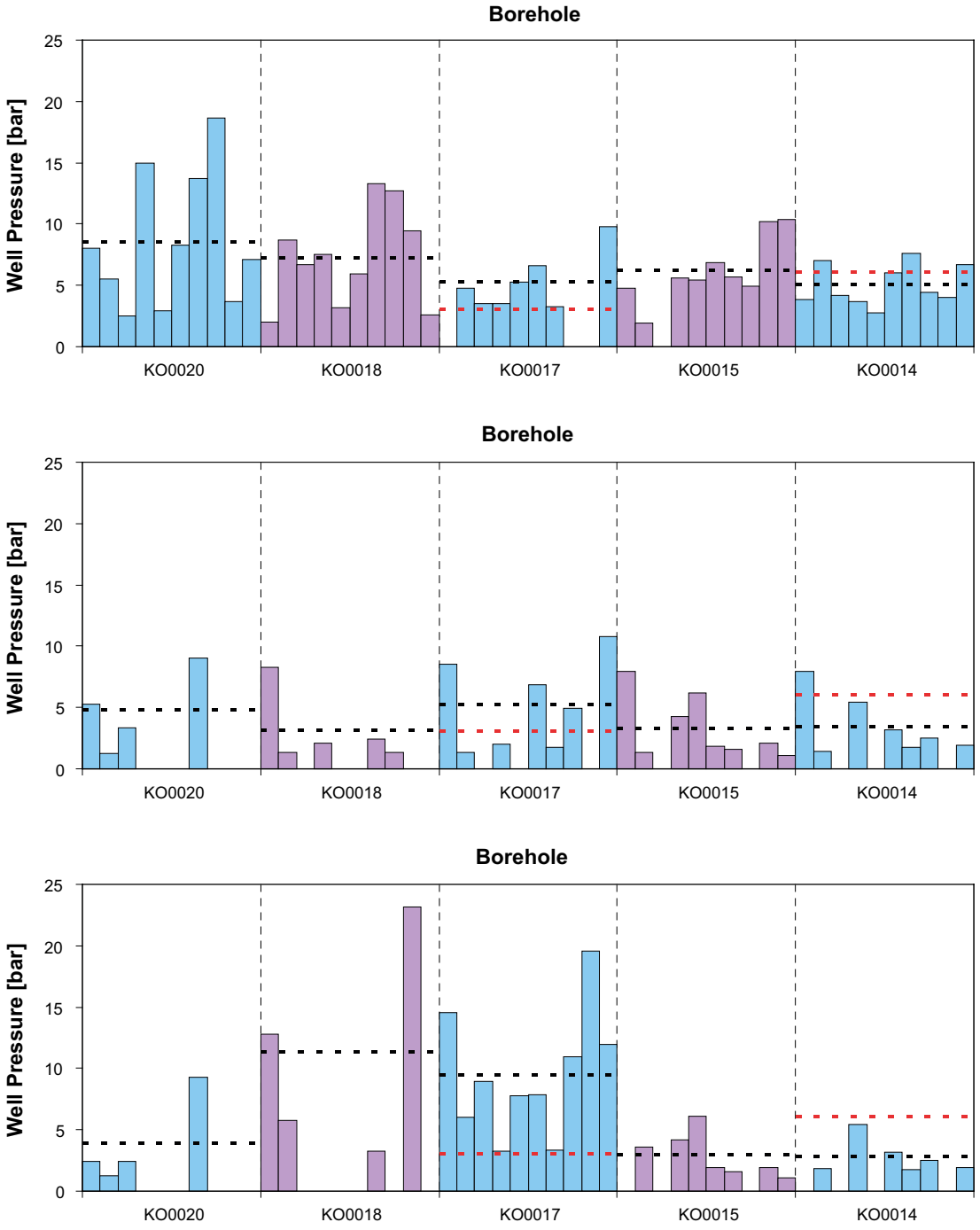

Figure A1-4. *Pressure build-up to 76 mm probe boreholes, packed off to a depth of 1 m below the TASO tunnel. Results are shown for ten realisations of each model case, top: Basecase; middle: Variant 3; and bottom: Variant 5. The black dashed lines represent average pressures to each probe borehole, calculated over the DFN realisations where the borehole connects to the wider fracture network. The red dashed line corresponds to measurements.*

Inflows to the probe boreholes

Results correspond to inflows to each of the five probe boreholes KO0014G01, KO0015G01, KO0017G01, KO0018G01 and KO0020G01. Each borehole is opened in turn to atmospheric conditions in the TASO tunnel. Results are presented for ten realisations of the stochastic fracture network, with simulations performed for each of the model cases considered during the calibration phase of Task 8D.

Effects of fracture intensity

Figure A1-5 illustrates inflows to each of the probe boreholes for each of the ten realisations. Results are shown for model cases

- Basecase,
- Variant 1, and
- Variant 2.

For details of the simulations, and definition of the model cases, the reader is referred to Section 5.1.1.

Effects of the fracture transmissivity model

Figure A1-6 illustrates inflows to each of the probe boreholes for each of the ten realisations. Results are shown for model cases

- Basecase,
- Variant 2, and
- Variant 3.

For details of the simulations, and definition of the model cases, the reader is referred to Section 5.1.2.

Effects of an alternative geometry of wfracture_01

Figure A1-7 illustrates inflows to each of the probe boreholes for each of the ten realisations. Results are shown for model cases

- Basecase,
- Variant 3, and
- Variant 4.

For details of the simulations, and definition of the model cases, the reader is referred to Section 5.1.3.

Effects of constraining intersections in KO0017G01 and KO0018G01

Figure A1-8 illustrates inflows to each of the probe boreholes for each of the ten realisations. Results are shown for model cases

- Basecase,
- Variant 3, and
- Variant 5.

For details of the simulations, and definition of the model cases, the reader is referred to Section 5.1.4.

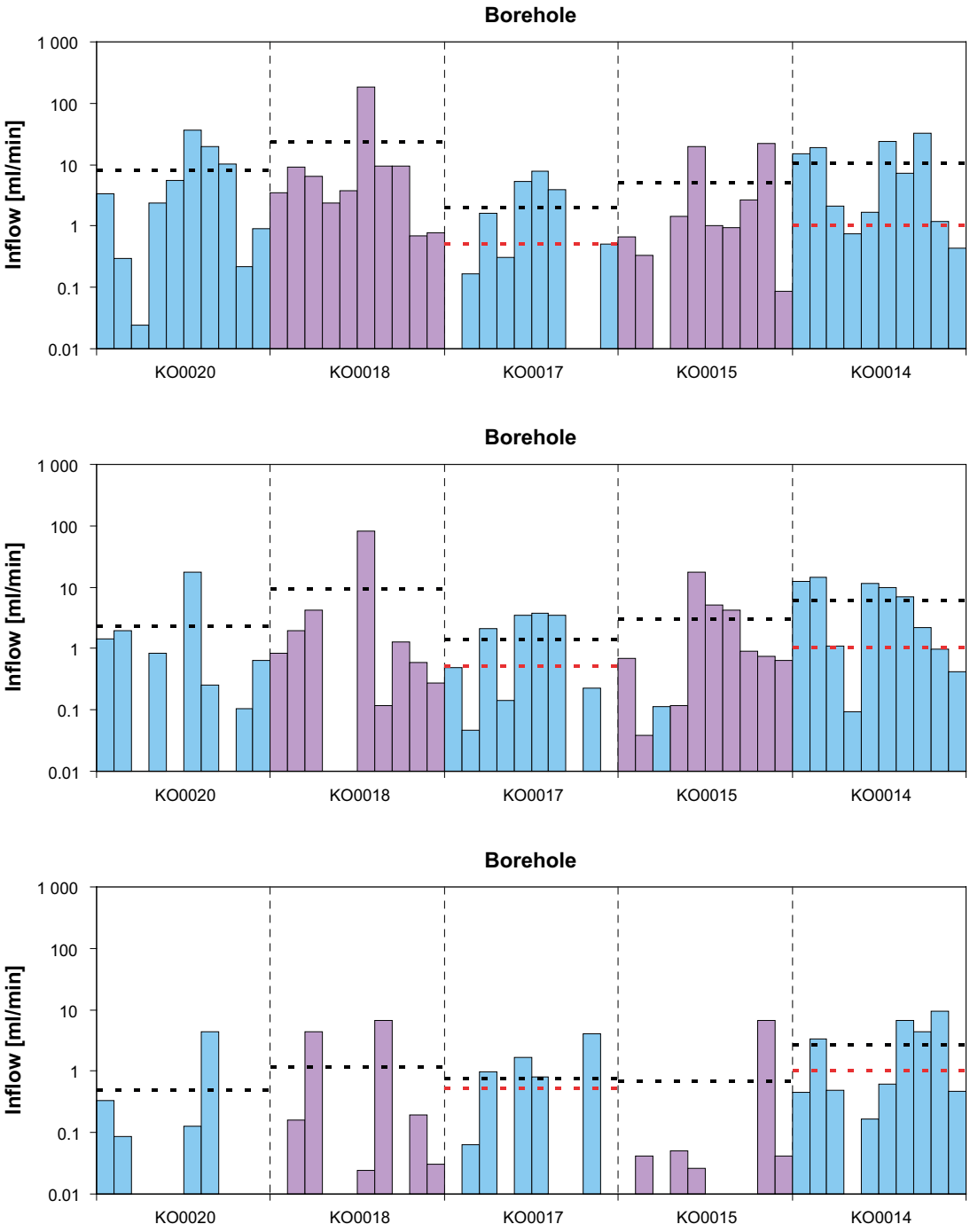

Figure A1-5. *Inflows to 76 mm probe boreholes, opened to the TASO tunnel which is at atmospheric conditions. Results are shown for ten realisations of each model case, top: Basecase; middle: Variant 1; and bottom: Variant 2. The black dashed lines represent inflows to each probe borehole, averaged over the 10 realisations. The red dashed line corresponds to measurements.*

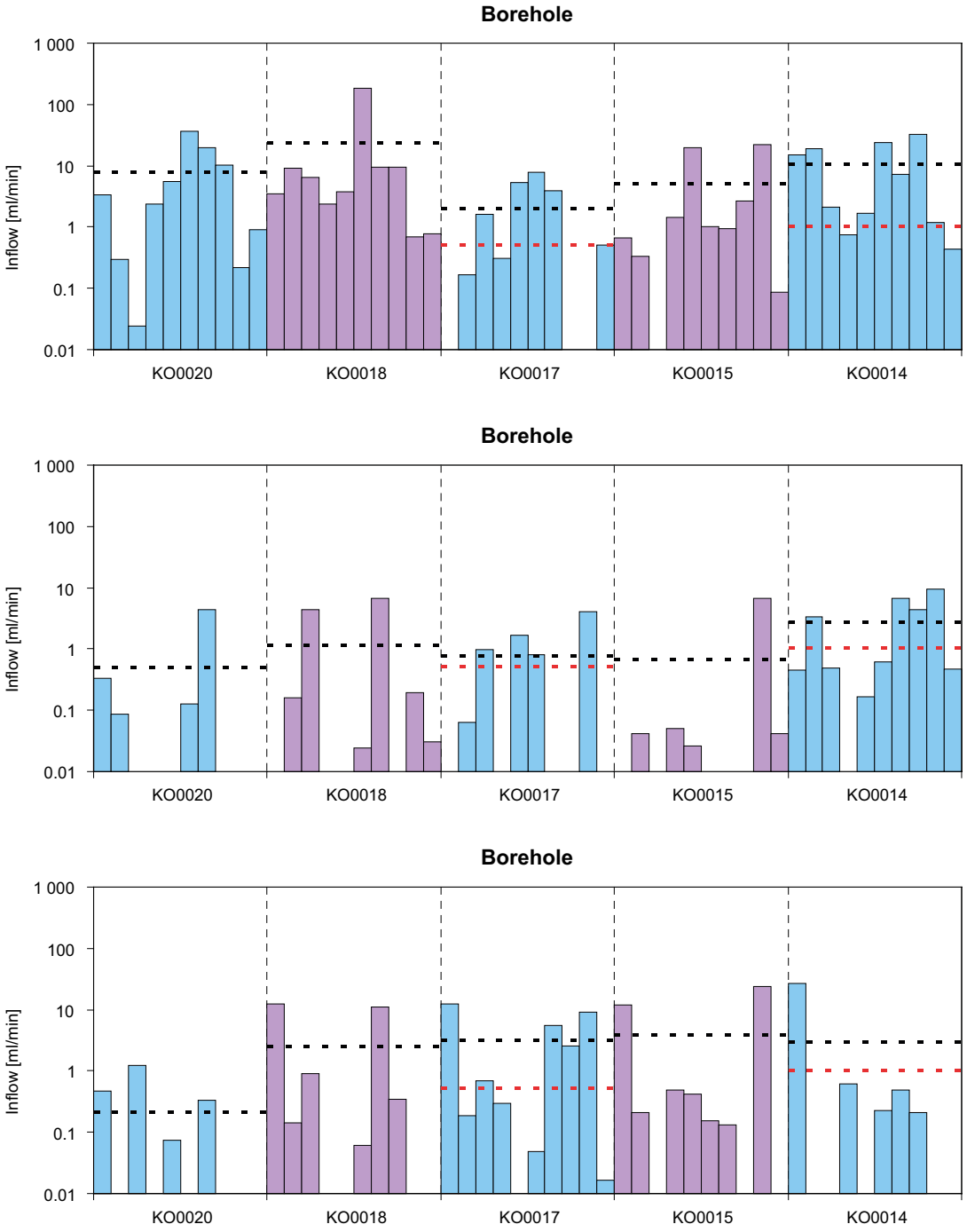

Figure A1-6. *Inflows to 76 mm probe boreholes, opened to the TASO tunnel which is at atmospheric conditions. Results are shown for ten realisations of each model case, top: Basecase; middle: Variant 2; and bottom: Variant 3. The black dashed lines represent inflows to each probe borehole, averaged over the 10 realisations. The red dashed line corresponds to measurements.*

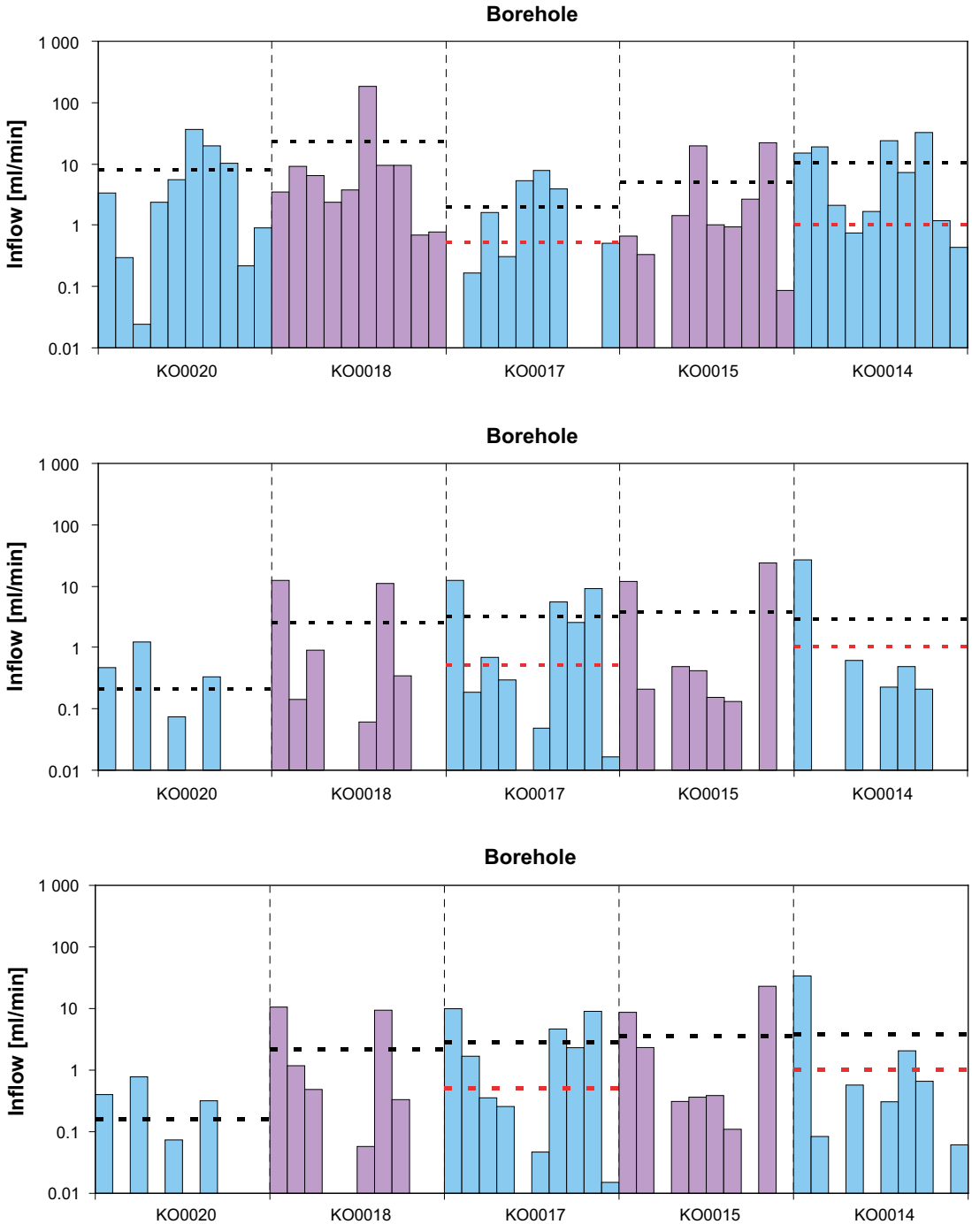

Figure A1-7. *Inflows to 76 mm probe boreholes, opened to the TASO tunnel which is at atmospheric conditions. Results are shown for ten realisations of each model case, top: Basecase; middle: Variant 3; and bottom: Variant 4. The black dashed lines represent inflows to each probe borehole, averaged over the 10 realisations. The red dashed line corresponds to measurements.*

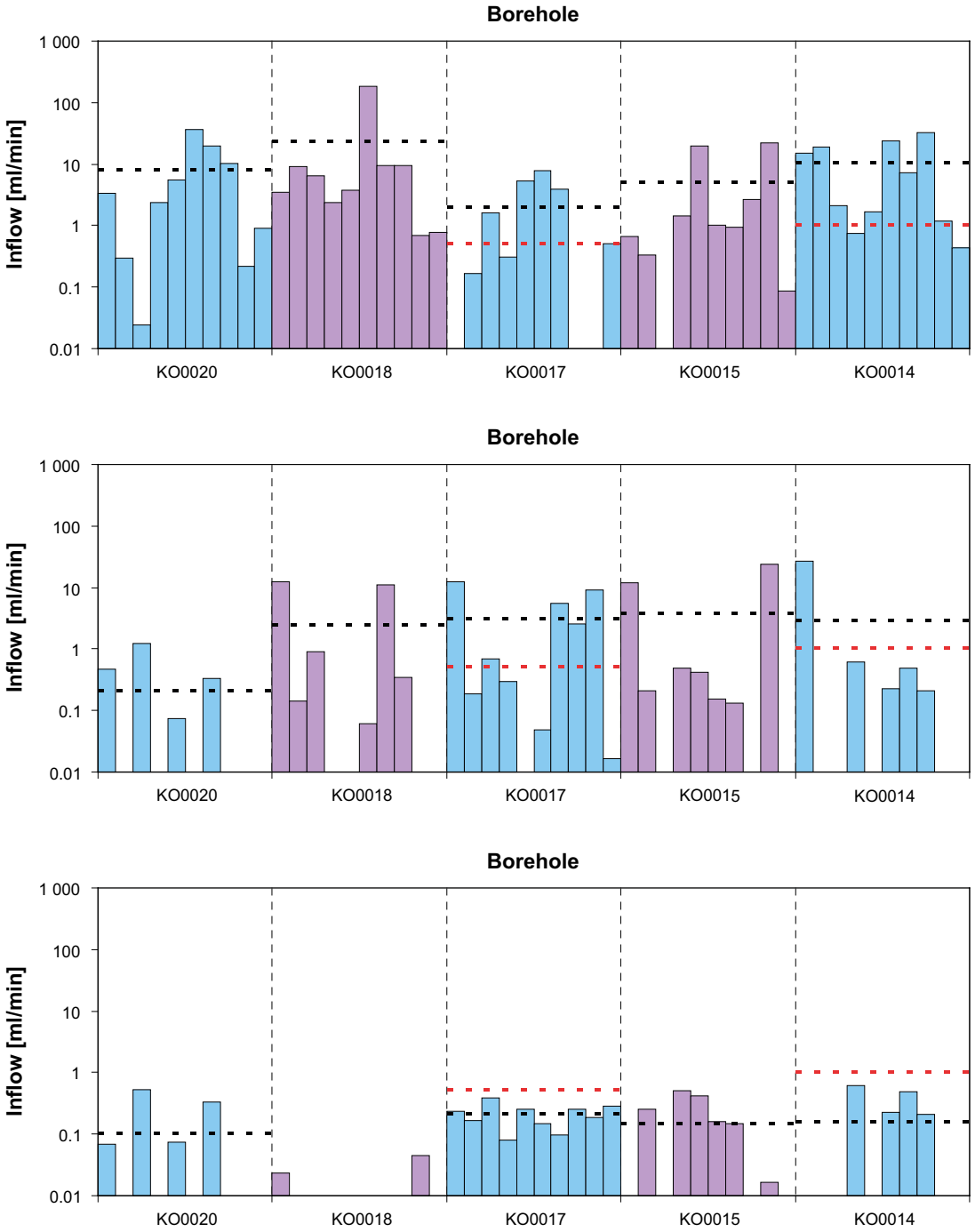

Figure A1-8. *Inflows to 76 mm probe boreholes, opened to the TASO tunnel which is at atmospheric conditions. Results are shown for ten realisations of each model case, top: Basecase; middle: Variant 3; and bottom: Variant 5. The black dashed lines represent inflows to each probe borehole, averaged over the 10 realisations. The red dashed line corresponds to measurements.*

The DFN representation local to the probe boreholes

Results corresponding to the fracture transmissivity network, and pressure field local to the five probe boreholes are shown below for nine realisations of the stochastic fracture network. Fractures are generated for model case Variant 5, described in detail in Section 5.1.4.

Fracture transmissivities

Figure A1-9 through Figure A1-17 illustrates slices for realisations 2 through 10 of the fracture network generated for model Variant 5. Slices are taken in the deposition hole near field, with fracture traces coloured by transmissivity. Two slices are shown, one vertical cross-section incorporating all five probing borehole, and one horizontal cross-section cutting through at the depth of −418.5 m. The corresponding result for realisation 1 of the fracture network is shown in Figure 5-5.

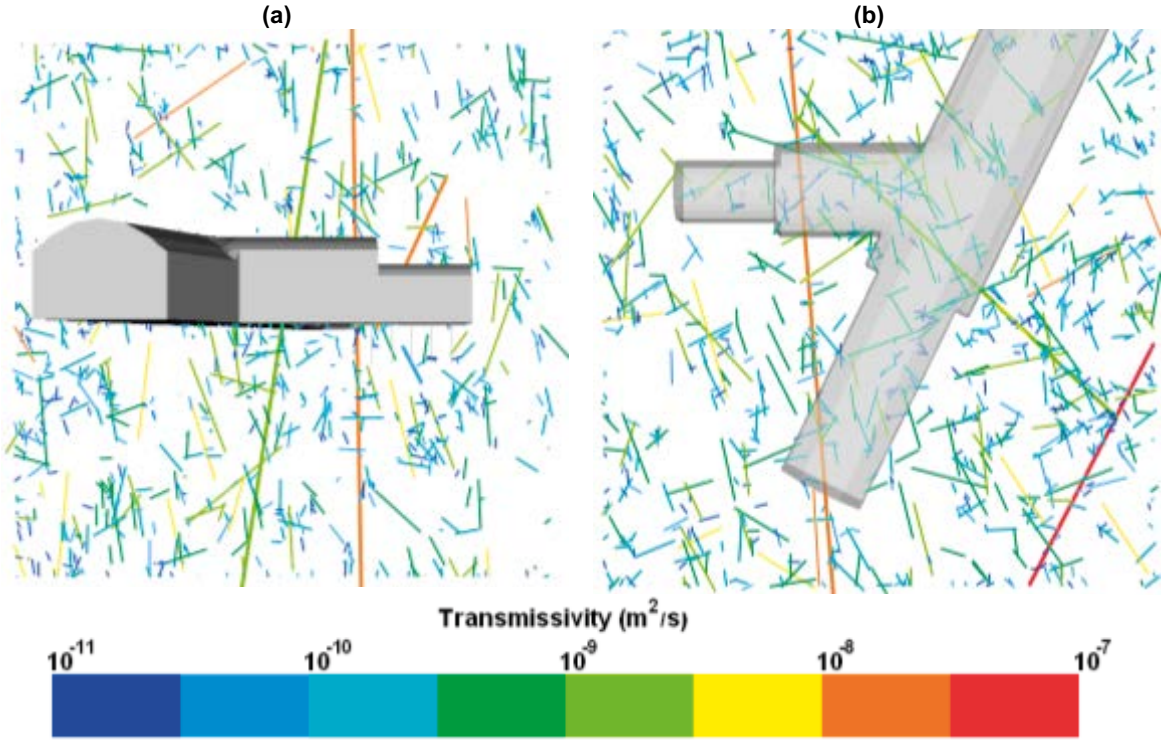

Figure A1-9. *Transmissivity (m^2/s) in the borehole near-field for (a) a vertical slice through all five probe boreholes; and (b) a horizontal slice at an elevation of −418.5 m. Results are shown for realisation 2 of the stochastic fracture network for model Variant 5.*

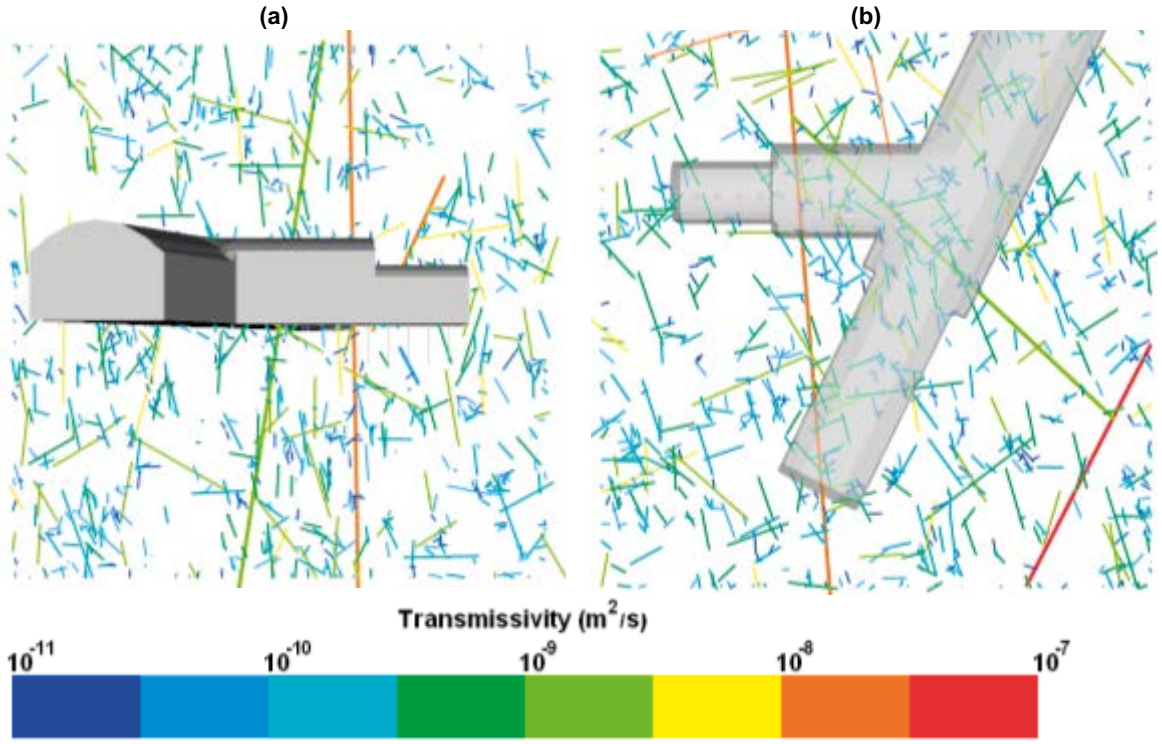

Figure A1-10. *Transmissivity (m^2/s) in the borehole near-field for (a) a vertical slice through all five probe boreholes; and (b) a horizontal slice at an elevation of −418.5 m. Results are shown for realisation 3 of the stochastic fracture network for model Variant 5.*

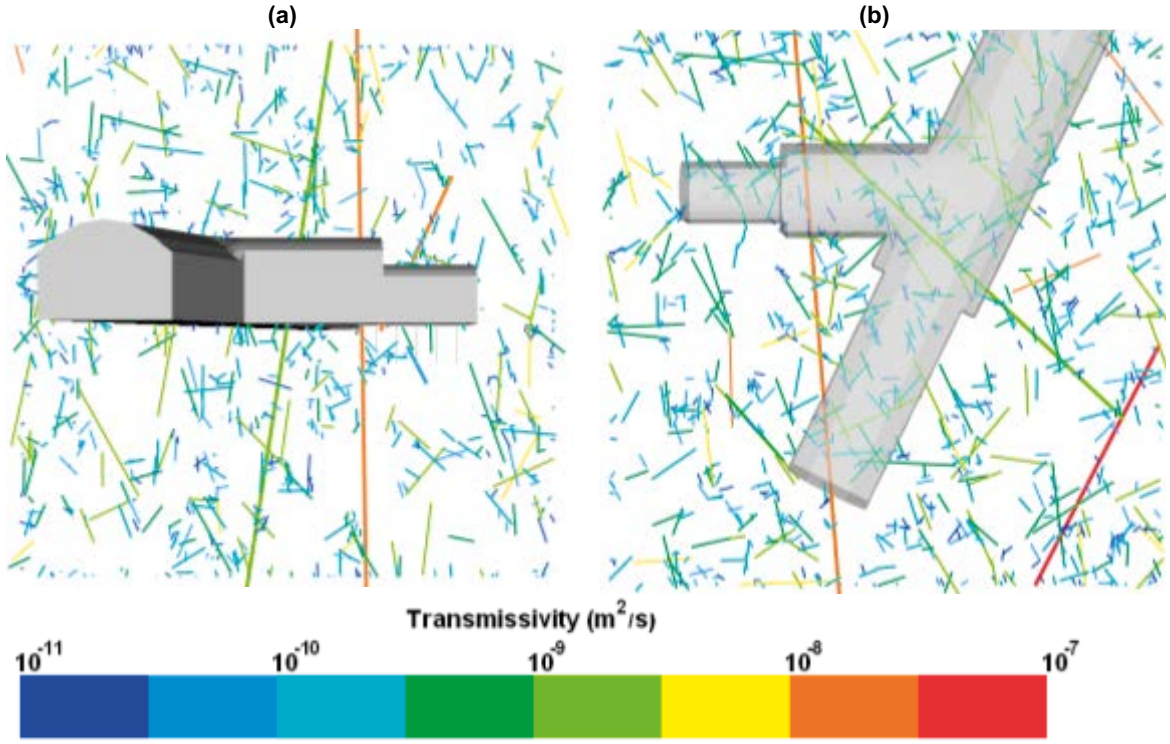

Figure A1-11. *Transmissivity (m^2/s) in the borehole near-field for (a) a vertical slice through all five probe boreholes; and (b) a horizontal slice at an elevation of −418.5 m. Results are shown for realisation 4 of the stochastic fracture network for model Variant 5.*

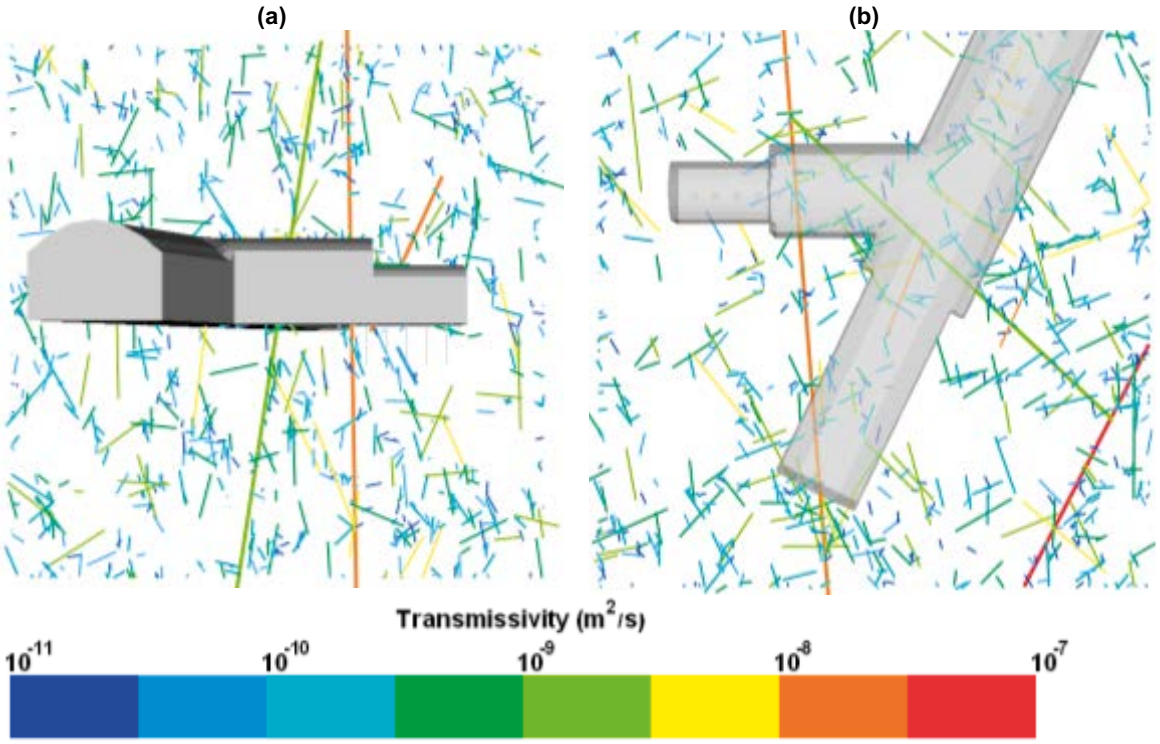

Figure A1-12. *Transmissivity (m^2/s) in the borehole near-field for (a) a vertical slice through all five probe boreholes; and (b) a horizontal slice at an elevation of −418.5 m. Results are shown for realisation 5 of the stochastic fracture network for model Variant 5.*

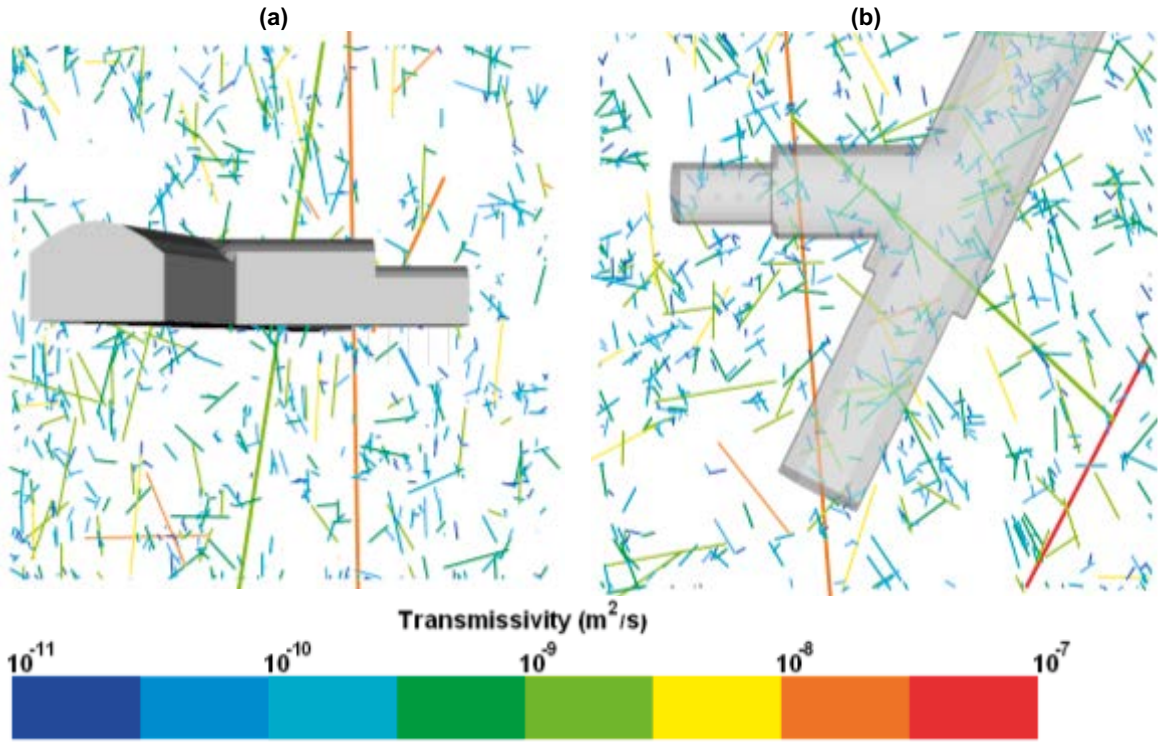

Figure A1-13. *Transmissivity (m^2/s) in the borehole near-field for (a) a vertical slice through all five probe boreholes; and (b) a horizontal slice at an elevation of −418.5 m. Results are shown for realisation 6 of the stochastic fracture network for model Variant 5.*

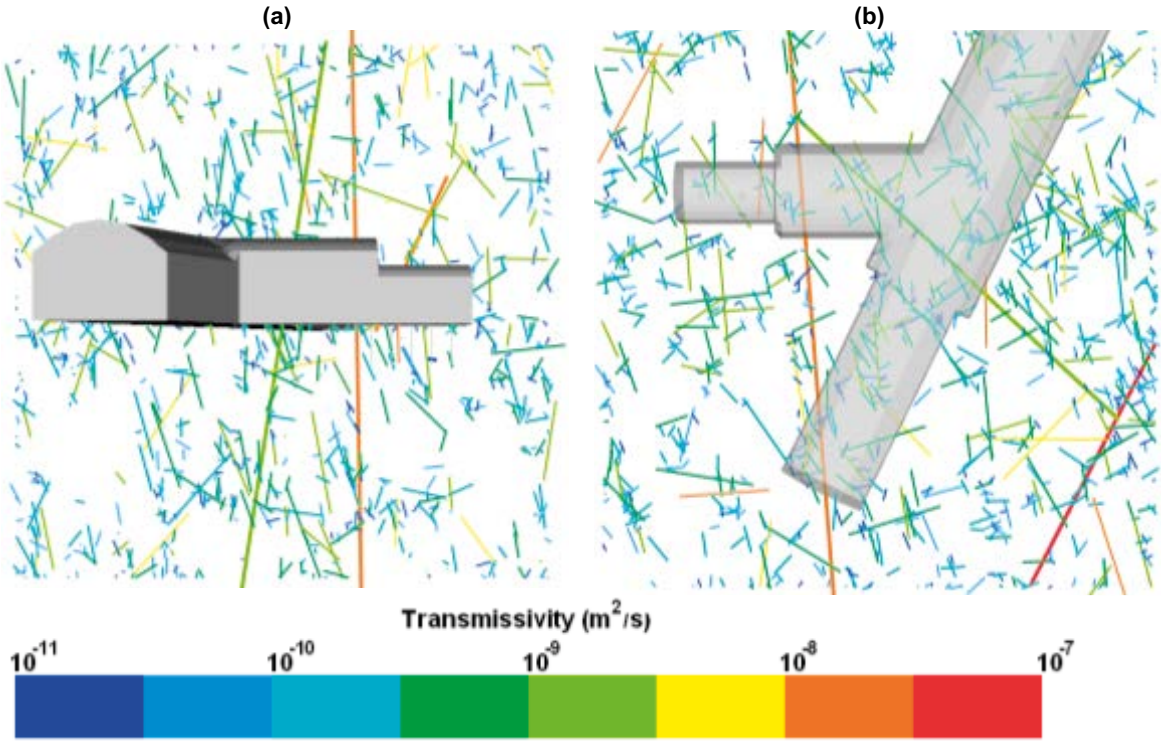

Figure A1-14. *Transmissivity (m^2/s) in the borehole near-field for (a) a vertical slice through all five probe boreholes; and (b) a horizontal slice at an elevation of −418.5 m. Results are shown for realisation 7 of the stochastic fracture network for model Variant 5.*

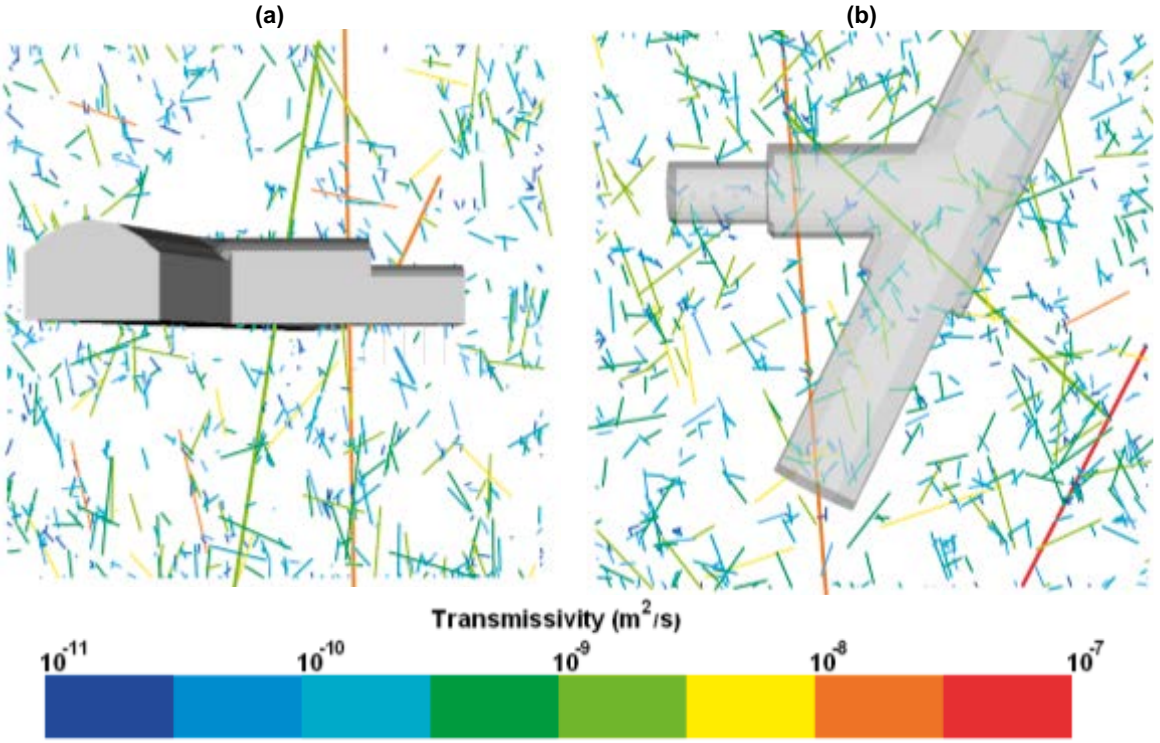

Figure A1-15. *Transmissivity (m^2/s) in the borehole near-field for (a) a vertical slice through all five probe boreholes; and (b) a horizontal slice at an elevation of −418.5 m. Results are shown for realisation 8 of the stochastic fracture network for model Variant 5.*

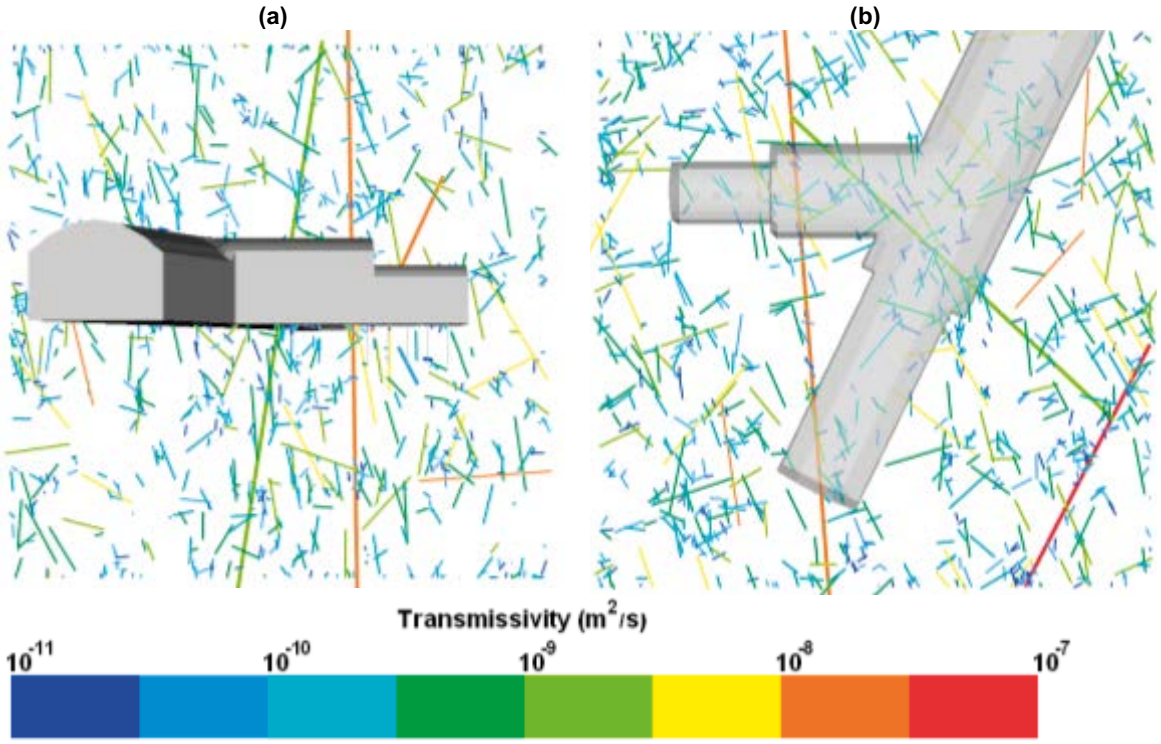

Figure A1-16. *Transmissivity (m^2/s) in the borehole near-field for (a) a vertical slice through all five probe boreholes; and (b) a horizontal slice at an elevation of −418.5 m. Results are shown for realisation 9 of the stochastic fracture network for model Variant 5.*

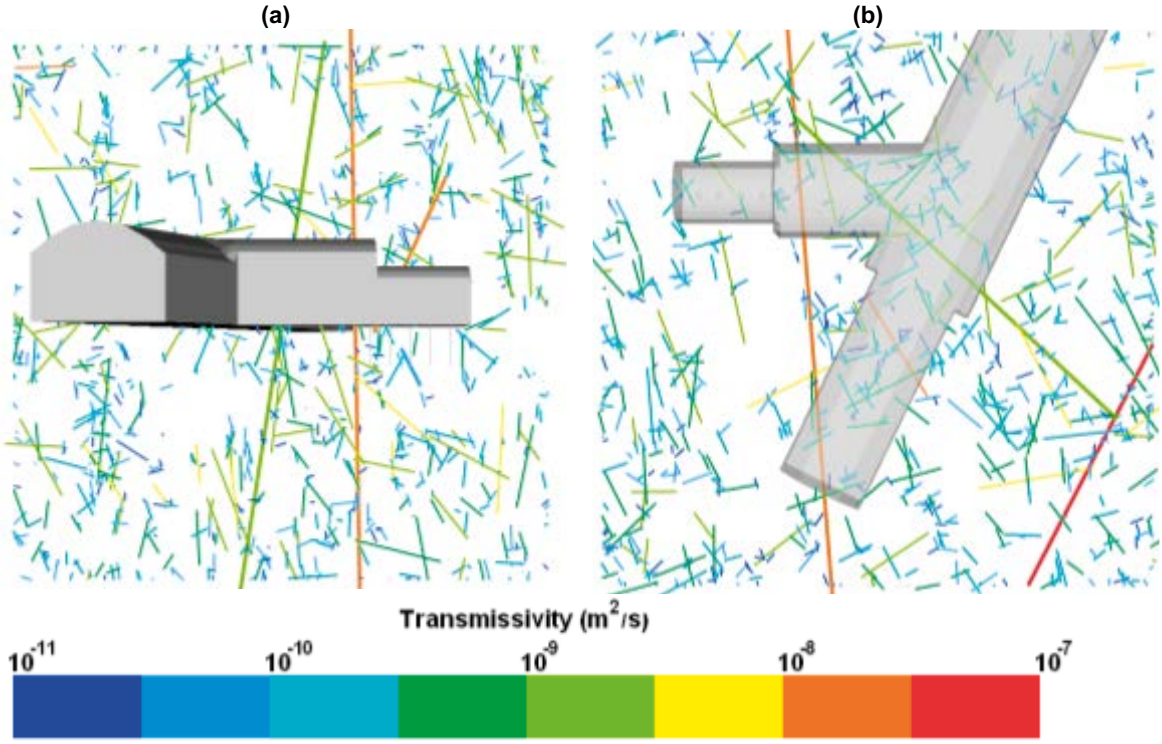

Figure A1-17. *Transmissivity (m^2/s) in the borehole near-field for (a) a vertical slice through all five probe boreholes; and (b) a horizontal slice at an elevation of −418.5 m. Results are shown for realisation 10 of the stochastic fracture network for model Variant 5.*

Pressures within the Fracture Network

Figure A1-18 through Figure A1-26 illustrates slices for realisations 2 through 10 of the fracture network generated for model Variant 5. Slices are taken in the deposition hole near field, with fracture traces coloured by pressure. Simulations correspond to the scenario of all five boreholes packed off to 1 m. Two slices are shown, one vertical cross-section incorporating all five probing borehole, and one horizontal cross-section cutting through at the depth of −418.5 m. The corresponding result for realisation 1 of the fracture network is shown in Figure 5-6.

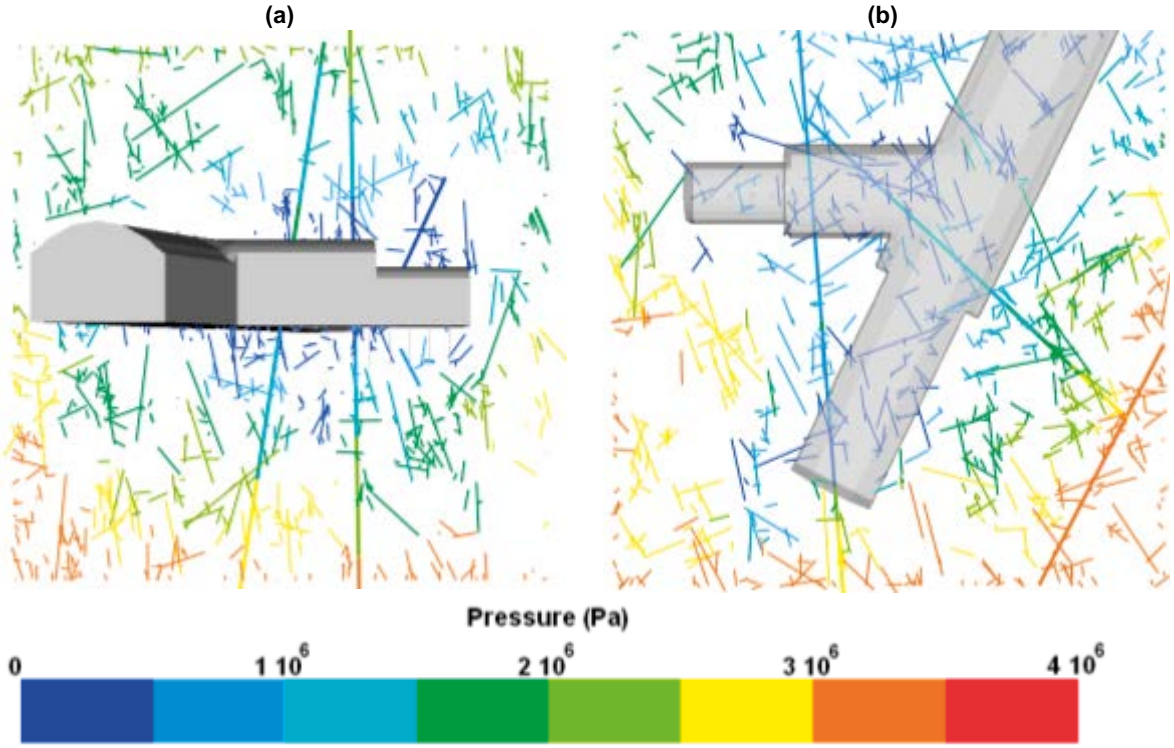

Figure A1-18. *Pressure (Pa) in the deposition hole near-field for (a) a vertical slice through all five probe boreholes; and (b) a horizontal slice at an elevation of −418.5 m. Results are shown for realisation 2 of the stochastic fracture network for model Variant 5.*

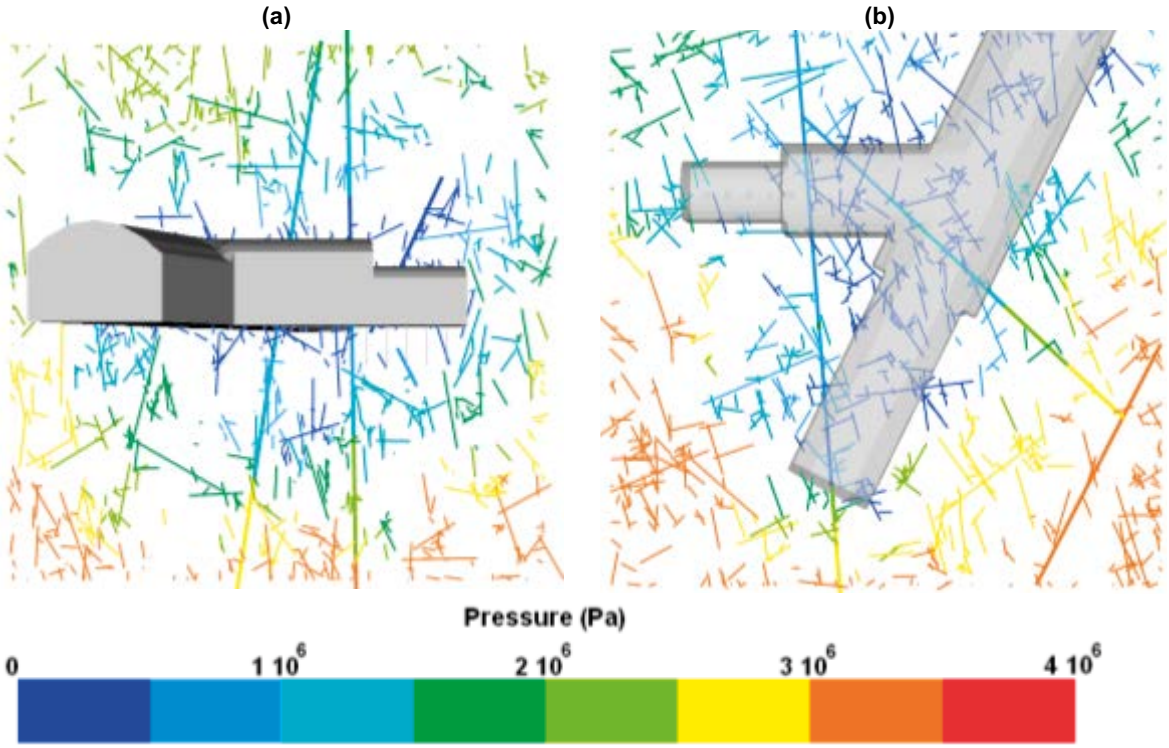

Figure A1-19. *Pressure (Pa) in the deposition hole near-field for (a) a vertical slice through all five probe boreholes; and (b) a horizontal slice at an elevation of −418.5 m. Results are shown for realisation 3 of the stochastic fracture network for model Variant 5.*

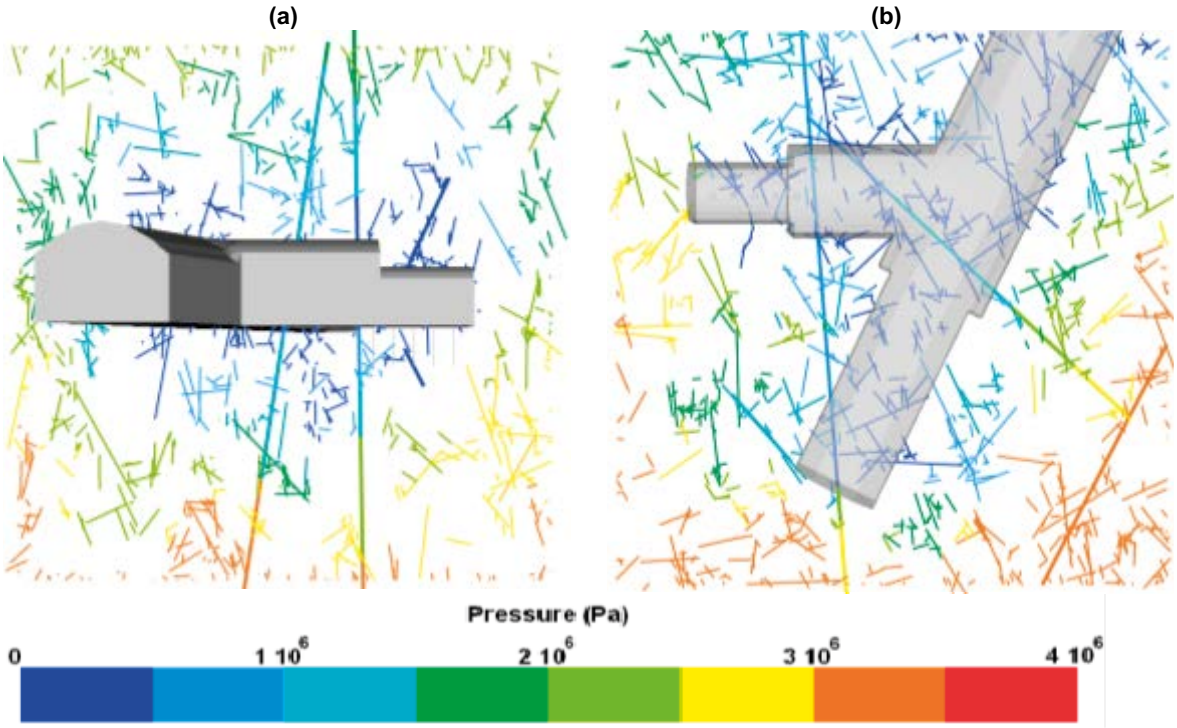

Figure A1-20. *Pressure (Pa) in the deposition hole near-field for (a) a vertical slice through all five probe boreholes; and (b) a horizontal slice at an elevation of −418.5 m. Results are shown for realisation 4 of the stochastic fracture network for model Variant 5.*

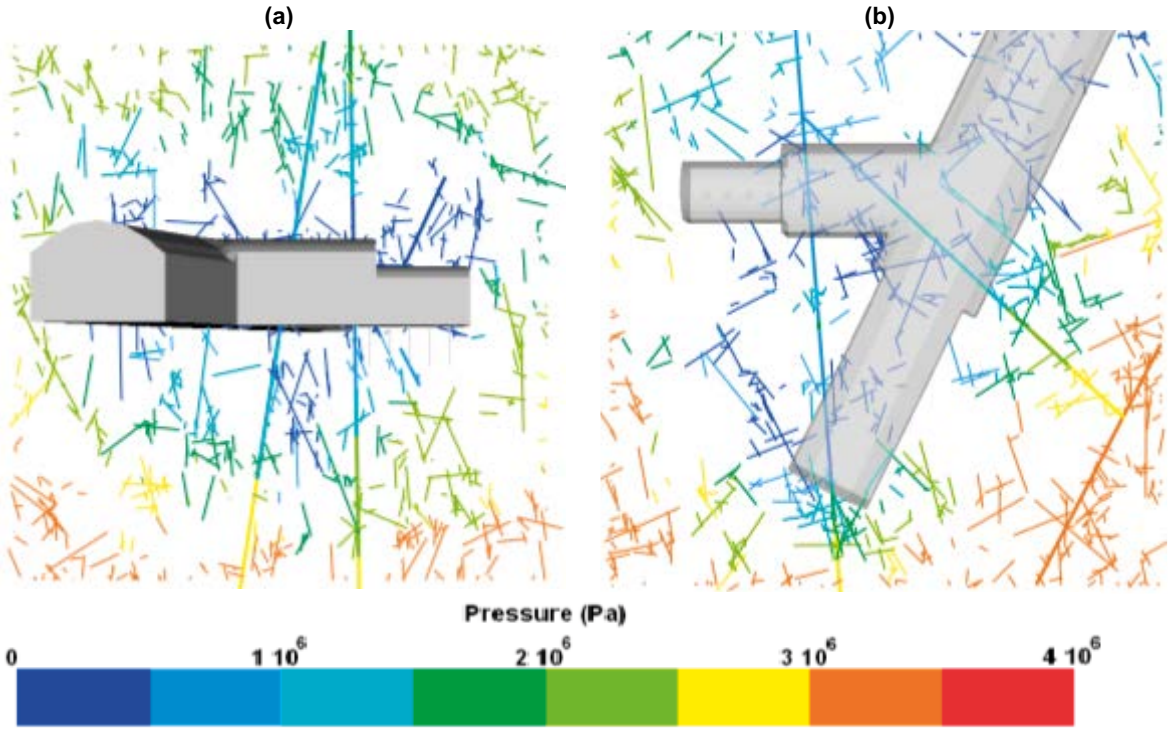

Figure A1-21. *Pressure (Pa) in the deposition hole near-field for (a) a vertical slice through all five probe boreholes; and (b) a horizontal slice at an elevation of −418.5 m. Results are shown for realisation 5 of the stochastic fracture network for model Variant 5.*

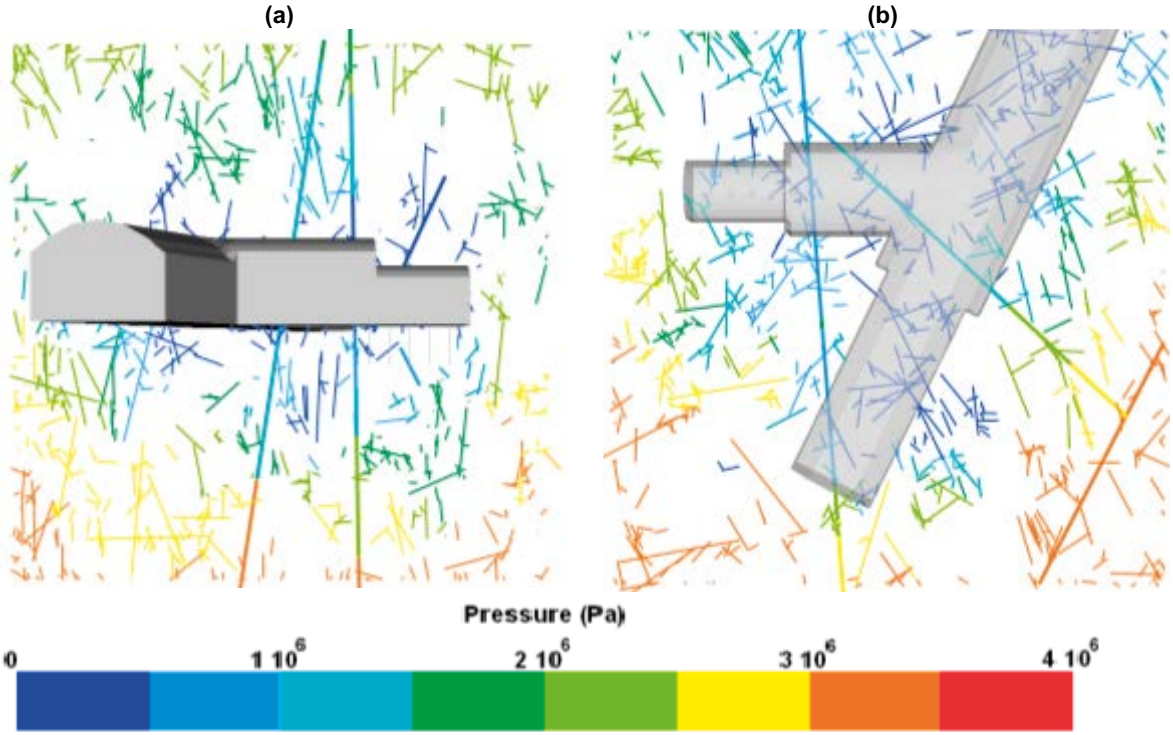

Figure A1-22. *Pressure (Pa) in the deposition hole near-field for (a) a vertical slice through all five probe boreholes; and (b) a horizontal slice at an elevation of −418.5 m. Results are shown for realisation 6 of the stochastic fracture network for model Variant 5.*

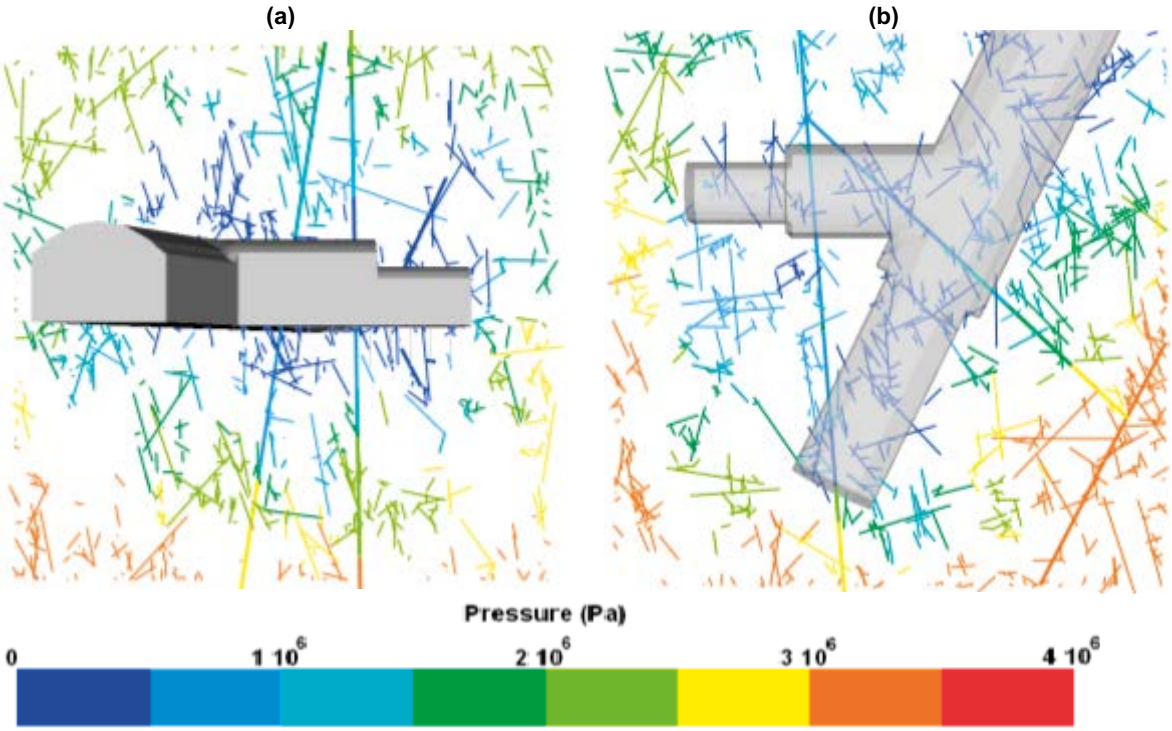

Figure A1-23. *Pressure (Pa) in the deposition hole near-field for (a) a vertical slice through all five probe boreholes; and (b) a horizontal slice at an elevation of −418.5 m. Results are shown for realisation 7 of the stochastic fracture network for model Variant 5.*

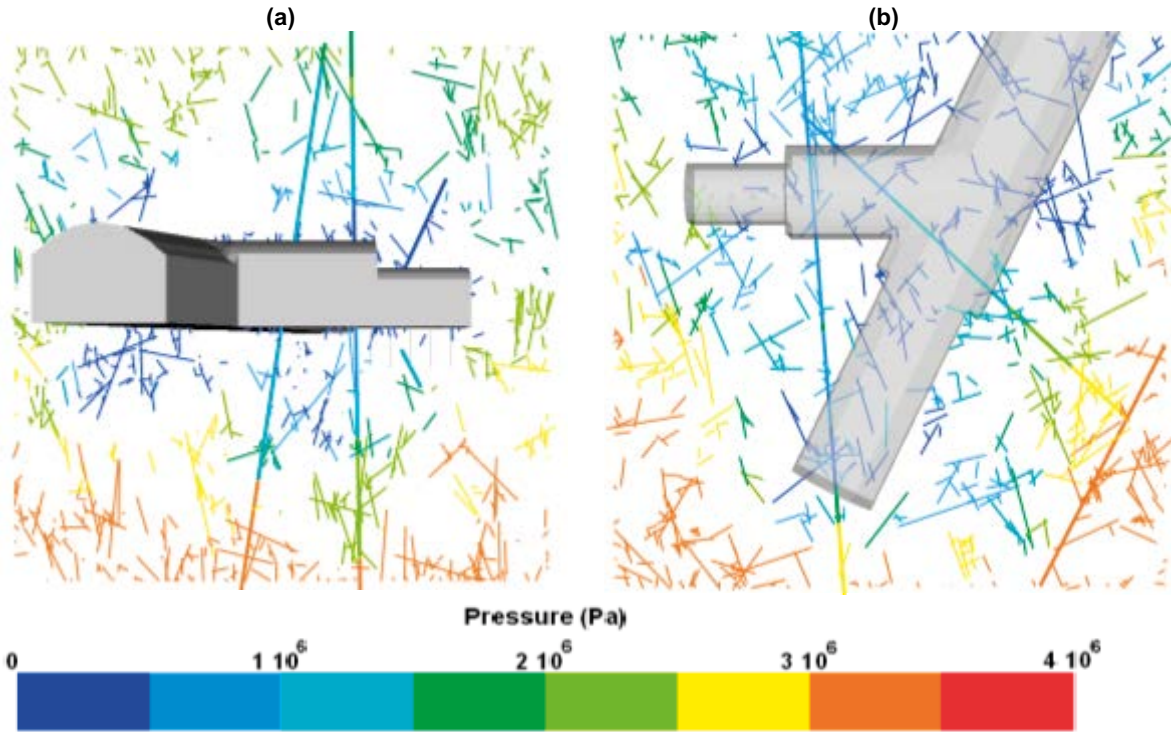

Figure A1-24. *Pressure (Pa) in the deposition hole near-field for (a) a vertical slice through all five probe boreholes; and (b) a horizontal slice at an elevation of −418.5 m. Results are shown for realisation 8 of the stochastic fracture network for model Variant 5.*

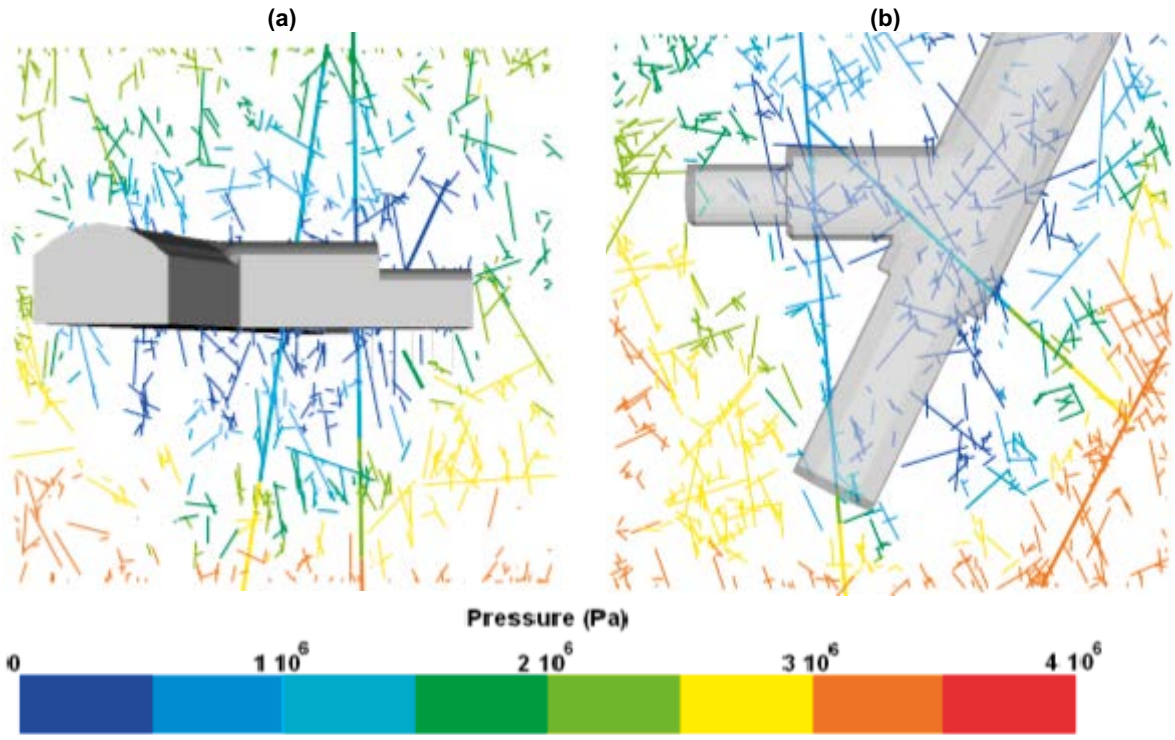

Figure A1-25. *Pressure (Pa) in the deposition hole near-field for (a) a vertical slice through all five probe boreholes; and (b) a horizontal slice at an elevation of −418.5 m. Results are shown for realisation 9 of the stochastic fracture network for model Variant 5.*

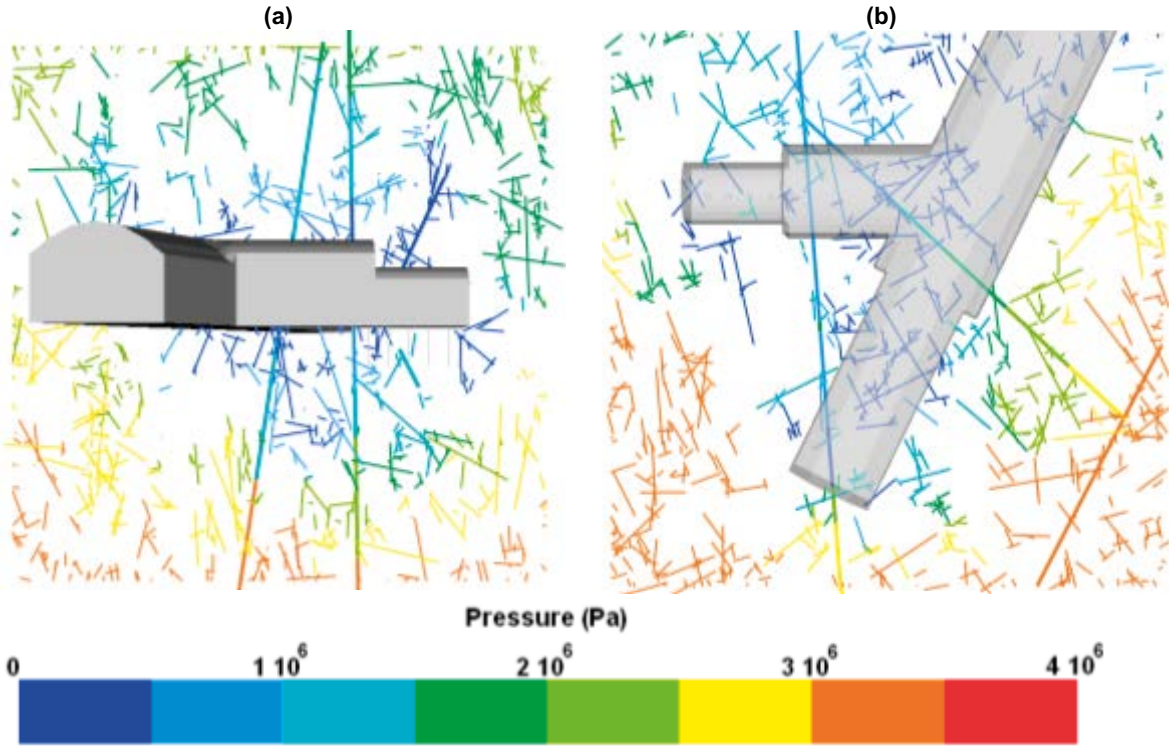

Figure A1-26. *Pressure (Pa) in the deposition hole near-field for (a) a vertical slice through all five probe boreholes; and (b) a horizontal slice at an elevation of −418.5 m. Results are shown for realisation 10 of the stochastic fracture network for model Variant 5.*

The DFN / ECPM representation local to the deposition holes

Upscaled permeabilities local to the probe boreholes

Two slices local to the deposition holes are shown inFigure A1-27 through Figure A1-35, corresponding to nine realisations of the stochastic fracture network (realisation 2 through 10). Each figure is subdivided as follows

- subfigures (a, c) slice vertically, incorporating overcored boreholes KO0017G01 and KO0018G01, and
- subfigures (b, d) take a horizontal cross-section cutting through at a depth of −418.5 m.

Fracture traces are coloured by transmissivity, with equivalent continuous porous medium (ECPM) properties, formed from upscaling the fracture network, coloured by the vertical permeability component k_{33}. For all realisations, regions of intense fracturing and/or high transmissivity yield correspondingly permeable blocks in the upscaled model. Equivalent results for the first realisation of the stochastic fracture network are shown in Figure 5-8.

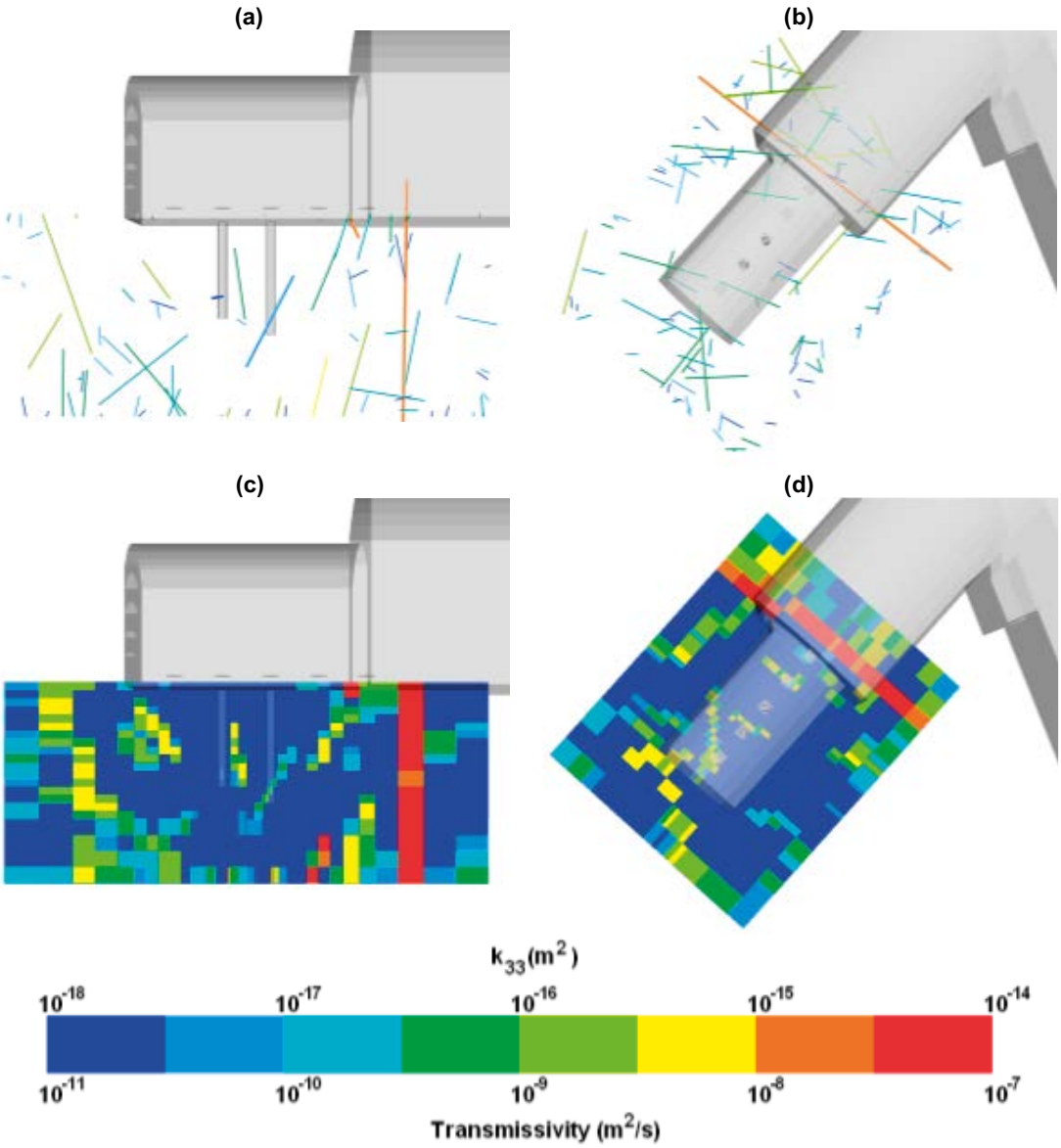

Figure A1-27. *Transmissivity (m^2/s) (a,b) and upscaled permeability (m^2) (c,d) in the deposition hole near-field for (a,c) a vertical slice through all five probe boreholes; and (b,d) a horizontal slice at an elevation of −418.5 m. Results are shown for the second realisation of the stochastic fracture network.*

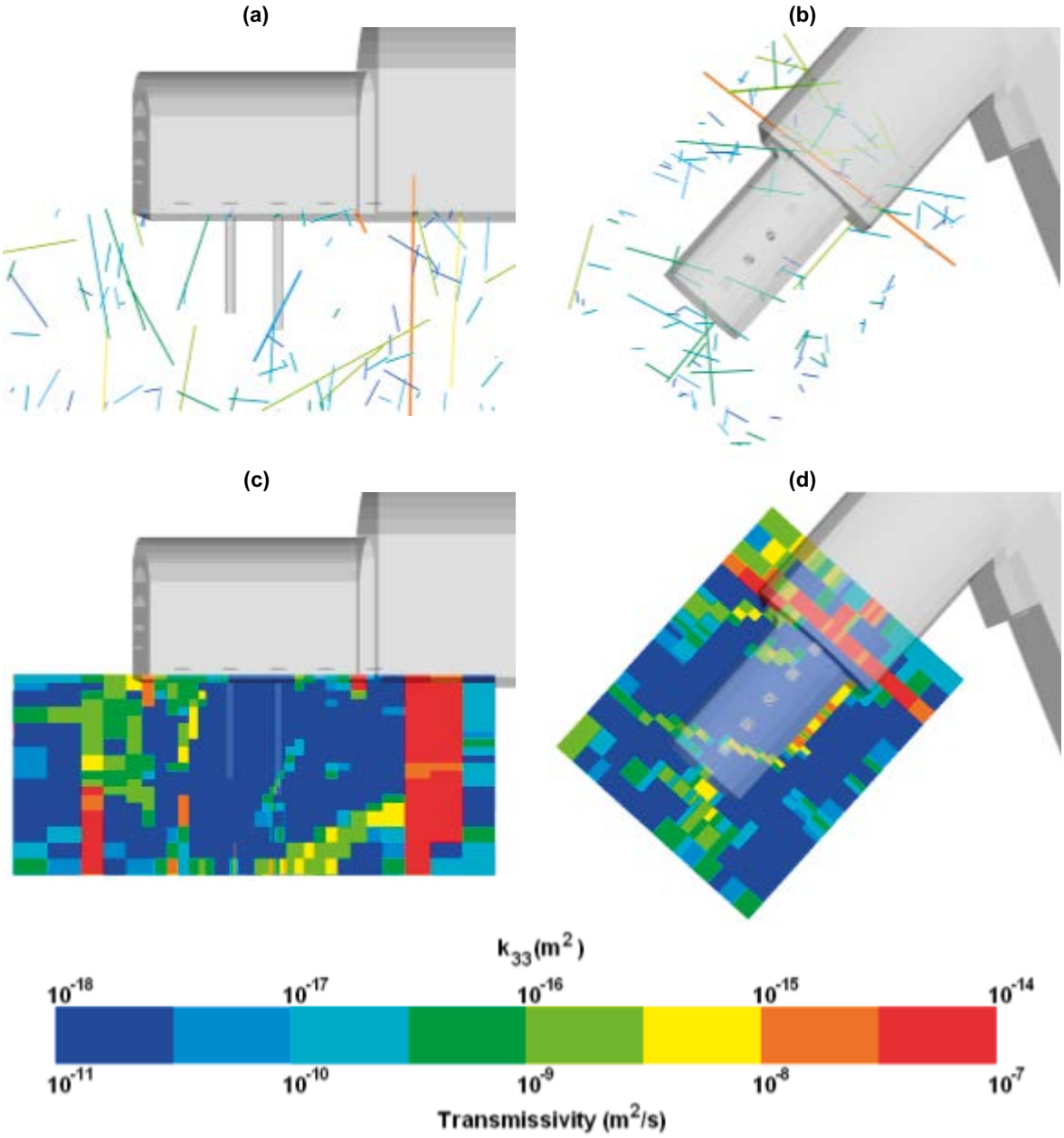

Figure A1-28. *Transmissivity (m^2/s) (a,b) and upscaled permeability (m^2) (c,d) in the deposition hole near-field for (a,c) a vertical slice through all five probe boreholes; and (b,d) a horizontal slice at an elevation of −418.5 m. Results are shown for the third realisation of the stochastic fracture network.*

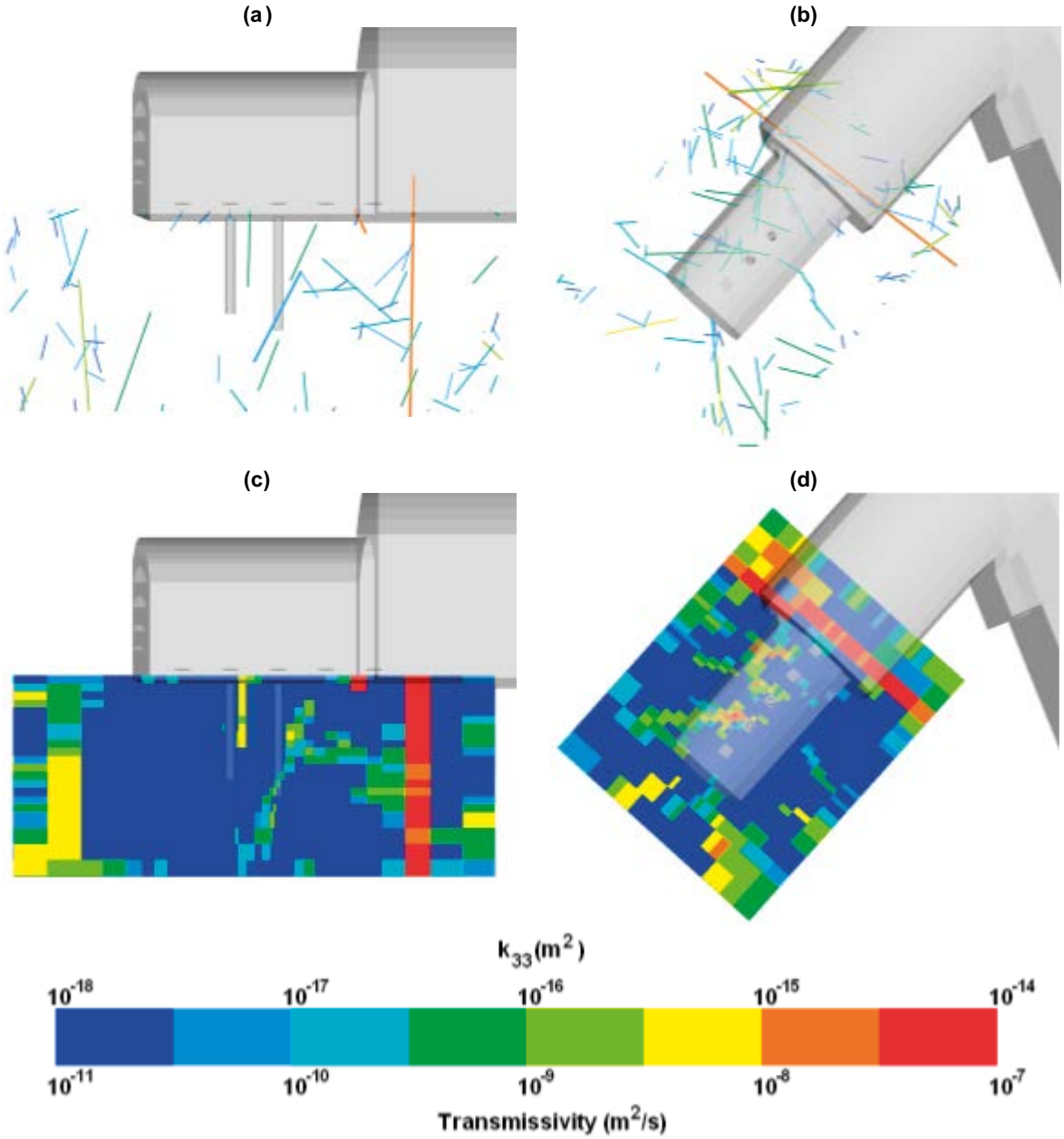

Figure A1-29. *Transmissivity (m^2/s) (a,b) and upscaled permeability (m^2) (c,d) in the deposition hole near-field for (a,c) a vertical slice through all five probe boreholes; and (b,d) a horizontal slice at an elevation of −418.5 m. Results are shown for the fourth realisation of the stochastic fracture network.*

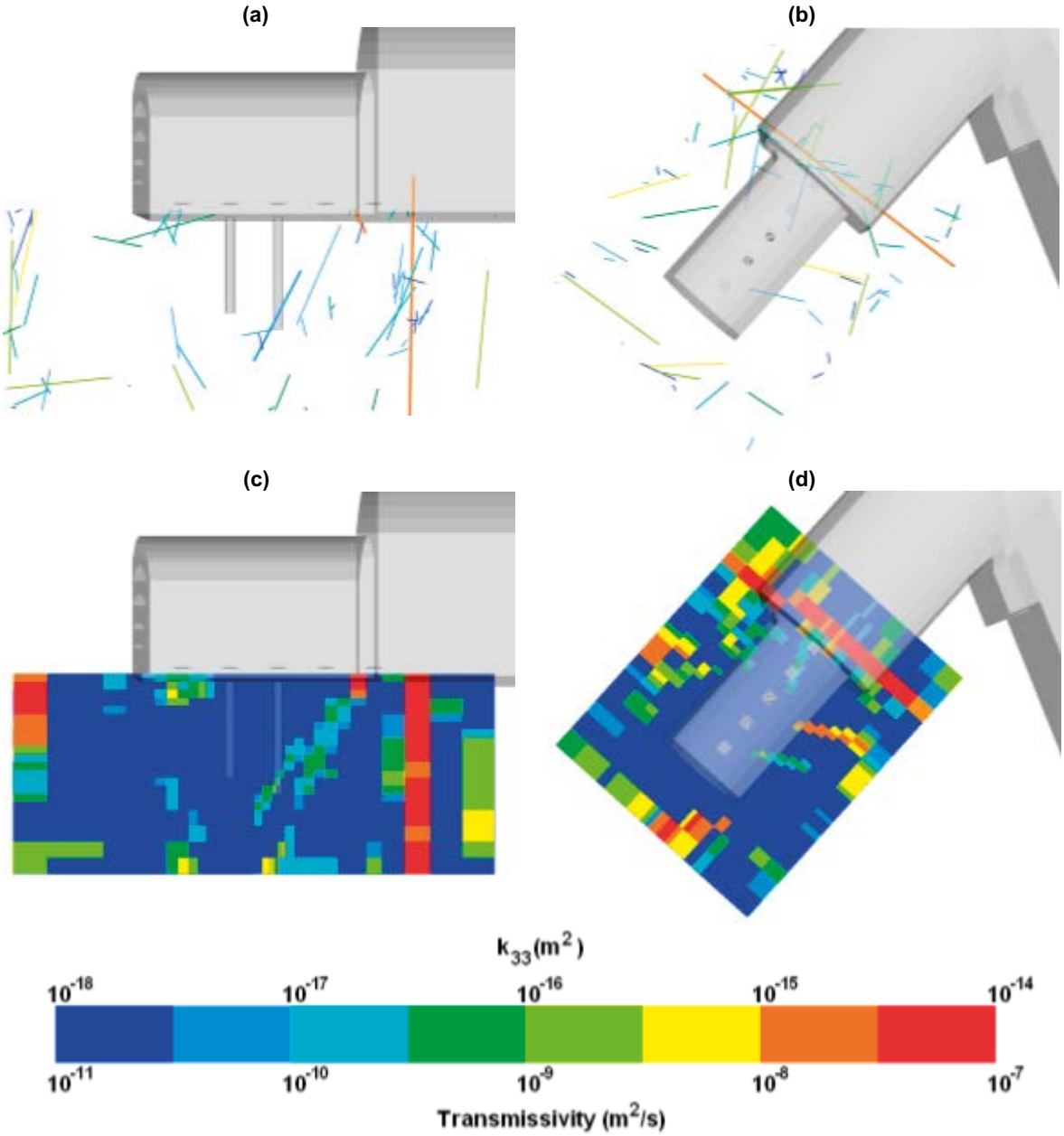

Figure A1-30. *Transmissivity (m^2/s) (a,b) and upscaled permeability (m^2) (c,d) in the deposition hole near-field for (a,c) a vertical slice through all five probe boreholes; and (b,d) a horizontal slice at an elevation of −418.5 m. Results are shown for the fifth realisation of the stochastic fracture network.*

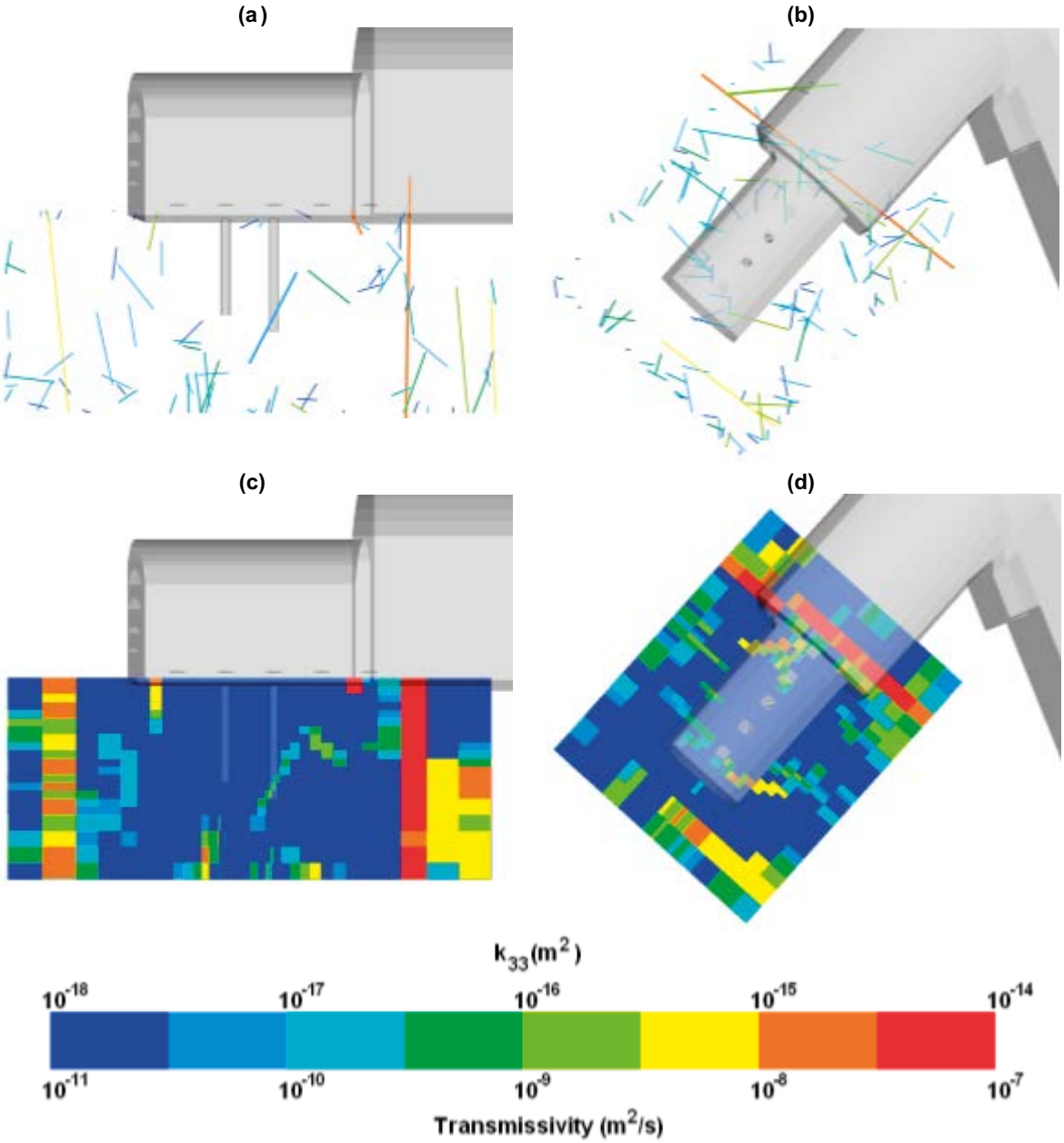

Figure A1-31. *Transmissivity (m^2/s) (a,b) and upscaled permeability (m^2) (c,d) in the deposition hole near-field for (a,c) a vertical slice through all five probe boreholes; and (b,d) a horizontal slice at an elevation of −418.5 m. Results are shown for the sixth realisation of the stochastic fracture network.*

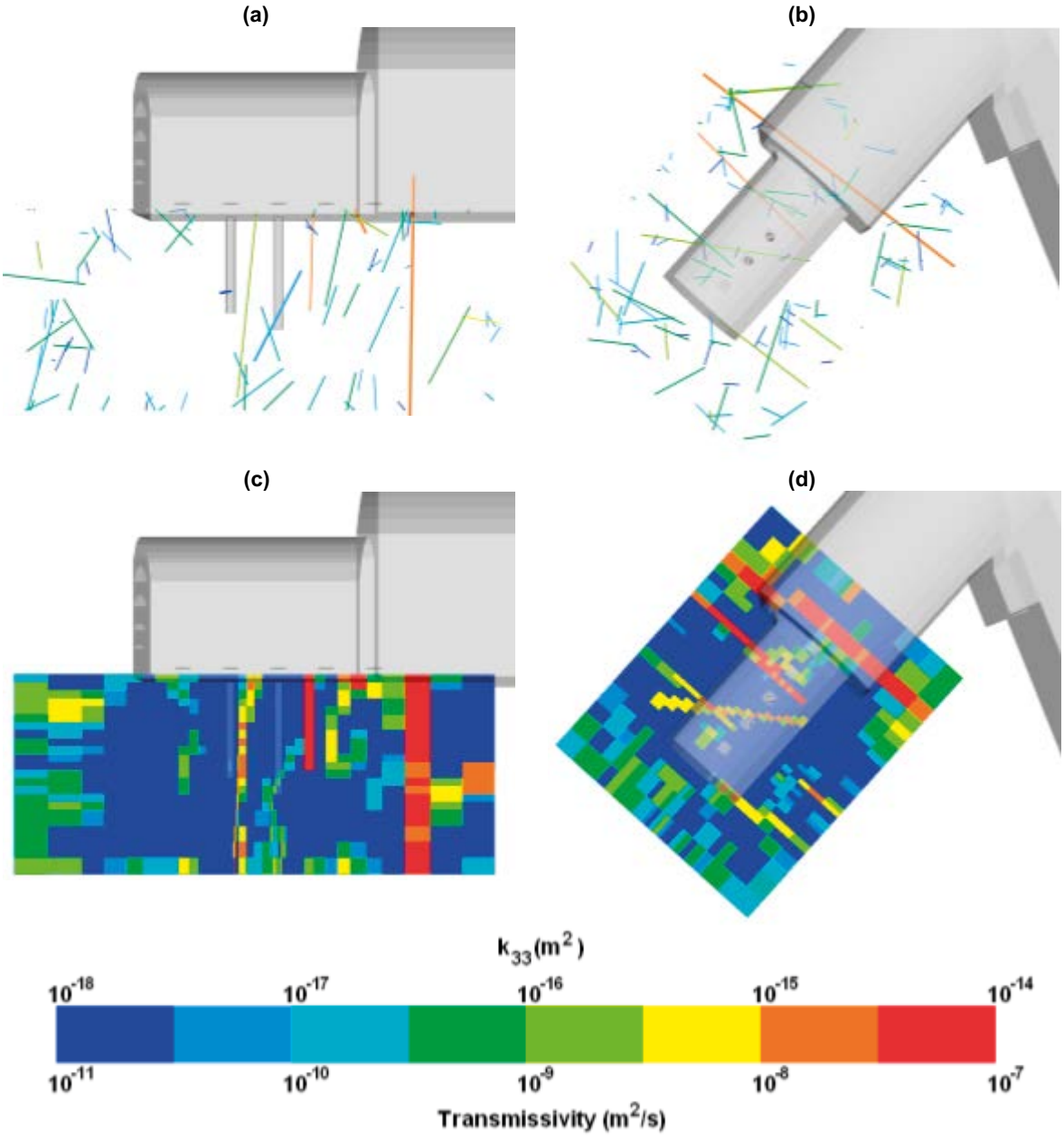

Figure A1-32. *Transmissivity (m^2/s) (a,b) and upscaled permeability (m^2) (c,d) in the deposition hole near-field for (a,c) a vertical slice through all five probe boreholes; and (b,d) a horizontal slice at an elevation of −418.5 m. Results are shown for the seventh realisation of the stochastic fracture network.*

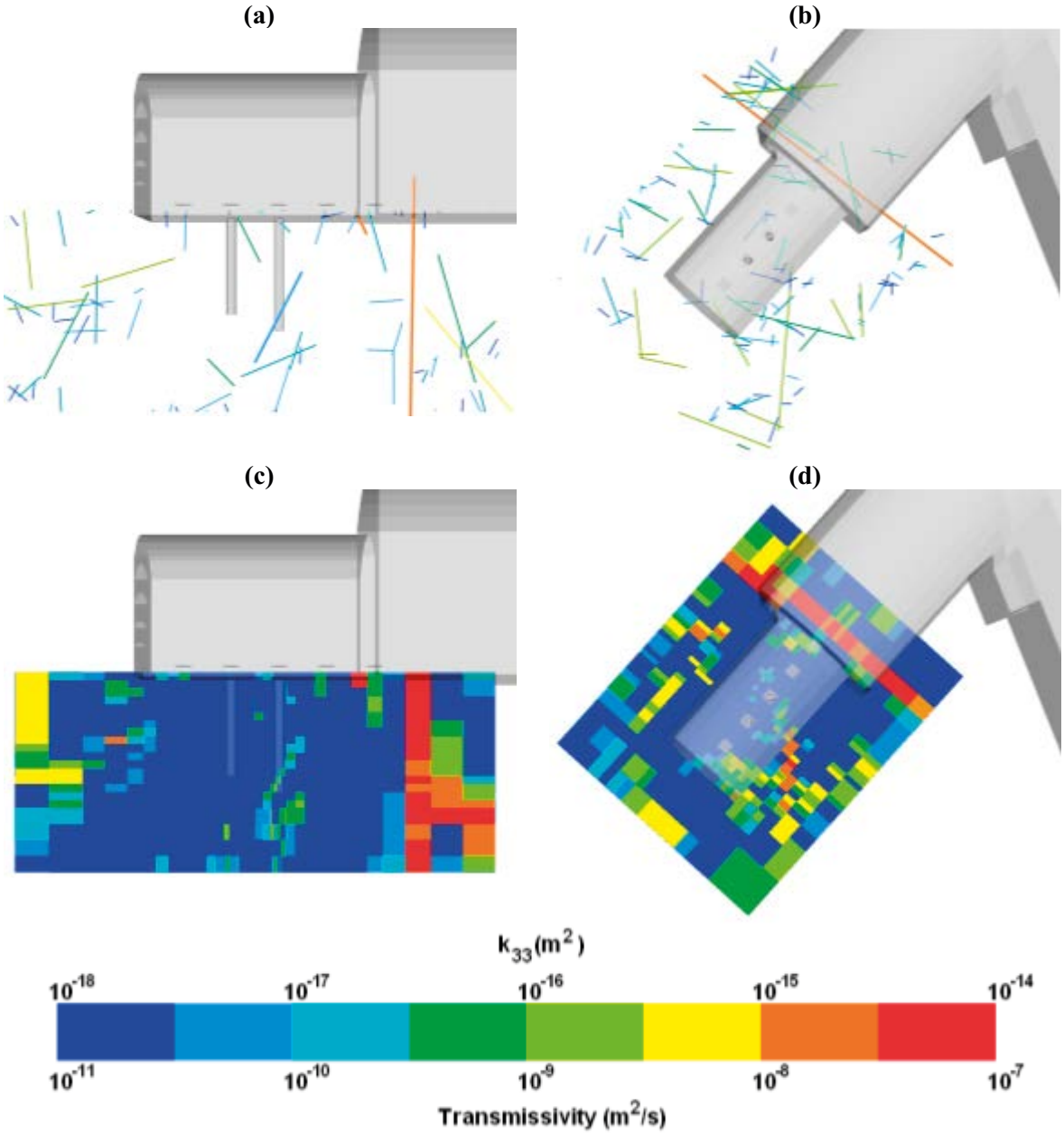

Figure A1-33. *Transmissivity (m^2/s) (a,b) and upscaled permeability (m^2) (c,d) in the deposition hole near-field for (a,c) a vertical slice through all five probe boreholes; and (b,d) a horizontal slice at an elevation of −418.5 m. Results are shown for the eighth realisation of the stochastic fracture network.*

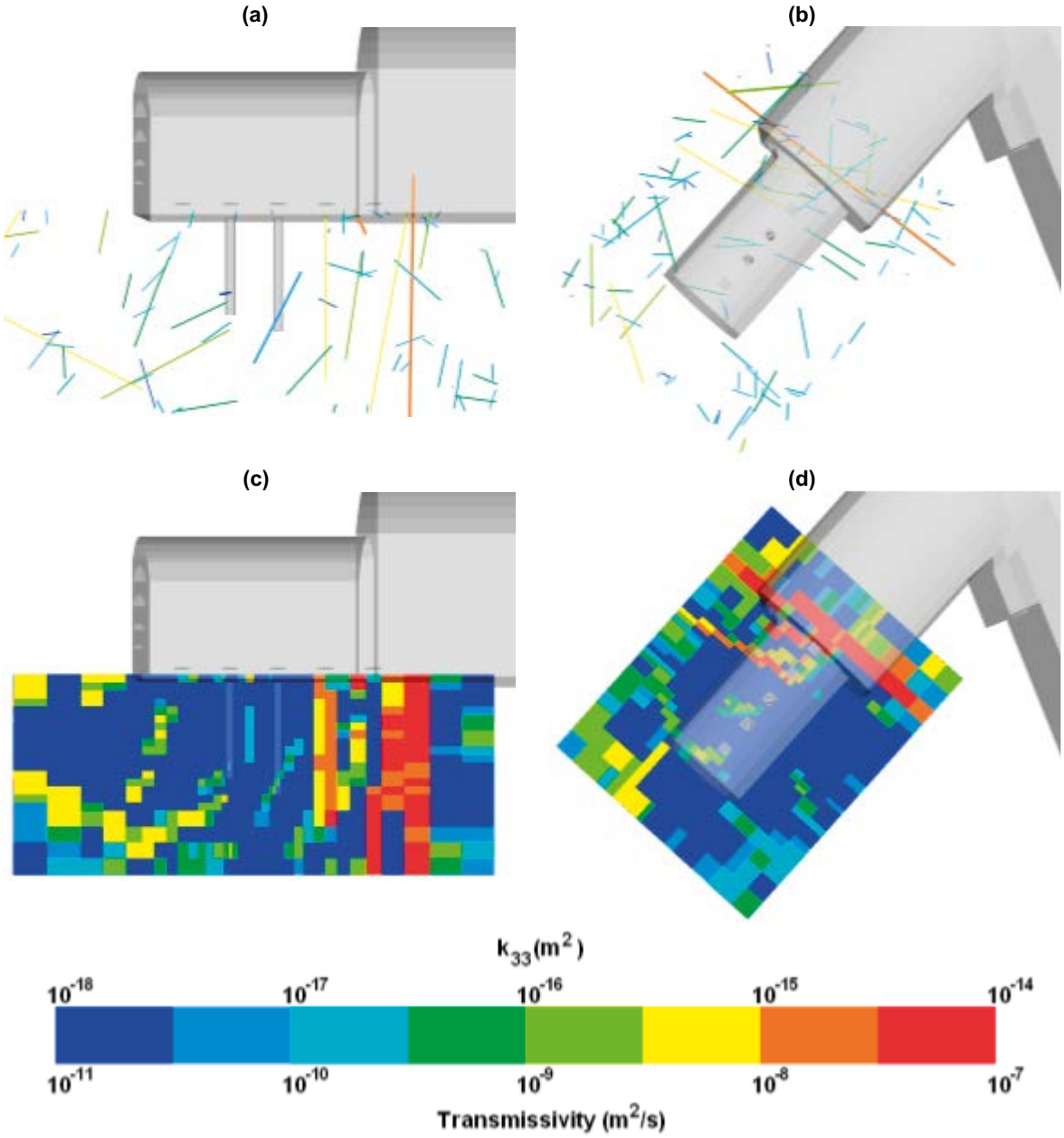

Figure A1-34. *Transmissivity (m^2/s) (a,b) and upscaled permeability (m^2) (c,d) in the deposition hole near-field for (a,c) a vertical slice through all five probe boreholes; and (b,d) a horizontal slice at an elevation of −418.5 m. Results are shown for the ninth realisation of the stochastic fracture network.*

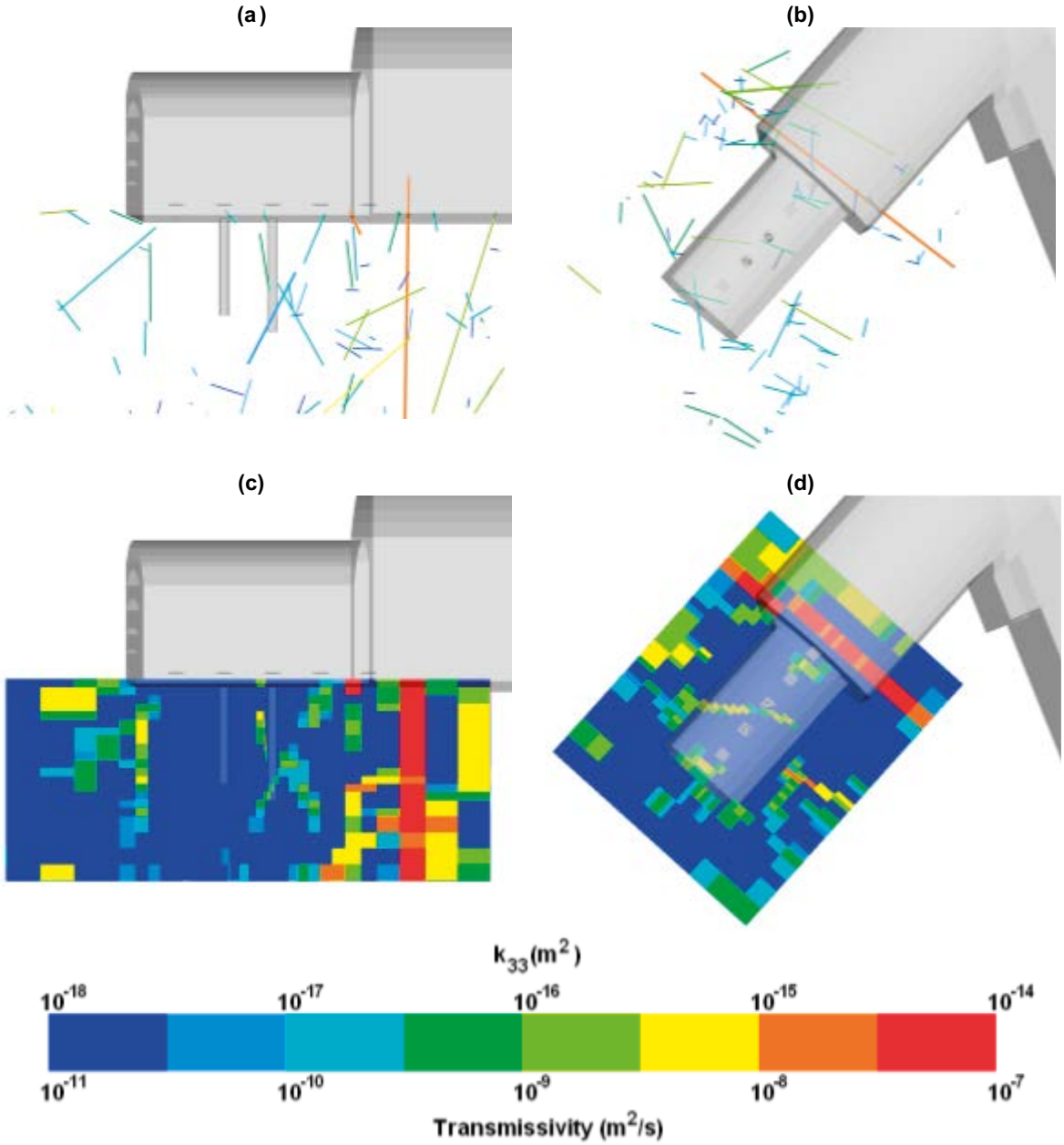

Figure A1-35. *Transmissivity (m^2/s) (a,b) and upscaled permeability (m^2) (c,d) in the deposition hole near-field for (a,c) a vertical slice through all five probe boreholes; and (b,d) a horizontal slice at an elevation of −418.5 m. Results are shown for the tenth realisation of the stochastic fracture network.*

Appendix 2

Task 8D2: Stochastic variability of the Fracture Network

Inflow maps

Bentonite Resaturation Profiles (Task 8D)

Resaturation of emplaced bentonite.

Bentonite hydration at sensor locations.

Pressures in the deposition hole near field.

Saturations in the deposition hole near field.

Inflow maps

Contour plots of inflows to deposition holes KO0017G01 and KO0018G01 are shown in Figure A2-1 through Figure A2-3, corresponding to the second, seventh and ninth realisation of the stochastic fracture network. The model case considered corresponds to optimal calibration (Variant 5, defined in Section 5.1). In each case, the distribution of inflows is shown on the over-cored borehole wall.

Contours of inflow corresponding to the first realisation of the fracture network are shown in Figure 6-2.

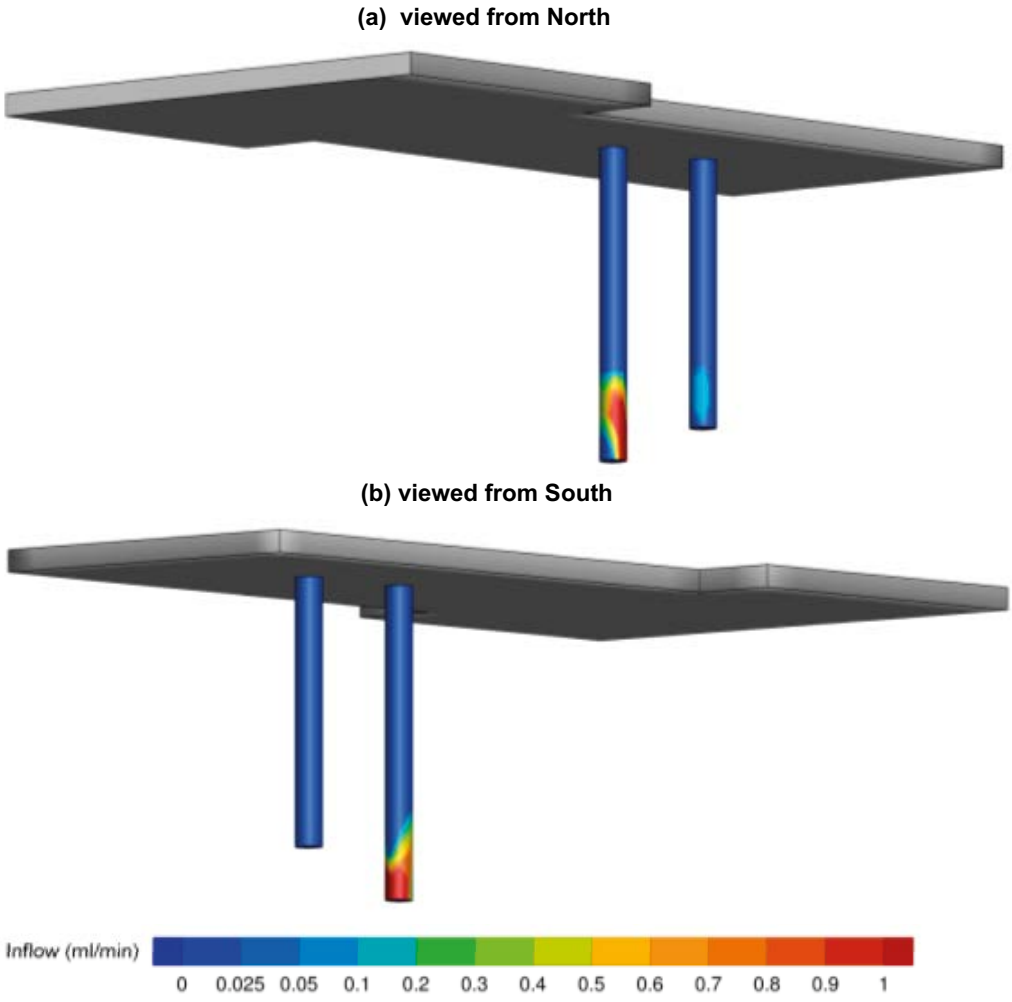

Figure A2-1. *Inflows illustrated against the walls of deposition boreholes KO0017G01 and KO0018G01, for realisation 2 of the upscaled fracture network. The view in figure (a) is taken from North, and the view in figure (b) is from the South.*

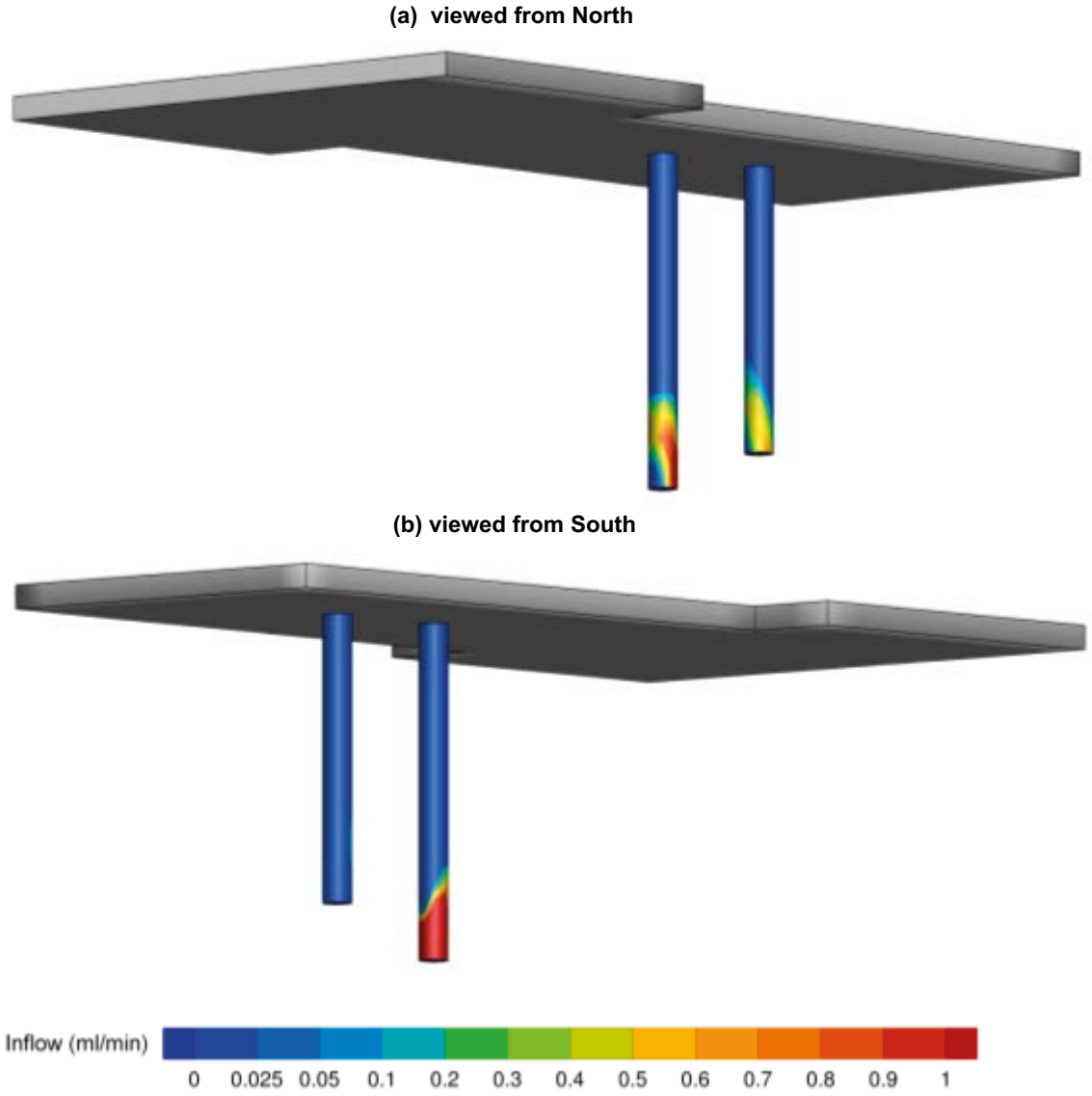

Figure A2-2. *Inflows illustrated against the walls of deposition boreholes KO0017G01 and KO0018G01, for realisation 7 of the upscaled fracture network. The view in figure (a) is taken from North, and the view in figure (b) is from the South.*

Bentonite resaturation profiles (Task 8D)

Resaturation of emplaced bentonite

The initial liquid saturation on the outer surface of the emplaced bentonite is shown in Figure A2-4, along with five subsequent times (0.1 years, 0.5 years, 1 year, 10 years, and 100 years). Results correspond to realisation 7 of the stochastic fracture network, with corresponding results for realisation 2 shown in Figure 6-6. Bentonite hydration is initiated from the base of the deposition holes, corresponding to the intersection of hydraulically active fractures. In addition, after 100 years, KO0017G01 has still to reach 95 % liquid saturation at the top of the deposition hole.

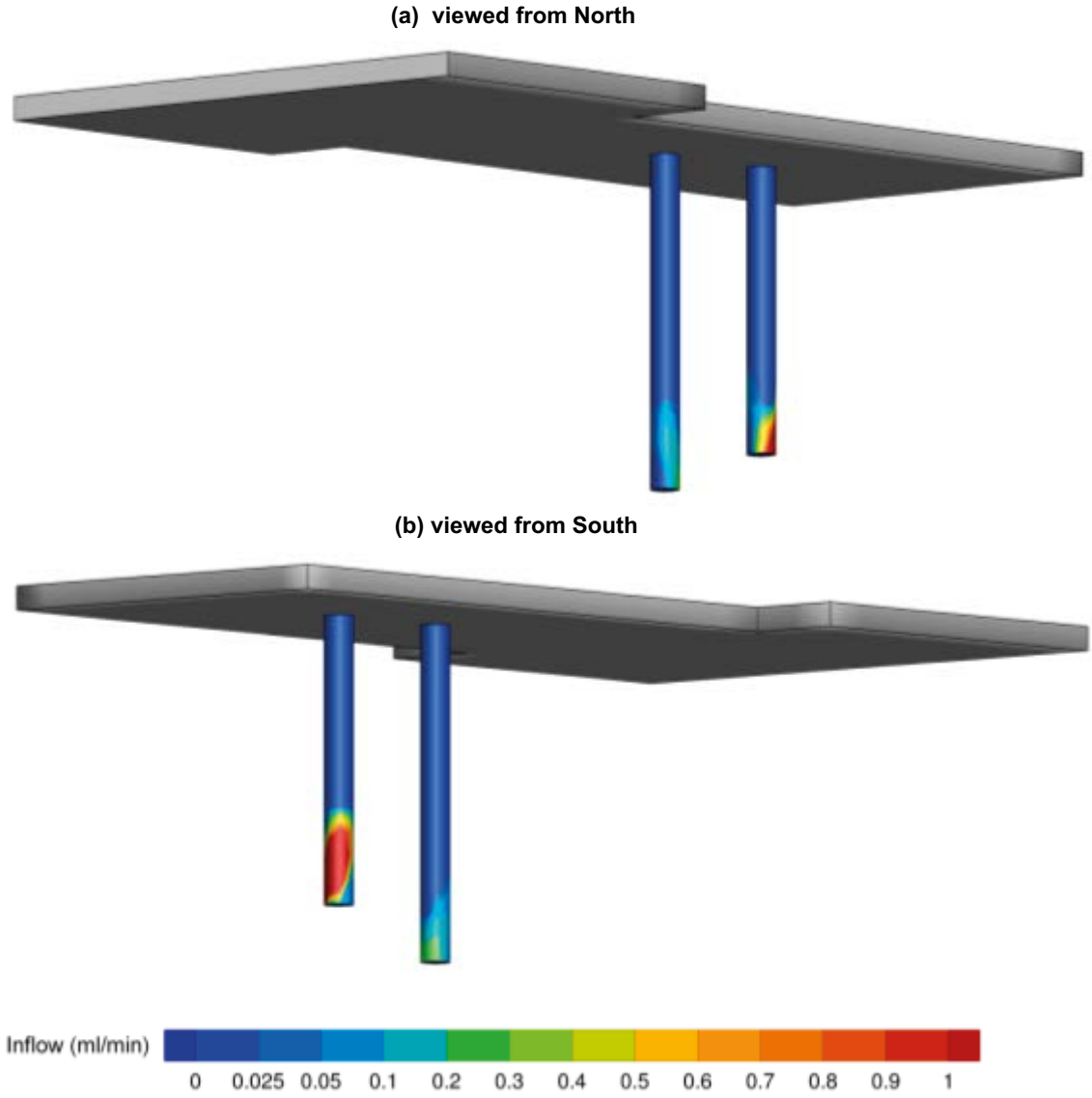

Figure A2-3. *Inflows illustrated against the walls of deposition boreholes KO0017G01 and KO0018G01, for realisation 9 of the upscaled fracture network. The view in figure (a) is taken from North, and the view in figure (b) is from the South.*

Bentonite hydration at sensor locations

Calculated profiles for relative humidity at six sensor locations in KO0017G01 are shown in Figure A2-5 for the first 500 days post installation of the bentonite. Results are presented for realisation 7 of the stochastic fracture network, with equivalent results shown in Figure 6-8 for realisation 2.

Relative humidity profiles calculated at six sensor locations in KO0018G01 for realisation 7 of the stochastic fracture network are shown in Figure A2-6. Again, results are shown for the first 500 days post installation of the bentonite stack. Equivalent results for realisation 2 of the upscaled DFN are presented in Figure 6-9.

For both deposition holes considered, the relative humidity profiles are broadly consistent between the two realisations of the calibrated fracture network model considered.

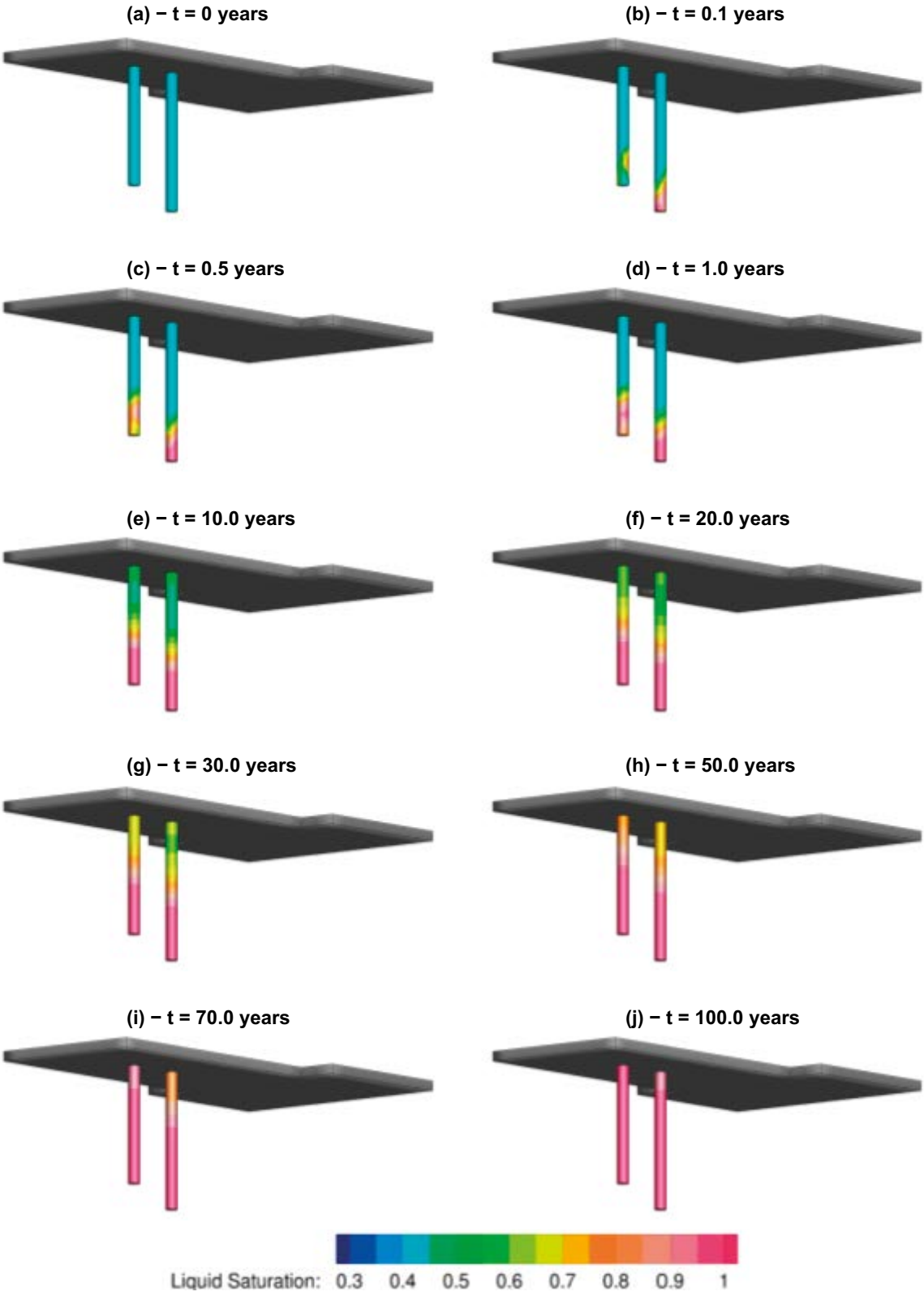

Figure A2-4. *The bentonite saturation calculated for each deposition hole at a number of different times. Results are presented for realisation seven of the upscaled stochastic fracture network. Results are comparable to Figure 6-6, calculated from realisation 2 of the DFN.*

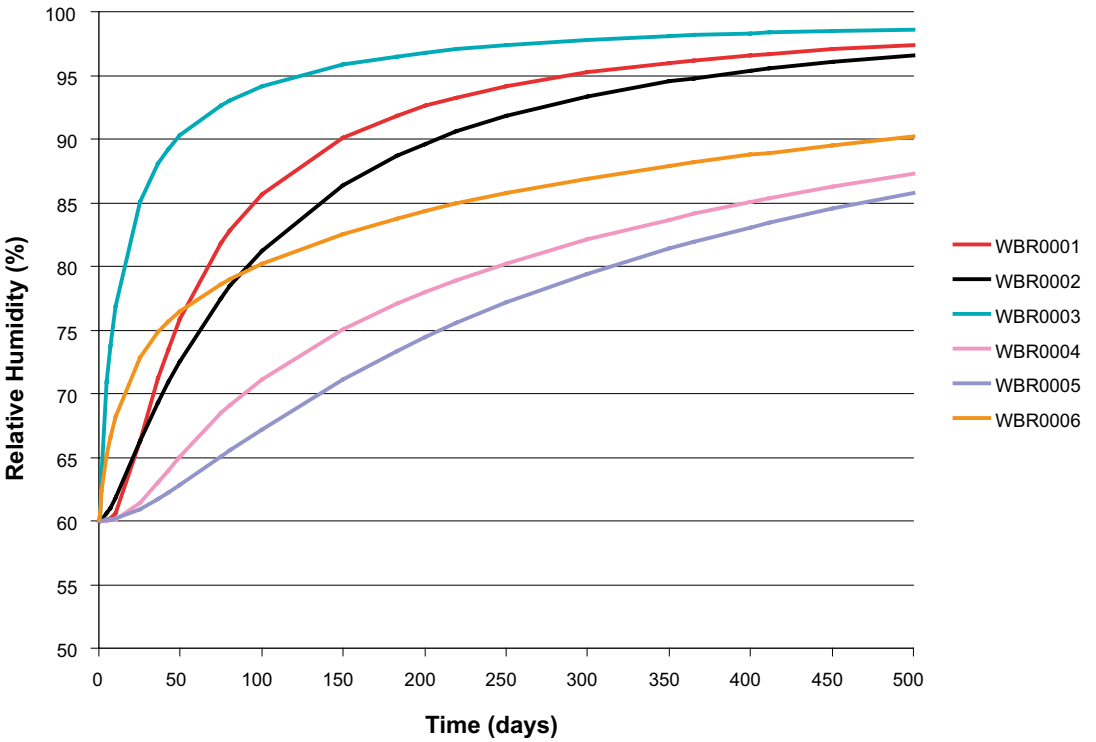

Figure A2-5. *The evolution of relative humidity calculated at sensor locations within the bentonite during the first 500 days post installation. Results are presented for sensors WBR0001 through WBR0006, corresponding to deposition hole KO0017G01.*

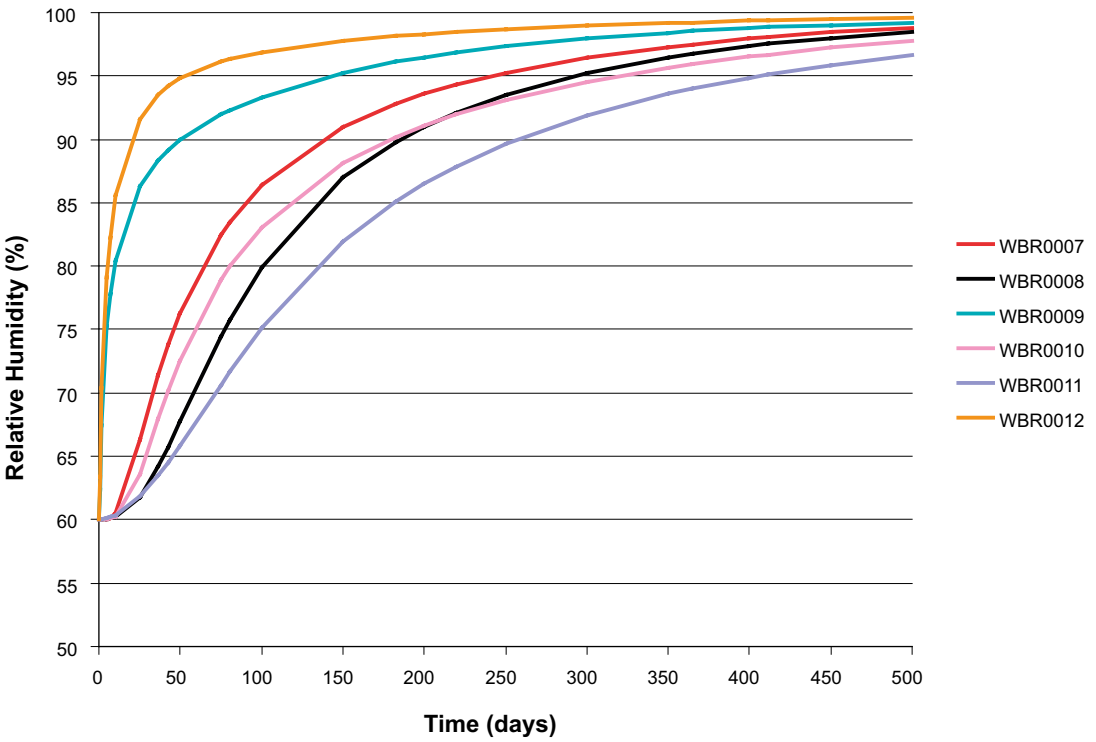

Figure A2-6. *The evolution of relative humidity calculated at sensor locations within the bentonite during the first 500 days post installation. Results are presented for sensors WBR0007 through WBR0012, corresponding to deposition hole KO0018G01.*

Pressures in the deposition hole near field

Contour plots of liquid pressures local to KO0017G01 and KO0018G01 are shown in Figure A2-7 and Figure A2-8, for two separate slices through the seventh realisation of the upscaled DFN model. These correspond to

- a vertical cross-section incorporating both deposition holes, and oriented parallel with the TASO tunnel central line is shown in Figure A2-7 at 0, 0.1, 0.5, 1, 10, and 100 years.
- a horizontal cross-section positioned at an elevation of −418.5 m, and cutting through both deposition holes is shown in Figure A2-8 at 0, 0.1, 0.5, 1, 10, and 100 years.

Equivalent results for realisation 2 of the stochastic fracture network are shown in Figure 6-14 and Figure 6-16. Profiles of liquid pressure are broadly unchanged between realisations, with resaturation dominated by the orientation and location of hydraulically active intersecting fractures.

Saturations in the deposition hole near field

Contour plots of liquid saturation local to KO0017G01 and KO0018G01 are shown in Figure A2-9 and Figure A2-10, for two separate slices through the seventh realisation of the upscaled fracture network model:

- Liquid saturation on a vertical cross-section, corresponding to Figure A2-7 and incorporating both deposition holes is shown in Figure A2-9 at 0, 0.1, 0.5, 1, 10, and 100 years.
- Liquid saturation on a horizontal cross-section, corresponding to Figure A2-8, and cutting through both deposition holes at −418.5 m is shown in Figure A2-10 at 0, 0.1, 0.5, 1, 10, and 100 years.

Equivalent results for realisation 2 of the stochastic fracture network are shown in Figure 6-16 and Figure 6-17. Profiles of liquid saturation are broadly unchanged between realisations, with resaturation dominated by the orientation and location of hydraulically active intersecting fractures.

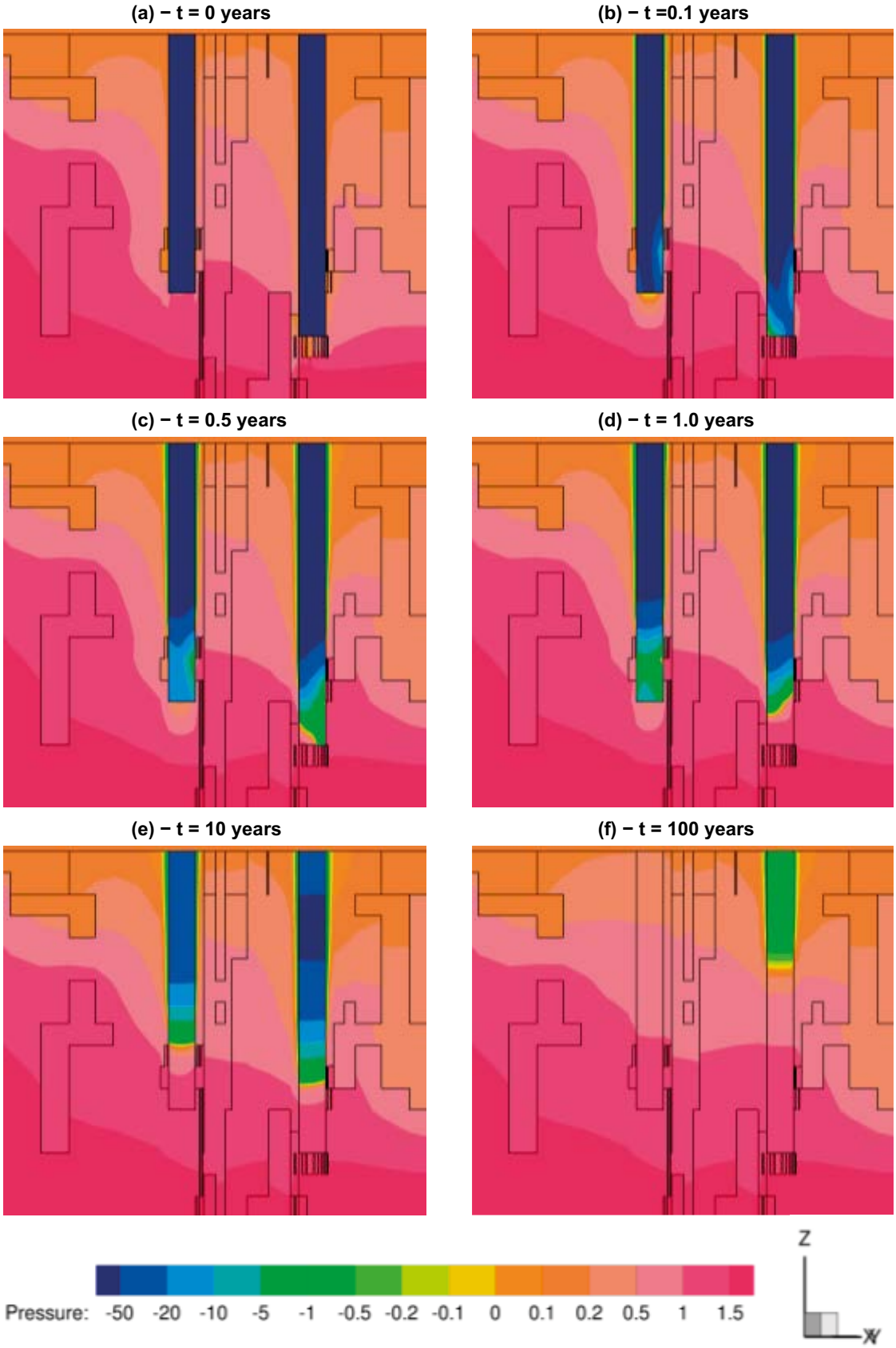

Figure A2-7. *Evolution of liquid pressure (MPa) within the bentonite for a vertical slice, oriented to include the two overcored boreholes KO0017G01 and KO0018G01. Results are shown for the seventh realisation of the upscaled stochastic fracture network.*

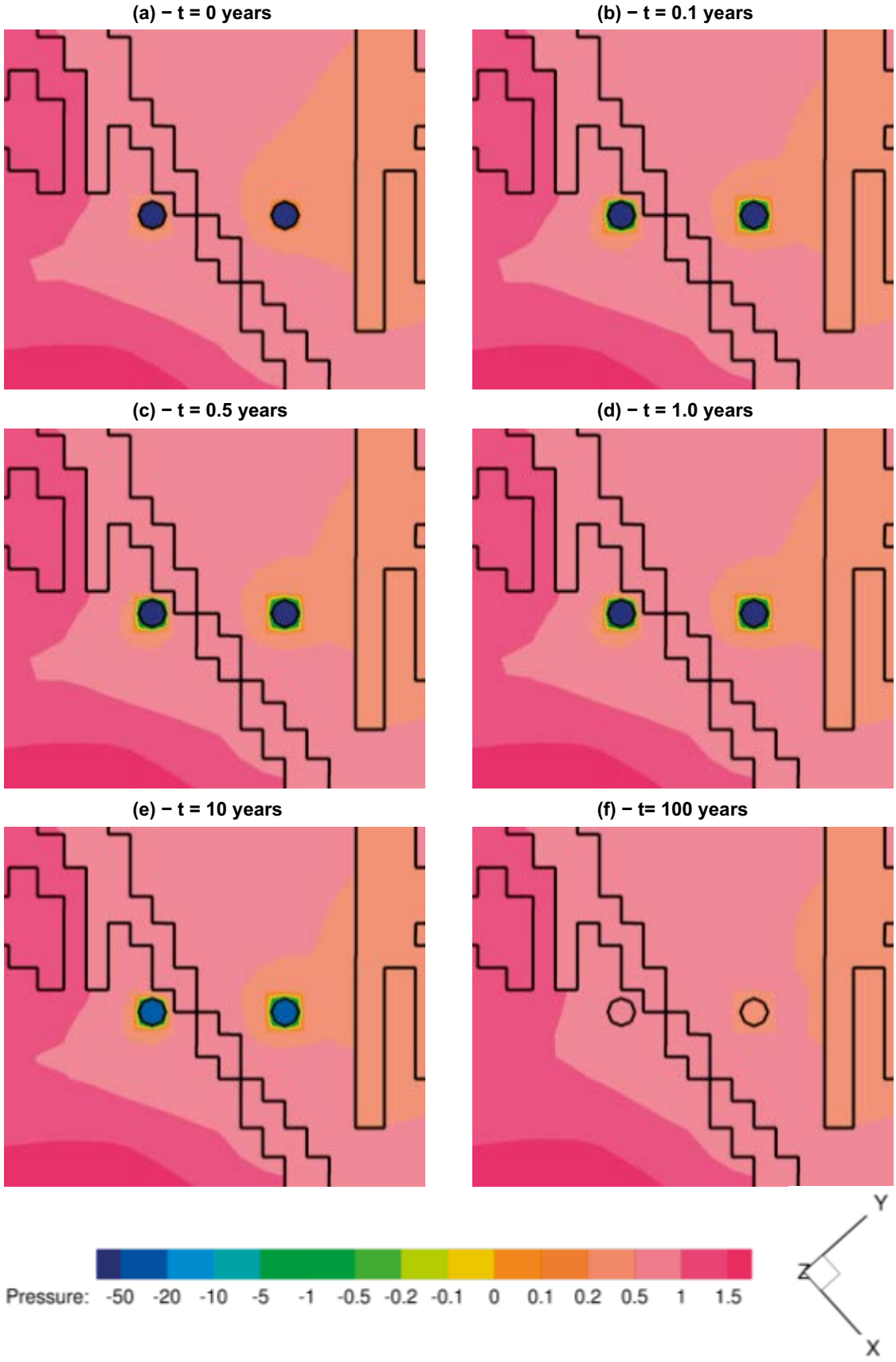

Figure A2-8. *Evolution of liquid pressure (MPa) within the bentonite across a horizontal slice, taken 1.5 m below the TASO tunnel at an elevation of −418.5 m. Results are shown for the seventh realisation of the upscaled stochastic fracture network.*

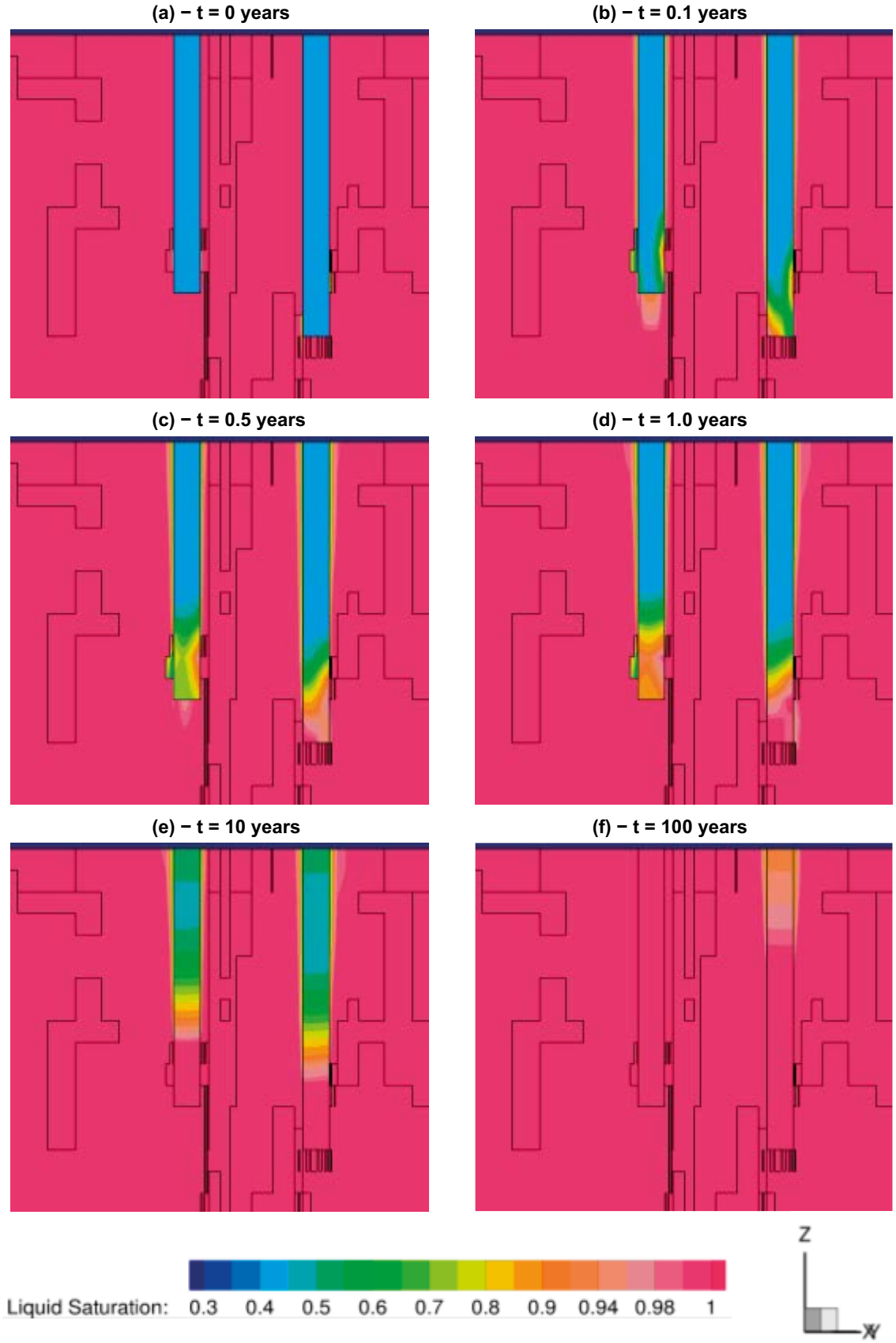

Figure A2-9. *Evolution of liquid saturation within the bentonite for a vertical slice oriented to include the two overcored boreholes KO0017G01 and KO0018G01. Results are shown for the seventh realisation of the stochastic fracture network.*

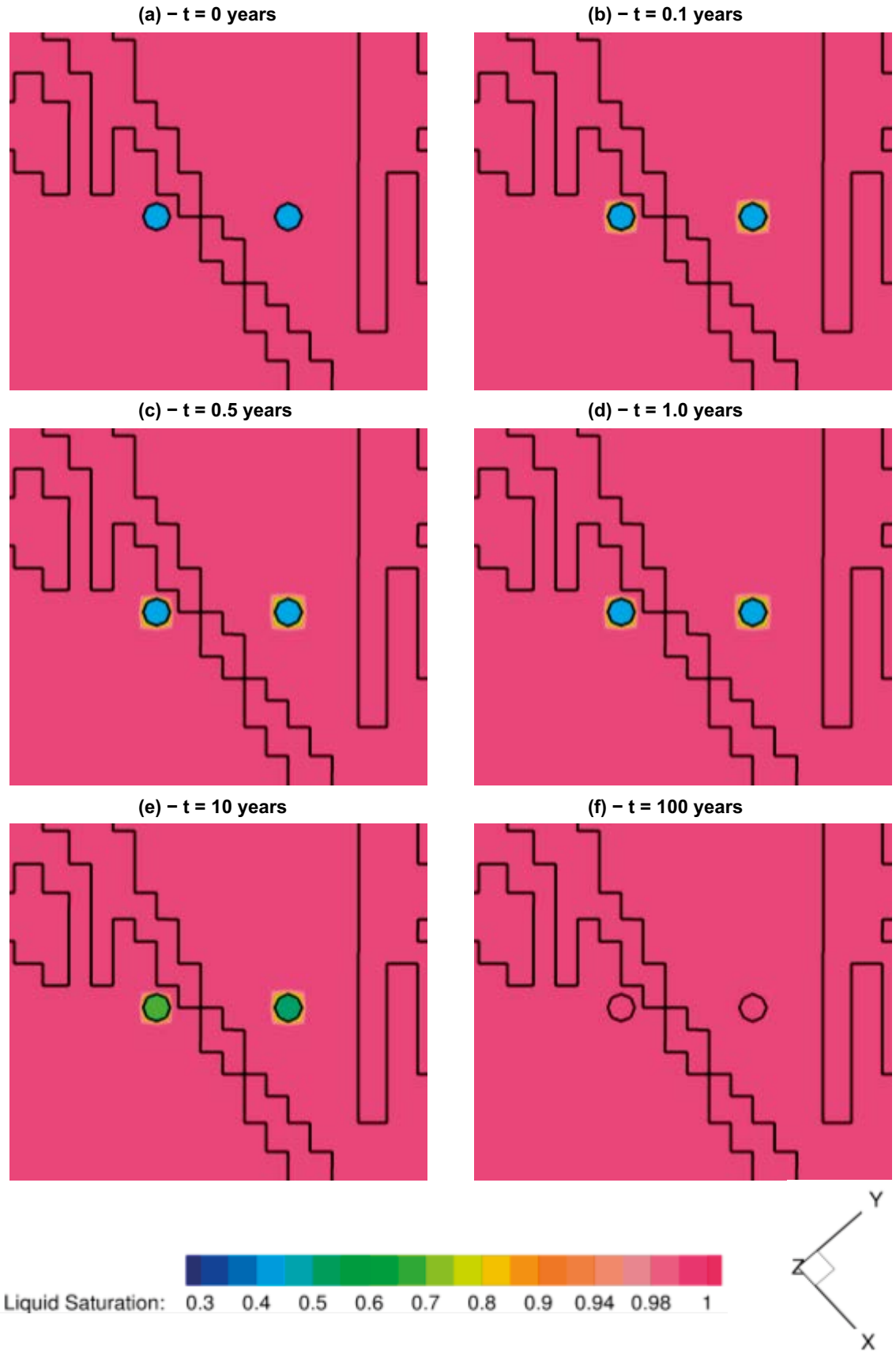

Figure A2-10. *Evolution of liquid saturation within the bentonite across a horizontal slice, taken 1.5 m below the TASO tunnel at an elevation of −418.5 m. Results are shown for the seventh realisation of the stochastic fracture network.*

Arkitektkopia AB, Bromma, 2017

SKB is responsible for managing spent nuclear fuel and radioactive waste produced by the Swedish nuclear power plants such that man and the environment are protected in the near and distant future.

skb.se